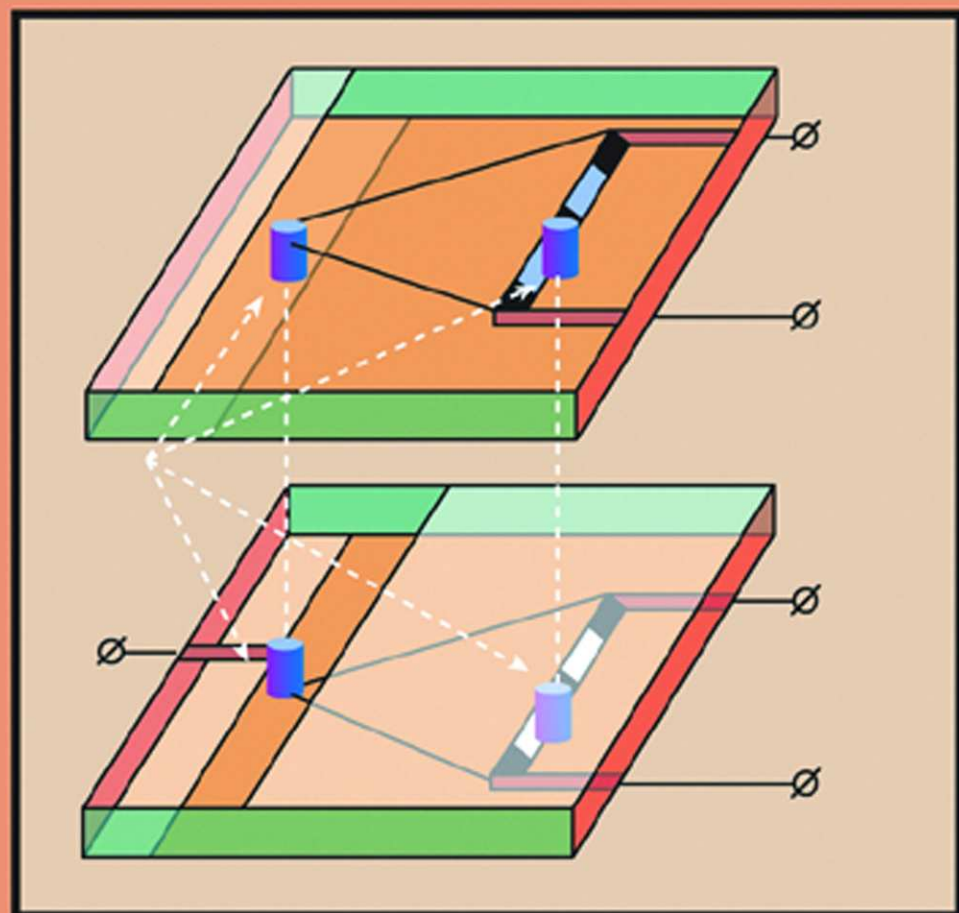# Passive RF & Microwave Integrated Circuits

Leo G. Maloratsky

RF and Microwave Integrated Circuits

Passive Components and Control Devices

This Page Intentionally Left Blank

RF and Microwave Integrated Circuits

Passive Components and Control Devices

by Leo G. Maloratsky

ELSEVIER

Amsterdam • Boston • Heidelberg • London
New York • Oxford • Paris • San Diego
San Francisco • Singapore • Sydney • Tokyo

Newnes

To my mother, Slava Maloratsky.

This Page Intentionally Left Blank

Contents

Preface

I have primarily intended this book to be a text for RF and microwave engineers just entering the field of integrated circuit design. However, it should also be instructive to students in advanced electronics courses and useful to experienced engineers as a reference text. This book is based largely on my personal development work, publications, and patents in the field of passive components, control devices, and subsystems, and it particularly stresses the integration of circuit functions. In addition to my own designs, it refers to extensive results obtained by many scientists and engineers who have published their works in textbooks, journals, and conference proceedings.

<div align="right">

Leo G. Maloratsky
Indialantic, Florida
2004

</div>

This Page Intentionally Left Blank

Acknowledgments

This Page Intentionally Left Blank

CHAPTER 1

Introduction

The last four decades have been marked by rapid developments in RF and microwave integrated circuits and by their wide application in a variety of commercial and military systems. Examples of systems in which such integrated circuits have been applied range from cellular telephones and microwave links on the commercial side to missile and electronic warfare systems on the military side, with many dual-use types of applications such as in radar and navigation systems.

It is well proven in many areas of electronics that integrated circuits offer the advantages of compact, lightweight designs with enhanced performance, higher reliability, and lower cost. Integration of RF and microwave circuits offers similar advantages for the most part; however, performance and cost can sometimes be compromised, as will be discussed later.

RF and microwave integrated circuits, which we will generically refer to as "MICs" throughout this book, are based on the use of:

- Planar transmission lines;
- Distributed and lumped passive components;
- Solid-state devices;
- Special fabrication technologies.

In order to focus on the fundamentals of RF and microwave circuit design, this book will treat *passive components* and *control devices* only. Thus, the solid-state devices considered will all be two-terminal in nature (i.e., the application of transistors in circuits will be omitted and only diodes will be included). The fundamental principles learned in handling diode circuits can be later applied by the student to the more complex, active circuits, which, of course, include transistors.

Historically, the development of planar passive components and devices was in the 1950s, when Barret and Barnes invented a symmetrical stripline [1]. After that, Wheeler [2] and others introduced planar directional couplers, along with a series of new devices. The search for new solutions in passive components and control devices, as well as integrated circuits based on them, continues today. Passive components are prevalent in RF and microwave integrated circuits. For example, it is estimated that in a single-mode telephone, passive components account for 90% of the component count, 80% of the size, and 70% of the cost [3].

This book is unique in several ways, notably for following topics:

- Detailed analysis of symmetrical networks that are used widely in RF and microwave integrated circuits (Chapter 6);
- Systematic classification of directional couplers and correlation between different types of directivity and symmetry (Chapter 7);
- Detailed analysis of effects of termination mismatching, transmission line losses, fabrication tolerances, and discontinuities of parameters of passive elements (Chapters 7 and 8);
- Discussion of irregular lines, that is, a new configuration of transmission lines that extends possibilities for future design (Chapters 3, 9, and 11);
- Description of a series of novel passive elements and devices, including terminations and planar inductors (Chapters 4 and 9); miniature directional coupler (Chapter 7); dividers/combiners (Chapter 8); wiggly coupled line BPF (Chapter 9); phase shifter (Chapter 11); switch channel attenuator (Chapters 10 and 13); and ferrite and nonferrite isolators/circulators (Chapter 12);
- Discussion of microwave integrated subassemblies (Chapter 13), including multifunctional TX/RCV module, electrically tunable preselector, switchable balanced amplifier, high-accuracy high-power step attenuator, multichannel receiver, and single antenna radio altimeter TX/RCV;

TABLE 1.1. Components and Devices Considered in This Book

Transmission Lines	Simple Elements	Components	Ferrite Devices	Diode Control Devices
Planar lines	Capacitors	Directional couplers	Isolators	Switches
Coupled lines	Inductors	Dividers/ Combiners	Circulators	Variable attenuators
Irregular lines	Resistors	Filters	Phase shifters	Limiters
	Terminations			Phase shifters
	Attenuators			
	Resonators			
	Discontinuities			

- Discussion of principal concepts of design and fabrication technology (Chapter 14).

The reader of this book will accomplish the ascension from microwave fundamental transmission lines and simplest elements to more complicated devices and subassemblies, meeting more than 20 novel transmission lines, components, devices, and subassemblies in this way.

Passive components and control devices will be considered in the following order. First, we will discuss planar transmission lines, which are the basis of RF and microwave integrated circuits. Then we will consider the simplest circuit elements, and finally we will consider more complicated semiconductor and ferrite devices and also several subsystems and systems using these elements and devices. All base components and devices considered in this book are summarized in Table 1.1.

REFERENCES

1. Barret, R. M., and M. H. Barnes, "Microwave Printed Circuits," *National Conf. on Airborne Electronics, IRE,* Ohio, May 1951.
2. Wheeler, H. A., "Directional Coupler," U.S. Patent No. 2,606,974, filed May 16, 1946, issued August 12, 1952.
3. Pulsford, N., "Passive Integration Technology: Targeting Small, Accurate RF Parts," *RF Design,* November 2002, pp. 40–48.

This Page Intentionally Left Blank

CHAPTER 2

Characteristics of Planar Transmission Lines
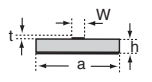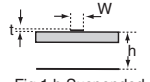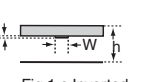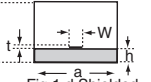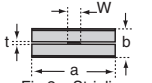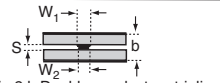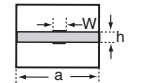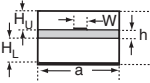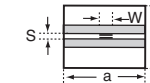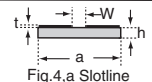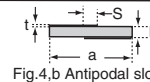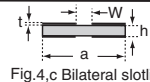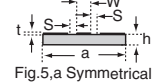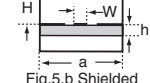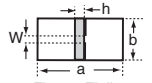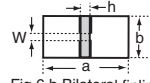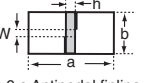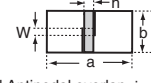
2.1. INTRODUCTION

There are several reasons for the wide use of planar transmission lines [1–4]. First of all, they are broadband, while providing compact dimensions and light weight. Foremost, they are generally economical to produce as they are readily adaptable to hybrid and monolithic integrated circuit fabrication technologies at RF and microwave frequencies.

Commonly used types of planar transmission lines for MICs are shown in Table 2.1 [1]. Each of these types offers certain advantageous features with respect to other types. The various features of the different types illustrated in Table 2.1 will be discussed in the remainder of this chapter.

In general, planar transmission lines consist of strip metallic conductors, usually produced by some photographic process, on a nonconducting substrate. Typical substrate materials are slabs of dielectric, ferrite, or high-resistivity semiconductors. In most cases, there are metal ground planes that can either be printed on the same substrate or be a part of the metal housing of a microwave integrated circuit (MIC). It is to be noted in the figures in Table 2.1 that the substrate materials are denoted by gray areas, and conductors and ground planes by bold lines.

TABLE 2.1. Commonly Used Types of Planar Transmission Lines for MIC

	BASIC LINES	MODIFICATIONS		
microstrip line	Fig.1,a Microstrip line	Fig.1,b Suspended microstrip line	Fig.1,c Inverted microstrip line	Fig.1,d Shielded microstrip line
stripline	Fig.2,a Stripline	Fig.2,b Double-conductor stripline		
suspended stripline	Fig.3,a Shielded high Q suspended stripline	Fig.3,b Shielded suspended stripline	Fig.3,c Shielded suspended double-substrate stripline	
slotline	Fig.4,a Slotline	Fig.4,b Antipodal slotline	Fig.4,c Bilateral slotline	
coplanar waveguide	Fig.5,a Symmetrical coplanar waveguide	Fig.5,b Shielded coplanar waveguide		
finline	Fig.6,a Finline	Fig.6,b Bilateral finline	Fig.6,c Antipodal finline	Fig.6,d Antipodal overlapping finline

2.2. STRIPLINE

The earliest form of planar transmission lines was stripline [illustrated in Figure 2(a) of Table 2.1]. Stripline consists of a strip conductor centered between two parallel ground planes with two equal slabs of a dielectric, ferrite, or semiconductor medium separating the center conductor from the ground planes. Usually, the medium is a solid material, but in some applications air is the actual dielectric used. The advantages of striplines are good electromagnetic shielding and low attenuation losses, which make them suitable for high-Q and low-interference applications.

However, striplines require strong symmetry and thereby present difficulties in the design of many circuit functions. Also, the tuning of circuits becomes difficult, because it usually requires destruction of the symmetry

to access the center conductor. Any vertical asymmetry in the stripline structure could couple to waveguide-type modes bounded by the ground planes and the side walls. Also, with few exceptions of circuit configuration, the stripline structure is not convenient for incorporating chip elements and associated bias circuitry.

Transverse electric and magnetic (TEM) waves propagate within the stripline. Such waves have electric and magnetic components in a plane transverse to the direction of propagation. For dielectric and semiconductor media, the maximum operating frequency f_{max} in this type of line is limited by the appearance of a higher-order waveguide mode of H-type and determined by

$$f_{max} = \frac{300}{\sqrt{\varepsilon}\left[2W + \dfrac{\pi b}{2}\right]}\,(GHz),$$

where ε is the relative dielectric constant of the substrate medium and W and b are, respectively, the stripline width and ground-plane spacing expressed in millimeters.

To prevent the excitation of higher-order modes in stripline, screws or eyelets run on each side of the stripline center conductor. These grounded elements have less than a quarter-wavelength spacing between them. In the case of dielectric or semiconductor substrates, the actual stripline wavelength Λ is given by the well-known expression:

$$\Lambda = \frac{\lambda}{\sqrt{\varepsilon}}, \tag{2.1}$$

where λ is the free-space wavelength. Since ε is generally greater than unity, the stripline wavelength is less than the free-space wavelength.

The characteristic impedance of a stripline is given by [5]

$$Z_0 = \frac{\eta}{2\pi\sqrt{\varepsilon}}\ln\left\{1 + \frac{4(b-t)}{\pi W_{eff}}\left[\frac{8(b-t)}{\pi W_{eff}} + \sqrt{\left(\frac{8(b-t)}{\pi W_{eff}}\right)^2 + 6.27}\right]\right\}(\Omega), \tag{2.2}$$

where

$$\eta = 120\pi,$$
$$W_{eff} = W + \Delta W,$$
$$\Delta W = \frac{t \ln \left[\dfrac{5(b-t)}{t} \right]}{3.2} \quad \text{(from [6])},$$

(2.3)

where t is the center-conductor thickness.

The characteristic impedance of stripline depends on the dielectric constant and on the cross-sectional geometry of the strip center-conductor and ground planes. Figure 2.1 shows how it varies as a function of the line parameters [7, 8]. Note that it is normalized to the product $\sqrt{\varepsilon}Z_0$ so that the effect of the dielectric constant is removed from the curves; also, the center-conductor width and thickness are normalized to the ground-plane spacing to allow scaling. Characteristic impedance is evidently very sensitive to the ratio of center-conductor width to substrate thickness and relatively insensitive to the ratio of center-conductor thickness to substrate thickness. Consequently, mechanical tolerances would be most critical for relatively thin substrates or relatively narrow center conductors.

Besides characteristic impedance, another important parameter of striplines is loss, or attenuation. Total power losses per unit axial length obey the following equation:

$$\alpha = \alpha_d + \alpha_c,$$

(2.4)

where α_d is the contribution due to dissipative losses within the dielectric substrate material, and α_c is the conductor (or ohmic) loss, or the contribution due to power dissipation in the metallic conductors.

The dielectric loss is governed by the expression

$$\alpha_d = \frac{27.3\sqrt{\varepsilon}\tan\delta}{\lambda} \quad \text{(dB/unit length)},$$

(2.5)

where $\tan\delta$ is the loss tangent of the dielectric material.[*] The dielectric loss is proportional to frequency, and it is the dominant loss factor at

---

*With a ferrite substrate, a magnetic loss component will be present; also, the expression for wavelength will be different. We have considered only nonferrite materials thus far; ferrite materials and their losses will be discussed later.
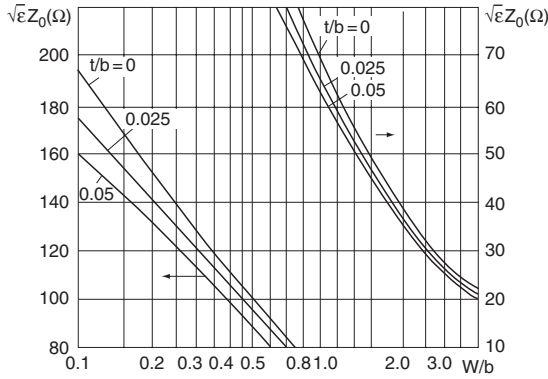
Figure 2.1. Characteristic impedance of stripline transmission line.

higher frequencies. Dielectric losses may be considered very low when the dissipation factor $\tan\delta$ is below 0.0005; medium when $\tan\delta$ is between 0.0005 and 0.002; and high when $\tan\delta$ is greater than 0.002.

The ohmic skin losses in the strip conductor and the ground plane depend on the conductivity of the metal conductors and on any surface roughness such as may be caused by etching or machining in fabrication of the transmission line. The conductor loss can be found by Wheeler's incremental inductance rule:

for $\sqrt{\varepsilon}\,Z_0 < 120\,\Omega$

$$\alpha_c = \frac{23.4 \cdot 10^{-3}\,\mathrm{R_s}\,\varepsilon\,Z_0}{30\pi\left(b-t\right)}A\ \text{(dB/m)},$$

for $\sqrt{\varepsilon}\,Z_0 > 120\,\Omega$

$$\alpha_c = \frac{1.39 R_S}{Z_0 b}B\ \text{(dB/m)}$$

with

$$A = 1 + \frac{2W}{b-t} + \frac{1}{\pi}\frac{b+t}{b-t}\ln\left(\frac{2b-t}{t}\right),$$

$$B = 1 + \frac{b}{\left(0.5W + 0.7t\right)}\left(0.5 + \frac{0.414t}{W} + \frac{1}{2\pi}\ln\frac{4\pi W}{t}\right),$$

where

$$R_s = \sqrt{\frac{\pi f \mu}{\sigma}} \tag{2.6}$$

is the surface resistance for the metal conductor and the ground plane, σ is the conductivity of the metal conductor and the ground plane, and μ is the magnetic permeability of the metal.

Conductor losses dominate over dielectric losses for $\tan\delta$ less than 0.001 (for $f = 10$ GHz) and less than 0.003 (for $f = 1$ GHz).

To evaluate the relative loss contributions by the dielectric substrate and the metal conductors, it is instructive to consider the quality factor Q. Unloaded Q depends on both conductor loss and dielectric loss, according to the following relationship:

$$Q = \frac{Q_c}{\left(1 + Q_c\right)tg\delta}, \tag{2.7}$$

where Q_c is the unloaded Q due to the loss in conductor. Typically, high unloaded Q-factor of stripline is about 400 [9].

In the basic stripline [Figure 2(a) of Table 2.1], small air gaps can exist between the two substrate slabs because of conductor thickness and fabrication faults. They are particularly unavoidable when large area substrates and long transmission lines are required for particular circuit applications. A dominant leaky mode can exist in such structures. This mode radiates into the fundamental TM_0 mode of the background structure and results in undesirable crosstalk and spurious performance [10].

The detrimental effect of such gaps can be eliminated by using mirror-image conductors on the top of the bottom substrate and on the bottom of the top substrate [Figure 2(b) of Table 2.1]. Since the two conductors would naturally be in contact with the dielectric with about the same random periodicity, the electromagnetic propagation in both substrates tends to be equalized. This nominally cancels the electric field in the gaps. In practice, the widths of two center conductors are purposely made slightly different ($W_1 \neq W_2$). The wider conductor is given the required width for the desired characteristic impedance, and the other conductor is made slightly smaller. In this way, even if the conductors are somewhat misaligned, the effective width appears constant at the proper value.

2.3. MICROSTRIP LINE

The microstrip line [Figure 1(a) of Table 2.1] is a transmission line geom-
etry with a single conductor trace on one side of a dielectric substrate and
a single ground plane on the other side. Since it is an open structure,
microstrip line has a major fabrication advantage over the stripline. It also
features ease of interconnection and adjustments.

As with stripline, the wavelength Λ in the microstrip line is given by

$$\Lambda = \frac{\lambda}{\sqrt{\varepsilon_{eff}}}, \tag{2.8}$$

where ε_{eff} is the effective dielectric constant, which depends on substrate
dielectric constant and physical dimensions of the microstrip line; again,
λ is the free-space wavelength.

In the microstrip line, the electromagnetic fields exist partly in the air
above the dielectric substrate and partly within the substrate itself. Intu-
itively, the effective dielectric constant of the line is expected to be greater
than the dielectric constant of air ($\varepsilon = 1$) and less than that of the dielectric
substrate. The expression for ε_{eff} is given approximately by [11, 12]

$$\varepsilon_{eff} = \frac{\varepsilon+1}{2} + \frac{\varepsilon-1}{2} \frac{1}{\sqrt{1+12h/W}}. \tag{2.9}$$

In this expression, the influence of a conducting cover and walls is not
taken into account (i.e., the shielding is assumed to be far enough).

For most practical purposes, microstrip can be treated as a TEM trans-
mission line with an effective dielectric constant that is a weighted aver-
age between air and the substrate material. The curves for effective
dielectric constant are shown in Figure 2.2 as a function of physical
dimensions and dielectric constant.

The actual propagation of electromagnetic waves in microstrip is not
purely TEM due to the combination of an open air space and a dielectric
medium. It is largely TEM, but in reality, microstrip lines, unlike strip-
lines, are dispersive, which means that the wave velocity varies with fre-
quency rather than remaining a constant. This results in the varying of the
effective dielectric constant—and the characteristic impedance—with the
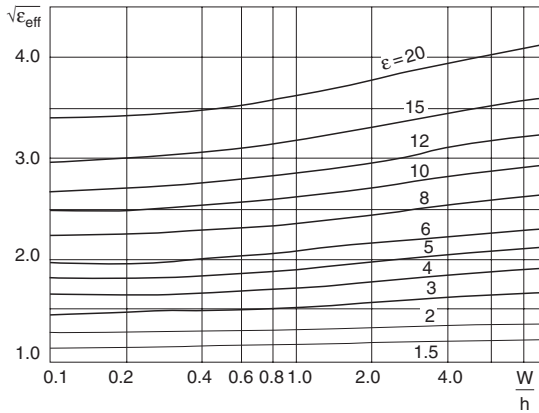
Figure 2.2. Microstrip line effective dielectric constant for different substrate relative dielectric constants and W/h.

frequency of the transmitted signal. Dispersion in microstrip lines exists for all frequencies, but may be ignored for the following frequencies:

$$f = 0.3 \sqrt{\frac{Z_0}{h(\varepsilon - 1)}} \text{ (GHz)},$$

where h is in millimeters.

In most practical applications of microstrip lines, dielectric materials and dimensions are chosen so that dispersion is negligible. The propagation is dispersive in that the effective dielectric constants vary with the free-space wavelength λ; in nondispersive systems, ε_{eff} would be constant with λ. The dispersion becomes more pronounced with the decreasing ratio of strip width to substrate thickness, W/h. Conversely, dispersion is less pronounced as the strip width becomes relatively wider and the microstrip line (ML) physically starts to approach an ideal parallel-plate transmission line, which of course supports a dominant (nondispersive) TEM mode.

2.3.1. Shielded Microstrip Line

We mentioned several practical considerations in the foregoing discussion on microstrip. Referring to Table 2.1 and the basic microstrip line in Figure 1(a) of Table 2.1, we note that it is not really a practical structure. It is
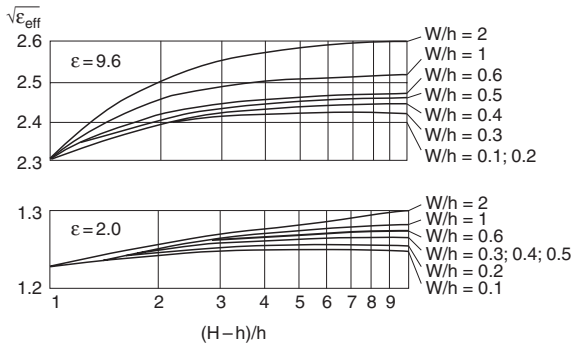
Figure 2.3. Effective dielectric constant as a function of relative dielectric constant and physical dimensions for a shielded microstrip line.

open to the air, and in reality, it is desirable to have circuits that are covered to protect them from the environment, as well as to prevent radiation and electromagnetic interference (EMI). Also, the microstrip configurations that we have been discussing are transversally infinite in extent, which deviates from reality. Covering the basic microstrip with metal plates on the top and sides leads to a more realistic *shielded microstrip line* [Figure 1(d) of Table 2.1]. The top and side covers essentially redistribute the field of the more theoretical microstrip and understandably have an influence on the effective dielectric constant.

Figure 2.3 illustrates the relationship between effective dielectric constant and physical dimensions of the shielded microstrip line for different values of the relative dielectric constant of substrate material [13]. In these curves, it has been assumed that the side walls are sufficiently spaced so that they see only weak, fringing fields and, therefore, have a negligible effect on ε_{eff}. The top cover tends to lower the effective dielectric constant, which is consistent with intuition—the top wall enables electric fields in the air above the strip conductor, thereby giving the air more influence in determining the propagation characteristics.

2.3.2. Characteristic Impedance of the Microstrip Line

The characteristic impedance of the microstrip line may be approximately calculated by assuming that the electromagnetic field in the line is quasi-TEM. The characteristic impedance of a microstrip line can be calculated as follows [11, 12]

$$Z_0 = \frac{60}{\sqrt{\varepsilon}} \ln\left(\frac{8h}{W} + \frac{W}{4h}\right) (\Omega) \qquad\qquad \left.\begin{array}{l} \text{for } \dfrac{W}{h} \le 1; \\[2ex] \text{for } \dfrac{W}{h} \ge 1 \end{array}\right\} . (2.10)$$

$$Z_0 = \frac{120\pi}{\sqrt{\varepsilon}\left[\dfrac{W}{h} + 1.393 + 0.667\ln\left(\dfrac{W}{h} + 1.444\right)\right]} (\Omega)$$

The characteristic impedance of microstrip lines for various geometries and different relative dielectric constants of substrates is plotted in Figure 2.4(a, b). The curves in Figure 2.5(a, b) illustrate relationships
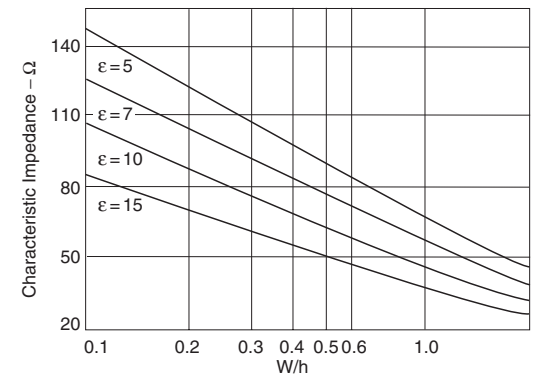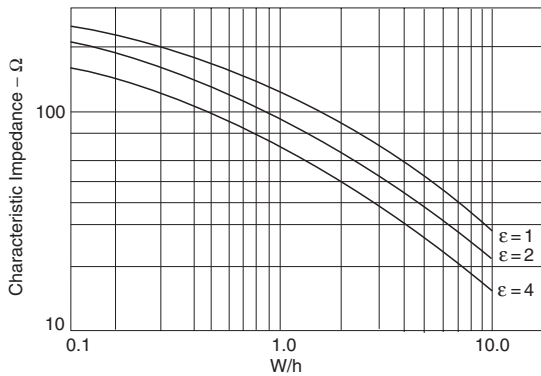
Figure 2.4. Microstrip line characteristic impedance for high (a) and low (b) substrate dielectric constants.

between the characteristic impedance and physical dimensions of shielded microstrip line for two examples: low ($\varepsilon = 2$) and high ($\varepsilon = 9.6$) relative dielectric constants [13]. The top cover tends to lower impedances. When the ratio of the distance from the top cover to the dielectric substrate and the substrate thickness ($(H - h)/h$) is greater than 10, enclosure effects are negligible. The characteristic impedance range of the microstrip line is 20 to 120Ω. The upper limit is set by production tolerances and the lower limit by the appearance of higher-order modes.
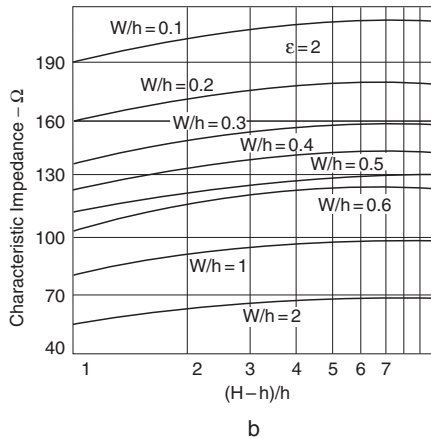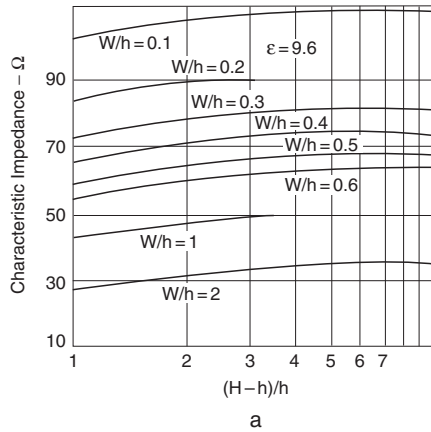
Figure 2.5. Relationship between characteristic impedance and physical dimensions of shielded microstrip line with different substrate dielectric constants: high $\varepsilon = 9.6$ (a) and low $\varepsilon = 2.0$ (b).

2.3.3. Effects of Finite Strip Thickness in Microstrip Lines

Our treatment of microstrip lines started with a TEM nondispersive approximation, which was expanded by taking into account dispersive effects. These effects were due to the fact that the electromagnetic field configuration is not really TEM. This was further expanded upon by considering that a practical structure cannot be completely open to the air, but must be enclosed. It has been implicit that the strip conductor was of negligible thickness. Now we consider the further refinement that real strip conductors have finite thickness, and it is sometimes necessary to correct the physical strip width for it. In Figure 1(a–d) in Table 2.1, the finite thickness, t, leads to an increase of fringing fields that can be taken into account in all the preceding expressions involving the strip width W, by an effective width, recommended by Wheeler:

$$W_{eff} = W + \Delta W,$$

where

$$\Delta W = \frac{t}{\pi}\left(\ln\frac{2h}{t} + 1 \right) \qquad \text{for } \frac{W}{h} \geq 2\pi,$$

$$\Delta W = \frac{t}{\pi}\left(\ln\frac{4\pi W}{t} + 1 \right) \quad \text{for } \frac{2t}{h} < \frac{W}{h} \leq \frac{1}{2\pi}.$$

2.3.4. Attenuation in Microstrip Lines

There are three types of losses that occur in microstrip lines:

1. Conductor (or ohmic) losses;
2. Dielectric losses;
3. Radiation losses.

We now consider each of these three contributions to loss, or attenuation.

Radiation Losses

An idealized microstrip line, being open to a semi-infinite air space, acts similarly to an antenna and tends to radiate energy. Radiation losses are a

major problem for open microstrip lines with low ε. Low dielectric constant substrates ($\varepsilon \leq 5$) are used when cost reduction is a priority. Similar materials are also used with millimeter waves to avoid excessively tight mechanical tolerances. However, the lower the dielectric constant, the less the concentration of energy in the substrate region, and, hence, the greater the radiation losses. Radiation losses depend on the dielectric constant, the substrate thickness, and the circuit geometry. For the matched microstrip line, radiation losses are [14]

$$\alpha_r = 60 \left(\frac{2\pi h}{\lambda} \right)^2 \left[1.0 - \frac{\varepsilon_{eff} - 1}{2\sqrt{\varepsilon_{eff}}} \log \left(\frac{\sqrt{\varepsilon_{eff}} + 1}{\sqrt{\varepsilon_{eff}} - 1} \right) \right]. \tag{2.11}$$

Of course, radiation losses are not a consideration in closed microstrip lines with top cover and side walls. However, there is a related phenomenon, crosstalk, which will be considered later.

The use of high dielectric constant substrates reduces radiation losses because most of the electromagnetic field is concentrated in the dielectric between the conductive strip and the ground plane. The real benefit in having a higher dielectric constant is that the package size decreases by approximately the square root of the dielectric constant. This is an advantage at low frequencies, but may be a problem at higher frequencies due to tolerances.

Conductor Losses

In most conventional microstrip designs with high substrate dielectric constant, conductor losses in the strip conductor and the ground plane dominate over dielectric and radiation losses. Conductor losses are a result of several factors related to the metallic material composing the ground plane and walls, among which are conductivity, skin effect, and surface roughness. In idealized lines, the conductivity is taken as infinite and the current distribution in the metal becomes a surface, sheet current. With finite conductivity, there is a nonuniform current density starting at the surface and exponentially decaying into the bulk of the conductive metal. This is the alleged skin effect, and its effects can be visualized by an approximation consisting of a uniform current density flowing in a layer near the surface of the metallic elements to a uniform skin depth δ (see Figure 2.6). The skin depth, δ, of the conductor is given by

$$\delta = \sqrt{\frac{1}{\pi f \mu \sigma}}, \tag{2.12}$$

where f is the frequency, σ is the conductivity of the metal composing the strip conductor and the ground plane, and μ is the magnetic permeability of the metal (which for nonferromagnetic materials is μ_0, the permeability of free space).

Appendix B lists values of skin depth and volume resistivity for frequently used conductors. To minimize conductor loss and simultaneously minimize the amount of metallic material flanking the dielectric, the conductor thickness should be greater than approximately three to five times the skin depth. The ohmic losses in the metallic conductors can be related to a surface resistance, R_s [see (2.6)].

For the range of strip-width/dielectric-thickness ratios $1/2\pi < W/h \leq 2$, the attenuation due to conductor losses α_c is expressed by [15]

$$\alpha_c = \frac{8.68 R_s}{2\pi Z h}\left[1 - \left(\frac{W}{4h}\right)^2\right]\left[1 + \frac{h}{W} + \frac{h}{\pi W}\left(\ln\frac{2h}{t} - \frac{t}{h}\right)\right]\left(\frac{dB}{unit\ length}\right).$$
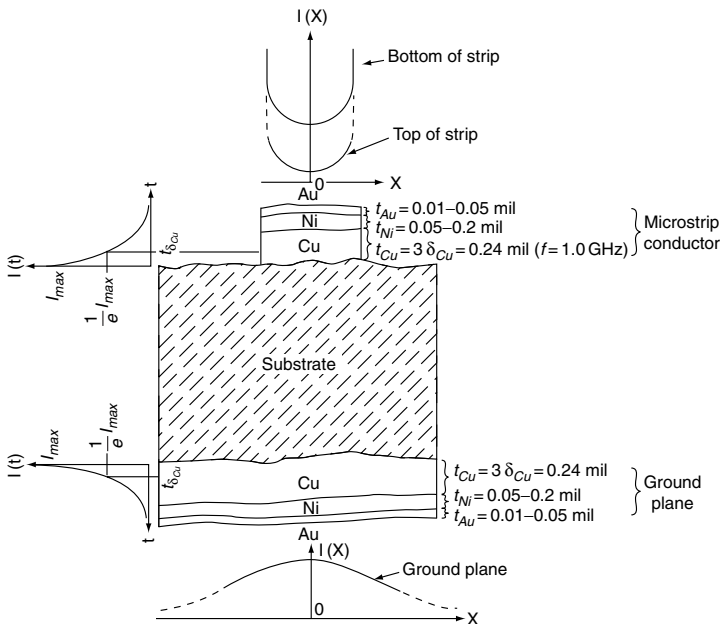
Figure 2.6. Current distribution across microstrip conductor and ground plane.

For $W/h \leq 1/2\,\pi$, conductor losses are

$$\alpha_c = \frac{8.68R_s}{2\pi Z h}\left[1-\left(\frac{W}{4h}\right)^2\right]\left[1+\frac{h}{W}+\frac{h}{\pi W}\left(\ln\frac{4\pi W}{t}+\frac{t}{W}\right)\right]\quad\left(\frac{dB}{unit\ length}\right).$$

In a microstrip line, conductor losses increase with increasing charac-teristic impedance due to the greater resistance of narrow strips. Conduc-tor losses follow a trend that is opposite to radiation loss [see (2.11)] with respect to W/h.

The fabrication process of real microstrip devices creates scratches and bumps on the metal surfaces. A cross-section of the microstrip line conductor is shown in Figure 2.7(a) [1, 13]. The inside surfaces of the strip conductor and the ground plane facing the substrate repeat the shape of the substrate. The current, concentrated in the metal surface next to the substrate, follows the uneven surface of the substrate and encounters greater resistance as compared with the case of a smooth substrate. As the roughness of the substrate surface increases, the length of the current path increases, and, therefore, the losses increase.

Consider a substrate surface which, for example, coincides with the shape of the diamond abrasive material that is used to polish the substrate. The path of the current in conductor segment $a\text{-}d$ [see Figure 2.7(a)] is shown by the line $abcd$. For an ideally smooth surface, the length of the current path AB is

$$l_{AB} = Dn,$$

where n is the number of diamond abrasives within the segment AB. The length of the current path for an uneven surface is

$$l_{abcd} = D\left(1+\varphi-\sin\varphi\right)n,$$

where $\varphi = \arccos(1 - 4\,r_a/D)$, and r_a is the arithmetical mean deviation of uneven profile from average line.

The ratio of conductor losses in the case of an uneven surface, α_{cr}, to losses in the case of a perfectly smooth surface, α_{c0} is

$$\frac{\alpha_{cr}}{\alpha_{c0}} = \frac{l_{abcd}}{l_{AB}} = 1+\varphi-\sin\varphi = 1+\arccos\left(1-\frac{4r_a}{D}\right)-2\sqrt{\frac{2r_a}{D}\left(1-\frac{2r_a}{D}\right)}. \quad (2.13)$$
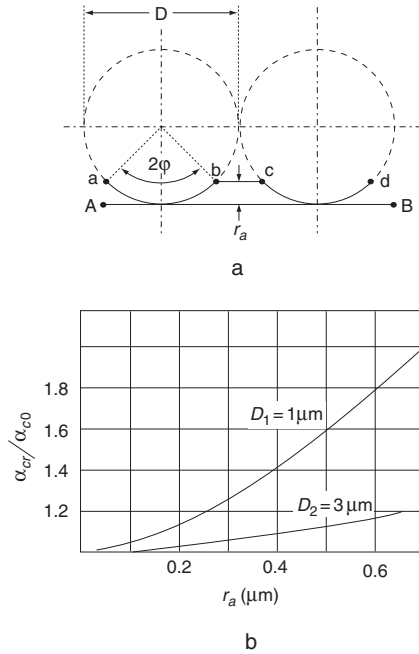
Figure 2.7. Microstrip line conductor losses vs. surface roughness: profile of uneven surface (a); normalized conductor losses vs. surface roughness (b).

Using relationship (2.13), α_{cr}/α_{c0} is plotted as a function of r_a for $D_1 =$ 1 μm and $D_2 = 3$ μm [see Figure 2.7(b)]. Analysis of the resulting functions shows that for smaller diameters, conductor losses in the microstrip line are more dependent on the unevenness of the substrate roughness because the extra path length a surface (or skin) current sees is less. For example [2], consider a copper microstrip line with sapphire substrate where typically the roughness is 1 μm. The skin depth at a few gigahertz is 1 μm, and the loss is increased approximately 60% when the surface roughness is taken into account.

Dielectric Losses

We now consider the losses in the bulk of the dielectric substrates. Dielectric losses per wavelength are usually written as [15, 16]

$$\alpha_d = 27.3 \left(\frac{q\varepsilon}{\varepsilon_{eff}} \right) \frac{\tan\delta}{\Lambda} \quad \left(\frac{dB}{unit\ length} \right),$$

where q is the dielectric filling factor, which is equal to

$$q = \frac{\varepsilon_{eff} - 1}{\varepsilon - 1}.$$

The filling factor is strongly dependent on the ratio of the strip width to ground plane spacing and varies only slightly with the relative dielectric constant of the substrate.

To minimize dielectric losses, high-quality low-loss dielectric substrates like alumina, quartz, and sapphire (see Appendix A), are typically used in hybrid integrated circuits. For most microstrip lines, conductor losses greatly exceed dielectric losses. However, in monolithic microwave integrated circuits, silicon or gallium arsenide substrates result in much larger dielectric losses (approximately 0.04 dB/mm) [2].

Combined Loss Effect

Earlier we considered the individual contributions to losses in microstrip by radiation, ohmic, and dielectric effects. These individual loss components are at most first-order perturbations in the overall electromagnetic wave propagation and consequently can be combined linearly. To do so, it is convenient to consider the total Q-factor, which can be expressed by

$$\frac{1}{Q} = \frac{1}{Q_c} + \frac{1}{Q_d} + \frac{1}{Q_r},$$

where Q_c, Q_d, and Q_r are quality factors corresponding to conductor, dielectric, and radiation losses, respectively.

Quality factor Q_c of the wide microstrip line is expressed as

$$Q_c = 39.5\left(\frac{h}{R_s}\right)f,$$

where h is in centimeters, f is in gigahertz, and R_s is given by (2.6).

Quality factor Q_d is equal to

$$Q_d = \frac{\Lambda}{\tan\delta},$$

where Λ is the guide wavelength in centimeters. The unloaded Q-factor of the microstrip line is typically on the order of 250.

2.3.5. Choosing Physical Dimensions for Microstrip Applications

Peak power-handling capability in microstrip lines is relatively low for two reasons. First, the small thickness of the substrate provides a very narrow region for the electric field. Second, the electromagnetic field concentrates at the sharp edges of the strip. To increase peak power these edges should be rounded, and the thickness of the dielectric substrate should be maximized.

The average power capability of the microstrip line is a function of the permissible temperature rise of the thin strip, which in turn is related to the thermal conductivity of the dielectric substrate. In practice, microstrip lines can be used for an average power of a few tens of watts.

Besides power handling, let us now turn to some other recommendations for choosing the physical dimensions of the microstrip line. For all circuit considerations, a basic approach involves starting with particular ranges of the dimension ratios required to achieve a desired characteristic impedance. Following that, the strip width should be minimized in order to decrease the overall dimensions, as well as to suppress higher-order modes. It is important to remember, however, that a smaller strip width leads to higher losses.

Factors that affect the choice of substrate thickness are the most controversial. The positive effects of decreasing substrate thickness are:

1. Compact circuits;
2. Ease of integration;
3. Less tendency to launch higher-order modes or radiation;
4. The via holes drilled through dielectric substrate contributing smaller parasitic inductances.

However, a decrease in substrate thickness h, while maintaining a constant characteristic impedance Z_o, must be accompanied by a narrowing of the conductor width W. Narrowing W leads to higher conductor losses along with a lower Q-factor. Also, for smaller W and h, fabrication tolerances become more severe. Careless handling of thin substrates can cause

stress and strain, which can modify the performance of the substrate. Thus, one must compromise when choosing substrate thickness.

Microstrip circuit dimensions decrease with increasing substrate dielectric constant. Losses then usually increase because higher dielectric constant materials usually have higher loss tangents, $\tan\delta$, and also because for the same characteristic impedance, reduced conductor line widths have higher ohmic losses. This is a typical conflict between the requirements of small dimensions and low loss. For many applications, lower dielectric constants are preferred since losses are reduced, conductor geometries are larger (and, therefore, more producible), and the cutoff frequency of the circuit increases.

For microwave device applications, microstrip generally offers the smallest sizes and the easiest fabrication. However, it does not offer the highest electrical performance. Attenuation losses and power handling are compromised. In devices where miniaturization is not critical and higher performance is required, it is advisable to use striplines with their accompanying low losses and high Q-factors.

2.4. SUSPENDED STRIPLINE

The suspended stripline (SS) is a modified version of the stripline (see Table 2.2). In the SS, the strip conductor is placed on the surfaces of the thin dielectric substrate, and the substrate is then suspended in a metal enclosure. The major portion of the electromagnetic field is symmetrically confined to the air gaps between the dielectric substrate and the two ground plates. The SS propagation is purely TEM because of the uniform dielectric (air) and symmetrical configuration.

The suspended stripline has the following advantages [17]:

- There are low losses and high Q-factor (up to 500) because most of the propagation energy is in the air dielectric;
- The air dielectric also helps to increase the integrated circuit dimensions, which is crucial for higher microwave frequencies and millimeter-wave devices.
- The dielectric characteristics of the supported substrate have a negligible effect on the attenuation and phase velocity of the transmission medium.

- A wide range of impedance values (up to 150Ω) is available.
- It possesses good temperature stability.
- With good design, it has no waveguide modes.
- It operates over wide bandwidth.
- There is no radiation to the outside.
- Both sides of the suspended substrate are available for circuit patterns enabling broadside strong coupling or combination with microstrip, coplanar, or slotline.

The disadvantages of the suspended striplines are difficulties in miniaturization and critical housing technology.
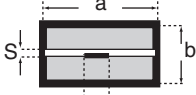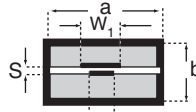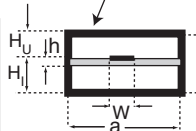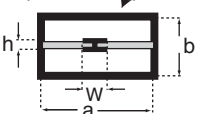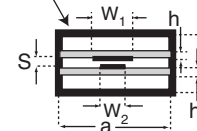
Three different configurations of suspended stripline are shown in Table 2.2 (Figures 3, 4, and 5). In the basic shielded high-Q SS (Figure 4), the parallel strips are printed on both sides of the dielectric substrate in a symmetrical configuration. The top-to-bottom circuit board interconnections are achieved via plated through-holes. This is realized by drilling a hole through the dielectric substrate and then chemically depositing electroless copper inside the walls of the hole in order to bridge the two conductors of the SS.

When the dual-center conductors in the SS are located symmetrically over each other, they are excited in phase, causing most of the electromagnetic field to propagate in the air dielectric. Therefore, dielectric losses of the carrier substrate and variation in its dielectric constant have negligible effects on the attenuation and phase velocity of the transmitted waves. An added benefit of the symmetrical positioning of the conductors is that it prevents the launching of parasitic modes. The symmetrical geometry of SS (Figure 4 of Table 2.2) requires tight tolerances on the etched pattern alignment and additional vias to connect top and bottom strips.

In the one-conductor SS (Figure 3 of Table 2.2), the transmission characteristics depend on the substrate thickness h, the substrate dielectric constant ε, the width of the strip conductor W, and air-space height. Optimization of the characteristic impedance, as well as its weakest dependence on h, occurs when the position of the dielectric substrate inside the housing is somewhat asymmetrical. The spacing above the conductor is slightly smaller than that below the dielectric ($H_U < H_L$). This asymmetrical configuration also slightly reduces the losses.

The ohmic losses in the above two suspended striplines (Figures 3 and 4 of Table 2.2) are a concern. The RF currents become concentrated near

TABLE 2.2. Suspended Striplines Are Modification Versions of Striplines

		Highest Q-factor	No special requirements for plating
Advantages	Simple Configuration	Temperature stability	High integration index
			Low ohmic losses
Disadvantages	Special requirements for plating	Additional vias	
	Non-symmetrical	Special requirements	Dielectric losses
	configuration(high modes)	for plating	
	Dielectric losses		

the outer surface of the metal for an approximate three-skin depth. The highest current density is in top and bottom plated surfaces (Figure 2.8), except silver, that have a lower conductivity than the main copper conductors of printed circuit boards (PCBs).

While bare copper circuits can be etched to high precision, the poor corrosion properties of the metal make it undesirable for practical applications. Therefore, in a great many cases, a microwave PCB has a copper pattern covered with gold plating. Gold is not only a very good conductor, but also has excellent corrosion resistance. However, when the copper-gold combination is etched, accelerated etching takes place because of electromagnetic potentials, resulting in poor edge definition. An additional nickel barrier between copper and gold is used to prevent gold/copper interdiffusion (see Chapter 14). In suspended striplines at lower frequencies, the presence of a nickel-plated layer can produce additional losses due to the skin effect. An alternative is to avoid using nickel or use a thicker gold plating (~100 μinch).

Figure 2.8. SS conductor skin depth and current density $I(t)$.
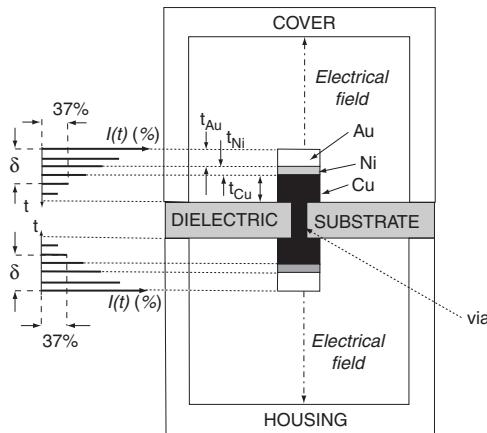
	ONE SKIN DEPTH, δ (μ *inch*) x 10^3			TYPICAL METAL THK (μ *inch*) x 10^3
	Frequency (GHz)			
Material	1.0	5.0	10.0	
Au	97	43.4	30.7	100
Ni	164.4	73.5	52.0	20
Cu	82	36.7	25.9	1400

The new high-Q double-substrate SS (Figure 5 of Table 2.2) [17] offers the advantage of lower ohmic losses, because microwave currents are concentrated in the high-conductivity copper conductors of PCB. This feature also expands the choice of plating material as far as its conductivity, thickness, and technology process. Other advantages of this line are simple contact between the two conductors (no plated-through holes) and more integration by increasing the dielectric thickness or dielectric constant of the two substrates.

In the double-substrate SS, the widths of the two center conductors are purposely made slightly different ($W_1 \neq W_2$), similar to the stripline in Figure 2 in Table 2.2. The wider conductor is given the dimension required for the desired characteristic impedance, and the other conductor is made slightly smaller. In this way, even if the conductors are somewhat misaligned, the effective width appears constant with the proper value.

A suspended stripline circuit consists of a substrate photolithographi-cally etched on a thin copper clad suspended in air between identical housing and cover. The substrate is secured with internal and external walls to add further support to the PCB and provide symmetrical position of the PCB according to the housing and cover. Plated through-holes (vias) and EMI gaskets in the area of the support walls provide grounding connection between the housing and cover, channel-to-channel isolation, and suppress RF leakage and moisture seal with housing and cover parts. The channel dimensions should be chosen so that the spurious waveguide mode propagation is inhibited.

Some recommendations for choosing the physical dimensions of the SS follow. Large height b (the distance between top and bottom ground planes) leads to a higher power capability and Q-factor of the SS. The strip width should be decreased in order to decrease the overall dimen-sions, as well as to suppress the high modes. It is important to remember, however, that a smaller strip width leads to higher losses. Also, a smaller strip for the same impedance requires smaller height. Mechanical toler-ances would be more critical for a relatively small height or relatively nar-row conductors. Any vertical asymmetry in the suspended stripline structure could couple to parasitic waveguide-type modes bounded by the ground planes and the side walls.

Surface modes cannot propagate at frequencies for which the channel is less than half a wavelength in width. The dimensions of the suspended stripline channel in which the substrate is supported must be sufficiently small to avoid propagation of waveguide modes. The cutoff frequency at which the TE_{01} mode becomes dominant is

$$f_c = \frac{c}{2a} \sqrt{1 - \frac{h}{b}\left(\frac{\varepsilon - 1}{\varepsilon}\right)},$$

where a is width of the enclosure.

The thickness of the SS dielectric substrate should be as small as pos-sible to minimize the losses and parasitic inductance of vias and to reduce price. For the new double-substrate SS of Figure 5 of Table 2.2, the sub-strate thickness can be chosen based upon compromise between integra-tion index and dielectric losses.

2.5. SLOTLINE

The slotline was first proposed by Cohn [18]. The three kinds of slotlines are unilateral [Figure 4(a) in Table 2.1], antipodal [Figure 4(b) in Table 2.1], and bilateral [Figure 4(c) in Table 2.1]. The basic unilateral slotline consists of a narrow gap in the conductive coating on one side of the dielectric substrate. The other side of the substrate is bare.

Slotline has the following advantages:

- It is easy to fabricate because it requires only single-sided board etching.
- Shunt mounting of elements is possible without holes through the substrate, since conductors are placed on only one side of the substrate.
- It can be incorporated with microstrip lines for new types of circuits.
- The substrate gives it rigidity.
- The substrate concentrates the field density between the plates, suppressing higher-order modes or radiation.

The disadvantage of the slotline is that its Q-factor is low (around 100), so it is relatively lossy. Another disadvantage arises from the fact that the field configuration deviates greatly from TEM. Thus, the dominant mode is similar to the dominant mode in rectangular waveguide; it is mainly a TE (transverse electric) field. This result in a highly dispersive behavior, which means that slotline is not usually applicable for broadband applications. The presence of both longitudinal and transverse RF magnetic fields in slotline provides elliptic polarization that is useful for nonreciprocal ferrite circulators and isolators.

As would be expected from what we have seen in stripline and microstrip, the characteristic impedance and wavelength in the slotline depend on free-space wavelength, physical dimensions, and dielectric constant. The characteristic impedance of slotline increases with slot width and is less sensitive to substrate height. Typically, the characteristic impedance of the slotline is in the range of 60 to 200Ω.

Effective dielectric constant of the slotline is equal to the average dielectric constant of the two media (dielectric substrate and air):

$$\varepsilon_{eff} = \frac{\varepsilon + 1}{2}. \tag{2.14}$$

As with stripline, the losses in a slotline are the result of the conductor, dielectric, and radiation losses. The conductor losses are generally higher than the dielectric losses [3, 19]. They increase with frequency but decrease with slot width. The bilateral or double-sided slotline [Figure 4(c) of Table 2.1] has two symmetrical identical slots that are on opposite sides of a dielectric substrate. This line needs good accuracy in fabrication because of its two-sided circuit etching, precise alignment, and two-board bonding. Characteristic impedance of the bilateral line decreases with substrate height and increases with the dielectric constant of substrate material.

2.6. COPLANAR WAVEGUIDE

The coplanar waveguide (CPW) was first proposed as an MIC transmission line by Wen [20]. Wen's form of the CPW is shown in Figure 5(a) of Table 2.1. The CPW structure consists of a center strip with two parallel ground planes equidistant from it on either side. The center conductor and ground planes are located in one plane on the substrate surface.

Coplanar waveguides have the advantages of:

* Low dispersion;
* No need for via holes, which introduce undesirable parasitic inductances and limit performance at high frequencies;
* Ease of attaching both shunt and series circuit elements because of no need for via holes;
* Simple realizations of short-circuited ends.

The gap in the coplanar waveguide is usually very small and supports electric fields primarily concentrated in the dielectric. With little fringing field in the air space, the coplanar waveguide exhibits low dispersion. In order to concentrate the fields in the substrate area and to minimize radiation, the dielectric substrate thickness is usually set equal to about twice the gap width.

The coplanar waveguide, in contrast to the microstrip and the stripline, has shielding between adjacent lines, which creates a better isolation between them. Like microstrip and stripline, CPW supports a quasi-TEM dominant mode. At higher frequencies, the field becomes less-TEM, and

more TE in nature. The magnetic field is elliptically polarized and the CPW becomes suitable for nonreciprocal ferrite devices, as with slotline.

In the coplanar waveguide, two fundamental modes are supported: the coplanar mode and the parasitic slotline mode. Air bridges between ground planes have to be applied to suppress the undesired slotline mode. These air bridges must be located at short intervals (less than $\Lambda/4$ apart). Gold ribbons are sometimes used as "bridges" over the center conductor. Conductive bridges can be formed using plated through holes to connect etched line on the underside of the board. Unhappily, ribbons increase insertion losses and make fabrication costly. As in the case of the slotline, the Q-factor of the coplanar waveguide is low (on the order of 150). Besides the parasitic mode and low-Q problems, coplanar waveguides also have other disadvantages: heat sinking capabilities are poor, substrates are required to be relatively thick, and there are higher ohmic losses due to the concentration of its currents near the metal edges.

In practice, the distance b [Figure 5(b) of Table 2.1] should be less than $\Lambda/2$ to prevent propagation of higher-order modes, and the ground planes should extend by more than $5b$ on each side of the gap.

In the CPW, the effective dielectric constant is the same as the slotline solution (2.14), approximately independent of geometry, and simply equal to the average of dielectric constants of air and the dielectric substrate. This equation holds for the coplanar waveguides with dimensions smaller than $h/3$.

Although frequency dispersion for coplanar waveguides is generally small, it should be noted that there is a mild dependence on line dimensions, and narrow lines are less dispersive than wide lines.

Relationships between characteristic impedance of the symmetrical CPW and its dimensions for different relative dielectric constants of substrate are shown in [21]. The characteristic impedance limits are obtained by combining maximum strip width with minimum slot space for the lower limit, and minimum strip width with maximum slot space for the upper limit. CPW is not very sensitive to substrate thickness and allows a wide range of impedance values (20–250Ω) on relatively thick substrates. Upper metal cover has no effect upon characteristic impedance if space $H > 2h$ [see Figure 5(b) of Table 2.1]. When this limit is exceeded, the effect of the cover will be to lower characteristic impedance.

2.7. FINLINE

A finline was proposed by Meier [22]. Different configurations of the finline are shown in Table 2.1 [Figure 6(a–d)] [22, 23]. Basically, finline consists of various forms of slotline placed within a rectangular waveguide. These lines operate typically in the frequency range of 30 to 100 GHz. The main characteristics of the finline are broad bandwidth, moderate attenuation, low dispersion, and compatibility with semiconductor elements. Losses in finlines are approximately on the order of 0.1 dB/wavelength.

In all forms of finline, the substrates employed have low relative dielectric constant ($\varepsilon = 2.2$) substrates, and the resulting dominant mode is

TABLE 2.3. Comparison of the Various Transmission Lines

Transmission Line	Q-Factor	Radiation	Dispersive	Impedance Range (Ohm)	Chip Mounting
Microstrip line	250 (dielectric substrate) 100–150 (Si, GaAs substrate)	Low (for high ε) High (for low ε)	Low	20–120	Difficult for shunt; easy for series
Stripline	400	Low	None	35–250	Poor
Suspended stripline	500	Low	None	40–150	Fair
Slotline	100	Medium	High	60–200	Easy for shunt; difficult for series
Coplanar waveguide	150	Medium	Low	20–250	Easy for series and shunt
Finline	500	None	Low	10–400	Fair

a combination of TE and TM modes, rather than a quasi-TEM. The resulting structure has a wider bandwidth and higher Q values than those of a microstrip line. Losses of the finline are comparable to those of ridged waveguide of the same geometrical dimensions [22].

Since the characteristic impedance range of the finline is from about 10 to 400Ω, it is greater than other printed transmission lines. Also, the finline structure is easy to mate with standard rectangular waveguide structures. Another advantage is that the guide wavelength Λ in finline is longer than that in microstrip, thus permitting less stringent dimensional tolerances at high microwave frequencies. The finline produces circularly polarized fields. This is an advantage for nonreciprocal applications (isolators, circulators, and phase shifters).

2.8. SUMMARY OF PLANAR TRANSMISSION LINES

Table 2.3 compares the various transmission lines [1, 4, 24–33].

REFERENCES

1. Maloratsky, L. G., "Reviewing the Basics of Microstrip Lines," *Microwaves & RF,* March 2000, pp.79–88.
2. Edwards, T. C., *Foundations for Microstrip Circuit Design,* New York: John Wiley & Sons, 1991.
3. Gupta, K. C., et al., *Microstrip Lines and Slotlines,* Norwood, MA: Artech House, 1996.
4. Howe, H., *Stripline Circuit Design,* Dedham, MA: Artech House, 1974.
5. Wheeler, H. A., "Transmission-Line Propitious of a Strip Line Between Parallel Planes," *IEEE Trans. on Microwave Theory Tech.,* Vol. MTT-26, No. 11, November 1978, pp. 866–876.
6. Nauwelaers, B., and A. V. Capelle, "Characteristic Impedance of Stripline," *Electronic Letters,* Vol. 23, No. 18, August 27, 1987, pp. 930–931.
7. Cohn, S. B., "Problems in Strip Transmission Lines," *IRE Trans.,* MTT- 3(2), March 1955, pp. 119–126.

8. Gunston, M. A. R., *Microwave Transmission-Line Impedance Data,* London, England: Van Nostrand Reinhold, 1972.

9. Vendeline, G. D., "Limitations on Stripline Q," *Microwave Journal,* May 1970, pp. 63–69.

10. Nghiem, D., et al., "The Effect of Substrate Anisotropy on the Dominant-Mode Leakage from Stripline with an Air Gap," *IEEE MTT-S International Microwave Symposium,* Vol. 1, 1995, pp. 141–144.

11. Hammerstard, E. O., "Equations for Microstrip Circuit Design," *Proc. of the European Microwave Conference*, Hamburg, Germany, September 1975, pp. 268–272.

12. Bahl, I. J., and D. K. Trivedi, "A Designer's Guide to Microstrip Line," *Microwaves,* May 1977, pp. 174–182.

13. Maloratsky, L. G., *Microminiaturization of Microwave Elements and Devices,* Moscow, Russia: Soviet Radio, 1976.

14. Abouzahra, M. D., and L. Lewin, "Radiation from Microstrip Discontinuities," *IEEE Trans. on Microwave Theory Tech.*, Vol. 27, No. 8, August 1979, pp. 722–723.

15. Pucel, R. A., D. J. Masse, and C. P. Hartwig, "Losses in Microstrip," *IEEE Trans. on Microwave Theory Tech.,* Vol. 16, No. 6, June 1968, pp. 342–350; Correction in IEEE Trans., Vol. MTT-16, December 1968, p. 1064.

16. Schneider, M. V., "Dielectric Loss in Integrated Microwave Circuits," *Bell System Technical Journal,* Vol. 48, 1969, pp. 2325–2332.

17. Maloratsky, L. G., "Reviewing the Basics of Suspended Striplines," *Microwave Journal,* October 2002, pp. 82–98.

18. Cohn, S. B., "Slot-Line on a Dielectric Substrate," *IEEE Trans. on Microwave Theory Tech.,* Vol. 17, 1969, pp. 768–778.

19. Rozzi, T., et al., "Hybrid Modes, Substrate Leakage, and Losses of Slotline at Millimeter-Wave Frequencies," *IEEE Trans. on Microwave Theory Tech.,* Vol. MTT-38, 1990, pp. 1069–1078.

20. Wen, C. P., "Coplanar Waveguide: A Surface Strip Transmission Line Suitable for Nonreciprocal Gyromagnetic Device Applications," *IEEE Trans. Microwave Theory Tech.,* Vol. MTT-17, December 1969, pp. 1087–1090.

21. Simons, R.N., *Coplanar Waveguide Circuits, Components, and Systems,* New York: John Wiley & Sons, 2001.

22. Meier, P. J., "Two New Integrated-Circuit Media with Special Advantages of Millimeter Wave-Length," *IEEE MTT-S Int. Microwave Symp. Digest,* 1972, pp. 221–223.

23. Bhat, B., and S. K. Koul, *Analysis, Design, and Applications of Fin Lines,* Norwood, MA: Artech House, 1987.

24. Wadell, B. C., *Transmission Line Design Handbook,* Norwood, MA: Artech House, 1991.

25. Pozar, D. M., *Microwave Engineering,* New York: John Wiley & Sons, 1998.

26. Maas, S. A., *The RF and Microwave Circuit Design Cookbook,* Norwood, MA: Artech House, 1998.

27. Besser, L., *RF Circuit Fundamentals,* Norwood, MA: Artech House, 2000.

28. Edwards, T. C., and M. B. Steer, *Foundation of Interconnect and Microstrip Design,* New York: John Wiley & Sons, 2000.

29. Itoh, T. (ed.), *Planar Transmission Line Structures,* New York: IEEE Press, 1987.

30. Wheeler, H. A., "Transmission-Line Properties of a Strip on a Dielectric Sheet on a Plane," *IEEE Trans. on Microwave Theory Tech.,* Vol. 25, No. 8, August 1977, pp. 631–647.

31. Volman, V. I. (ed.), *Handbook: Calculation and Design of Microwave Stripline Devices,* Radio and Svyaz, Moscow, Russia, 1982.

32. Choung, Y. H., and W. C. Wong, "Microwave and Millimeter-Wave Slotline Transition Design," *Microwave Journal,* March 1994, pp. 77–89.

33. Ishii, T. K., *Handbook of Microwave Technology: Components and Devices*, Vol. 1, New York: Academic Press, 1995.

CHAPTER 3

Characteristics of Print Coupled Lines
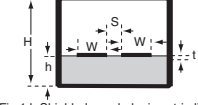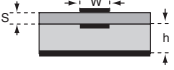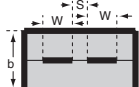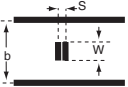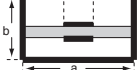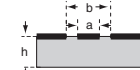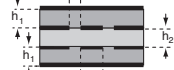
3.1. INTRODUCTION

In this chapter we consider the coupling that occurs when two or more individual transmission lines of the types discussed in Chapter 2 are brought within proximity of one another. Now, not only are there the electromagnetic fields within the individual lines, but modifications, or distortions, in the fields are introduced that link, or *couple*, the individual lines together [1–4]. Coupled lines are very useful and widely applied structures that provide the basis for many types of components: directional couplers, power splitters and combiners, diplexers, filters, phase shifters, and so forth.

Coupled lines can be classified by several different characteristics:

• Coupling value (i.e., whether the coupling is strong or weak);
• The characteristic impedances of the coupled lines [i.e., whether they are equal (symmetrical lines) or nonequal (asymmetrical lines)];
• The type of coupled transmission lines [i.e., whether they are striplines, microstrip lines, and so forth (see Table 3.1)];
• The structure of the coupled lines (i.e., whether they are homogeneous or inhomogeneous);

TABLE 3.1. Commonly Used Types of Planar Coupled Transmission Lines

- The type of output ports (i.e., whether they are terminated, open-circuited, short-circuited, or otherwise loaded);
- Whether or not the lines are regular or irregular (i.e., whether or not the coupling mechanism is dominated by the time-varying electric fields or magnetic fields).

In this chapter, we will not treat all of the types of coupled transmission lines listed above. Certainly, we will treat lines that have both strong and weak coupling. Also, we will consider regular and irregular lines because of some interesting applications. Most importantly of all, we will treat symmetrical coupled transmission lines because of their wide practicality and ease of analysis.

A pair of identical transmission lines in proximity is illustrated, in general, in Figure 3.1. Geometrically, the configuration of the metal conductors possesses symmetry about a vertical axis. There are two views of this configuration to illustrate pictorially some general properties of the electric field under two different types of excitation, the so-called *even*
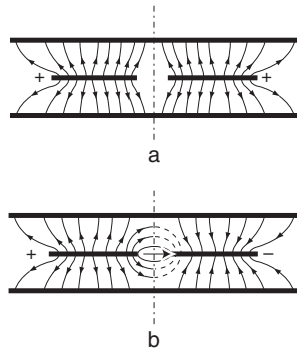
Figure 3.1. Even (a) and odd (b) electrical fields of parallel coupled striplines.

and *odd* modes. When they are separated, the individual transmission lines each have a single, dominant mode, as discussed in Chapter 2. When the individual lines are brought together, electromagnetic fields are shared between them and coupling results. With the two lines together, qualitatively, there are more degrees of freedom, or more modes, possible. It is a natural result, that with symmetrical coupled lines, there are the two dominant modes: the even mode and the odd mode. All combinations of excitation of the two lines can be expressed as a combination of the even and odd modes.

In the even mode, fundamentally, both transmission lines are identically excited by electromagnetic fields that are equal in amplitude and phase. The electric field is distributed symmetrically, as pictorially indicated in Figure 3.1(a). As the electric lines of force approach the vertical axis, they become tangent to it. Conversely, the magnetic lines of force (which are not illustrated) would become normal to the vertical axis because they are orthogonal to the lines of electric force. The symmetrical system behaves as if each transmission line is separated from the other by an ideal magnetic wall (i.e., a vertical plane having infinite permeability, μ).

In the odd mode, fundamentally, both transmission lines are identically excited by electromagnetic fields that are equal in amplitude but 180° out of phase. The electric field is distributed antisymmetrically, as pictorially indicated in Figure 3.1(b). As the electric lines of force approach the vertical axis, they become normal to it. Conversely, the magnetic lines of force (which are not illustrated) would become tangent to the vertical axis, again because they are orthogonal to the lines of electric

force. The antisymmetrical excitation produces a system behavior as if each transmission line is separated from the other by an ideal electric wall (i.e., a vertical plane having infinite conductivity, σ).

Associated with both the odd and even modes are effective dielectric constants (ε_{eff}), which, as in the case of the different transmission lines discussed in Chapter 2, determine a wave velocity v and characteristic impedance Z_0. However, the characteristic impedances and the wave velocities are each different for the even and odd modes. The characteristic impedances for the even and odd modes are denoted by Z_{0e} and Z_{0o},[*] respectively.

Expressions for the even- and odd-mode characteristic impedances of the coupled lines are:

$$Z_{0e} = \frac{1}{v_e C_e}, \quad Z_{0o} = \frac{1}{v_o C_o}, \tag{3.1}$$

where C_e and C_o are even and odd unit-length capacitances, and v_e and v_o are the even and odd wave propagation velocities. These wave velocities are in turn given by

$$v_e = \frac{c}{\sqrt{\varepsilon_{eff\,e}}}, \quad v_o = \frac{c}{\sqrt{\varepsilon_{eff\,o}}}, \tag{3.2}$$

where c is the speed of light in a vacuum, and $\varepsilon_{eff\,e}$ and $\varepsilon_{eff\,o}$ are the effective dielectric constants for the even mode and odd mode, respectively.

Table 3.2 shows different regular coupled-line networks, scattering matrix elements, and possible applications, where

$$\Theta = \frac{2\pi l}{\Lambda}$$

is the electrical length of the coupled lines; l is the physical length;

$$\Lambda = \frac{\lambda}{\sqrt{\varepsilon_{eff}}}$$

*The last subscript identifies the mode.

is the coupled-lines guide wavelength,

$$\sqrt{\varepsilon_{eff}} = \frac{\sqrt{\varepsilon_{eff\,e}} + \sqrt{\varepsilon_{eff\,o}}}{2},$$

$$\rho = \frac{Z_{0e} + Z_{0o}}{2}, \quad r = \frac{Z_{0e} - Z_{0o}}{2}.$$

In the remainder of this chapter, we will consider the characteristics of the even and odd modes in various forms of coupled transmission lines. The characteristics of these modes will, of course, depend upon the various dimensions and substrate materials, as did the individual transmission lines considered in the previous chapter, but, as expected, the relationships will be more complex. In later chapters, we will consider how these

TABLE 3.2. Different Regular Coupled Line Networks

	Regular Coupled Line Schematic	Scattering Matrix Parameters	Appilication
1		$S_{13} = S_{24} = S_{31} = S_{42} = \dfrac{1}{\cos\Theta + i\rho\,\sin\Theta}$ $S_{12} = S_{21} = S_{34} = S_{43} = \dfrac{ir\,\sin\Theta}{\cos\Theta + i\rho\,\sin\Theta}$	Directional Coupler, Power Divider and Combiner
2		$S_{11} = S_{44} = \dfrac{1 - r^2\,\sin^2\Theta}{\cos\Theta + i\rho\,\sin\Theta}$ $S_{14} = S_{41} = \dfrac{-i\,2r\,\sin\Theta}{\cos\Theta + i\rho\,\sin\Theta}$	Bandpass Filter, Transformer, DC Block
3		$S_{11} = S_{44} = \dfrac{1 - r^2\,\sin^2\Theta}{\cos\Theta + i\rho\,\sin\Theta}$ $S_{14} = S_{41} = \dfrac{i2r\,\sin\Theta}{\cos\Theta + i\rho\,\sin\Theta}$	Bandpass Filter
4		$S_{11} = S_{22} = -i\,\dfrac{(r^2 - \rho^2 + 1)\sin 2\Theta}{2(\rho\cos 2\Theta + r) + i\sin 2\Theta(1 - r^2 + \rho^2)}$ $S_{12} = S_{21} = \dfrac{2(r\cos 2\Theta + \rho)}{2(\rho\cos 2\Theta + r) + i\sin 2\Theta(1 - r^2 + \rho^2)}$	Shiffman Phase Shifter

coupled transmission lines with their even and odd modes are used in the performance of certain circuit functions and in the design of various components.

3.2. COUPLED STRIPLINES

Various forms of coupled striplines are shown in Figure 2(a–e) of Table 3.1. Since striplines are basically filled with a homogeneous dielectric between conductors, the dominant mode of propagation is a pure TEM mode. This is not only true for individual striplines, but also for coupled striplines. The even and odd modes are both TEM, and the effective dielectric constant is equal to the material dielectric constant. Thus the wave velocities associated with each the even and odd modes are equal to each other and to that in the uncoupled, individual lines. Because of these simplifications, coupled striplines present a convenient starting point for studying coupled transmission lines.

Edge-coupled striplines [Figure 2(a) of Table 3.1] consist of a pair of stripline center conductors in the center plane between two ground planes. The two different field distributions shown are each for even and odd modes (Figure 3.1). Because the dominant even and odd modes are both TEM, the electric field distributions for each are independent of frequency (i.e., the electric field at any frequency is the same as the static field). As such, in determining coupling, it is convenient to consider unit length capacitances for the even and odd modes as illustrated in Figure 3.2. In this figure:

- C_p is the parallel-plate capacitance between each center conductor and each ground plane.
- C_f is the fringing capacitance between the outside edge of each center conductor and each ground plane.
- C_{fe} is the fringing capacitance between the inside edge of each center conductor and each ground plane for the even mode.
- C_{fo} is the mutual capacitance between the inside edges of the center conductors for the odd mode.

These capacitances depend on the physical dimensions of the coupled lines and the relative dielectric constant of the medium. The parallel plate
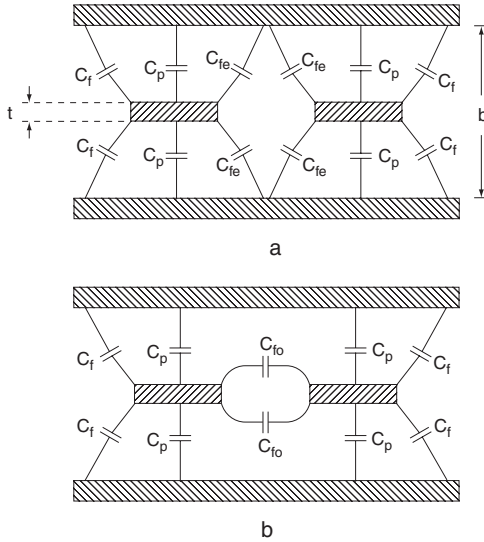
Figure 3.2. Even (a) and odd (b) mode static capacitances for coupled striplines.

capacitance C_p is derived straightforwardly in electrostatics and is given in normalized form as follows:

$$\frac{C_p}{\varepsilon} = \frac{2W/b}{\left(1 - t/b\right)},$$

(3.3)

where ε is the dielectric constant of the medium, W is the width of the center conductor, t is the thickness of it, and b is the spacing between the two ground planes.

The relationship between the normalized fringing capacitance C_f/ε as a function of the normalized center conductor thickness t/b is shown in [5]. This relationship (which is too complex to show as a closed form expression) has also been derived from electrostatics. Before we proceed with presenting the relationships for the very critical capacitance parameters C_{fe} and C_{fo}, it is useful to see where we are headed by looking at the general expressions for the total capacitance per unit length in the even mode, C_e, and that for the odd mode, C_o. These each become the summation of the parallel plate capacitance C_p and of the outside-edge fringing

capacitances C_f, as well as C_{f_e} and C_{f_o} for both the even and odd modes, as follows:

$$C_e = 2\left(C_p + C_f + C_{f_e}\right), \quad C_o = 2\left(C_p + C_f + C_{f_o}\right). \tag{3.4}$$

We note from these two expressions that the difference

$$C_{12} = C_{fo} - C_{fe} = (C_o - C_e)/2. \tag{3.5}$$

If we regard the capacitance C_e, which is associated with the even mode, as the self capacitance of the individual, uncoupled stripline, then C_{12} can be regarded as the mutual capacitance between the lines, which expresses the coupling between the two lines.

Since we are regarding the coupled striplines as uniformly filled with a dielectric material, it should be clear that dominant even and odd modes are TEM and that capacitances can be normalized to the dielectric constant ε. Also, all dimensional dependencies should be scalable and can be normalized to one of the dimensions, which for striplines is most conveniently the ground-plane spacing b. In coupled striplines, the dimension that first comes into play is the normalized line width W/b, which determines the normalized parallel-plate capacitance C_p/ε. To a first order, the normalized line thickness t/b determines the fringing capacitance C_f; the contributions from W/b and the normalized spacing between the coupled lines S/b are negligible to a first order. Also, the normalized spacing between the coupled lines S/b, together with the normalized line thickness t/b, determines the capacitances associated with the coupling mechanism C_{fe}/ε, C_{fo}/ε, and C_{12}/ε; the contribution from W/b is negligible. The interdependencies between all these were developed by Getsinger [5].

We are now in a position to determine the key impedance parameters Z_{0e} and Z_{0o} for edge-coupled striplines. We have the expression for the parallel-plate capacitance C_p [see (3.3)] and the graph for the fringing capacitance C_f [5]. We also have the graphs showing the capacitances C_{12}, C_{fe}, and C_{fo} [5].

Cohn [6] showed that for center conductors having zero thickness, the even- and odd-mode impedances become

$$Z_{0e} = \frac{30\pi}{\sqrt{\varepsilon}} \frac{K(k'_e)}{K(k_e)} \quad (\Omega),$$

$$Z_{0o} = \frac{30\pi}{\sqrt{\varepsilon}} \frac{K(k'_o)}{K(k_o)} \quad (\Omega),$$

where

$$k_e = \tanh\left(\frac{\pi W}{2b}\right) \tanh\left[\frac{\pi(W+S)}{2b}\right],$$

$$k_o = \tanh\left(\frac{\pi W}{2b}\right) \coth\left[\frac{\pi(W+S)}{2b}\right],$$

$$k'_e = \sqrt{1 - k_e^2},$$

$$k'_o = \sqrt{1 - k_o^2}.$$

Cohn [6] also presented very convenient nomograms representing these expressions.

Broadside coupled striplines [Figure 2(c) of Table 2.1] provide a tighter coupling between the lines (tighter than about −8 dB) than the edge-coupled lines. For zero conductor thickness of these coupled lines, the even- and odd-mode impedances and physical dimensions [7] are

$$Z_{0e} = \frac{60\pi}{\sqrt{\varepsilon}} \frac{K(k')}{K(k)},$$

$$Z_{0o} = \frac{30\pi^2 \, S/b}{\sqrt{\varepsilon} \tanh^{-1} k'},$$

$$\frac{W}{b} = \left\{ \tanh^{-1} \sqrt{\frac{k\frac{b}{S} - 1}{\frac{1}{k}\frac{b}{S} - 1}} - \frac{S}{b} \tanh^{-1}\left[\frac{1}{k}\sqrt{\frac{k\frac{b}{S} - 1}{\frac{1}{k}\frac{b}{S} - 1}}\right] \right\},$$

where

$$k = \tanh\left(\frac{\pi}{2}\frac{W}{b}\right)\tanh\left(\frac{\pi}{2}\frac{W+S}{b}\right),$$

$$k = \sqrt{1-k'},$$

$K(k)$ and $K(k')$ are complete elliptic integrals of the first kind of modulus k and k'. The function $\tanh^{-1}$ can be evaluated from

$$\tanh^{-1}(x) = \frac{1}{2}\ln\left(\frac{1+x}{1-x}\right).$$

3.3. MICROSTRIP COUPLED LINES

For the microstrip coupled lines illustrated in Figure 1(a) in Table 3.1, the dielectric medium is not homogeneous, as it is in the case of striplines. The dielectric substrate only partially fills the cross section of the trans-mission lines, and, because the dielectric constant ε is greater than unity, the electromagnetic field is concentrated more in the substrate than in the air.

The even and odd modes in microstrip coupled lines are illustrated conceptually in Figure 3.3. In the even mode, the fields are excited equally in amplitude and phase with respect to each of the center conduc-tors. As previously discussed, the electric field lines are normal to the plane of symmetry and the electromagnetic field behaves as if a planar magnetic wall were inserted coincident with the axis of symmetry [Figure 3.3(b)].

In the odd mode, the fields are excited equally in amplitude, but in directly opposing phase (180°) with respect to each of the center conduc-tors. As previously discussed, the electric field lines vanish at the plane of symmetry and the electromagnetic field behaves as if a planar electric wall were inserted coincident with the axis of symmetry [Figure 3.3(c)].

Conceptually and pictorially, the even and odd modes in the coupled microstrip lines exhibit the same general field distributions as in the cou-pled striplines. But, the similarities end there. Because the dielectric does not fill the microstrip structure homogeneously, there must be an effective
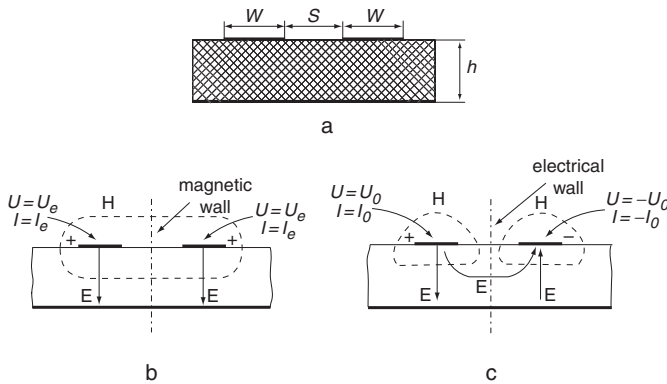
Figure 3.3. Microstrip coupled lines: basic configuration (a); even-mode electromagnetic field (b); odd-mode electromagnetic field (c).

dielectric constant that is some kind of weighted average between the dielectric constant of the material and that of the air space above the center conductors. With different field distributions being associated with both the even and odd modes, not only is there an effective dielectric constant, but there are considerably different effective dielectric constants and phase velocities associated with the even and odd modes. The large imbalance between the effective dielectric constants and the related phase velocities can lead to some limitations in the application of microstrip lines.

Extensive calculations have been performed to obtain practical design information for coupled microstrip lines [8]. Some of these relationships are shown in Figures 3.4 through 3.7 for various dimensions and substrate dielectric constants. Figure 3.4 illustrates relationships between the even- and odd-mode impedances and physical dimensions of the microstrip coupled lines. These characteristics can be used in two ways: for analysis to calculate z_{0e} and z_{0o} values from the physical dimensions S, W, and h of the coupled lines or for synthesis to find dimensions of the coupled lines from z_{0e} and z_{0o}.

Let us consider the synthesis technique when the even- and odd-mode characteristic impedances are determined. The z_{0e} and z_{0o} are marked on the vertical axis [see, for example, Figure 3.4(a)] of a graph for the dielectric constant of substrate material $\varepsilon = 5$. It is then we can select two points (for the even- and odd-mode sets of curves). These points are lying on the same relative width abscissa value, and on curves with an identical rela-
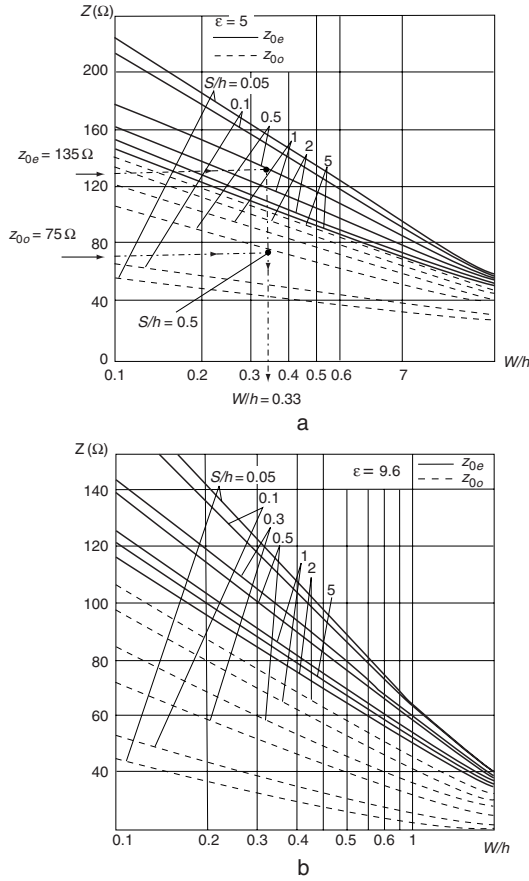
Figure 3.4. Even- and odd-mode impedances of coupled microstrip lines for $\varepsilon = 5$ (a) and $\varepsilon = 9.6$ (b).

tive space (i.e., they must both have identical values W/h and S/h for odd and even modes).

The plots of the effective dielectric constant of microstrip coupled lines versus physical dimensions and different dielectric constants of substrate materials are shown in Figure 3.5 [8]. For $S/h \rightarrow \infty$, these characteristics become identical to the characteristics of a single microstrip line (see Figure 2.2).

When coupled microstrip lines are enclosed in a real metallic housing, the electrical field lines change configuration. In this case, capacitances will increase, but impedances and effective dielectric constants will decrease. Figure 3.6 [8] gives the plot of the characteristic impedance of
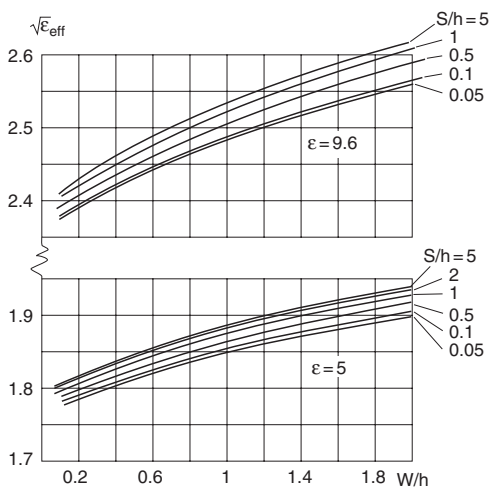
Figure 3.5. Effective dielectric constant vs. physical dimensions of microstrip coupled lines for different ε.
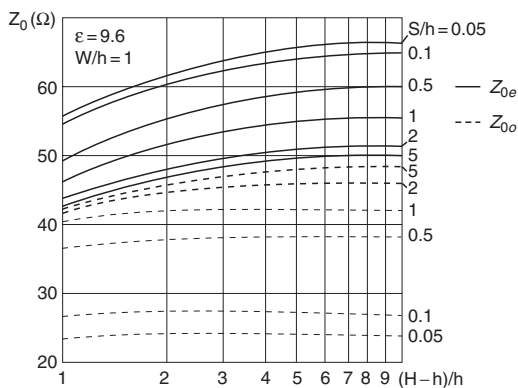
Figure 3.6. Characteristic impedance of shielded microstrip coupled lines vs. physical dimensions for $\varepsilon = 9.6$.
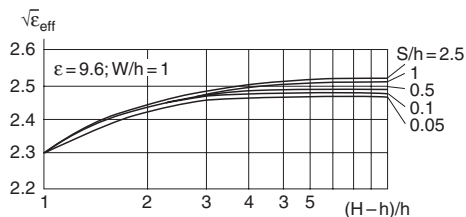
Figure 3.7. Effective dielectric constant of shielded microstrip coupled line vs. physical dimensions for $\varepsilon = 9.6$.

shielded coupled microstrip lines with equal relative width $W/h = 1$ versus physical dimensions of the shielded microstrip lines with substrate dielectric constant $\varepsilon = 9.6$. Relationships between the effective dielectric constant of the shielded coupled microstrip lines with substrate material relative dielectric constants of 9.6 and physical dimensions are shown in Figure 3.7 [8]. The upper metal cover can be neglected, provided that its distance from the substrate $(H–h) > (6–8)h$. Otherwise, the cover will affect z_{0e}, z_{0o}, and ε_{eff}.

3.4. COUPLED SUSPENDED STRIPLINES

Coupled suspended striplines are shown in Figure 3(a, b) of Table 3.1. These coupled lines offer lower insertion loss, the ability to achieve an improved equalization of the even- and odd-mode phase velocities. In the coupled suspended striplines, electromagnetic fields propagate in the isotropic media, and phase velocities for even and odd modes are equal. The even- and odd-mode impedances and effective dielectric constants for these lines are given in [9].

The broadside coupled suspended striplines allow the capacitive coupling to be realized by coupling through the supporting dielectric as shown in Figure 3(b) of Table 3.1. Relatively large capacitance values can be achieved using such an overlap section. The coupling between the top and the bottom conductors is a result of the odd-mode excitation. Broadside coupled suspended striplines are useful in the realization of directional couplers with tight coupling.

Coupled suspended striplines have lower losses and a lower sensitivity to fabrication tolerances than microstrip or stripline coupled lines.

3.5. COUPLED SLOTLINES AND COPLANAR WAVEGUIDES

Coupled slotlines and CPW coupled lines are shown in Figures 4 and 5 of Table 3.1, respectively. For a narrow center conductor of edge coupled slotlines, the structure becomes similar to a single slotline. For a very wide center conductor ($a/h \gg 1.0$), the structure loses coupling and becomes two uncoupled slotlines or coplanar waveguides.

Phase velocities and characteristic impedances of CPW coupled lines differ by 5% for the two modes, which is much less than the 17% for the microstrip coupled lines. This property of coplanar CPW is very useful for the design of high directivity directional couplers.

3.6. IRREGULAR LINES

The term *irregular line* will stand for coupled conductors with strong magnetic coupling, with minimal influence of the RF ground plane on the parameters of the line (ideally, the absence of ground plane in the coupling area) [10]. The strong magnetic coupling is realized without magnets or ferrites. Since the irregular line is almost unaffected by the RF ground plane, capacitances between the line and the ground plane are negligible compared to the capacitances between conductors.

Strong magnetic coupling between lines supports miniature dimensions and an increased bandwidth. This coupling is characterized by the coefficient of magnetic coupling, k_m. In many cases [11–14], iron (Fe) of ferrite cores with large permeabilities is used to maximize k_m ($k_m \to 1$). However, this approach has some disadvantages, including diminished temperature stability, high cost, and larger component dimensions. Additionally, the permeability (μ) and dielectric constant (ε) of ferrites may vary dramatically with frequency. The high-frequency limitation of these devices arises from core losses, winding lengths, and parasitic elements that become dominant above 1 GHz.

In irregular lines, magnetic coupling activization can be achieved without any cores by bringing the conductors close to each other. At that point, capacitance per unit of length (C) increases, while inductance per unit of length (L) decreases, so that the product LC, which determines the wave velocity in the transmission line, remains constant.

The inductance per unit of length of irregular coupled lines is given by

$$L = 2\left(L_0 - M\right) = 2L_0\left(1 - \frac{M}{L_0}\right) = 2L_0\left(1 - k_m\right),$$

where L_0 is self-inductance per unit length of one conductor (which can be determined by isolating this line from all other parts, including the second

TABLE 3.3. Different Irregular Coupled Line Networks

Type of Irregular Network	Schematic	Non-normalized Classic Transfer Matrix [a]	Application
1. Diagonal connection		$$\begin{bmatrix} 1 - \dfrac{2\cot 0.5\Theta}{F_1} & -\dfrac{i2Z}{F_1} \\ -i\dfrac{2}{Z}\left(1 - \dfrac{\cot 0.5\Theta}{F_1}\right)\cdot \cot 0.5\Theta & 1 - \dfrac{2\cot 0.5\Theta}{F_1} \end{bmatrix}$$ $$F_1 = \tan 0.5\Theta + \cot 0.5\Theta - \frac{1-k_m}{1-k_m}\frac{2}{\Theta}$$	180° phase shifter, transformer, balun, BPF
2. Diagonal connection with one dc grounded pole			Ruthroff 4:1 transformer [11]
3. Horizontal connection		$$\begin{bmatrix} 1 - \dfrac{2\tan 0.5\Theta}{F_2} & \dfrac{i2Z}{F_2} \\ i\dfrac{2}{Z}\left(1 - \dfrac{\tan 0.5\Theta}{F_2}\right)\tan 0.5\Theta & 1 - \dfrac{2\tan 0.5\Theta}{F_2} \end{bmatrix}$$ $$F_2 = \tan 0.5\Theta + \cot 0.5\Theta + \frac{2}{\Theta}\frac{1-k_m}{1+k_m}$$	1:1 in-phase transformer

TABLE 3.3. Different Irregular Coupled Line Networks *(continued)*

Type of Irregular Network	Schematic	Non-normalized Classic Transfer Matrix [a]		Application
4. Diagonal connection with isolation of one pole		$\dfrac{1}{2}\left(1 - \tan^2 0.5\Theta + \dfrac{\tan 0.5\Theta}{0.5\Theta}\dfrac{1 - k_m}{1 + k_m}\right)$ $i\dfrac{1}{Z}\left(\tan 0.5\Theta - \dfrac{2}{\Theta}\dfrac{1 - k_m}{1 + k_m}\right)$	$iZ \tan 0.5\Theta$ 2	Autotransformer
5. Horizontal isolation of one pole		$1 - \tan^2 0.5\Theta$ $i\dfrac{2}{Z}\tan 0.5\Theta$	$-i\dfrac{Z\Theta}{4}\dfrac{1 + k_m}{1 - k_m}\times\left(1 - \tan^2 0.5\Theta\right) + i\dfrac{Z}{2}\tan 0.5\Theta$ $1 - 0.5\Theta\dfrac{1 + k_m}{1 - k_m}\tan 0.5\Theta$	LPF; matching circuit
6. Vertical isolation of one pole		$1 - \dfrac{1 - k_m}{1 + k_m}\dfrac{2}{\Theta}\cot 0.5\Theta$ $\dfrac{4}{iZ\Theta}\dfrac{1 - k_m}{1 + k_m}$	$-iZ\left(\cot\Theta + \dfrac{1}{\Theta}\dfrac{1 - k_m}{1 + k_m}\right)$ $1 + \dfrac{1 - k_m}{1 + k_m}\dfrac{2}{\Theta}\tan 0.5\Theta$	HPF

conductor); M is mutual inductance per unit length of the two conductors; and $k_m = M/L_0$ is the coefficient of magnetic coupling between the lines $(0 \le k_m \le 1)$.

Table 3.3 illustrates various methods of irregular-line connections. In the circuit shown in row 1 of the Table 3.3, the output port of the first coupled conductor 1-3 is electrically connected to the diagonal end of the second coupled conductor 2-4 and dc-coupled to ground. The segment providing the diagonal connection should be as short as possible. This can be achieved by bending the line into a ring frame. The RF ground has to be apart from the irregular line and close to the appropriate input/output lines, that is, there should be no RF ground plane in the area of coupled conductors.

The circuit depicted in row 2 of Table 3.3 is the well-known Ruthroff 4:1 transformer [11]. This circuit has a high frequency limitation due to transmission-line lengths and parasitic inductance. It is possible to get a good performance up to 2 or 4 GHz. This transmission line transformer has the advantage of higher efficiency, greater bandwidth, and simpler construction compared with the conventional transformer. The insertion loss for the matched 4:1 transformer versus line length is given in [11, 12].

This transformer can be used for impedance matching, balanced-unbalanced (balun) circuits, or as dividers and combiners. The irregular line devices can be used in an MMIC technology, which provides the ability to realize a multilayer structure.

REFERENCES

1. Howe, H., Jr., *Stripline Circuit Design,* Dedham, MA: Artech House, 1974.
2. Edwards, T. C., *Foundations for Microstrip Circuit Design,* New York: John Wiley & Sons, 1981.
3. Wadell, C. B*., Transmission Line Design Handbook*, Norwood, MA: Artech House, 1991.
4. Mongia, R., I. Bahl, and P. Bhartia, *RF and Microwave Coupled-Line Circuits,* Norwood, MA: Artech House, 1999.
5. Getsinger, W. J., "Coupled Rectangular Bars Between Parallel Plates," *IEEE Trans. Microwave Theory Tech.,* Vol. 10, No. 1, January 1962, pp. 65–72.

6. Cohn, S. B., "Shielded Coupled-Strip Transmission Line," *IRE Trans., Microwave Theory Tech.,* Vol. MTT-3, October 1955, pp. 29–38.

7. Cohn, S. B., "Characteristic Impedances of Broadside-Coupled Strip Transmission Lines," *IEEE Trans. Microwave Theory Tech.,* Vol. MTT-8, No. 11, November 1960, pp. 633–637.

8. Maloratsky, L. G., *Microminiaturization of Microwave Elements and Devices,* Moscow, Russia: Soviet Radio, 1976.

9. Koul, S. K., and B. Bhat, "Broadside-Edge Coupled Symmetric Strip Transmission Lines," *IEEE Trans. Microwave Theory Tech.,* Vol. MTT-30, 1982, pp. 1874–1880.

10. Zelyah, E. V., et al., *Miniature Devices on Base Segments of Transmission Lines at VHF and UHF Frequency Range,* Moscow, Russia: Radio and Svyaz, 1989.

11. Ruthroff, C. L., "Some Broadband Transformers," *Proceedings of the IRE.,* Vol. 47, August 1959, pp. 1337–1342.

12. MacDonald, M., "Design Broadband Passive Components with Ferrites," *Microwave & RF,* October 1993, pp. 81, 82, 84, 86, 132.

13. Maloratsky, L. G., "Design Regular- and Irregular-Print Coupled Lines," *Microwaves & RF,* September 2000, pp. 97–106.

14. Sevick, J., *Transmission Line Transformers,* Atlanta, GA: Noble Publishing, 1996.

This Page Intentionally Left Blank

CHAPTER 4

Distributed and Lumped Elements of Integrated Circuits

4.1. INTRODUCTION

Passive RF and microwave integrated circuits are made up of distributed elements, lumped elements, or combinations of both these types of elements. Distributed elements consist of segments of transmission lines of the different types that we have discussed in the preceding chapters. These transmission-line segments can be of various lengths, ranging from small fractions of the guide wavelength (Λ) to several wavelengths.

In this chapter, we consider primary *lumped elements*, which by definition are small in size in comparison with the guide wavelength in any transmission line that may be associated with them. Examples of lumped elements are resistors, capacitors, inductors, discontinuities, and resonators [1–6]. For sufficiently small dimensions, there are no significant variations in resistance, capacitance, inductance, and so forth, except as associated with any frequency dependence of material resistivities, permitivities, and permeabilities. There are no appreciable variations in phase over the lumped element, and the current distributions and associated potential drops are essentially uniform, such that the currents and voltages we utilize in classical circuit theory apply. Usually, the linear dimensions of lumped elements are less than $\Lambda/10$ or $\Lambda/16$.

Lumped elements are usually easily realized in RF or low-frequency microwave applications. At higher microwave frequencies, and particularly at millimeter-wave frequencies, lumped elements are very difficult, or even impossible, to achieve because of dimensional limitations in fabrication technologies. The upper limit for the use of lumped elements is approximately 40 GHz, and for higher frequencies, only distributed elements are practical.

In applications where it is possible to utilize lumped elements, the advantages are usually small dimensions, wideband characteristics, and low production cost. Their drawbacks are lower Q and lower power-handling capability as compared with distributed circuits.

4.2. CAPACITORS

Capacitors are lumped circuit elements that store energy by virtue of electric fields. For MICs, capacitors can be conveniently realized in several different configurations. It is clear that fundamental parallel-plate capacitors consisting of a pair of parallel planar metallic surfaces separated by a dielectric are available in chip forms as discrete components. In the parallel-plate configuration, the capacitance is given by the classical expression from electrostatics:

$$C = \varepsilon \cdot \varepsilon_0 \frac{A}{h}, \tag{4.1}$$

where ε is the dielectric constant of the medium, ε_0 is the permittivity of free space (8.85×10^{-12} farads/m), A is the cross-sectional area, and h is the spacing between the plates. This basic formula applies not only to simple configurations, but also to capacitors formed by multilayer techniques.

Chip capacitors are frequently used in the construction of MICs when relatively high capacitance values are required in circuit applications. In these cases, the chips are attached to the transmission lines by various bonding techniques. When relatively low values of capacitance are required, capacitors can be effected by modifications to the actual planar transmission lines. For example, Figure 4.1(f) shows a low-impedance microstrip section that is simply a widening of the center conductor, which could possibly be produced through photolithography. The result is
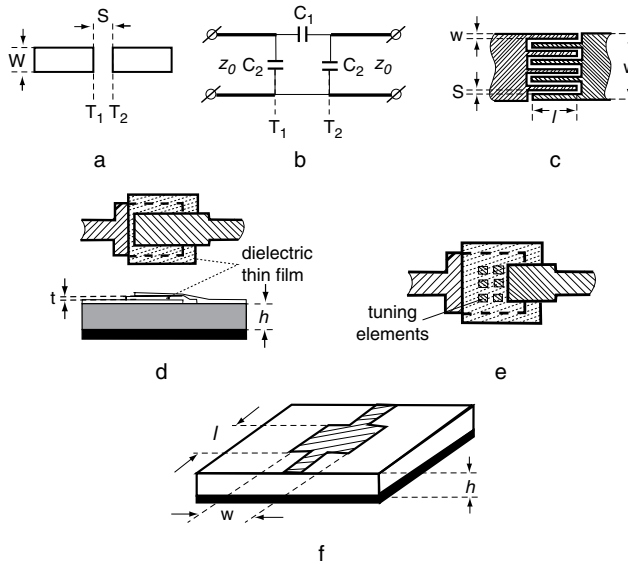
Figure 4.1. Print capacitors: series gap in the center conductor (a); equivalent circuit of the series gap (b); interdigital configuration (c); end-coupled overlay (d); end coupled overlay with discrete tuning elements (e); low impedance microstrip section (f).

a parallel-plate capacitor, in shunt with the microstrip line, with a capacitance straightforwardly determined by the dielectric constant, area, and spacing as follows:

$$C = \frac{0.0885 \, \varepsilon \, W \, l}{h} \, (\text{pF}), \tag{4.2}$$

where *W, l,* and *h* are dimensions in centimeters.

For applications requiring relatively low capacitances, planar series capacitors can be formed as shown in Figure 4.1(a, c) through edge coupling. These capacitors are simply formed by gaps in the center conductor of the transmission lines. They do not require any dielectric films, which simplify the design. However, due to high current densities at the edges, they exhibit low Q-factors, typically less than 50 at operating frequencies in the 10-GHz range. Capacitance values for these edge-coupled types are typically less than 0.5 pF.

The gap capacitor in Figure 4.1(a), with its equivalent circuit [Figure 4.1(b)], will be described in Section 4.6. We now discuss the planar interdigital capacitor shown in Figure 4.1(c), which is realized by a meandered

gap in a microstrip or stripline center conductor. By design, dimensions are much less than a quarter wavelength, and the capacitance depends on finger width w, finger length l, and finger spacing S (usually $S = w$), as follows [1]:

$$C = \frac{\varepsilon + 1}{w} l \left[A_1 (N - 3) + A_2 \right],$$

where A_1 (the interior) and A_2 (the two exterior) are the capacitances of the fingers; for infinity substrate thickness (or no ground plane), $A_1 = 8.86 \times 10^{-6}$ pF/μm and $A_2 = 9.92 \times 10^{-6}$ pF/μm, N is the number of fingers, and ε is the relative dielectric constant of the substrate.

Series capacitors with larger values can be realized by using an additional thin dielectric layer (typically 0.5 μm thick) between two metal plates, as shown in Figure 4.1(d, e). These overlay structures use dielectric film materials, such as silicon nitride Si_3N_4 ($\varepsilon = 6.8$), SiO_2 ($\varepsilon = 4$–5), Ta_2O_5 ($\varepsilon = 20$–25), Al_2O_3 ($\varepsilon = 6$–10), and so forth. Dielectric-film losses limit Q-factors to about 100 at around 10 GHz. These capacitors are used to achieve higher values in small areas. Tolerances of these capacitance normally run from 10% to 15%. For better capacitance control and tuning capability, we can use overlay configurations with tuning elements [Figure 4.1(e)]. Overlay capacitor values as high as 10 pF can be realized within small areas.

4.3. INDUCTORS

4.3.1. Print Inductors Consideration

Lumped inductors in planar transmission lines can be realized using several different configurations, as shown in Figure 4.2. The simplest configuration [Figure 4.2(a)] consists of a short section of high-impedance line that is achieved by simply narrowing the center conductor over a short length. In this case, the inductance is given by the following formula [7, 8]:

$$L = 2 \cdot 10^{-3} l \left(\ln \frac{l}{W + t} + 1.193 + 0.2235 \frac{W + t}{l} \right) k_g \ (nH), \qquad (4.3)$$

where *l, W,* and *t* (conductor thickness) are in centimeters, and k_g is a correction factor to take into account the effect of a ground plane:

$$k_g = 0.57 - 0.145 \ln \frac{W}{h} \tag{4.4}$$

for

$$\frac{W}{h} > 0.05,$$

where *h* is the spacing from the ground plane.

Typical inductance values for this simple type of inductor are 0.5 to 3.0 nH.
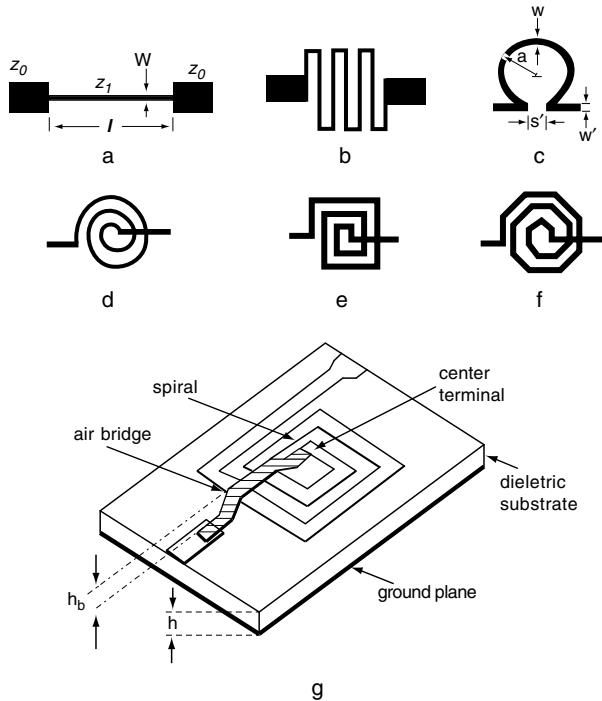
Figure 4.2. Planar inductors: high impedance line section (a); meander line (b); single turn (c); circular spiral (d); rectangular spiral (e); octagonal spiral (f); spiral inductor with air bridge (g).

Considering the inductor strip in Figure 4.2(a) as a high-impedance transmission line, we can write:

$$L = Z_1 l \frac{\sqrt{\varepsilon_{eff}}}{c} (\text{H}),$$

where l is the length of the strip in millimeters, $c = 3 \times 10^{11}$ mm/s, Z_1 is the characteristic impedance of the inductor strip in ohms, and ε_{eff} is the effective dielectric constant of the inductor strip. In practice, a straight strip is used for the low inductance values between 1 and 3 nH.

The meander line inductor [Figure 4.2(b)] is used to reduce the area occupied by the element. In the meander inductor, adjacent conductors have equal and opposite current flows, which reduce the total inductance. Mutual coupling effects are usually small if the spacing is greater than three strip widths. The strip width is much smaller than the substrate thickness.

A single-turn circular inductor in Figure 4.2(c) has an inductance [9]

$$L = 1.257 \cdot 10^{-3} a \left[\ln \left(\frac{a}{W + t} \right) + 0.078 \right] k_g \text{ (nH)},$$

where a, W, and t are in centimeters.

Spiral inductors can have a circular [Figure 4.2(d)], a rectangular [Figure 4.2(e)], or an octagonal [Figure 4.2(f)] configuration. The connection from the center of the spiral inductor to the outside can be made with a via and a trace on the opposite side of the substrate, an air bridge [see Figure 4.2(g)], or a bond wire. The general relationship for a circular spiral is [9, 10]:

$$L = \frac{39.39 \, n^2 a^2}{8 \, a + 11 \, c} \text{ (nH)},$$

where $a = (D + d)/4$, $c = (D - d)/2$, D and d are, respectively, the maximum and minimum diameters of a circular spiral, in millimeters, and n is the number of turns.

An improved equation that is more appropriate for use with planar spiral inductors was derived by Burkett [11]:

$$L = \frac{31.5\,n^2 a^2}{6\,a + 10\,c} \quad (\text{nH}).$$

Typical inductance values for monolithic circuits fall in range 0.5 to 10 nH.

Unloaded Q of an inductor may be calculated from

$$Q = \frac{\omega L}{R},$$

where ω is angular frequency (in hertz), L is inductance (in nanohenries),

$$R = \frac{2n\pi a}{W}\sqrt{\pi f \mu \rho}$$

is resistance (in ohms), ρ is resistivity in ohm-meters, μ is permeability in henrys per meter, W is width in meters, and f is frequency in hertz.

The resistance of spiral inductors depends on frequency because of the skin effect. The Q of an inductor depends directly on the inductance. The two most important geometric parameters affecting Q are the conductor width-to-spacing ratio and the inductor outside diameter [11]. The Q increases with an increase in the outside diameter. The Q-factor increases as the square root of the frequency due to the skin effect. Circular spiral inductors have higher Q than rectangular inductors; however, they also have lower inductance for an equivalent area. To realize high-quality inductors, thicker metal with higher conductivity (e.g., copper and gold) can be used to overcome the series resistive loss.

Parasitic capacitances will cause a spiral inductor to have a self-resonance. The most basic parasitic capacitance is that which is created by the coupling between the turns of the inductor. When a ground plane is under the spiral inductor, we have additional parasitic capacitance between spiral and ground. The self-resonant frequency must be at least twice the maximum operating frequency for the inductance to have a constant value.

The ideal case of the inductor is in free space with no ground plane. The presence of a ground plane affects the inductance value, which decreases as the ground plane is brought nearer. This decrease can be taken into account by means of a correction factor k_g [see (4.4)]. When a

ground plane is necessary in a hybrid circuit, the maximum inductance is limited for a print spiral inductor.

The spiral inductor should have the widest possible line, while keeping the overall diameter small [10]. This implies that the separation between the turns should be as small as possible. However, in monolithic circuits processing limits require $W > 5$ μm and $S > 5$ μm, and in hybrid MICs $W > 10$ μm and $S > 10$ μm. The ratio of inner diameter to outer diameter equal to 0.5 optimizes the value Q, but not the maximum inductance value.

4.3.2. Dual-Spiral "Surprise"

The conventional spiral inductors [see Figure 4.2(d–g)] have some disadvantages. The spiral inductor requires two metal layers, one for the spiral inductor itself and another for an air bridge [Figure 4.2(g)] to provide crossover connection between the inductor center and outer circuitry. In this case, the bridge crossing the turns of the spiral produces parasitic feedback, increases insertion losses, and makes fabrication costly. Technology of the air bridge structure includes additional processes, for example, the deposition of a photoresist, which then should be removed from between the bridge and the substrate. The air bridge's physical dimensions are critical and should be determined as a compromise between electrical and mechanical requirements.

These disadvantages can be eliminated by using novel *single-layer* spiral inductors (Figure 4.3) [12]. These dual-spiral inductors consist of two spirals. The first spiral is realized by a conductor moving from the input to the center terminal at a monolithically decreasing distance from the center terminal traveling in a clockwise (or counterclockwise) direction. The second spiral is realized by a conductor moving from the center terminal to the output terminal at a monolithically increasing distance from the center terminal traveling in a counterclockwise (or clockwise) direction.

To minimize parasitic capacitance between the spiral conductor and ground plane, these inductors can be realized without a ground plane under the spiral conductor, or the bottom metal plane can be distant from the spiral inductor turns and close to appropriate input/output lines [see Figure 4.3(d)].
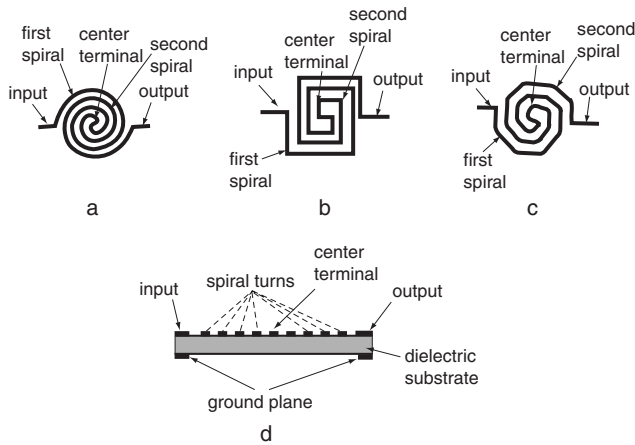
Figure 4.3. Single-layer spiral inductors: circle configuration (a); square configuration (b); octagonal configuration (c); side view (d).

The three most important geometric parameters affecting loss and *Q*-factor are the conductor space, conductor width, and spiral-inductor outside dimensions. The maximum outside dimensions of these single-layer spiral inductors should be less than ~Λ/300 (Λ is the guide spiral wavelength), or total spiral line length should be a small fraction of the guided wavelength in order to avoid distributed effect. Therefore, for example, spiral inductors with dimensions 0.3" × 0.3" can be used at HF and VHF frequency ranges.

Four single-layer square spiral inductors (see Table 4.1) differing in dimensions were simulated[*] and the results compared (see Figure 4.4 and Table 4.1). All inductors were fabricated on G-10 substrate with 65 mil thickness.

The inductor loss and mismatching are increased radically with increasing frequency above 200 MHz [see Figure 4.4(c)] because the phase-shift effect along the spiral length causes out-of-phase currents from segment to segment at higher frequencies.

When the space between turns becomes narrow (see spirals A and D in Table 4.1), spiral return loss and insertion loss are improved. When the line width increases (see spirals D and A or B in Table 4.1), there is no improving of *S*-parameter characteristics. Wider line dimension reduces

*These inductors were simulated by T. A. Miracco (Applied Wave Research, Inc.).
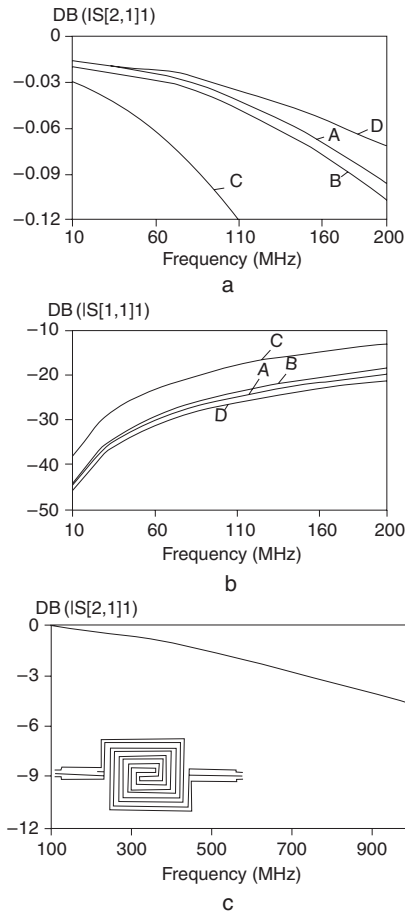
Figure 4.4. Single-layer square inductor frequency characteristics: insertion loss at VHF range (a); return loss at VHF range (b); insertion loss at UHF range (c).

the dc resistance of the spiral. However, the parasitic capacitance of the inductor increases with the line width.

The ability to miniaturize spiral inductors, together with the reduction in technology and assembly cost, makes planar inductors (Figure 4.3) very attractive for HMIC and MMIC elements and devices at HF and VHF ranges.

TABLE 4.1. Simulation Results for the Four Single-Layer Square Spiral Inductors

Square Spiral Inductors	A	B	C	D
Width (mil)	14.0	14.0	14.0	19.6
Space (mil)	8.4	14.0	28.0	8.4
Outside dimensions (mil)	162 × 154	196 × 182	280 × 266	207.2 × 190.4
Spiral length (in)	1.123	1.274	1.862	1.247
Inductance (nH)	10.1	13.3	22.2	10.1
Q-factor	29.7	33.9	37.8	29.5
Resistance (Ω)	0.034	0.039	0.059	0.034
Capacitance (pF)	0.3	0.4	0.7	0.3
S_{11} (dB)	24.5	26.0	18.0	25.9
S_{21} (dB)	0.043	0.035	0.12	0.036
S_{21} Ang (deg)	4.5	5.6	10.1	4.7

4.4. RESISTORS, TERMINATIONS, AND ATTENUATORS

The desirable characteristics of film resistors are:

- Low temperature coefficient of resistance (TCR);
- Good adhesion of the resistive film to substrate and conductors;
- Minimal dimensions because transmission line effects are to be ignored;
- Adequate dissipation capability;
- Good stable resistance value, which should not change with time.

Lumped-element resistors can be used in attenuators, dividers/combiners, and biasing circuits, and they can also act as matched terminations. Resistors for MIC may be realized in chip form or fabricated by planar construction.
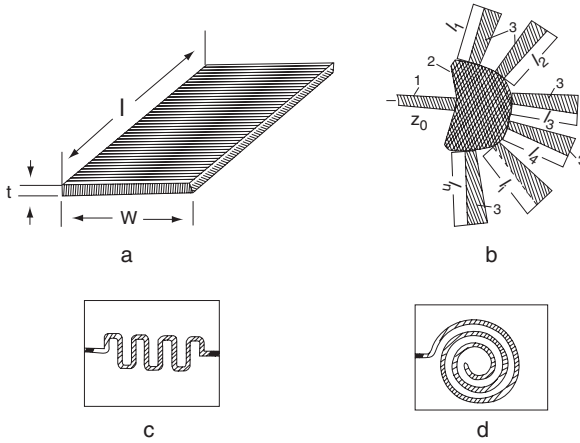
Figure 4.5. Planar resistors, terminations, and attenuators: rectangular resistor (a); multi-stub termination (b); meander attenuator (c); spiral termination (d).

The size selected depends on a trade-off between power requirements and frequency range. The smaller chips may be used at a higher frequency due to their lower parasitic shunt capacitance. Higher-power resistors have a larger area, and, therefore, they exhibit greater parasitic capacitance to ground.

Planar resistors are produced by depositing films of lossy metal on the dielectric base. Nichrome and tantalum are widely used due to their good stability and low TCR.

The resistance of a film rectangular resistor [Figure 4.5(a)] of length l, width W, and thickness t is given by

$$R = \frac{\rho_s l}{tW} = R_s \frac{l}{W} = R_s n \quad (\Omega), \tag{4.5}$$

where ρ_s is the resistivity of the resistor material in ohm-centimeters; l, W, and t are dimensions in centimeters; and $R_s = \rho_s/t$ (Ω/square) is the surface resistivity (resistance of a square of metal film of thickness t).

For a square film resistor when $l = W$ ($n = 1$), we obtain

$$R = \frac{\rho_s}{t} \quad (\Omega).$$

Therefore, resistance of the square of a film resistor does not depend on resistor area.

Let us discuss the main considerations in picking the thickness t of the film. Usually thickness is much less than skin depth. Very thin films are nonhomogeneous in their chemical composition and structure. This leads to a lower percentage of quality resistors produced and to aging—a drift of resistance from the original value over a period of time. Besides, there is an optimum film thickness which produces the lowest TCR. Typical thickness values are 0.01 to 0.1 μm. The thickness t of the film determines the surface resistance R_s.

The length and width of a film resistor determine the number of film squares [see (4.5)]. The minimum width (W) is determined by the limitations of the fabrication process and the necessity of preventing the parasitic effects of the neighboring elements. Having picked the width, one can then pick the length (l) of the resistor according to the number (n) of squares required for the given resistance R [see (4.5)]. The resistor area should be as large as possible to provide maximum power dissipation. Thus, for high-power applications, it is advisable to pick l and W so as to maximize the area. A larger size also allows for better precision in fabrication. One has to keep in mind, however, that linear dimensions of a lumped-element resistor must be less than $\Lambda/10$.

The biggest problems in planar resistor are the parasitic capacitance and inductance, which make the film resistor exhibit a frequency dependence at high frequency range.

Lumped resistors are used in the design of matched terminations. The termination consists of a segment of a transmission line with a gap for a connection of the resistor. One of the outputs of the resistor is connected to the transmission line, and the other is grounded. A direct connection with ground is sometimes difficult to accomplish in production. Grounding can be achieved by virtual configuration. For the virtual grounding, an open-circuited stub of the length

$$l = (2n+1)\frac{\Lambda}{4}$$

acts as short circuit at its input terminal. For a wider bandwidth, Z/Z_{in} (Z is the characteristic impedance of the input line and Z_{in} is the input impedance of the stub) can be increased.

Another option is a parallel connection of two or more open-circuited stubs directly to the output of the resistor. Figure 4.5(b) shows a planar broadband termination [13] that consists of input strip conductor 1, film

resistor 2, and open-circuited stubs 3. The lengths of the stubs l_1, l_2, ..., l_i, ..., l_n are equal to $\Lambda_i/4$, where Λ_i is the guide wavelength corresponding to the subrange of the given frequency range. The configuration of a film resistor and lengths and number of stubs are determined by the required bandwidth and the maximum power. Tapered stubs [Figure 4.5(b)] are shorter than the equivalent regular transmission line stubs and provide a wider bandwidth.

Distributed planar attenuator or termination can be realized by using a high-loss uniform microstrip line, which is several wavelengths long [Figure 4.5(c, d)] [14]. This line is realized by a film with a high surface resistance R_S. To increase the surface resistance, the thickness t of the line is chosen to be significantly less than skin layer thickness. An alternative is using a low-conductivity material.

The conductive losses are equal:

$$\alpha_c = \frac{R_S}{Z \times W} \text{ [Nep/unit length]}. \tag{4.6}$$

It is important to remember that the high-loss line connected to a regular transmission line with low loss produces reflection characterized by coefficient [14]

$$|\Gamma| = \frac{\alpha_c \Lambda}{4\pi} \approx 0.08 \frac{R_S \Lambda}{Z \times W}. \tag{4.7}$$

Therefore, a compromise must be reached in selecting R_S.

For high attenuation values with limited dimensions, conductor of attenuator or termination can be given a meander or spiral line shape [Figure 4.5(c, d)]. The distance between the adjacent conductors of such line must be greater than the doubled width of the conductors. The present attenuator/termination does not require a special configuration of the resistive film, which may have a constant width equal to the width of the regular input transmission line. In this case, the absorption of energy in the film resistor is more uniform, and the maximum dissipated power is greater than in attenuator/termination with a varied conductor width (nonuniform line).

Resistive attenuators (pads) have many applications as series loss elements, step attenuators (see Chapter 13), and return loss control devices. It is known that matched attenuators can be realized either as a *TEE*-section [Figure 4.6(a)] or as a *π*-section [Figure 4.6(b)].
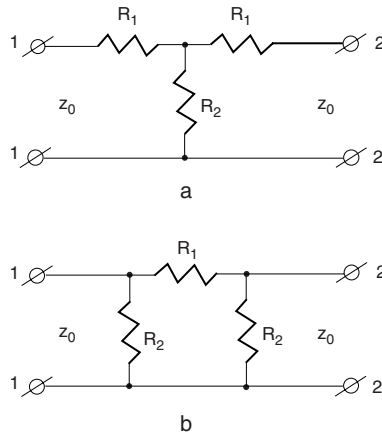
Figure 4.6. Lumped element resistive attenuators: TEE-section (a); π-section (b).

For the *TEE*-section we can see the following:

$$R_1 = \frac{A-1}{A+1},$$

$$R_2 = \frac{2A}{A^2-1},$$

$$R_2 = \frac{R_1^2-1}{2R_1},$$

where $A = 10^{a/20}$ is a numerical ratio of input to output voltage (attenuation, not a decibel notation), and a is attenuation in decibels, as follows:

$$a = 20\log\frac{1+R_1^2+2R_1}{1-R_1^2} \ (\text{dB}).$$

These equations assume an infinity input/output return loss. The next equations should be used for nonperfect return loss:

- Attenuation:

$$a = 20\log\frac{2+2R_1+Y_2\left(1+2R_1+R_1^2\right)}{2} \ (\text{dB}),$$

where $Y_2 = 1/R_2$ is normalized conductance;

- Return loss:

$$20\log 1/|S_{11}| = 20\log \Big/_{|S_{22}|} = 20\log \frac{2 + 2R_1 + Y_2\left(1 + 2R_1 + R_1^2\right)}{2R_1 - Y_2\left(1 - R_1^2\right)}\ (\text{dB}).$$

For the π-section [Figure 4.6(b)] normalized resistor values are

$$R_1 = \frac{1}{2}\left(A - \frac{1}{A}\right),$$

$$R_2 = \frac{A+1}{A-1},$$

$$R_1 = \frac{1}{R_2 + 1},$$

and attenuation is equal to

$$a = 20\log \frac{2R_2^3 + 5R_2^2 + 4R_2 + 1}{2}\ \left(\text{dB}\right).$$

For nonperfect return loss, attenuation is

$$a = 20\log \frac{2 + R_1 + Y_2\left(2 + 2R_1 + Y_2 R_1\right)}{2}\ \left(\text{dB}\right),$$

and return loss is
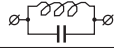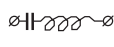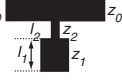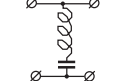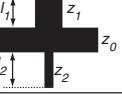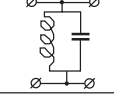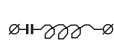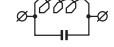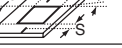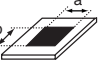
$$20\log \Big/_{|S_{11}|} = 20\log \Big/_{|S_{22}|} = 20\log \frac{R_1 - Y_2\left(2 + Y_2 R_1\right)}{2 + R_1 + Y_2\left(2 + 2R_1 + Y_2 R_1\right)}\ \left(\text{dB}\right).$$

4.5. RESONATORS

Two-dimensional (or planar) and three-dimensional resonators are used in MICs (filters, oscillators, amplifiers, and so forth).

Let us consider different types of planar resonators (see Table 4.2) [15]. Open- and short-circuited distributed transmission lines (Figures 1 and 2 of Table 4.2) are often used as resonators in the microwave range. It

TABLE 4.2. Different Types of Planar Resonators

#	GEOMETRY	LENGTH	EQUIVALENT CIRCUIT	EXPRESSIONS
1		$l = \Lambda/4$		$f_{res} = (2n-1)f_0$ $(n = 1, 2...)$
2	a) b) $\uparrow$S	$l = \Lambda/2$		$f_{res} = nf_0$ $(n = 1, 2...)$
3	z_0 z_0 l_2 z_2 l_1 z_1			$z_1 \ll z_2$; $z_2 > z_0$; $C = \dfrac{33.3}{z_1} l_1 \sqrt{\varepsilon}$; $L = \dfrac{z_2}{30} l_2 \sqrt{\varepsilon}$ $l\,[cm];\ z\,[\Omega];\ C\,[pF];\ L\,[nH]$
4	l_1 z_1 z_0 z_0 l_2 z_2			$z_1 \ll z_2$; $z_2 > z_0$; $C = \dfrac{33.3}{z_1} l_1 \sqrt{\varepsilon}$; $L = \dfrac{z_2}{30} l_2 \sqrt{\varepsilon}$ $l\,[cm];\ z\,[\Omega];\ C\,[pF];\ L\,[nH]$
5				
6				
7	d S S	$l = n\Lambda$		$\lambda = nd\sqrt{\varepsilon_{eff}}$
8	b a W S	$l = 2(a+b) = n\Lambda$		$\lambda_{res} = \dfrac{l\sqrt{\varepsilon_{eff}}}{n}$; $a \gg W$, $b \gg W$
9	d			$\lambda = \dfrac{2\pi r_{eff}\sqrt{\varepsilon_{eff}}}{d_{m,n}}$; $d_{m,n}$ is Bessel's function in order n; $r_{eff} = f(d,h)$
10	a b			$\lambda_{res} = \dfrac{2\sqrt{\varepsilon_{eff}}}{\sqrt{\left(\dfrac{m}{a_{eff}}\right)^2 + \left(\dfrac{n}{b_{eff}}\right)^2}}$; $b_{eff} = \left[\dfrac{120\pi b^3 h}{z(b,h,\varepsilon)\sqrt{\varepsilon_{eff}}}\right]^{1/4}$; $a_{eff} = \left[\dfrac{120\pi a^3 h}{z(a,h,\varepsilon)\sqrt{\varepsilon_{eff}}}\right]^{1/4}$

is difficult in practice to build a short-circuited resonator of exactly the desired length. It is also difficult to control the ground point of shorted resonators, but easy to control an open point. One disadvantage of an opened resonator is radiation from the open end and, therefore, a low Q-factor. In practice the open-circuited resonators are preferred.

A half-wavelength microstrip or stripline resonator is shown in row 2(a) of Table 4.2. Its equivalent length is

$$l_{eq} = l + 2\Delta l = \frac{\Lambda_0}{2} = \frac{\lambda_0}{2\sqrt{\varepsilon}},$$

where Δl is the edge-effect length due to the fringing field at each end (see next paragraph). This resonator can also resonate at $f = nf_0$ ($n = 2, 3, \ldots$).

To decrease radiation from the edges, we can use the hairpin configuration [see Figure 2(b) of Table 4.2]. As the spacing S is reduced, the canceling of the oppositely phased radiation fields in the open ends becomes more complete.

Fringe effects are eliminated in ring- and square-shaped resonators [Figures 7 and 8 of Table 4.2). However, with certain dimensions, these resonators can radiate energy perpendicularly to the substrate surface. The wider the ring, the higher the possible mode of oscillations. When the width of the ring is greater than $\Lambda_0/2$, the high modes arise. In the limiting case, when $2\,W/d \geq 1$, the ring resonator becomes a disk resonator (Figure 9 of Table 4.2). The bigger the radius of the disk, the higher the oscillation mode that arises. Patch resonators (Figures 9 and 10 of Table 4.2) permit the increase the power-handling capability and decrease conductor losses as compared with narrow print line resonators.

Three-dimension dielectric or ferrite resonators can be realized in various configurations. Resonators of cylindrical (or disk) shape are most frequently used in microwave circuits. In most applications, the ratio of height to diameter of a cylindrical resonator is chosen to be close to 0.4. The unloaded Q of a resonator depends on dielectric, conductive, and radiation losses:

$$\frac{1}{Q} = \frac{1}{Q_c} + \frac{1}{Q_d} + \frac{1}{Q_{rad}},$$

where Q_c and Q_d are determined by dissipation in conductor and dielectric respectively, and Q_{rad} is the radiation factor. The quality factor Q of dielectric resonator decreases with increased frequency.

Dielectric resonators are evaluated by their dielectric constant ε, dielectric loss tangent, $\tan\delta$, and the temperature coefficient of the resonant frequency.

Materials used for three-dimensional resonators are dielectrics or ferrites with high dielectric constants, typically around 40 to 70, so that most of the electromagnetic energy is concentrated within the dielectric resonator. As a result, these resonators reduce the volume approximately by

$$1\Big/\sqrt{\varepsilon_{eff}} \ .$$

We have to remember, however, that the total volume also includes housing.

A major problem with high-ε and high-Q materials is poor temperature stability of the dielectric constant and the resulting instability of the resonance frequency. In the best modern materials $Ba_2Ti_9O_{20}$, $BaTi_4O_9$, (Zr –Sn)TiO_4, and so forth [2], with $\varepsilon = 30$–40, the variation of resonance frequency with temperature is approximately +4 ppm/°C.

The principle of ferrite resonators is based on ferrimagnetic resonance which arises when a dc magnetic field is applied (see Chapter 12). The resonance frequency can be adjusted by changing the field strength.

4.6. DISCONTINUITIES

Discontinuities in microwave circuits include open and short ends, air bridges, gaps, steps in width, bends (or corners), and T- and Y-junctions. The influence of discontinuities on parameters of MIC grows with an increase in operation frequency, because physical dimensions of discontinuities become commensurable with wavelength in transmission line.

We have to take into account discontinuity effects to minimize parasitic reactances and improve electrical characteristics of microwave and RF circuits.

Gap in the strip conductor [Figure 4.1(a)] is used to build up, for example, a coupling element in filters and dc blocks. However, it can have

parasitic properties as a part of a print circuit where surface-mount components require a definite space between strip conductors. There are electrical fields between each strip conductor end and the ground plane, as well as between the two conductor ends. A gap in stripline or microstrip line can be equivalently represented as a π-capacitor circuit [see Figure 4.1(b)]. This circuit between the two reference planes T_1 and T_2 at each end of the gap consists of a series coupling capacitance C_1 and two parallel fringing capacitances C_2 between the conductor open ends and the ground [16]. For the gap in microstrip line, normalized capacitances C_1/h and C_2/h versus normalized gaps S/h for $W/h = 0.5, 1.0, 1.5, 2.0, 3.0, 4.0$ are illustrated in [17, 18]. For narrow gaps, C_2 approaches zero and C_1 increases. Practical series capacitance values are approximately 0.01 to 0.5 pF. For a very large gap, the capacitance values C_1 approach zero and this discontinuity becomes equivalent to an open-circuit end.

Open-circuit ends of planar transmission lines are part of open matching stubs, open-circuit resonators used in filters and other devices. The open end of a strip conductor emits some radiation and fringing field that can be seen as either adding to capacitance between the open end and ground or increasing the effective line length [19–21]. The relationship between the two equivalent parameters was described in [22]. The end capacitance is equivalent to edge-effect length for which normalized value $\Delta l/h$ versus normalized conductor width and relative dielectric constant of substrate are shown in [20].

Short circuits (Figure 4.7) are used in filters, matching stub lines, and resonators to obtain grounded points on the upper surface of substrate. A real short circuit causes field and current distortions in the strip conductor. Different versions of short circuits are shown in Figure 4.7(a, b). A short plated through-hole, or via, provides low inductance between the top conductor and ground plane or between two microstrip lines [Figure 4.7(a)]. Vias can be realized by depositing the metal around the cylindrical surface. The short circuit [Figure 4.7(b)] is a metal ribbon of length h and width w bonded to both the microstrip conductor and the ground plane.

An equivalent of a short circuit may be represented by the *T*-circuit in Figure 4.7(c). All parameters of this circuit have inductive characteristics because the magnetic field dominates in this discontinuity. Short circuit can be described by an ideally short-circuited uniform extension Δl_s of the microstrip line [see Figure 4.7(d)] [21, 23].
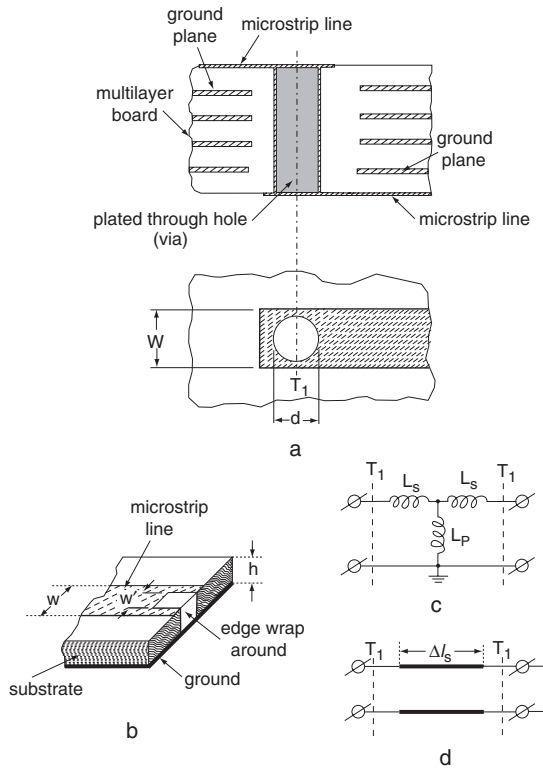
Figure 4.7. Short circuit: base configuration (via) (a); version of short circuit (b); equivalent circuit (c); equivalent extension Δl_s (d).

Air bridges [Figure 4.2(g)] are now a common practice in spiral inductors and coplanar waveguides. The air bridge technique is used in order to reduce parasitic capacitances due to the high-permittivity substrate. The parasitic capacitance in this structure depends on the air gap h_b between the two metal lines in the area of crossover. This parallel-plate capacitance can be given as (4.2) multiplied by 1.7 [24] to include the effect of fringing or stray capacitances. Air bridges have low parasitic capacitance because the low dielectric constant of air and relatively large spacing between two metal lines.

Bends or *corners* [Figure 4.8(a)] are used for changing the direction of a strip conductor, as well as in rectangular resonators, coupled line directional couplers, filters, and so forth. A right-angled bend can be equivalently represented by the circuit in Figure 4.8(b), where parallel capacitor
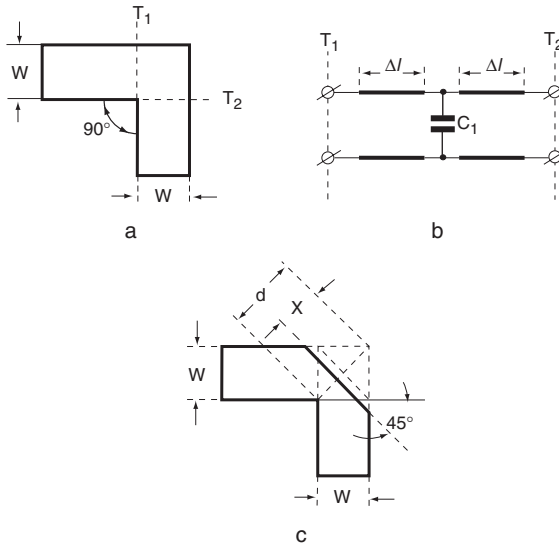
Figure 4.8. Right-angle microstrip bend: uncompensated bend (a); equivalent circuit (b); compensated bend (c).

C_1 accounts for the stored electric energy, and Δl accounts for the current and stored magnetic energy. C_1 and Δl are determined with respect to the structurally defined reference planes T_1 and T_2. Parameters of the present equivalent circuit have been evaluated in [16, 23, 25–27]. For compensation of parasitic reactances and, hence, improving matching of the microstrip bend, it is necessary to reduce the bend capacitance in a symmetrical manner, as illustrated in Figure 4.8(c). The relative chamfer X/d, in percent, is determined by

$$\frac{X}{d}100\% = \left(1 - \frac{d - X}{d}\right)100\% = \left(1 - \frac{W\sqrt{2} - X}{W\sqrt{2}}\right)100\%,$$

where d is the total diagonal and X is that part of the diagonal that has been cut off. Douville and James [27] analyzed microstrip bends with various amounts of chamfering.

Steps are changes in width of a strip conductor [Figure 4.9(a)] or, in other words, junction of two cascaded planar transmission lines with different characteristic impedances. These discontinuities occur in transformers, filters, directional couplers, dividers/combiners, and matching
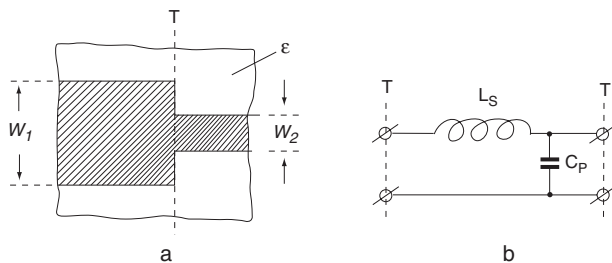
Figure 4.9. Step: base configuration (a); equivalent circuit (b).
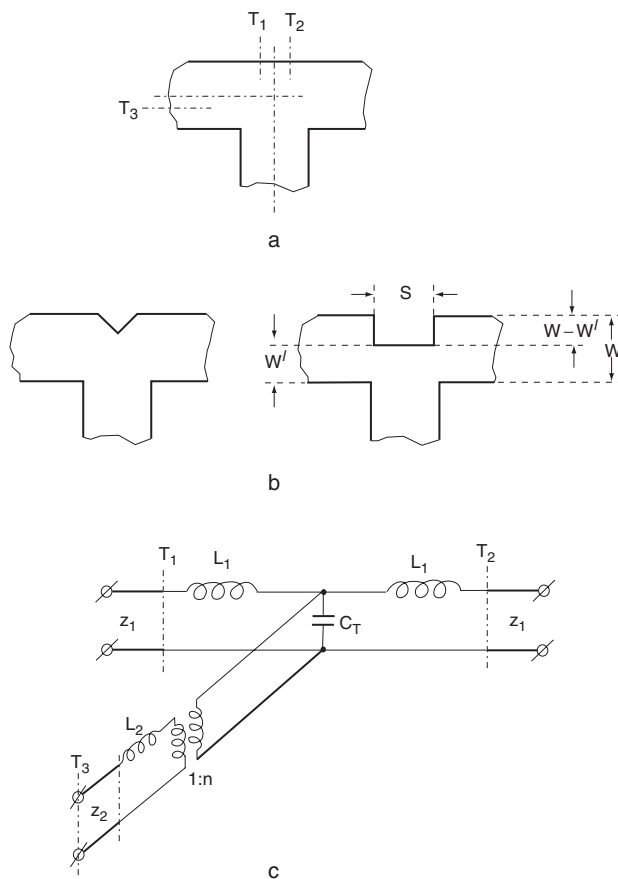
Figure 4.10. T junction: base configuration (a); compensation techniques (b); equivalent circuit (c).

networks. The equivalent circuit of a step discontinuity is shown in Figure 4.9(b). The electric field at the border between the narrow and the wide conductors is distorted, and excess fringing electrical field can be made equivalent by the step capacitance C_p. The current compression can be modeled by a series inductance L_S. The reactive elements of this equivalent circuit for a microstrip step are given in [4, 16, 23].

T-junctions connect two print lines in parallel to a common input line [see Figure 4.10(a)]. This connection is used in dividers/combiners, directional couplers, bias networks, and PIN-diode switches, and so forth. The static equivalent circuit [Figure 4.10(c)] includes two series inductances L_1 in the main line, one series inductance L_2 in the branch line, parallel capacitance C_T in the center junction, and an ideal transformer with turns ratio 1:n (if there is no dispersion, $n = 1$). The normalized inductances and capacitances as functions of physical dimensions of the microstrip line are given in [10, 16, 26, 28]. Discontinuities should be compensated for to improve matching of input/output ports. This is possible, for example, by using triangular and rectangular notches [see Figure 4.10(b)] and by adjusting the lengths of the tree lines forming the junction.

Notch [Figure 4.10(b)] into microstrip width yields an equivalent series inductance. As a slit S is widened, the structure begins to appear as a asymmetrical step between microstrip line of width W and W'. For relatively small S of notch, there is a gap capacitance between two microstrip lines of width W separated by gap S.

REFERENCES

1. Caulton, M., "Lumped Elements in Microwave Integrated Circuits," *Advances in Microwaves*, Vol. 8, 1974, pp. 144–202.
2. Bahl, I., and P. Bhartia, *Microwave Solid State Circuit Design,* New York: John Wiley & Sons, 1988.
3. Howe, H., Jr., *Stripline Circuit Design,* Dedham, MA, Artech House, 1974.
4. Fooks, E. H., and R. A. Zakarevicius, *Microwave Engineering Using Microstrip Circuits,* Upper Saddle River, NJ: Prentice Hall, 1990.
5. Sobol, H., "Applications of Integrated Circuit Technology to Microwave Frequencies," *Proc. IEEE,* Vol. 59, No. 8, August 1971, pp. 1200–1211.

6. Caulton, M., J. J. Hughes, and H. Sobol, "Measurements on the Properties of Microstrip Transmission Lines for Microwave Integrated Circuits," *RCA Review,* Vol. 27, September 1966, pp. 377–391.

7. Terman, F. E., *Radio Engineer's Handbook,* New York: McGraw-Hill, 1945.

8. Chaddock, R. E., "The Application of Lumped Element Techniques to High Frequency Hybrid Integrated Circuits," *Radio and Electronics Engineer,* Vol. 44, 1974, pp. 414–420.

9. Wheeler, H. A., "Simple Inductance Formulas for Radio Coils," *Proc. IRE,* Vol. 16, October 1928, pp. 1398–1400.

10. Gupta, K. C., R. Gard, and R. Chadha, *Computer-Aided Design of Microwave Circuits,* Dedham, MA: Artech House, 1981.

11. Burkett, F. S., "Improved Designs for Thin Film Inductors," *21st Proceedings Electronic Components Conference*, Washington, D.C., May 10–12, 1971, pp. 184–194.

12. Maloratsky, L. G., Single-Layer Print Spiral Inductors, patent pending.

13. Gololobov, V. M., and L. G. Maloratsky, "Miniature Stripline Termination," Patent USSR, # 811373, July 1977.

14. Maloratsky, L. G., *Miniaturization of Microwave Elements and Devices,* Moscow, Russia: Soviet Radio, 1976.

15. Chernushenko, A. M., B. V. Petrov, L. G. Maloratsky, N. E. Melanchenko, A. S. Balsevich, *Design of Screens and Microwave Devices, Textbook*, Moscow, Russia: Radio and Svyaz, 1990.

16. Gupta, K. C., et al., *Microstrip Lines and Slotlines, Second Edition*, Norwood, MA: Artech House, 1996.

17. Benedek, P., and P. Silvester, "Equivalent Capacitances of Microstrip Gaps and Steps," *IEEE Trans. Microwave Theory Tech.,* Vol. 11, November 1972, pp. 729–733.

18. Garg, R., and I. J. Bahl, "Microstrip Discontinuities," *International Journal of Electronics,* Vol. 45, July 1978.

19. Silvester, P., and P. Benedek, "Equivalent Capacitance of Microstrip Open Circuits," *IEEE Trans. Microwave Theory Tech.,* Vol. MTT-20, No. 8, August 1972, pp. 511–516.

20. Kirschning, M., R. H. Jansen, and N. H. L. Koster, "Accurate Model for Open End Effect of Microstrip Lines," *Electronics Letters,* Vol. 17, February 1981, pp. 123–125.

21. Schultz, V., "Bestimmung der Modellparameter von Stiften and Blenden in Wellenleitern mit Hilfe der Methode der Geraden," *Arch. Elektron. Vebertragungstech.,* Vol. 39, March 1985, pp. 203–207.

22. Edwards, T., *Foundations for Microstrip Circuit Design,* 2nd ed., New York: John Wiley & Sons, 1991.

23. Hoffman, R. K., *Handbook of Microwave Integrated Circuits,* Norwood, MA: Artech House, 1987.

24. Jansen, R. H., et al., "Theoretical and Experimental Broadband Characterization of Multiturn Square Spiral Inductors in Sandwich Type GaAs MMICs," *15th European Microwave Symposium,* Paris, France, 1985, pp. 946–951.

25. Gopinath, A., and P. Silvester, "Calculation of Inductance of Finite-Length Strips and Its Variation with Frequency," *IEEE Trans. Microwave Theory Tech.,* Vol. MTT-21, No. 6, June 1973, pp. 380–386.

26. Silvester, P., and P. Benedek, "Microstrip Discontinuity Capacitances for Right-Angle Bands, *T*-Junctions and Crossing," *IEEE Trans. Microwave Theory Tech,* Vol. MTT-21, No. 5, May 1973, pp. 341–346.

27. Douville, R. J. P., and D. S. James, "Experimental Study of Symmetrical Microstrip Bends and Their Compensation," *IEEE Trans. Microwave Theory Tech.,* Vol. MTT-26, March 1978, pp. 175–181.

28. Neale, B. M., and A. Gopinath, "Microstrip Discontinuity Inductances," *IEEE Trans. Microwave Theory Tech.,* Vol. MTT-26, No. 10, October 1978, pp. 827–831.

CHAPTER 5

Common Features and Parameters of Networks

5.1. MULTIPORT NETWORK AS "PANDORA'S BOX"

In Greek mythology, a beautiful woman was created by Hephaestus from earth and water and given many gifts by the gods. Pandora ("the multi-gifted") became her name. Zeus gave her a box that he told her never to open. Unable to resist the temptation, Pandora opened the box and all of life's sufferings and misfortunes, which had been kept inside, spread around the world.

Any multiport network, however complicated, is often represented as a "black box," referring to the mysteriousness of its contents. To open it and to see what is inside is often as troublesome as opening Pandora's box. Not only are microwave modules practically impossible to test on the inside, but opening it can easily alter its characteristics. For these reasons, the black box is usually left unopened during the last stages of design and measurement. Instead, one concentrates on what happens at the ports, which can provide all the necessary information. Such an approach is widely known in microwave as the "wave approach," because it takes into account only the voltage and current waves of inputs and outputs of multiport networks. The wave approach is useful also

because practical measurement uses wave parameters and reflection and transmission coefficients.

It should be noted that in the earlier stages of the design process, when a careful calculation of a device is needed, one considers one-, two-, three-, and four-port networks as elementary black boxes forming the desired circuit. Therefore, it is important to become fluent in the calculation and design of the above elementary networks before turning to the more complicated multiport networks.

5.2. COMMON FEATURES AND PARAMETERS OF TWO-PORT NETWORKS

A two-port network is an electrical device that has two ports, one that serves to connect it to an energy source (e.g., an oscillator) and one that serves to connect it to a load. We will call the first port the input and the second port the output. Let us consider a regular two-port network in which currents are equal and opposite at each pair of terminals [Figure 5.1(a)]. In this case, a port may be regarded as a pair of terminals in which the current into one terminal is equal to the current out of the other. The flow of energy from port 1 to port 2 (from left to right) corresponds to the positive direction of current [Figure 5.1(a)].
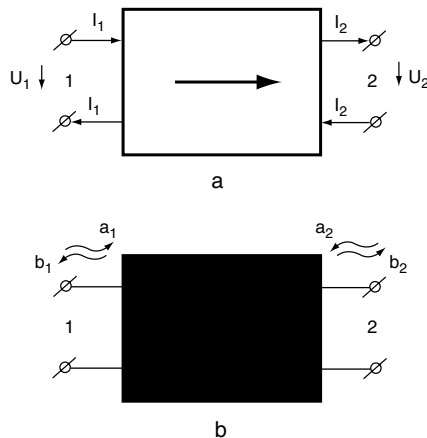
Figure 5.1. A basic two-port network: currents and voltages relevant to the definition of matrices $[A]$ (or $[ABCD]$), $[z]$, and $[y]$ (a); incident and reflected waves relevant to the definition of matrices $[T]$ and $[S]$ of a "black box" (b).

Consider the general linear two-port network in which voltage-current relationships are linear. These linear relationships may be defined as

$$\left.\begin{aligned}\tilde{U}_1 &= \tilde{a}_{11}\tilde{U}_2 + \tilde{a}_{12}\tilde{I}_2\\ \tilde{I}_1 &= \tilde{a}_{21}\tilde{U}_2 + \tilde{a}_{22}\tilde{I}_2\end{aligned}\right\}, \tag{5.1}$$

$$\left.\begin{aligned}\tilde{U}_1 &= z_{11}\tilde{I}_1 + z_{12}\tilde{I}_2\\ \tilde{U}_2 &= z_{21}\tilde{I}_1 + z_{22}\tilde{I}_2\end{aligned}\right\}, \tag{5.2}$$

$$\left.\begin{aligned}\tilde{I}_1 &= y_{11}\tilde{U}_1 + y_{12}\tilde{U}_2\\ \tilde{I}_2 &= y_{21}\tilde{U}_1 + y_{22}\tilde{U}_2\end{aligned}\right\}. \tag{5.3}$$

The above equations can be represented in matrix notation as

$$\begin{bmatrix} U_1\\ I_1 \end{bmatrix} = \begin{bmatrix} a_{11} & a_{12}\\ a_{21} & a_{22} \end{bmatrix}\begin{bmatrix} U_2\\ I_2 \end{bmatrix} = [a]\begin{bmatrix} U_2\\ I_2 \end{bmatrix},$$

$$\begin{bmatrix} U_1\\ U_2 \end{bmatrix} = \begin{bmatrix} z_{11} & z_{12}\\ z_{21} & z_{22} \end{bmatrix}\begin{bmatrix} I_1\\ I_2 \end{bmatrix} = [z]\begin{bmatrix} I_1\\ I_2 \end{bmatrix},$$

$$\begin{bmatrix} I_1\\ I_2 \end{bmatrix} = \begin{bmatrix} y_{11} & y_{12}\\ y_{21} & y_{22} \end{bmatrix}\begin{bmatrix} U_1\\ U_2 \end{bmatrix} = [y]\begin{bmatrix} U_1\\ U_2 \end{bmatrix},$$

where $[a]$ is the classic transfer matrix, $[z]$ is the impedance matrix, $[y]$ is the admittance matrix, and

$$\begin{bmatrix} I_1\\ I_2 \end{bmatrix}, \begin{bmatrix} U_1\\ U_2 \end{bmatrix}, \begin{bmatrix} U_1\\ I_1 \end{bmatrix}, \begin{bmatrix} U_2\\ I_2 \end{bmatrix}$$

are the corresponding vectors for the two-port network.

The individual parameters are specified when the current in the second port is zero ($I_2 = 0$), which corresponds to the second port being open-circuited. In this case from (5.1) and (5.2), open-circuit parameters can be written as

$$a_{11} = \frac{U_1}{U_2}, \quad a_{21} = \frac{I_1}{U_2}, \quad z_{11} = \frac{U_1}{I_1}, \quad z_{21} = \frac{U_2}{I_1}.$$

Coefficient

$$z_{11} = z_0 = \frac{a_{11}}{a_{21}}$$

is the input impedance, and coefficient a_{11} is the voltage transmission coefficient. Characteristics a_{22}, a_{12}, z_{22}, z_{12} can be defined similarly when the input is opened ($I_1 = 0$).

In the short-circuit mode, we have the following short-circuit parameters:

$$a_{22} = \frac{I_1}{I_2}, \, a_{12} = \frac{U_1}{I_2}, \, y_{11} = \frac{I_1}{U_1}, \, y_{21} = \frac{I_2}{U_1}.$$

Coefficient $y_{11} = a_{22}/a_{12}$ is the input admittance, and a_{22} is the current transmission coefficient.

Figure 5.1(b) shows a schematic diagram of a two-port network represented by a black box with the incident traveling waves $\tilde{a}_1, \tilde{a}_2$ flowing into the two-port and the reflected traveling waves $\tilde{b}_1, \tilde{b}_2$ flowing out of the two-port. These waves are related by

$$\left. \begin{array}{l} \tilde{a}_1 = t_{11}\tilde{a}_2 + t_{12}\tilde{b}_2 \\ \tilde{b}_1 = t_{21}\tilde{a}_2 + t_{22}\tilde{b}_2 \end{array} \right\}, \tag{5.4}$$

$$\left. \begin{array}{l} \tilde{b}_1 = s_{11}\tilde{a}_1 + s_{12}\tilde{b}_2 \\ \tilde{a}_2 = s_{21}\tilde{a}_1 + s_{22}\tilde{b}_2 \end{array} \right\}, \tag{5.5}$$

where t_{11}, t_{12}, t_{21}, t_{22} are transfer matrix coefficients, and s_{11}, s_{12}, s_{21}, s_{22} are scattering parameters (or s-parameters).

In matrix notation, (5.4) and (5.5) are then written as

$$\begin{bmatrix} \tilde{a}_1 \\ \tilde{b}_1 \end{bmatrix} = \begin{bmatrix} t_{11} & t_{12} \\ t_{21} & t_{22} \end{bmatrix} \begin{bmatrix} \tilde{a}_2 \\ \tilde{b}_2 \end{bmatrix} = [t] \begin{bmatrix} \tilde{a}_2 \\ \tilde{b}_2 \end{bmatrix},$$

$$\begin{bmatrix} \tilde{b}_1 \\ \tilde{a}_2 \end{bmatrix} = \begin{bmatrix} s_{11} & s_{12} \\ s_{21} & s_{22} \end{bmatrix} \begin{bmatrix} \tilde{a}_1 \\ \tilde{b}_2 \end{bmatrix} = [s] \begin{bmatrix} \tilde{a}_1 \\ \tilde{b}_2 \end{bmatrix},$$

where $[t]$ is the transfer matrix, $[s]$ is the scattering matrix, and

$$\begin{bmatrix} \tilde{a}_1 \\ \tilde{b}_1 \end{bmatrix}, \begin{bmatrix} \tilde{a}_2 \\ \tilde{b}_2 \end{bmatrix}, \begin{bmatrix} \tilde{b}_1 \\ \tilde{a}_2 \end{bmatrix}, \begin{bmatrix} \tilde{a}_1 \\ \tilde{b}_2 \end{bmatrix}$$

are the column matrices.

RF and microwave range test equipment is not capable of measuring the voltages and currents of networks. For the given range, power in inputs (or outputs) of networks is a more convenient characteristic to measure. In order to account for the phase relationships, it is necessary to think of power as the product of complex values of current and voltage.

Wave processes at the inputs and outputs of networks are usually described by the normalized wave matrices. It is helpful to define normalized voltages, currents, and incident and reflected waves as follows:

$$U_1 = \frac{\tilde{U}_1}{\sqrt{z_1}}, U_2 = \frac{\tilde{U}_2}{\sqrt{z_2}}, I_1 = \tilde{I}_1 \sqrt{z_1}, I_2 = \tilde{I}_2 \sqrt{z_2};$$

$$a_1 = \frac{\tilde{a}_1}{\sqrt{z_1}}, b_1 = \frac{\tilde{b}_1}{\sqrt{z_1}}, a_2 = \frac{\tilde{a}_2}{\sqrt{z_2}}, b_2 = \frac{\tilde{b}_2}{\sqrt{z_2}},$$

where all elements of normalized matrices are dimensionless.

Relationships between normalized and non-normalized matrices are given in Appendix C, where

- $[z]$, $[y]$, and $[a]$ are non-normalized impedance, admittance, and classical transfer matrices, respectively.
- $[A]$ (or $[ABCD]$) is the classical normalized transfer matrix.
- $[T]$ and $[S]$ are normalized wave transfer and scattering matrices, respectively.

Calculations are most easily made using a-, A- (or $ABCD$-), and T-parameters, because elements are cascaded simply by multiplying their matrices. This, however, applies only to transfer matrices, not to scattering matrices. On the other hand, the scattering matrix is more convenient for measurement. Transfer matrices based on voltages and currents are not directly measurable at RF and microwave frequencies.

Let us consider the physical interpretation of wave matrix elements. Transfer matrix element T_{11} is the voltage transmission coefficient of a two-port network with input and output lines having characteristic impedances z_1 and z_2. Scattering matrix element S_{11} is the voltage reflection

coefficient of the input port 1 with output 2 matched when energy travels from the first port to the second port. Scattering matrix coefficient $S_{21} = 1/T_{11}$ is the reverse voltage transmission coefficient when the direction of energy flow is positive (from port 1 to port 2). Element S_{12} is the reverse voltage transmission coefficient for the negative flow of energy (from port 2 to port 1). Element S_{22} is the voltage reflection coefficient of port 2 with port 1 matched for the negative flow of energy.

When the direction of energy flow is changed, indexes of scattering matrix coefficients are changed to their opposite: $S_{mn} \Leftrightarrow S_{nm}$.

Let us consider the properties of two-port networks. If a two-port network is reciprocal, the scattering matrix is symmetrical or the S-parameters are equal to their corresponding transpose [1], that is,

$$[S] = [S]_t, \tag{5.6}$$

where the subscript t means "transposed." In this case

$$S_{12} = S_{21},$$

and for transfer matrix coefficients

$$|T| = 1, \quad |A| = 1, \quad |a| = 1,$$

where

$$|T| = T_{11}T_{22} - T_{12}T_{21} = \frac{S_{12}}{S_{21}},$$
$$|A| = A_{11}A_{22} - A_{12}A_{21},$$
$$|a| = a_{11}a_{22} - a_{12}a_{21}.$$

Reciprocity is a very important property of many RF and microwave devices.

For symmetrical and reciprocal two-port networks, matrix elements remain the same when the direction of energy flow is changed; therefore,

$$[S] = \begin{bmatrix} S_{11} & S_{12} \\ S_{12} & S_{11} \end{bmatrix}, \quad [T] = \begin{bmatrix} T_{11} & T_{12} \\ -T_{12} & T_{22} \end{bmatrix},$$
$$[A] = \begin{bmatrix} A_{11} & A_{12} \\ A_{21} & A_{11} \end{bmatrix}, \quad [a] = \begin{bmatrix} a_{11} & a_{12} \\ a_{21} & a_{11} \end{bmatrix}.$$

A symmetrical two-port network is also reciprocal, but a reciprocal two-port network can be symmetrical or asymmetrical.

An antimetric two-port is a network in which the normalized input impedance with an open-circuit output during the positive flow of energy is equal to the normalized input admittance during the negative flow of energy. For such a two-port, matrices $[S]$, $[T]$, and $[A]$ are

$$[S] = \begin{bmatrix} S_{11} & S_{12} \\ S_{12} & -S_{11} \end{bmatrix}, \quad [T] = \begin{bmatrix} T_{11} & T_{12} \\ T_{12} & T_{22} \end{bmatrix}, \quad [A] = \begin{bmatrix} A_{11} & A_{12} \\ A_{21} & A_{22} \end{bmatrix}.$$

The scattering matrix $[S]$ of a lossless network meets the unitary condition

$$[\overline{S}]_t [S] = [1], \tag{5.7}$$

where $[\overline{S}]_t$ is the complex conjugate transpose of $[S]$; $[1]$ is the unit matrix.

For a reciprocal lossless two-port network,

$$[S][\overline{S}]_t = [1] \tag{5.8}$$

or

$$|S_{11}|^2 + |S_{12}|^2 = 1,$$
$$|S_{21}|^2 + |S_{22}|^2 = 1,$$
$$S_{11}^* S_{21} + S_{21}^* S_{22} = 0,$$

where S_{11}^*, S_{21}^* are the complex conjugates of the corresponding terms.

The first two equations characterize the principle of conservation of energy: if the RF or microwave device is lossless, the output power must be equal to the input power, minus the power reflected from the input. The third equation shows phase relation between the corresponding matrix coefficients.

For a reciprocal and lossless two-port network, relationships between transfer matrix coefficients are

$$T_{11} = T_{22}^*, \quad T_{12} = T_{21}^*,$$
$$|T_{11}|^2 = 1 + |T_{21}|^2 = 1 + |T_{12}|^2 = \frac{1}{1 - |S_{11}|^2}.$$

Insertion loss of any two-port network is

$$C = 10\log\left|0.5\left(A_{11} + A_{12} + A_{21} + A_{22}\right)\right|^2 \ (\text{dB}),$$

for a lossless two-port

$$C = 10\log\left[1 + \left|0.5\left(A_{11} - A_{12} + A_{21} - A_{22}\right)\right|^2\right](\text{dB}),$$

and for a lossless and symmetrical four-port

$$C = 10\log\left[1 + \left|0.5\left(A_{12} - A_{21}\right)\right|^2\right](\text{dB}).$$

In an *active* two-port network for at least one direction of energy flow, the energy dissipated on the passive termination exceeds the input energy between $t = 0$ (start of transmission) and t→ ∞. In a *passive* two-port network, the energy dissipated on the passive termination never exceeds the input energy. In a linear two-port network, input and output currents and voltages are linearly related. The discussed methods for analyzing two-port networks will now be extended to multiport networks, in particular, the four-ports.

5.3. PARAMETERS AND FEATURES OF FOUR-PORT NETWORKS

The relationships between normalized currents and voltages at different ports of a four-port network [Figure 5.2(a)] are described by

$$\left.\begin{array}{l} U_1 = A_{11}U_3 + A_{12}U_4 + A_{13}I_3 + A_{14}I_4 \\ U_2 = A_{21}U_3 + A_{22}U_4 + A_{23}I_3 + A_{24}I_4 \\ I_1 = A_{31}U_3 + A_{32}U_4 + A_{33}I_3 + A_{34}I_4 \\ I_2 = A_{41}U_3 + A_{42}U_4 + A_{43}I_3 + A_{44}I_4 \end{array}\right\}. \tag{5.9}$$

In matrix notation, (5.9) is then written as

$$
\begin{bmatrix} U_1 \\ U_2 \\ I_1 \\ I_2 \end{bmatrix} = \begin{bmatrix} A_{11} & A_{12} & A_{13} & A_{14} \\ A_{21} & A_{22} & A_{23} & A_{24} \\ A_{31} & A_{32} & A_{33} & A_{34} \\ A_{41} & A_{42} & A_{43} & A_{44} \end{bmatrix} \begin{bmatrix} U_3 \\ U_4 \\ I_3 \\ I_4 \end{bmatrix} = \begin{bmatrix} A \end{bmatrix} \begin{bmatrix} U_3 \\ U_4 \\ I_3 \\ I_4 \end{bmatrix}.
$$

Matrix $[A]$ is known as the normalized classical transfer matrix, or matrix $[ABCD]$.

The schematic diagram of a four-port network showing incident and reflected waves is illustrated in Figure 5.2(b). The standard relations between these waves are

$$
\left.\begin{aligned}
b_1 &= S_{11}a_1 + S_{12}a_2 + S_{13}a_3 + S_{14}a_4 \\
b_2 &= S_{21}a_1 + S_{22}a_2 + S_{23}a_3 + S_{24}a_4 \\
b_3 &= S_{31}a_1 + S_{32}a_2 + S_{33}a_3 + S_{34}a_4 \\
b_4 &= S_{41}a_1 + S_{42}a_2 + S_{43}a_3 + S_{44}a_4
\end{aligned}\right\}, \tag{5.10}
$$
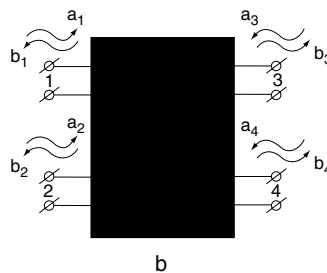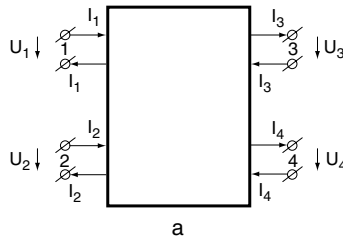
Figure 5.2. A basic four-port network: currents and voltages relevant to the definition of matrices $[A]$ (or $[ABCD]$), $[z]$, and $[y]$ (a); incident and reflected waves relevant to the definition of matrices $[T]$ and $[S]$ of a "black box" (b).

where a_1, a_2, a_3, a_4 are incident normalized voltage waves; b_1, b_2, b_3, b_4 are reflected normalized voltage waves; and S_{11}, S_{12}, ..., S_{34}, S_{44} are normalized S-parameters.

Equation (5.10) can be rewritten in matrix form as follows:

$$
\begin{bmatrix} b_1 \\ b_2 \\ b_3 \\ b_4 \end{bmatrix} = \begin{bmatrix} S_{11} & S_{12} & S_{13} & S_{14} \\ S_{21} & S_{22} & S_{23} & S_{24} \\ S_{31} & S_{32} & S_{33} & S_{34} \\ S_{41} & S_{42} & S_{43} & S_{44} \end{bmatrix} \begin{bmatrix} a_1 \\ a_2 \\ a_3 \\ a_4 \end{bmatrix} = [S] \begin{bmatrix} a_1 \\ a_2 \\ a_3 \\ a_4 \end{bmatrix},
$$

where $[S]$ is the normalized scattering matrix:

$$
[S] = \begin{bmatrix} S_{11} & S_{12} & S_{13} & S_{14} \\ S_{21} & S_{22} & S_{23} & S_{24} \\ S_{31} & S_{32} & S_{33} & S_{34} \\ S_{41} & S_{42} & S_{43} & S_{44} \end{bmatrix}. \tag{5.11}
$$

Each element on the main diagonal of the scattering matrix is a reflection coefficient of a corresponding port when the other ports are terminated by perfect matched loads. The off-diagonal elements are transmission coefficients between the ports.

Another useful representation (for a cascade connection) is given by the following expressions:

$$
\begin{aligned}
a_1 &= T_{11}b_3 + T_{12}b_4 + T_{13}a_3 + T_{14}a_4, \\
a_2 &= T_{21}b_3 + T_{22}b_4 + T_{23}a_3 + T_{24}a_4, \\
b_1 &= T_{31}b_3 + T_{32}b_4 + T_{33}a_3 + T_{34}a_4, \\
b_2 &= T_{41}b_3 + T_{42}b_4 + T_{43}a_3 + T_{44}a_4.
\end{aligned}
$$

In matrix form:

$$
\begin{bmatrix} a_1 \\ a_2 \\ b_1 \\ b_2 \end{bmatrix} = \begin{bmatrix} T_{11} & T_{12} & T_{13} & T_{14} \\ T_{21} & T_{22} & T_{23} & T_{24} \\ T_{31} & T_{32} & T_{33} & T_{34} \\ T_{41} & T_{42} & T_{43} & T_{44} \end{bmatrix} \begin{bmatrix} b_3 \\ b_4 \\ a_3 \\ a_4 \end{bmatrix} = [T] \begin{bmatrix} b_3 \\ b_4 \\ a_3 \\ a_4 \end{bmatrix},
$$

where $[T]$ is the normalized wave transfer matrix:

$$
[T] = \begin{bmatrix} T_{11} & T_{12} & T_{13} & T_{14} \\ T_{21} & T_{22} & T_{23} & T_{24} \\ T_{31} & T_{32} & T_{33} & T_{34} \\ T_{41} & T_{42} & T_{43} & T_{44} \end{bmatrix}.
$$

The relationship between the entries of $[A]$ (or $[ABCD]$), $[S]$, and $[T]$ are summarized in Appendix C.

Let us consider the properties of four-port networks. For a four-port network described by matrix $[S]$, the reciprocity condition is expressed through the equation

$$
[S] = [S]_t, \tag{5.12}
$$

where $[S]_t$ is the transposed scattering matrix.

For a lossless passive four-port network the scattering matrix satisfies the unitary condition:

$$
[\bar{S}]_t [S] = [1], \tag{5.13}
$$

where $[\bar{S}]_t$ is the transposed scattering matrix with all elements replaced by their complex conjugates.

For a four-port that is both reciprocal and lossless [see (5.12) and (5.13)],

$$
[S][\bar{S}]_t = [1]. \tag{5.14}
$$

The result of (5.14) is

$$
\left.\begin{aligned}
&|S_{11}|^2 + |S_{12}|^2 + |S_{13}|^2 + |S_{14}|^2 = 1 \\
&|S_{21}|^2 + |S_{22}|^2 + |S_{23}|^2 + |S_{24}|^2 = 1 \\
&|S_{31}|^2 + |S_{32}|^2 + |S_{33}|^2 + |S_{34}|^2 = 1 \\
&|S_{41}|^2 + |S_{42}|^2 + |S_{43}|^2 + |S_{44}|^2 = 1 \\
&S_{11}S_{12}^* + S_{12}S_{22}^* + S_{13}S_{32}^* + S_{14}S_{42}^* = 0 \\
&S_{11}S_{13}^* + S_{12}S_{23}^* + S_{13}S_{33}^* + S_{14}S_{43}^* = 0 \\
&S_{11}S_{14}^* + S_{12}S_{24}^* + S_{13}S_{34}^* + S_{14}S_{44}^* = 0 \\
&S_{21}S_{13}^* + S_{22}S_{23}^* + S_{23}S_{33}^* + S_{24}S_{43}^* = 0 \\
&S_{21}S_{14}^* + S_{22}S_{24}^* + S_{23}S_{34}^* + S_{24}S_{44}^* = 0 \\
&S_{31}S_{14}^* + S_{32}S_{24}^* + S_{33}S_{34}^* + S_{34}S_{44}^* = 0
\end{aligned}\right\},
\tag{5.15}
$$

where the asterisk indicates a complex conjugate.

A four-port network has *electrical symmetry* if a 180° rotation around the plane of symmetry with mutual replacement of ports does not change the parameters of the network. Symmetry can be *partial* or *full (completely)*. For partial symmetry with respect to the *YY* plane [Figure 5.3(a)], scattering and transfer matrices are

$$
\left.\begin{aligned}
[S] &= \begin{bmatrix} S_{11} & S_{12} & S_{13} & S_{14} \\ S_{12} & S_{11} & S_{14} & S_{13} \\ S_{13} & S_{14} & S_{33} & S_{34} \\ S_{14} & S_{13} & S_{34} & S_{33} \end{bmatrix}, \\
[T] &= \begin{bmatrix} T_{11} & T_{12} & T_{13} & T_{14} \\ T_{12} & T_{11} & T_{14} & T_{13} \\ T_{31} & T_{32} & T_{33} & T_{34} \\ T_{32} & T_{31} & T_{34} & T_{33} \end{bmatrix}
\end{aligned}\right\},
\tag{5.16}
$$
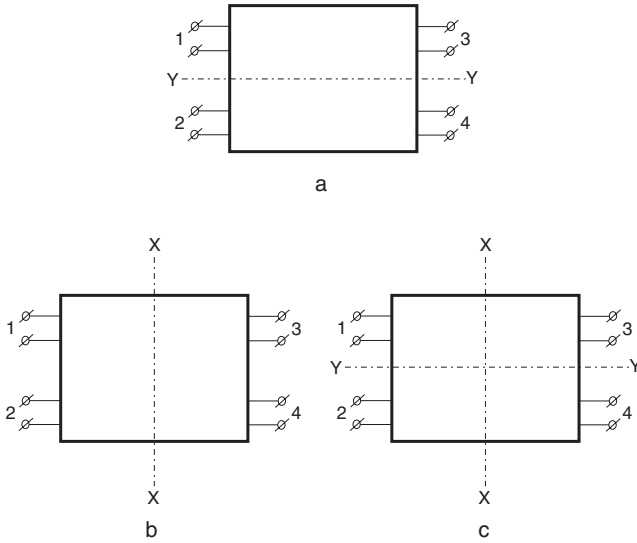
Figure 5.3. Four-port networks with different symmetry types: partial symmetry with plane *YY* (a); partial symmetry with plane *XX* (b); full symmetry with planes *YY* and *XX* (c).

For a partial symmetry with respect to the *XX* plane [Figure 5.3(b)], they are

$$
\left.
\begin{aligned}
[S] &= \begin{bmatrix} S_{11} & S_{12} & S_{13} & S_{14} \\ S_{12} & S_{22} & S_{14} & S_{24} \\ S_{13} & S_{14} & S_{11} & S_{12} \\ S_{14} & S_{24} & S_{12} & S_{22} \end{bmatrix} \\[4pt]
[T] &= \begin{bmatrix} T_{11} & T_{12} & T_{13} & T_{14} \\ T_{12} & T_{22} & T_{23} & T_{24} \\ -T_{13} & -T_{23} & T_{33} & T_{34} \\ -T_{14} & -T_{24} & T_{34} & T_{44} \end{bmatrix}
\end{aligned}
\right\}.
\tag{5.17}
$$

For full symmetry (planes *YY* and *XX*) [Figure 5.3(c)], we obtain the following

$$
\left.
\begin{aligned}
[S] &= \begin{bmatrix}
S_{11} & S_{12} & S_{13} & S_{14} \\
S_{12} & S_{11} & S_{14} & S_{13} \\
S_{13} & S_{14} & S_{11} & S_{12} \\
S_{14} & S_{13} & S_{12} & S_{11}
\end{bmatrix} \\
[T] &= \begin{bmatrix}
T_{11} & T_{12} & T_{13} & T_{14} \\
T_{12} & T_{11} & T_{14} & T_{13} \\
-T_{13} & -T_{14} & T_{33} & T_{34} \\
-T_{14} & -T_{13} & T_{34} & T_{33}
\end{bmatrix}
\end{aligned}
\right\}.
\tag{5.18}
$$

Relationships between the elements of the scattering matrices for reciprocal four-port networks with different types of symmetry are summarized in Table 5.1 [2]. The underlined expressions hold for any type of symmetry.

TABLE 5.1. Relationships Between Scattering Matrix Coefficients for Reciprocal Four-Port Network with Different Types of Symmetry

	Symmetry		
	Partial		
None	Axis XX	Axis YY	Full
S_{11}	$S_{11} = S_{33}$	$S_{11} = S_{22}$	$S_{11} = S_{22} = S_{33} = S_{44}$
$S_{12} = S_{21}$	$S_{12} = S_{21} = S_{34} = S_{43}$	$S_{12} = S_{21}$	$S_{12} = S_{21} = S_{34} = S_{43}$
$S_{13} = S_{31}$	$S_{13} = S_{31}$	$S_{13} = S_{31} = S_{24} = S_{42}$	$S_{13} = S_{31} = S_{24} = S_{42}$
$S_{14} = S_{41}$	$\underline{S_{14} = S_{41} = S_{23} = S_{32}}$	$\underline{S_{14} = S_{41} = S_{23} = S_{32}}$	$\underline{S_{14} = S_{41} = S_{23} = S_{32}}$
S_{22}	$S_{22} = S_{44}$	$S_{33} = S_{44}$	
$S_{23} = S_{32}$	$S_{24} = S_{42}$	$S_{34} = S_{43}$	
$S_{24} = S_{42}$			
S_{33}			
$S_{34} = S_{43}$			
S_{44}			

5.4. SOME ADVANTAGES OF WAVE MATRICES

There are several advantages to the wave matrix representation of a network at RF and microwave frequencies.

The elements of a scattering matrix are relatively easy to measure experimentally. *S*-parameters are related to the power incident on and waves reflected from network ports. In the microwave range, besides frequency we can measure only power and reflection coefficients (module and phase). These measurements are equivalent to measurements of incident and reflected waves. The *Y*- and *Z*-parameters related to the terminal voltages and currents cannot be measured because appropriate microwave test equipment does not exist, and also because broadband short and open circuits are very difficult to achieve.

The principle of conservation of energy for a given device is easily expressed through the unitary condition of the scattering matrix; it is not easy to verify this condition when *Z*- and *Y*-matrices are used.

When reference planes of networks are changed, only the phases of scattering matrix elements are altered. By contrast, *Z*- and *Y*-elements change both in module and phase.

An additional advantage of the transfer matrix is revealed in cascaded structures, where the matrix of the cascaded connection can be determined by simply multiplying the transfer matrices of its components.

The disadvantage of using wave matrices is that there is no information about input structure and processes because the matrix describes characteristics of outside parameters only.

5.5. MATRIX CORRELATION FOR COUPLED LINES

The basic problem in the design of coupled lines is the establishment of a relationship between the physical dimensions and electrical parameters of these lines. In Chapter 3 we discussed coupled lines and the relationships between physical dimensions and wave impedances for even- and odd-modes (z_{0e}, z_{0o}). Now we can see why these relationships are essential. It turns out that it is impossible to relate the dimensions of coupled lines directly to their electrical characteristics or matrix coefficients, which is necessary for analysis or synthesis. This is why we introduced the additional characteristics of coupled lines—z_{0e}, z_{0o}. These impedances bridge

COUPLED LINES

Physical Dimensions **W, S, h** *(or **b**)*
Dielectric Constant ε

Even-Mode Impedance z_{0e}
Odd-Mode Impedance z_{0o}

Analysis

Synthesis

Electrical Characteristics
Scattering Matrix Coefficients
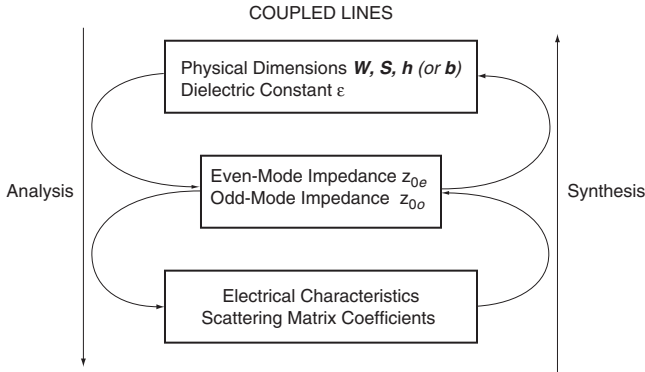
Figure 5.4. Procedure for analysis and synthesis of coupled line devices.

the dimensions and electrical characteristics of coupled lines, as illustrated in Figure 5.4. The top part of this bridge (physical dimensions ⇔ z_{0e}, z_{0o}) was considered in Chapter 3. Now we will determine the bottom part—relationships between electrical parameters of coupled lines or matrix coefficients and z_{0e}, z_{0o}.

Let us consider a four-port network with identical coupled lines (i.e., lines with identical dimensions of conductors). We will be discussing the most frequently used connection of coupled lines to input/output lines with identical impedances.

The normalized transfer matrix [A] (or [ABCD]) for identical coupled lines is [3]

$$[A] = \begin{bmatrix} \cos\Theta & 0 & i\rho\sin\Theta & ir\sin\Theta \\ 0 & \cos\Theta & ir\sin\Theta & i\rho\sin\Theta \\ i\dfrac{\sin\Theta}{w} & -i\dfrac{\sin\Theta}{v} & \cos\Theta & 0 \\ -i\dfrac{\sin\Theta}{v} & i\dfrac{\sin\Theta}{w} & 0 & \cos\Theta \end{bmatrix}, \tag{5.19}$$

where

$$\rho = \frac{z_{0e} + z_{0o}}{2}, \qquad r = \frac{z_{0e} - z_{0o}}{2};$$
$$z_{0e} = \rho + r, \qquad z_{0o} = \rho - r. \tag{5.20}$$

$$\frac{1}{2}\left(\frac{1}{z_{0o}}-\frac{1}{z_{0e}}\right)=\frac{r}{\rho^2-r^2}=\frac{1}{v},$$

$$\frac{1}{2}\left(\frac{1}{z_{0o}}+\frac{1}{z_{0e}}\right)=\frac{\rho}{\rho^2-r^2}=\frac{1}{w}.$$

For coupled lines with equalized electrical and magnetic coupling,

$$\rho v = 1, \tag{5.21}$$

and for reciprocal coupled lines we can write the following conditions:

$$\rho w = r v = 1,$$

$$\rho^2 - r^2 = r v = 1.$$

If two ports of the four-port network are terminated by matched loads, the coupling between voltage and current waves of the other two ports obeys the equations of the two-port network. In most practical cases, four-ports have shorted or opened diagonal ports.

In the case where ports 2 and 3 (or ports 1 and 4) are shorted [Figure 5.5(a)], the classical transfer matrix $[A]$ (or $[ABCD]$), wave transfer matrix $[T]$, and wave scattering matrix $[S]$ of the two-port network are equal:

$$[A]=\frac{-1}{r}\begin{bmatrix} \rho\cos\Theta & i\dfrac{\left[-\cos^2\Theta+1+\sin^2\left(\rho^2-r^2\right)\right]}{2\sin\Theta} \\[3mm] i\dfrac{\left[\cos^2\Theta+1-\sin^2\Theta\left(\rho^2+r^2\right)\right]}{2\sin\Theta} & \rho\cos\Theta \end{bmatrix},$$

$$[T]=\frac{1}{i2r\sin\Theta}\begin{bmatrix} -(\cos\Theta+i\rho\sin\Theta)^2 & -\left(1-r^2\sin^2\Theta\right) \\[2mm] 1-r^2\sin^2\Theta & (\cos\Theta+i\rho\sin\Theta)^2 \end{bmatrix},$$

$$[S]=-\frac{1}{(\cos\Theta+i\rho\sin\Theta)^2}\begin{bmatrix} 1-r^2\sin^2\Theta & i2r\sin\Theta \\[2mm] i2r\sin\Theta & 1-r^2\sin^2\Theta \end{bmatrix}.$$

If the same diagonal ports are opened [Figure 5.5(b)], these matrices are

$$[A] = \frac{1}{r}\begin{bmatrix} \rho\cos\Theta & -i\dfrac{\left(\cos^2\Theta - \rho^2\sin^2\Theta\right)}{2\sin\Theta} \\ -i\dfrac{\left(\cos^2\Theta - \rho^2\sin^2\Theta\right)}{2\sin\Theta} & \rho\cos\Theta \end{bmatrix},$$

$$[T] = \frac{1}{i2r\sin\Theta}\begin{bmatrix} \left(\cos\Theta + i\rho\sin\Theta\right)^2 & -\left(1 - r^2\sin^2\Theta\right) \\ 1 - r^2\sin^2\Theta & -\left(\cos\Theta + i\rho\sin\Theta\right)^2 \end{bmatrix},$$

$$[S] = \frac{1}{\left(\cos\Theta + i\rho\sin\Theta\right)^2}\begin{bmatrix} 1 - r^2\sin^2\Theta & i2r\sin\Theta \\ i2r\sin\Theta & 1 - r^2\sin^2\Theta \end{bmatrix}.$$

Thus, we have determined the relationship between the matrix coefficients and Z_{0e}, Z_{0o}. One can now determine the main electrical characteristics of coupled lines based on the discussed physical meaning of matrix coefficients. The above relationships will be used later in Chapters 7, 8, and 9 in discussing analysis and synthesis of directional couplers, dividers, combiners, and filters.
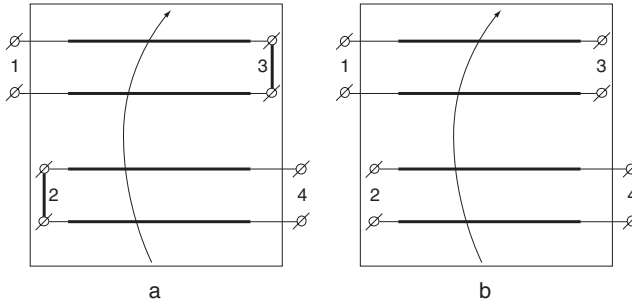
Figure 5.5. Parallel coupled lines: with shorted ports 2 and 3 (a); with opened ports 2 and 3 (b).

REFERENCES

1. Montgomery, C. G., R. H. Dicke, and E. M. Purcell (eds.), *Principles of Microwave Circuits*, Vol. 8, *MIT Radiation Laboratory Series*, New York: McGraw-Hill, 1948, pp. 146–149.

2. Maloratsky, L. G., and L. R. Yavich, *Design and Calculation of Microwave Elements on Strip-Line*, Moscow, Russia: Soviet Radio, 1972.

3. Feldstein, A. L., and L. R. Yavich, *Synthesis of Microwave Two-Ports and Four-Ports*, Moscow, Russia: Svyaz, 1971.

This Page Intentionally Left Blank

CHAPTER 6

Analysis of Symmetrical Networks

6.1. ANALYSIS OF TWO-PORT NETWORKS

Many complex RF two-port networks may be represented by a cascade arrangement of elementary two-port networks with known transfer matrices $[T]_i$, $[A]_i$, (or $[ABCD]_i$) (see, for example, Appendix C) [1, 2]. For n cascaded two-port networks, the transfer matrix is the product of the transfer matrices of the individual two-port networks:

$$\left.\begin{aligned} [T] &= \prod_{i=1}^{n}[T]_i \\ [A] &= \prod_{i=1}^{n}[A]_i \end{aligned}\right\}, \tag{6.1}$$

where n is the number of cascaded two-port networks.

Because matrix multiplication is not commutative, we have to multiply the matrices [see (6.1)] in the proper order (from the source of the energy to the load).

Calculations are significantly simplified if the two-port network is symmetrical. When there is symmetry with respect to plane XX, the two-port network can be divided into two two-port networks mirroring each
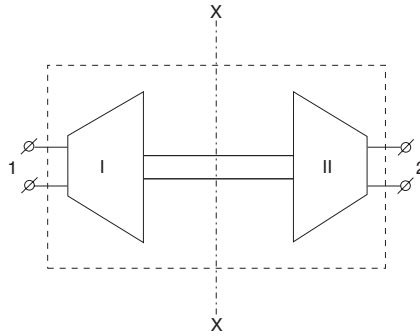
Figure 6.1. Analysis of symmetrical two-port network.

other (**I** and **II**, Figure 6.1) [3–5]. In this case, instead of calculating matrix $[T]$ (or $[A]$) for the whole two-port network, it is enough to determine $[T]^{(I)}$ (or $[A]^{(I)}$) for its left half.

Suppose a symmetric two-port network is described by transfer matrix

$$[T] = \begin{bmatrix} T_{11} & T_{12} \\ T_{21} & T_{22} \end{bmatrix},$$

and its left half (**I**, Figure 6.1) is described by

$$[T]^{(I)} = \begin{bmatrix} T_{11}^{(I)} & T_{12}^{(I)} \\ T_{21}^{(I)} & T_{22}^{(I)} \end{bmatrix}.$$

The right two-port network (**II**, Figure 6.1) with the straight energy transmission (from the source to the load) can be replaced by the left two-port network (**I**) with opposite energy transmission (from the load to the source). The relationship between transfer matrices for the two-port network with straight ($[T]$) and opposite ($[T']$) energy transmission is [3]:

$$\begin{bmatrix} T_{11}' & T_{12}' \\ T_{21}' & T_{22}' \end{bmatrix} = \frac{1}{|T|} \begin{bmatrix} T_{11} & T_{12} \\ T_{21} & T_{22} \end{bmatrix}, \tag{6.2}$$

where

$$|T| = T_{11}T_{22} - T_{12}T_{21} = \frac{S_{12}}{S_{21}}.$$

For the reciprocal two-port network (Figure 6.1):

$$|T| = \frac{S_{12}}{S_{21}} = 1. \tag{6.3}$$

From (6.1), (6.2), and Appendix C, scattering matrix coefficients are

$$\left. \begin{aligned} S_{11} &= \frac{T_{21}}{T_{11}} = \frac{T_{11}^{(I)}T_{21}^{(I)} - T_{22}^{(I)}T_{12}^{(I)}}{\left(T_{11}^{(I)}\right)^2 - \left(T_{12}^{(I)}\right)^2} \\ S_{12} &= \frac{1}{T_{11}} = \frac{1}{\left(T_{11}^{(I)}\right)^2 - \left(T_{12}^{(I)}\right)^2} \end{aligned} \right\}. \tag{6.4}$$

This gives insertion losses C_{12} of the two-port network:

$$C_{12} = 10\log|T_{11}|^2 = 10\log\frac{1}{|S_{21}|^2} = 10\log\left|\left(T_{11}^{(I)}\right)^2 - \left(T_{12}^{(I)}\right)^2\right|^2 \text{ (dB)} \tag{6.5}$$

and also the input reflection coefficient $\Gamma = S_{11}$.

Therefore, for calculation of a symmetrical two-port network, it is sufficient to determine the transfer matrix coefficients of its half.

6.2. ANALYSIS OF SYMMETRICAL FOUR-PORT NETWORKS

Four-port networks symmetric with respect to one or two planes (see Chapter 5) are frequently implemented in RF and microwave devices.

A mirror-reflection method [6] is widely used for analyzing four-port networks symmetric about the *YY* plane [Figure 6.2(a)]. In the following analysis, we extend this method to four-port networks with various types of symmetry.

Let us consider a four-port with partial symmetry with respect to the horizontal plane *YY* [Figure 6.3(a)]. We suppose that a signal of unit amplitude +1 is applied to port 1. Such a network can then be equivalently represented by two four-port networks with two signals of amplitude 1/2 each applied to ports 1 and 2 [Figure 6.2(b, c)].

In Figure 6.2(b), two in-phase signals of amplitude (+1/2, +1/2) are applied to ports 1 and 2. This corresponds to the even mode (++), where
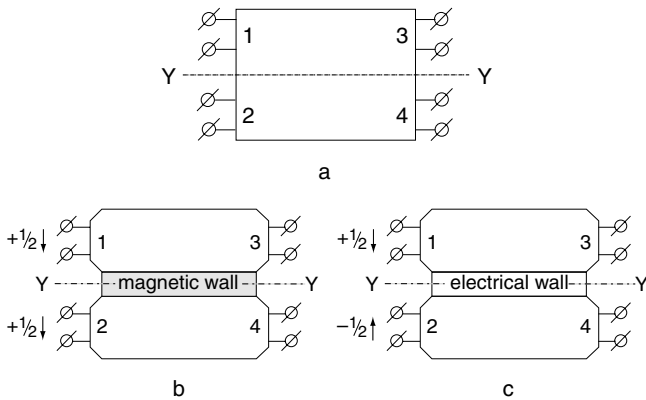
Figure 6.2. Analysis of symmetrical four-port network: basic four-port network (a); even mode excitation model (b); odd mode excitation model (c).

currents in ports 1 and 2 are equal in magnitude and direction. These currents cancel each other out in the plane of symmetry [Figure 6.2(b)], creating a virtual open circuit. Therefore, the plane of symmetry can be thought of as a "magnetic wall."

In Figure 6.2(c), two out-of-phase signals of amplitude (+1/2, –1/2) are applied to ports 1 and 2. This corresponds to the odd mode (+–), where currents in ports 1 and 2 are equal in magnitude and opposite in direction. On the symmetry plane, current is at the maximum, creating a virtual short circuit (an "electrical wall").

In the manner described above, a four-port network with an arbitrary number of connections in the symmetry plane [Figure 6.3(a)] can be equivalently represented by two pairs of two-port networks corresponding to the even and odd modes. Figure 6.3 shows one two-port network from

Figure 6.3. From four-port network to two-port network: basic four-port network (a); even-mode two-port network (b); odd-mode two-port network (c).

each pair, the even-mode two-port with open connections [Figure 6.3(b)], and the odd-mode two-port network with short-circuited connections [Figure 6.3(c)].

Thus, the calculation of the four-port network is reduced to a significantly simpler calculation of two independent two-port networks for the even and odd modes.

Wave transfer matrices of two-port networks for the two modes are

$$[T]^{++} = \begin{bmatrix} T_{11}^{++} & T_{12}^{++} \\ T_{21}^{++} & T_{22}^{++} \end{bmatrix}, \quad [T]^{+-} = \begin{bmatrix} T_{11}^{+-} & T_{12}^{+-} \\ T_{21}^{+-} & T_{22}^{+-} \end{bmatrix}. \tag{6.6}$$

For a cascaded connection of two-port networks, the following relationships hold [see (6.1)]:

$$[T]^{++} = [T]^{++}_{(I)} \times [T]^{++}_{(II)} \times ... \times [T]^{++}_{(n)},$$
$$[T]^{+-} = [T]^{+-}_{(I)} \times [T]^{+-}_{(II)} \times ... \times [T]^{+-}_{(n)}, \tag{6.7}$$

where

$$[T]^{++}_{(I)},...,[T]^{++}_{(n)} \text{ and } [T]^{+-}_{(I)},...,[T]^{+-}_{(n)}$$

are wave transfer matrices of the elementary two-port networks[*] of the cascaded connection. Similar relationships hold for classical transfer matrices of two-port networks.

A reciprocal four-port network, symmetric about the *YY* plane, is described by the transfer matrix

$$[T] = \begin{bmatrix} T_{11} & T_{12} & T_{13} & T_{14} \\ T_{12} & T_{11} & T_{14} & T_{13} \\ T_{31} & T_{32} & T_{33} & T_{34} \\ T_{32} & T_{31} & T_{34} & T_{33} \end{bmatrix}. \tag{6.8}$$

---

*From this point on, "elementary two-ports" will designate networks with known transfer matrices (see, for example, Appendix C).

It can be shown that here [see (6.6)]

$$T_{11} = \frac{1}{2}\left(T_{11}^{++} + T_{11}^{+-}\right), \qquad (6.9)$$

$$T_{12} = \frac{1}{2}\left(T_{11}^{++} - T_{11}^{+-}\right), \qquad (6.10)$$

$$T_{13} = \frac{1}{2}\left(T_{12}^{++} + T_{12}^{+-}\right), \qquad (6.11)$$

$$T_{14} = \frac{1}{2}\left(T_{12}^{++} - T_{12}^{+-}\right), \qquad (6.12)$$

$$T_{33} = \frac{1}{2}\left(T_{22}^{++} + T_{22}^{+-}\right), \qquad (6.13)$$

$$T_{34} = \frac{1}{2}\left(T_{22}^{++} - T_{22}^{+-}\right), \qquad (6.14)$$

$$T_{31} = \frac{1}{2}\left(T_{21}^{++} + T_{21}^{+-}\right), \qquad (6.15)$$

$$T_{32} = \frac{1}{2}\left(T_{21}^{++} - T_{21}^{+-}\right). \qquad (6.16)$$

These equations contain only six independent elements of the T-matrix: T_{11}, T_{12}, T_{13}, T_{14}, T_{33}, and T_{34}, by means of which T_{31} and T_{32} can be evaluated. However, (6.15) and (6.16) are useful for design purposes.

The elements of the scattering matrix are

$$S_{11} = \frac{1}{2}\left(\frac{T_{21}^{++}}{T_{11}^{++}} + \frac{T_{21}^{+-}}{T_{11}^{+-}}\right), \qquad (6.17)$$

$$S_{12} = \frac{1}{2}\left(\frac{T_{21}^{++}}{T_{11}^{++}} - \frac{T_{21}^{+-}}{T_{11}^{+-}}\right), \qquad (6.18)$$

$$S_{13} = \frac{1}{2}\left(\frac{1}{T_{11}^{++}} + \frac{1}{T_{11}^{+-}} \right), \tag{6.19}$$

$$S_{14} = \frac{1}{2}\left(\frac{1}{T_{11}^{++}} - \frac{1}{T_{11}^{+-}} \right), \tag{6.20}$$

$$S_{33} = -\frac{1}{2}\left(\frac{T_{12}^{++}}{T_{11}^{++}} + \frac{T_{12}^{+-}}{T_{11}^{+-}} \right), \tag{6.21}$$

$$S_{34} = -\frac{1}{2}\left(\frac{T_{12}^{++}}{T_{11}^{++}} - \frac{T_{12}^{+-}}{T_{11}^{+-}} \right). \tag{6.22}$$

The calculation can be simplified if there are extra symmetry conditions [3, 4] inside the two-port network consisting of a cascade connection of component two-port networks. If the symmetric four-port network has the structure shown in Figure 6.4(a) and consists of a cascade connection of three pairs of two-port networks described by the transfer matrices $[T_{(I)}]$, $[T_{(II)}]$, and $[T_{(III)}]$, with two-port networks **I** and **III** being mirror images of one another, while the reciprocal two-port network **II** can have any structure. For the case of the even mode,

$$[T]^{++} = [T]_{(I)}^{++} \times [T]_{(II)}^{++} \times [T]_{(III)}^{++} =$$
$$\begin{bmatrix} T_{11(I)}^{++} & T_{12(I)}^{++} \\ T_{21(I)}^{++} & T_{22(I)}^{++} \end{bmatrix} \times \begin{bmatrix} T_{11(II)}^{++} & T_{12(II)}^{++} \\ T_{21(II)}^{++} & T_{22(II)}^{++} \end{bmatrix} \times \begin{bmatrix} T_{11(I)}^{++} & -T_{21(I)}^{++} \\ -T_{12(I)}^{++} & T_{22(I)}^{++} \end{bmatrix}. \tag{6.23}$$
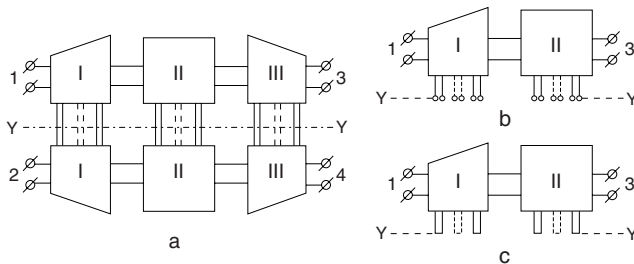
Figure 6.4. Mirror-reflection method for partial symmetrical four-port network: basic four-port network (a); even-mode two-port network (b); odd-mode two-port network (c).

Evaluating (6.23) gives

$$
\begin{aligned}
T_{11}^{++} &= \left(T_{11(I)}^{++}\right)^2 T_{11(II)}^{++} - \left(T_{12(I)}^{++}\right)^2 T_{22(II)}^{++} \\
&+ T_{11(I)}^{++} T_{12(I)}^{++} \left(T_{21(II)}^{++} - T_{12(II)}^{++}\right),
\end{aligned}
\tag{6.24}
$$

$$
\begin{aligned}
T_{12}^{++} &= -T_{11(I)}^{++} \left(T_{21(I)}^{++} T_{11(II)}^{++} - T_{22(I)}^{++} T_{12(II)}^{++}\right) \\
&- T_{12(I)}^{++} \left(T_{21(I)}^{++} T_{21(II)}^{++} - T_{22(I)}^{++} T_{22(II)}^{++}\right),
\end{aligned}
\tag{6.25}
$$

$$
\begin{aligned}
T_{21}^{++} &= T_{11(I)}^{++} \left(T_{21(I)}^{++} T_{11(II)}^{++} + T_{22(I)}^{++} T_{21(II)}^{++}\right) \\
&- T_{12(I)}^{++} \left(T_{21(I)}^{++} T_{12(II)}^{++} + T_{22(I)}^{++} T_{22(II)}^{++}\right),
\end{aligned}
\tag{6.26}
$$

$$
\begin{aligned}
T_{22}^{++} &= -\left(T_{21(I)}^{++}\right)^2 T_{11(II)}^{++} + \left(T_{22(I)}^{++}\right)^2 T_{22(II)}^{++} \\
&- T_{22(I)}^{++} T_{21(I)}^{++} \left(T_{21(II)}^{++} - T_{12(II)}^{++}\right).
\end{aligned}
\tag{6.27}
$$

Similar expressions are obtained for the case of the odd mode, when

$$
[T]^{+-} = [T]^{+-}_{(I)} \times [T]^{+-}_{(II)} \times [T]^{+-}_{(III)}.
\tag{6.28}
$$

Thus, to find $[T]$ for the four-port network, we need only know matrices

$$
[T]^{++}_{(I)},\ [T]^{+-}_{(I)}\ \text{and}\ [T]^{++}_{(II)},\ [T]^{+-}_{(II)}
$$

of the component two-port networks.

Let us consider the full symmetrical four-port network with *XX* and *YY* symmetry axes (Figure 6.5). This practical case can be obtained from the previous case if

$$
[T]^{++}_{(II)} = [T]^{+-}_{(II)} = \begin{bmatrix} 1 & 0 \\ 0 & 1 \end{bmatrix}.
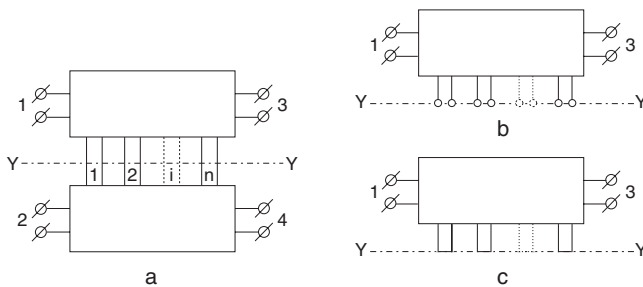\tag{6.29}
$$
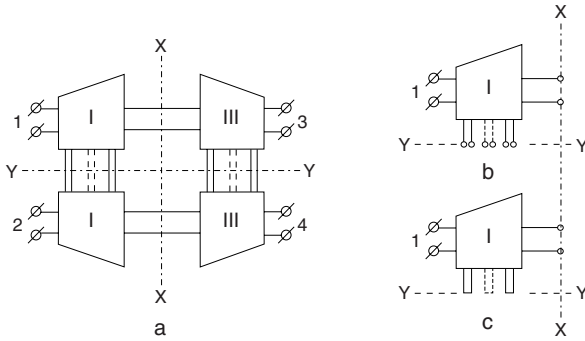
Figure 6.5. Mirror-reflection method for full symmetrical four-port network: basic four-port network (a); even-mode two-port network (b); odd-mode two-port network (c).

Substituting (6.24) to (6.27) [and similar expressions following from (6.28)] into (6.9) to (6.16) and using (6.29), we obtain

$$
\left.
\begin{aligned}
T_{11} &= \frac{1}{2}\left[\left(T_{11(I)}^{++}\right)^2 + \left(T_{11(I)}^{+-}\right)^2 - \left(T_{12(I)}^{++}\right)^2 - \left(T_{12(I)}^{+-}\right)^2\right] \\
T_{12} &= \frac{1}{2}\left[\left(T_{11(I)}^{++}\right)^2 - \left(T_{11(I)}^{+-}\right)^2 - \left(T_{12(I)}^{++}\right)^2 + \left(T_{12(I)}^{+-}\right)^2\right] \\
T_{13} &= \frac{1}{2}\left[-T_{11(I)}^{++}T_{21(I)}^{++} - T_{11(I)}^{+-}T_{21(I)}^{+-} + T_{12(I)}^{++}T_{22(I)}^{++} + T_{12(I)}^{+-}T_{22(I)}^{+-}\right] \\
T_{14} &= \frac{1}{2}\left[-T_{11(I)}^{++}T_{21(I)}^{++} + T_{11(I)}^{+-}T_{21(I)}^{+-} + T_{12(I)}^{++}T_{22(I)}^{++} - T_{12(I)}^{+-}T_{22(I)}^{+-}\right] \\
T_{33} &= \frac{1}{2}\left[-\left(T_{21(I)}^{++}\right)^2 - \left(T_{21(I)}^{+-}\right)^2 + \left(T_{22(I)}^{++}\right)^2 + \left(T_{22(I)}^{+-}\right)^2\right] \\
T_{34} &= \frac{1}{2}\left[-\left(T_{21(I)}^{++}\right)^2 + \left(T_{21(I)}^{+-}\right)^2 + \left(T_{22(I)}^{++}\right)^2 - \left(T_{22(I)}^{+-}\right)^2\right]
\end{aligned}
\right\}. \tag{6.30}
$$

From (6.30), it follows that the calculation of transfer matrix $[T]$ of a full symmetrical four-port network requires only the knowledge of transfer matrices

$$[T]_{(I)}^{++} \text{ and } [T]_{(I)}^{+-},$$

describing one-quarter of the four-port network [Figure 6.5(b, c)].

We now turn to the proper procedure for calculating the characteristics of a symmetric four-port network:

1. Determine the transfer matrices of the two-port networks having even- and odd-mode excitation. In case of a cascade connection of four-port networks, the transfer matrix is equal to the product of transfer matrices of the component four-port networks.
2. Determine the most important scattering element of the four-port network, for example, coefficient S_{11}, which characterizes the input matching. For some devices, matching is not the most important parameter. For example, sometimes determining the power split is the first priority. In this case, one should first calculate the corresponding elements S_{mn} $(m \neq n)$.
3. Determine relationships among admittances (or impedances) of line segments of the four-port network from the conditions of perfect matching ($S_{11} = 0$) (our example), ideal power split, and so forth.
4. Calculate the remaining elements of the scattering matrix accounting for the found relationships among admittances.
5. Determine the characteristics of the four-port network.

6.3. ANALYSIS OF SYMMETRICAL THREE-PORT NETWORKS

Let us consider a three-port network [Figure 6.6(a)] symmetric with respect to the horizontal plane YY, loaded with equal impedances z_0 of input (output) lines.

The three-port network can be represented by an equivalent four-port network symmetric about YY [inside dashed line in Figure 6.6(b)]. Ports 1 and 2 of this four-port network are terminated with impedances, z_0, while ports 3 and 4 are terminated with impedances $2z_0$. Differences between the impedances are taken into account when normalizing scattering matrix elements and voltage waves.

The normalized voltage waves are designated by a'_3, b'_3 [see Figure 6.6(c)]. The equations describing the properties of the three-port network then have the following form:

$$
\left.
\begin{aligned}
b_1 &= \hat{S}_{11}a_1 + \hat{S}_{12}a_2 + \hat{S}_{11}a'_3 \\
b_2 &= \hat{S}_{21}a_1 + \hat{S}_{22}a_2 + \hat{S}_{23}a'_3 \\
b'_3 &= \hat{S}_{31}a_1 + \hat{S}_{32}a_2 + \hat{S}_{33}a'_3
\end{aligned}
\right\},
\tag{6.31}
$$

where

$$
\hat{S}_{11}, \ \hat{S}_{12}, \ ..., \ \hat{S}_{32}, \ \hat{S}_{33}
$$

are elements of the scattering matrix of the three-port network.
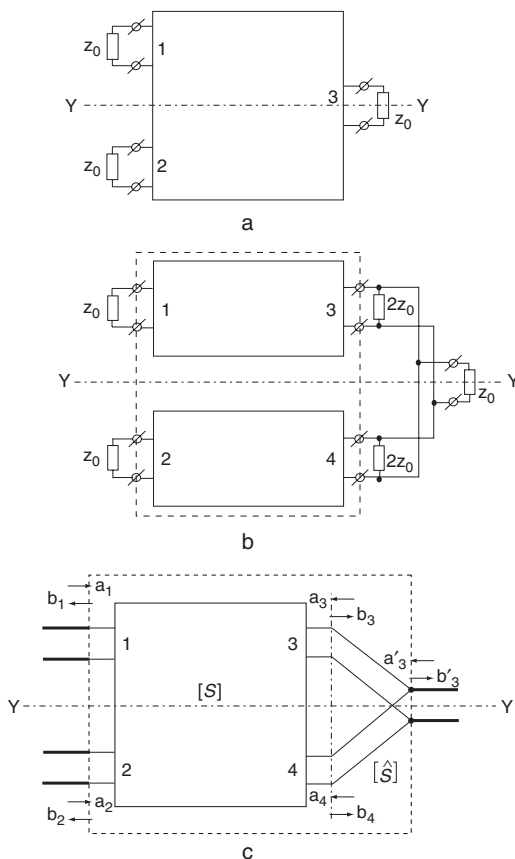
Figure 6.6. Symmetrical three-port network: basic three-port (a); equivalent four-port (b); incident and reflected voltage waves (c).

Using the rules for normalizing the voltage waves in the three-port network [Figure 6.6(a)] (equal terminations z_0) and in the four-port network [Figure 6.6(b)] (different terminations z_0 and $2z_0$), we obtain the relationships between normalized voltage waves a_3', b_3' in port 3 of the three-port network and a_3, b_3 in port 3 of the four-port network [Figure 6.6(c)]:

$$a_3 = \frac{a_3'}{\sqrt{2}}, \ b_3 = \frac{b_3'}{\sqrt{2}}.$$

From Figure 6.6(c), it can be seen that port 3 of the three-port network is represented by the parallel connection of ports 3 and 4 of the four-port network; therefore,

$$a_3 = a_4 = \frac{a_3'}{\sqrt{2}}, \ b_3 = b_4 = \frac{b_3'}{\sqrt{2}}.$$

Substituting these identities into (5.10) gives

$$\left.\begin{array}{l} b_1 = S_{11}a_1 + S_{12}a_2 + \dfrac{1}{\sqrt{2}}\left(S_{13} + S_{14}\right)a'_3 \\[2mm] b_2 = S_{21}a_1 + S_{22}a_2 + \dfrac{1}{\sqrt{2}}\left(S_{23} + S_{24}\right)a'_3 \\[2mm] b_3' = \sqrt{2}S_{31}a_1 + \sqrt{2}S_{32}a_2 + \dfrac{1}{\sqrt{2}}\left(S_{43} + S_{44}\right)a'_3 \end{array}\right\}. \qquad (6.32)$$

Comparing (6.31) and (6.32), we conclude

$$\left.\begin{array}{l} \hat{S}_{11} = S_{11}, \ \hat{S}_{12} = S_{12}, \ \hat{S}_{13} = \dfrac{1}{\sqrt{2}}\left(S_{13} + S_{14}\right) \\[2mm] \hat{S}_{21} = S_{21}, \ \hat{S}_{22} = S_{22}, \ \hat{S}_{23} = \dfrac{1}{\sqrt{2}}\left(S_{23} + S_{24}\right) \\[2mm] \hat{S}_{31} = \sqrt{2}S_{31}, \ \hat{S}_{32} = \sqrt{2}S_{32}, \ \hat{S}_{33} = S_{43} + S_{44} \end{array}\right\}. \qquad (6.33)$$

Identities (6.33) determine the relationships between elements of the scattering matrix of the four-port network and elements of the scattering matrix of the three-port network.
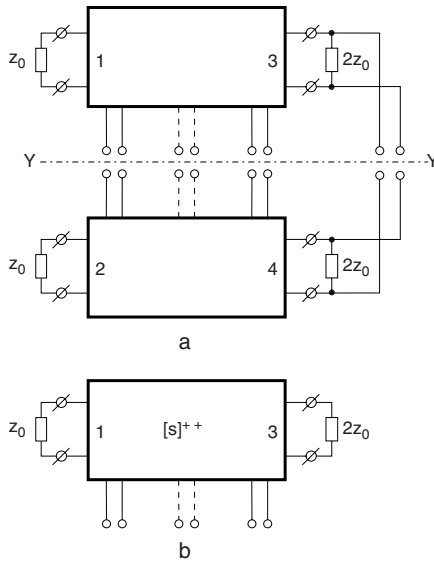
Figure 6.7. Even excitation model for the three-port network: basic three-port network (a); equivalent two-port network (b).

Using the mirror-reflection method, we obtain the two-port networks shown in Figures 6.7 and 6.8. Then, we determine input admittance y_{sc}^{+-} of the two-port network for the odd mode [Figure 6.8(b)]. We arrive at the equivalent two-port network with termination z_0 connected to the left port, while the right port is free. The scattering matrix of this two-port network is

$$[S]^{+-} = \begin{bmatrix} \dfrac{1 - Y_{sc}^{+-}}{1 + Y_{sc}^{+-}} & 0 \\ 0 & 1 \end{bmatrix},$$

where

$$Y_{sc}^{+-} = y_{sc}^{+-} z_0.$$

It follows that

$$S_{11}^{+-} = \frac{1 - Y_{sc}^{+-}}{1 + Y_{sc}^{+-}}, \ S_{12}^{+-} = S_{21}^{+-} = 0, \ S_{22}^{+-} = 1.$$
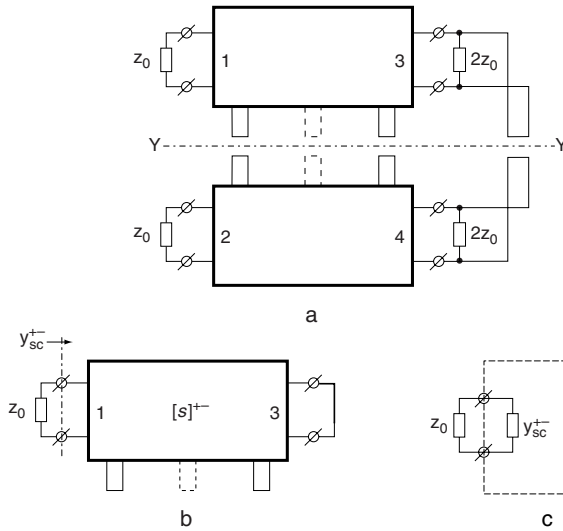
Figure 6.8. Odd excitation model for the three-port network: basic three-port network (a); equivalent two-port network (b); equivalent one-port network (c).

Substituting into (6.33), we obtain

$$\hat{S}_{11} = \hat{S}_{22} = \frac{1}{2}\left(S_{11}^{+-} + S_{11}^{+-}\right),$$

$$\hat{S}_{12} = \hat{S}_{21} = \frac{1}{2}\left(S_{11}^{+-} - S_{11}^{+-}\right),$$

$$\hat{S}_{13} = \hat{S}_{31} = \hat{S}_{23} = \hat{S}_{32} = \frac{1}{\sqrt{2}}S_{12}^{++},$$

$$\hat{S}_{33} = S_{22}^{++}.$$

In particular, in the even mode, when the two-port network is lossless, it follows from the unitary condition of the scattering matrix that

$$\left|S_{12}^{++}\right| = \sqrt{1 - \left|S_{11}^{++}\right|^2}, \ \left|S_{11}^{++}\right| = \left|S_{22}^{++}\right|.$$

In this case,

$$
\left.\begin{aligned}
\left|S_{11}\right| &= \left|S_{22}\right| = \frac{1}{2}\left|\left(S_{11}^{++} + S_{11}^{+-}\right)\right| \\
\left|S_{12}\right| &= \left|S_{21}\right| = \frac{1}{2}\left|\left(S_{11}^{++} - S_{11}^{+-}\right)\right| \\
\left|S_{13}\right| &= \left|S_{31}\right| = \left|S_{23}\right| = \left|S_{32}\right| = \frac{1}{2}\sqrt{1 - \left|S_{11}^{++}\right|^{2}} \\
\left|S_{33}\right| &= \left|S_{22}^{++}\right| = \left|S_{11}^{++}\right|
\end{aligned}\right\}.
\tag{6.34}
$$

With the help of (6.33) and Appendix C, elements of scattering matrix $[\hat{S}]$ of the three-port can be expressed through elements of matrices $[S]^{++}$, $[S]^{+-}$, $[A]^{++}$, and $[A]^{+-}$ of the two-port:

$$
\begin{aligned}
\hat{S}_{11} &= \frac{1}{2}\left(S_{11}^{++} + S_{11}^{+-}\right) \\
&= \frac{1}{2}\left(\frac{A_{11}^{++} + A_{12}^{++} - A_{21}^{++} - A_{22}^{++}}{A_{11}^{++} + A_{12}^{++} + A_{21}^{++} + A_{22}^{++}} + \frac{A_{11}^{+-} + A_{12}^{+-} - A_{21}^{+-} - A_{22}^{+-}}{A_{11}^{+-} + A_{12}^{+-} + A_{21}^{+-} + A_{22}^{+-}}\right), \\
\hat{S}_{12} &= \frac{1}{2}\left(S_{11}^{++} - S_{11}^{+-}\right) \\
&= \frac{1}{2}\left(\frac{A_{11}^{++} + A_{12}^{++} - A_{21}^{++} - A_{22}^{++}}{A_{11}^{++} + A_{12}^{++} + A_{21}^{++} + A_{22}^{++}} - \frac{A_{11}^{+-} + A_{12}^{+-} - A_{21}^{+-} - A_{22}^{+-}}{A_{11}^{+-} + A_{12}^{+-} + A_{21}^{+-} + A_{22}^{+-}}\right), \\
\hat{S}_{13} &= \hat{S}_{23} = \frac{S_{12}^{++}}{\sqrt{2}} = \frac{\sqrt{2}}{A_{11}^{++} + A_{12}^{++} + A_{21}^{++} + A_{22}^{++}}, \\
\hat{S}_{33} &= \hat{S}_{22} = \frac{A_{11}^{++} - A_{12}^{++} + A_{21}^{++} - A_{22}^{++}}{A_{11}^{++} + A_{12}^{++} + A_{21}^{++} + A_{22}^{++}}.
\end{aligned}
\tag{6.35}
$$

The relationships between elements of the scattering matrix of the three-port and elements of the transfer matrices of the two-ports are as follows (see Appendix C):

$$\left.\begin{aligned}
\hat{S}_{11} = \hat{S}_{22} &= \frac{1}{2}\left(\frac{T_{21}^{++}}{T_{11}^{++}} + \frac{T_{21}^{+-}}{T_{11}^{+-}}\right) \\[2mm]
\hat{S}_{12} = \hat{S}_{21} &= \frac{1}{2}\left(\frac{T_{21}^{++}}{T_{11}^{++}} - \frac{T_{21}^{+-}}{T_{11}^{+-}}\right) \\[2mm]
\hat{S}_{13} = \hat{S}_{31} = \hat{S}_{23} = \hat{S}_{32} &= \frac{1}{\sqrt{2}} \ \ \frac{1}{T_{11}^{++}} \\[2mm]
\hat{S}_{33} &= -\frac{T_{12}^{++}}{T_{11}^{++}}
\end{aligned}\right\}.
\qquad (6.36)$$

REFERENCES

1. Montgomery, C. G., R. H. Dicke, and E. M. Purcell, *Principles of Microwave Circuits,* Vol. 8, *MIT Radiation Laboratory Series*, New York: McGraw-Hill, 1948.
2. Young, L. (ed.), *Advances in Microwaves,* New York: Academic Press, 1966.
3. Malorartsky, L. G., and L. R. Yavich, *Design and Calculation of Microwave Elements on Stripline,* Moscow, Russia: Soviet Radio, 1972.
4. Maloratsky, L. G., and L. R. Yavich, "Design of Symmetric Four-Poles," *Telecommunications and Radioengineering,* Vol. 10, 1968, pp. 46–49.
5. Feldshtein, A. L., and L. R. Yavich, *Synthesis of Microwave Two-Ports and Four-Ports,* Moscow, Russia: Sviaz, 1971.
6. Reed, J., and G. Wheeler, "A Method of Analysis of Symmetric Four-Port Networks," *IRE Trans. Microwave Theory Tech.,* Vol. MTT-4, October 1956, pp. 246–252.

CHAPTER 7

Directional Couplers

Directional couplers are used frequently in dividers, combiners, attenuators, phase shifters, discriminators, balanced and double-balanced mixers, balanced amplifiers, and feed networks in antenna arrays.

7.1. DEFINITIONS AND CORRELATIONS BETWEEN DIRECTIVITY, SYMMETRY, AND PHASE DIFFERENCE

A directional coupler is a reciprocal four-port device, which provides two amplitude outputs when a signal is applied to its input.

A hybrid network (or 3-dB directional coupler) is a special class of directional coupler in which the signals at the two output ports are equal [1–3].

The important characteristics of directional couplers are coupling, directivity, isolation, matching, insertion loss, phase balance, power split, and bandwidth.

Coupling (*C*) is calculated as the ratio in decibels of the incident power fed into the input port of the main line of the directional coupler, to the coupled port power of the auxiliary line when all ports are terminated by reflectionless terminations. *Coupling tolerance* is the allowable unit-

117

to-unit variation in nominal coupling as specified. *Coupling flatness* is the
amount (in decibels) of the maximum variation in coupling that may be
expected over a specified frequency range.

Insertion loss is the ratio (in decibels) of input power and output
power of the main line with reflectionless terminations connected to ports
of the directional coupler.

Directivity is calculated as the ratio (in decibels) of power at the cou-
pled port and at the isolated port when all ports are terminated by reflec-
tionless terminations. Directional couplers can have three different types
of directivity (Figure 7.1) [4–6]. For the purposes of discussion we will
choose port 1 in Figure 7.1 as input from this point on. An ideal direc-
tional coupler should have an infinity directivity. In the **I**-st type, the codi-
rectional coupler, the coupled wave in the auxiliary line travels in the
same direction as that of the wave in the main line, while in the **II**-nd
type, the contradiction or backward wave coupler, the coupled wave trav-
els in the opposite direction. In an actual directional coupler, the isolated
port is never completely isolated due to mismatching of terminations,
losses, discontinuities, and tolerances.

Isolation is the ratio in decibels of power at an isolated port to avail-
able power at the input port. Isolation is equal to the sum of the coupling
and directivity. Directivity, rather than isolation, is usually specified on
couplers, but the tight coupling isolation of directional couplers usually is
specified.
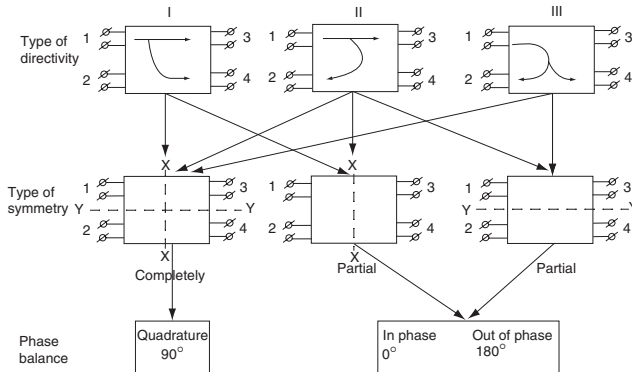
Figure 7.1. Various kinds of directivity, symmetry, and phase balance that a directional coupler can have.

TABLE 7.1. Parameters of Directional Couplers with Three Types of Directivity

Parameters (dB)	Type of Directivity		
	I	II	III
Coupling	$C_{14} = 10 \log (P_1/P_4)$	$C_{12} = 10 \log (P_1/P_2)$	$C_{12} = 10 \log (P_1/P_2)$
			$C_{14} = 10 \log (P_1/P_4)$
Directivity	$C_{42} = 10 \log (P_4/P_2)$	$C_{24} = 10 \log (P_2/P_4)$	$C_{43} = 10 \log (P_4/P_3)$
			$C_{23} = 10 \log (P_2/P_3)$
Isolation	$C_{12} = 10 \log (P_1/P_2)$	$C_{14} = 10 \log (P_1/P_4)$	$C_{13} = 10 \log (P_1/P_3)$
Insertion loss	$C_{13} = 10 \log (P_1/P_3)$	$C_{13} = 10 \log (P_1/P_3)$	$C_{14} = 10 \log (P_1/P_4)$
			$C_{12} = 10 \log (P_1/P_2)$
Power split	$C_{14}\text{-}C_{13} = 10 \log (P_3/P_4)$	$C_{12}\text{-}C_{13} = 10 \log (P_3/P_2)$	$C_{12}\text{-}C_{14} = 10 \log (P_4/P_2)$

Power split for directional couplers is calculated as the difference (in decibels) between the coupling and insertion loss.

Matching is determined by voltage standing-wave ratio (VSWR) or reflection coefficient of the input (or output) port, while the other ports are connected with reflectionless terminations.

Phase balance ($\Delta\varphi$) is the relative phase difference of output waves.

Quadrature ($\Delta\varphi = 90°$) and *in-phase-out-of-phase* ($\Delta\varphi = 0°$ or $180°$) directional couplers are the most popular devices (see Figure 7.1).

Bandwidth is the range of frequencies for which a parameter falls within a specified limit with respect to certain characteristics.

Parameters of directional couplers with three types of directivity are given in Table 7.1.

For the purposes of analysis and calculation, symmetry is a very important characteristic of directional couplers. There are three types of symmetry [5, 6]: complete symmetry (axes *XX* and *YY*), *XX*-axis partial symmetry, and *YY*-axis partial symmetry. Connections between types of symmetry, directivity, and phase differences are shown in Figure 7.1. Wave matrices for different types of symmetry and directivity are given in Table 7.2 [5].

TABLE 7.2. Wave Matrices for Different Types of Symmetry and Directivity

Type of Directivity	Type of Symmetry	Matrix [S]	Matrix [T]
I	Completely	$\begin{bmatrix} 0 & 0 & S_{13} & S_{14} \\ 0 & 0 & S_{14} & S_{13} \\ S_{13} & S_{14} & 0 & 0 \\ S_{14} & S_{13} & 0 & 0 \end{bmatrix}$	$\begin{bmatrix} T_{11} & T_{12} & 0 & 0 \\ T_{12} & T_{11} & 0 & 0 \\ 0 & 0 & T_{44} & T_{43} \\ 0 & 0 & T_{43} & T_{44} \end{bmatrix}$
I	Partial XX	$\begin{bmatrix} 0 & 0 & S_{13} & S_{14} \\ 0 & 0 & S_{14} & S_{34} \\ S_{13} & S_{14} & 0 & 0 \\ S_{14} & S_{24} & 0 & 0 \end{bmatrix}$	$\begin{bmatrix} T_{11} & T_{12} & 0 & 0 \\ T_{12} & T_{22} & 0 & 0 \\ 0 & 0 & T_{33} & T_{34} \\ 0 & 0 & T_{34} & T_{44} \end{bmatrix}$
II	Completely	$\begin{bmatrix} 0 & S_{12} & S_{13} & 0 \\ S_{12} & 0 & 0 & S_{13} \\ S_{13} & 0 & 0 & S_{12} \\ 0 & S_{13} & S_{12} & 0 \end{bmatrix}$	$\begin{bmatrix} T_{11} & 0 & 0 & T_{14} \\ 0 & T_{11} & T_{14} & 0 \\ 0 & T_{41} & T_{44} & 0 \\ T_{41} & 0 & 0 & T_{44} \end{bmatrix}$
II	Partial XX	$\begin{bmatrix} 0 & S_{12} & S_{13} & 0 \\ S_{12} & 0 & 0 & S_{24} \\ S_{13} & 0 & 0 & S_{12} \\ 0 & S_{24} & S_{12} & 0 \end{bmatrix}$	$\begin{bmatrix} T_{11} & 0 & 0 & T_{14} \\ 0 & T_{22} & T_{23} & 0 \\ 0 & -T_{23} & T_{33} & 0 \\ -T_{14} & 0 & 0 & T_{44} \end{bmatrix}$
II	Partial YY	$\begin{bmatrix} 0 & S_{12} & S_{13} & 0 \\ S_{12} & 0 & 0 & S_{13} \\ S_{13} & 0 & 0 & S_{34} \\ 0 & S_{13} & S_{34} & 0 \end{bmatrix}$	$\begin{bmatrix} T_{11} & 0 & 0 & T_{14} \\ 0 & T_{11} & T_{14} & 0 \\ 0 & T_{32} & T_{33} & 0 \\ T_{32} & 0 & 0 & T_{33} \end{bmatrix}$

TABLE 7.2. Wave Matrices for Different Types of
Symmetry and Directivity *(continued)*

Type of Directivity	Type of Symmetry	Matrix [S]	Matrix [T]
III	Completely	$\begin{bmatrix} 0 & S_{12} & 0 & S_{14} \\ S_{12} & 0 & S_{14} & 0 \\ 0 & S_{14} & 0 & S_{12} \\ S_{14} & 0 & S_{12} & 0 \end{bmatrix}$	$\begin{bmatrix} 0 & T_{12} & T_{13} & 0 \\ T_{12} & 0 & 0 & T_{13} \\ T_{42} & 0 & 0 & T_{34} \\ 0 & T_{42} & T_{34} & 0 \end{bmatrix}$
III	Partial *YY*	$\begin{bmatrix} 0 & S_{12} & 0 & S_{14} \\ S_{12} & 0 & S_{14} & 0 \\ 0 & S_{14} & 0 & S_{34} \\ S_{14} & 0 & S_{34} & 0 \end{bmatrix}$	$\begin{bmatrix} 0 & T_{12} & T_{13} & 0 \\ T_{12} & 0 & 0 & T_{13} \\ T_{31} & 0 & 0 & T_{34} \\ 0 & T_{31} & T_{34} & 0 \end{bmatrix}$

7.2. RING DIRECTIONAL COUPLERS

The name *ring* for this type of directional coupler is a historic tribute
because the first coupler shapes were circular. At present, though couplers
of this type vary in shape (see Figure 7.2), the original name has
remained. The two most popular ring directional couplers are of length
$3/2\Lambda$ and length Λ, where Λ is the guide wavelength.
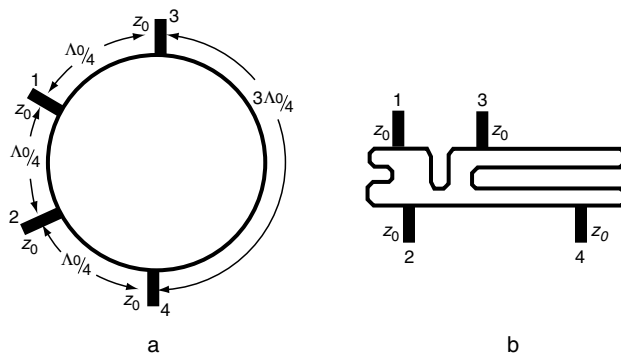
Figure 7.2. Print hybrid ring: conventional configuration (a); with meander lines (b).

7.2.1. Ring Directional Coupler of Length 3/2Λ

In the ring coupler of length $3/2\Lambda$ (or "rat-race" coupler) [Figure 7.2(a)] proposed by Tyrrel [7], spacing between two of adjacent ports 3 and 4 is $3/4\Lambda$ and $\Lambda/4$ between all other adjacent ports (3 and 1, 1 and 2, and 2 and 4).

　　The main parameters of the ring coupler and its operating characteristics can be determined by using the wave-matrix method (see Chapter 6 and [5, 8]). Referring to Figure 7.3, we assume that signal is applied to port 1. This ring coupler is a four-port network having partial symmetry with respect to the *YY*-axis. Using the mirror reflection method (see Chapter 6), the ring is equivalent to two pairs of two-port networks, each of which [Figure 7.3(b)] corresponds to conditions of the even (++) and odd (+–) modes.

　　The resulting transfer matrices of the equivalent two-port networks for even $[T]^{++}$ and odd $[T]^{+-}$ modes are equal to the product of the transfer matrices of the component two-port networks with known transfer matrices (see Appendix C) written down in the order of energy flow:

$$[T]^{++} = [T]_I^{++} [T]_{II}^{++} [T]_{III}^{++},$$

$$[T]^{+-} = [T]_I^{+-} [T]_{II}^{+-} [T]_{III}^{+-}.$$
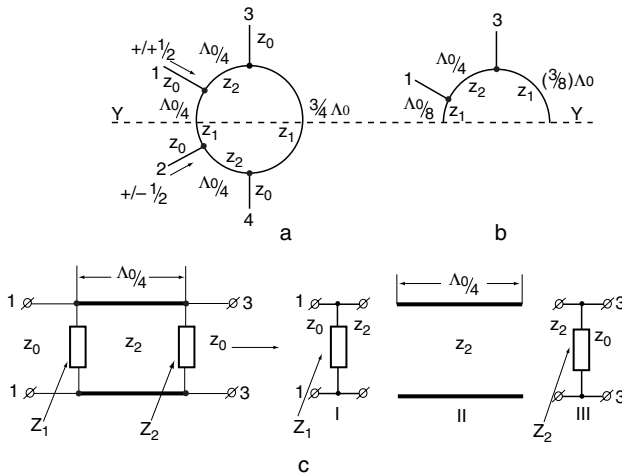
Figure 7.3. Ring directional coupler: even- and odd-mode excitation models (a); half section for even- and odd-mode analysis (b); equivalent circuit of (b) (c).

Multiplying the transfer matrices for the mid-band frequency and using relationships (6.17) to (6.22), we obtain

$$[S] = -\frac{1}{y_1^2 + y_2^2 + y_0^2} \begin{bmatrix} y_1^2 + y_2^2 - y_0^2 & 2i\,y_0 y_1 & 2i\,y_0 y_2 & 0 \\ 2i\,y_0 y_1 & y_1^2 + y_2^2 - y_0^2 & 0 & 2i\,y_0 y_2 \\ 2i\,y_0 y_2 & 0 & y_1^2 + y_2^2 - y_0^2 & -2i\,y_0 y_1 \\ 0 & 2i\,y_0 y_2 & -2i\,y_0 y_1 & y_1^2 + y_2^2 - y_0^2 \end{bmatrix}, \quad (7.1)$$

where $y_0 = 1/z_0$, $y_1 = 1/z_1$, and $y_2 = 1/z_2$.

When the input (port 1) matching is perfect, element S_{11} of the scattering matrix (7.1), which has the physical meaning of the reflection coefficient, must be equal to zero:

$$y_1^2 + y_2^2 - y_0^2 = 0. \qquad (7.2)$$

Equation (7.2) establishes a relationship between the admittances of the ring segments in the case of ideal matching.

According to (7.2), the scattering matrix (7.1) is

$$[S] = -\frac{1}{y_0} \begin{bmatrix} 0 & iy_1 & iy_2 & 0 \\ iy_1 & 0 & 0 & iy_2 \\ iy_2 & 0 & 0 & -iy_1 \\ 0 & iy_2 & -iy_1 & 0 \end{bmatrix}. \qquad (7.3)$$

Normalizing with respect to $y_0 = 1/z_0$, we obtain from (7.2)

$$Y_1^2 + Y_2^2 = 1, \qquad (7.4)$$

where $Y_1 = y_1/y_0$, $Y_2 = y_2/y_0$ are the normalized admittances of the ring coupler.

It follows from (7.3) that $\arg(S_{12}/S_{13}) = 0$ and $\arg(S_{42}/S_{43}) = \pi$, that is, this network is an in-phase-out-of-phase directional coupler. If the input signal is applied to port 1, the output voltages are in-phase with each other. If the input signal is applied to port 4, the output voltages are out-of-phase with each other. This property makes the ring coupler very useful, for example, in a balanced mixer application.

Since $S_{14} = S_{23} = S_{32} = S_{41} = 0$, this directional coupler provides ideal directivity of type **II** (see Table 7.2).

The simplest *hybrid ring* has equal segment admittances $Y_1 = Y_2$, which by substitution in (7.4), yields

$$Y_1 = Y_2 = \frac{1}{\sqrt{2}}. \qquad (7.5)$$

For the first input port, the main parameters of the ring directional coupler are

- VSWR:

$$VSWR_1^R = \frac{1 + |S_{11}|}{1 - |S_{11}|};$$

- Isolation between ports 1 and 4:

$$C_{14}^R = 10\log\frac{1}{|S_{14}|^2}(\mathrm{dB});$$

- Coupling and insertion loss:

$$C_{12}^R = 10\log\frac{1}{|S_{12}|^2}\ (\mathrm{dB}), \quad C_{13}^R = 10\log\frac{1}{|S_{13}|^2}(\mathrm{dB}).$$

Parameters of actual ring directional couplers differ from the ideal due to the mismatching of terminations, losses, and discontinuities, as well as manufacture tolerances. Usually the ring coupler is loaded by terminations at ports 1, 2, 3, and 4 with reflection coefficients Γ_1, Γ_2, Γ_3, and Γ_4, respectively. For these conditions, reflection coefficients, Γ_{1in}, Γ_{2in}, Γ_{3in}, and Γ_{4in}, and voltage transmitter coefficients of the hybrid ring are shown in Table 7.3 [5, 9], where entries φ_1 through φ_4 are given by

$$\varphi_1 = 2(1 + \Gamma_2\Gamma_3\Gamma_4) + (1 + \Gamma_4)(\Gamma_2 + \Gamma_3),$$
$$\varphi_2 = 2(1 + \Gamma_2\Gamma_3\Gamma_4) + (1 + \Gamma_3)(\Gamma_1 + \Gamma_3),$$
$$\varphi_3 = 2(1 + \Gamma_2\Gamma_3\Gamma_4) + (1 + \Gamma_2)(\Gamma_1 + \Gamma_4),$$
$$\varphi_4 = 2(1 + \Gamma_1\Gamma_2\Gamma_3) + (1 + \Gamma_1)(\Gamma_2 + \Gamma_3).$$

TABLE 7.3. Reflection Coefficients and Voltage Transmit Coefficients of the
Hybrid Ring Versus Termination Reflection Coefficients

Transmission from Port 1	Transmission from Port 2	Transmission from Port 3	Transmission from Port 4
$\Gamma_{1in} = -\dfrac{2\Gamma_2\Gamma_3\Gamma_4 + \Gamma_2 + \Gamma_3}{2 + \Gamma_4\left(\Gamma_2 + \Gamma_3\right)}$	$\Gamma_{2in} = -\dfrac{2\Gamma_1\Gamma_3\Gamma_4 + \Gamma_1 + \Gamma_4}{2 + \Gamma_3\left(\Gamma_1 + \Gamma_4\right)}$	$\Gamma_{3in} = -\dfrac{2\Gamma_1\Gamma_2\Gamma_4 + \Gamma_1 + \Gamma_4}{2 + \Gamma_2\left(\Gamma_1 + \Gamma_4\right)}$	$\Gamma_{4in} = -\dfrac{2\Gamma_1\Gamma_2\Gamma_3 + \Gamma_2 + \Gamma_3}{2 + \Gamma_1\left(\Gamma_2 + \Gamma_3\right)}$
$\dfrac{U_1}{U_2} = \dfrac{-i\varphi_1}{\sqrt{2}\left(1+\Gamma_2\right)\left(1+\Gamma_3\Gamma_4\right)}$	$\dfrac{U_2}{U_1} = \dfrac{-i\varphi_2}{\sqrt{2}\left(1+\Gamma_1\right)\left(1+\Gamma_3\Gamma_4\right)}$	$\dfrac{U_3}{U_1} = \dfrac{-i\varphi_3}{\sqrt{2}\left(1+\Gamma_1\right)\left(1+\Gamma_2\Gamma_4\right)}$	$\dfrac{U_4}{U_1} = \dfrac{\varphi_4}{\left(1+\Gamma_1\right)\left(\Gamma_2 - \Gamma_3\right)}$
$\dfrac{U_1}{U_3} = \dfrac{-i\varphi_1}{\sqrt{2}\left(1+\Gamma_3\right)\left(1+\Gamma_2\Gamma_4\right)}$	$\dfrac{U_2}{U_3} = \dfrac{\varphi_2}{\left(1+\Gamma_3\right)\left(\Gamma_1 - \Gamma_4\right)}$	$\dfrac{U_3}{U_2} = \dfrac{\varphi_3}{\left(1+\Gamma_2\right)\left(\Gamma_1 - \Gamma_4\right)}$	$\dfrac{U_4}{U_2} = \dfrac{-i\varphi_4}{\sqrt{2}\left(1+\Gamma_2\right)\left(1+\Gamma_1\Gamma_3\right)}$
$\dfrac{U_1}{U_4} = \dfrac{\varphi_1}{\left(1+\Gamma_4\right)\left(\Gamma_2 - \Gamma_3\right)}$	$\dfrac{U_2}{U_4} = \dfrac{-i\varphi_2}{\sqrt{2}\left(1+\Gamma_4\right)\left(1+\Gamma_1\Gamma_3\right)}$	$\dfrac{U_3}{U_4} = \dfrac{i\varphi_3}{\sqrt{2}\left(1+\Gamma_4\right)\left(1+\Gamma_1\Gamma_2\right)}$	$\dfrac{U_4}{U_3} = \dfrac{i\varphi_4}{\sqrt{2}\left(1+\Gamma_3\right)\left(1+\Gamma_1\Gamma_2\right)}$

From the expression (Table 7.3) for input reflection coefficient it is evident that any one input will be ideally matched if the two ports adjacent to the input are matched. Isolation of opposite ports will be perfect when the reflection coefficients of the terminations connected to the two other feeder lines are equal.

Graphs of operating parameters of the hybrid ring versus termination reflection coefficients are shown in Figure 7.4. Note that $VSWR_1^R$ is practically independent of matching the termination connected to the decoupled port 4. Input power (port 1) is equally divided if the termination reflection coefficients at ports 2 and 3 are equal ($|\Gamma_2| = |\Gamma_3|$), independent of mismatch of the termination connected to the decoupled port 4. Absolute values of reflection coefficients of terminations connected to adjacent ports (with respect to the input) mainly affect the input matching, while the isolation is determined by relative values of reflection coefficients.

Let us consider several commonly occurring relationships between reflection coefficients of terminations connected to hybrid ring ports.

1. Well-matched terminations:

$$\Gamma_1, \Gamma_2, \Gamma_3, \Gamma_4 < 0.1 \qquad\qquad (7.6)$$

In this case, from Table 7.3, we obtain

$$\Gamma_{1in} = \Gamma_{4in} \approx \frac{\Gamma_2 + \Gamma_3}{2}; \quad \Gamma_{2in} = \Gamma_{3in} \approx -\frac{\Gamma_1 + \Gamma_4}{2}, \qquad (7.7)$$

that is, reflection coefficients of opposite inputs are equal to the half-sum of reflection coefficients of terminations connected to the two adjacent ports. Thus, the $VSWR^R$ of any input is smaller than the $VSWR$ of the most mismatched termination, which means that a hybrid ring improves matching.

Also, from Table 7.3, we can find

$$\frac{U_1}{U_2} \approx \frac{2 + \Gamma_2 + \Gamma_3}{i\sqrt{2}\left(1 + \Gamma_2\right)}, \quad \frac{U_1}{U_3} \approx \frac{2 + \Gamma_2 + \Gamma_3}{i\sqrt{2}\left(1 + \Gamma_3\right)}, \quad \frac{U_1}{U_4} \approx \frac{2 + \Gamma_2 + \Gamma_3}{\Gamma_2 - \Gamma_3}. \qquad (7.8)$$

It follows from (7.6) to (7.8) that, in the case of well-matched terminations, the characteristics of a hybrid ring are practically determined by the reflection coefficients of terminations connected to ports adjacent to the input.
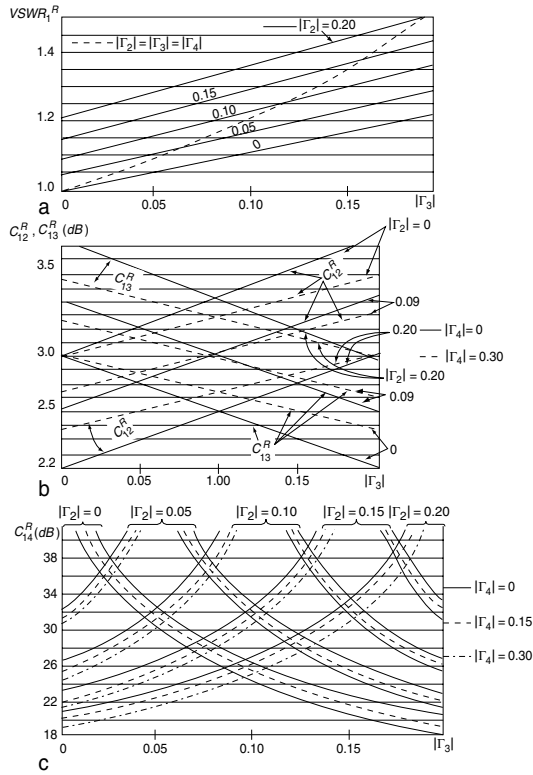
Figure 7.4. Graph of matching (a), insertion loss (b), and isolation (c) of hybrid ring as a function of termination reflection coefficients.

2. Identical terminations in opposite ports:

$$\Gamma_1 = \Gamma_4 \text{ or } \Gamma_2 = \Gamma_3. \tag{7.9}$$

From Table 7.3, by setting $\Gamma_1 = \Gamma_4$, we obtain

$$\Gamma_{1in} = \Gamma_{4in} = -\frac{\Gamma_2 + \Gamma_3 + 2\Gamma_1\Gamma_2\Gamma_3}{2 + \Gamma_1(\Gamma_2 + \Gamma_3)}, \tag{7.10}$$

$$\Gamma_{2in} = \Gamma_{3in} = -\Gamma_1 = -\Gamma_4,$$

and, by setting $\Gamma_2 = \Gamma_3$,

$$\left.\begin{aligned}
\Gamma_{1in} &= \Gamma_{4in} = -\Gamma_2 = -\Gamma_3, \\
\Gamma_{2in} &= \Gamma_{3in} = -\frac{\Gamma_1 + \Gamma_4 + 2\Gamma_1\Gamma_2\Gamma_4}{2 + \Gamma_2(\Gamma_1 + \Gamma_4)}, \\
\frac{U_1}{U_2} &= \frac{U_1}{U_3} = -i\sqrt{2}, \quad \frac{U_1}{U_4} = \infty.
\end{aligned}\right\} \qquad (7.11)$$

From (7.9) to (7.11), it follows that opposite ports of a ring coupler have equal matching.

3. All terminations identical:

$$\Gamma_1 = \Gamma_2 = \Gamma_3 = \Gamma_4 = \Gamma.$$

In this case, from Table 7.3

$$\Gamma_{1in} = \Gamma_{2in} = \Gamma_{3in} = \Gamma_{4in} = \Gamma,$$

from which it follows that the $VSWR^R$ of any input of a ring coupler equals the $VSWR$ of the termination [see the broken curve for $|\Gamma_2| = |\Gamma_3| = |\Gamma_4|$ of Figure 7.4(a)].

It should be noted that the previously discussed characteristics of the ring coupler do not account for power dissipated as a result of conductor, dielectric, and radiation losses.

We can define the resistive losses in terms of normalized attenuation

$$\alpha l = \frac{\pi}{Q\Lambda} l \; (\text{Nep}) \qquad (7.12)$$

where $Q = \beta/2\alpha$ is the quality factor of a quarter-wave resonator which is shorted at one end, and $\beta = 2\pi l/\Lambda$ is the phase constant.

For $l = \Lambda/4$, (7.12) becomes

$$\alpha l = \frac{\pi}{4Q} = \frac{0.785}{Q} \; (\text{Nep}). \qquad (7.13)$$

Characteristics of planar hybrid ring depending on transmission line losses, αl [5, 10], are

$$VSWR^R = \frac{13\sqrt{2}\alpha l + 4}{11\sqrt{2}\alpha l + 4},$$

$$C_{12}^R = 20\log\frac{6\sqrt{2}\alpha l + 2}{4\alpha l + \sqrt{2}}(\text{dB}),$$

$$C_{13}^R = 20\log\frac{6\sqrt{2}\alpha l + 2}{3\alpha l + \sqrt{2}}(\text{dB}), \qquad\qquad (7.14)$$

$$C_{14}^R = 20\log\frac{12\sqrt{2}\alpha l + 4}{\sqrt{2}\alpha l}(\text{dB}),$$

$$\Delta C^R = C_{13}^R - C_{12}^R = 20\log\frac{4\alpha l + \sqrt{2}}{3\alpha l}(\text{dB}).$$

In practice, minimum losses that influence characteristics of a hybrid ring depend on termination mismatching.

Consider the influence of fabrication tolerances on parameters of the hybrid ring. In practice, real production tolerances influence the impedance of a hybrid ring. The dependencies of scattering matrix elements from normalized impedance Z [11] are

$$S_{11} = \frac{Z^2 - 2}{Z^2 + 2}, \quad S_{12} = S_{13} = -i\frac{2Z}{Z^2 + 2}, \quad S_{14} = 0.$$

Thus, isolation and power split in the hybrid ring remain ideal independently of the value of impedance Z.

In the ring directional coupler, it is often necessary to account for the influence of discontinuities where the coupler connects to the input and output lines. This is most important for the high-frequency range when the size of the discontinuities is more than $\Lambda/10$.

This type of discontinuity is equivalent to a T-connection (see Chapter 4).

7.2.2. Broadband Ring Directional Coupler

The ring coupler of length $3/2\Lambda_0$ has the disadvantage of a narrow bandwidth (approximately 20%) due to the increased length of the three-quar-
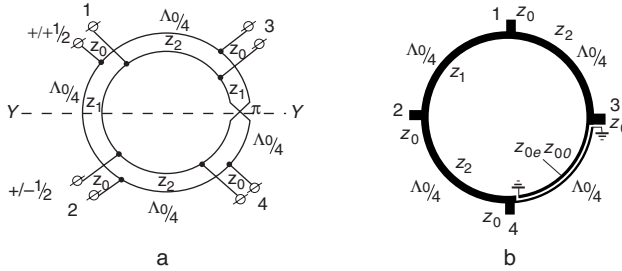
Figure 7.5. Λ- ring directional coupler: schematic (a), print circuit (b).

ter-wavelength section [Figure 7.3(a)]. Also, it occupies a large circuit area. There are modifications of this coupler in which the three-quarter-wavelength section is replaced by a one-quarter-wavelength section with a fixed 180° phase shifter (phase inverter) (Figure 7.5) [12]. The name of this modified device is a *ring coupler with phase overturn* or Λ-*ring*.

The Λ-*ring* coupler has perfect isolation and is independent of frequency. The phase difference between the two output ports (0° or 180°) is also independent of frequency. In practice, bandwidth is equal to one octave.

The broadband technique replaces the $3/4\Lambda_0$ segment with a $\Lambda_0/4$ coupled line section with two diagonal grounded ends [12]. This hybrid ring provides 20 dB of return loss over 40% bandwidth, and isolation greater than 24 dB. Realization of this ring directional coupler requires very tightly coupled lines that are difficult to fabricate with microstrip technology using chemical etching techniques. This circuit also requires ground vias for microstrip shorts. For the low-frequency band we can use the miniature 180° phase shifter, which will be described in Chapter 11. Other modified versions of Λ-ring that utilize a CPW-slotline, balun, and *T*-junction are given in [13].

7.3. BRANCH-LINE DIRECTIONAL COUPLERS

The branch-line coupler consists of a main line that is coupled to a secondary line by $\Lambda_0/4$-long branches spaced by $\Lambda_0/4$.

The bandwidth of the branch coupler can be enlarged by increasing the number of branches. Young [14, 15] has given a formulation to design branch-line couplers of two to eight branches. Levi and Lind [16] have given calculations for branch-line couplers of three to nine branches and

synthesis for maximally flat responses and Chebyshev characteristics. Most commonly used is the two-branch coupler.

7.3.1. Two-Branch Coupler

The two-branch couplers may be laid out in different ways. Some possibilities are shown in Figure 7.6(a–c). A two-branch coupler is a four-port network with complete symmetry about two perpendicular axes-*XX* and -*YY* [Figure 7.6(d)]. Figure 7.6(e) displays one-quarter of a four-port network, which consists of a cascade junction of an open-circuited (for the even mode) or a short-circuited (for the odd mode) segment of length $\Lambda_0/8$ and of a regular line of length $\Lambda_0/8$. Multiplying transfer matrices of these networks together and taking into account (6.17), we obtain for the mid-band operating frequency [5]

$$S_{11} = i\frac{-Z_1^2 + Z_1^2 Z_2^2 + Z_2^2}{-2Z_1 Z_2^2 + i\left(Z_1^2 Z_2^2 - Z_2^2\right)}. \qquad (7.15)$$

In the case of perfect matching of input port 1, element S_{11} (7.15) must be equal to zero, which yields:

$$Y_1^2 = Y_2^2 - 1, \qquad (7.16)$$

where $Y_1 = 1/Z_1$, $Y_2 = 1/Z_2$ are admittances normalized with respect to the input admittance Y_0.

A two-branch coupler is ideally matched if (7.16) is true, and its scattering matrix is

$$[S] = -\frac{1}{\sqrt{1+Y_1^2}}\begin{bmatrix} 0 & 0 & i & Y_1 \\ 0 & 0 & Y_1 & i \\ i & Y_1 & 0 & 0 \\ Y_1 & i & 0 & 0 \end{bmatrix}. \qquad (7.17)$$

It follows from (7.17) that

$$S_{12} = S_{21} = 0, \quad \arg\left(S_{13}\middle/S_{14}\right) = \pi\middle/2, \qquad (7.18)$$
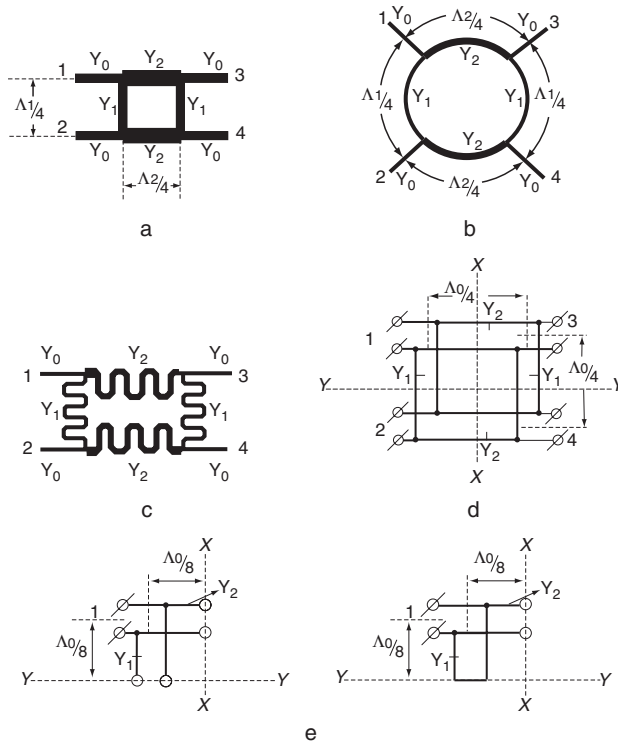
Figure 7.6. Two-branch coupler: rectangular format (a); circular format (b); with meander lines (c); basic view of full symmetry coupler (d); quarter circuit cut off by two symmetrical planes XX and YY for even- and odd mode (e).

which means that the two-branch coupler has an ideal directivity of type **I** (see Table 7.2), and that there exists an inherent 90° phase difference between the output ports.

Let us determine the two-branch coupler parameters when input signal is applied to port 1:

• Insertion loss:

$$C_{13}^{B} = 20\log\frac{1}{|S_{13}|} = 20\log\sqrt{1+Y_1^2}\ (\text{dB});$$

- Coupling:

$$C_{14}^B = 20\log\frac{1}{|S_{14}|} = 20\log\frac{\sqrt{1+Y_1^2}}{Y_1}\,(\text{dB});$$

- Power split between ports 3 and 4:

$$\Delta C^B = C_{14}^B - C_{13}^B = 20\log\frac{|S_{13}|}{|S_{14}|} = 20\log Y_1\,(\text{dB}).$$

For the 3-dB two-branch coupler (hybrid) $\Delta C^B = 0$, the normalized admittances of two segments are provided by

$$Y_1 = 1, \quad Y_2 = \sqrt{2}\,. \tag{7.19}$$

The isolation of the hybrid ring has wider bandwidth than the isolation of the two-branch hybrid [5]. Two-branch hybrid isolation is usable only over approximately 10% bandwidth.

Consider the parameters of a two-branch hybrid where the terminations have reflection coefficients $\Gamma_1, \Gamma_2, \Gamma_3$, and Γ_4. Input reflection coefficients and voltage transmitter coefficients are [5]

$$\Gamma_{1in} = -\frac{2\Gamma_2\Gamma_3\Gamma_4 + \Gamma_3 - \Gamma_4}{2 + \Gamma_2(\Gamma_4 - \Gamma_3)},$$

$$\frac{U_1}{U_2} = \frac{i\left[2(1+\Gamma_2\Gamma_3\Gamma_4) + (1-\Gamma_2)(\Gamma_3 - \Gamma_4)\right]}{(1+\Gamma_2)(\Gamma_3 + \Gamma_4)},$$

$$\frac{U_1}{U_3} = \frac{-i\left[2(1+\Gamma_2\Gamma_3\Gamma_4) + (1-\Gamma_2)(\Gamma_3 - \Gamma_4)\right]}{\sqrt{2}(1+\Gamma_3)(1+\Gamma_2\Gamma_4)}.$$

The graphs of two-branch hybrid parameters versus modules of termination reflection coefficients are shown in Figure 7.7. Comparing the parameters of the two-branch coupler with those of the ring coupler with mismatched terminations leads to the following conclusions. In the ring coupler, isolation is better, but matching is worse than in the two-branch coupler. If output ports have identical terminations, the ring coupler isola-
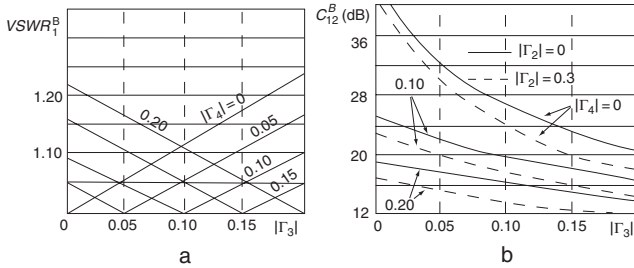
Figure 7.7. Graph of matching (a) and isolation (b) of two-branch hybrid as a function of termination reflection coefficients.

tion is ideal, but input matching is not, while for the two-branch coupler, matching is perfect, but its isolation is not.

If the terminations have good matching ($\Gamma_2, \Gamma_3, \Gamma_4 < 0.1$), the power split of the two-branch coupler is defined by the reflection coefficients of terminations in the output ports. For identical terminations ($\Gamma_3^B = \Gamma_4^B$), there is an equal power split that is independent of mismatching value.

Consider the parameters of a branch hybrid with loss α_1 in the branches and loss α_2 in the connection lines. The two-branch hybrid with ideal matching of all ports has the following characteristics [5]:

- Matching:

$$VSWR_1 = \frac{2 + 3\alpha_1 l + 3\sqrt{2}\alpha_2 l}{2 + \alpha_1 l + \sqrt{2}\alpha_2 l};$$

- Isolation:

$$C_{12}^B = 20\log\frac{2\left(1 + \alpha_1 l + \sqrt{2}\alpha_2 l\right)}{\alpha_1 l + \sqrt{2}\alpha_2 l}(\text{dB});$$

- Insertion loss:

$$C_{13}^B = C_{14}^B = 20\log\sqrt{2}\left(1 + \alpha_1 l + \sqrt{2}\alpha_2 l\right)(\text{dB}).$$

The power split in the two-branch hybrid, $C_{13}^B - C_{14}^B = 0$, unlike the hybrid-ring power split [see (7.14)], does not depend on losses. This is generally characteristic of full symmetry couplers.

For equal loss, $\alpha_1 = \alpha_2 = \alpha$, parameters of the two-branch hybrid are obtained by

$$VSWR_1^B = \frac{1 + 3.621\alpha l}{1 + 1.207\alpha l},$$

$$C_{12}^B = 6.02 + 20\log\left(1 + \frac{0.414}{\alpha l}\right)(\text{dB}),$$

$$C_{13}^B = C_{14}^B = 3.0 + 20\log(1 + 2.414\alpha l)(\text{dB}).$$

Table 7.4 illustrates comparative parameters of the two-branch hybrid and the hybrid ring as a function of loss αl and Q-factor, and shows that the hybrid ring isolation is 10.7 dB greater than the two-branch hybrid isolation.

TABLE 7.4. Comparative Parameters of the Two-Branch Hybrid and the Hybrid Ring As a Function of Loss and Q-Factor

Q-factor	αl (Nep)	$VSWR_1$		Isolation (dB)		Insertion Loss (dB)		
		$VSWR_1^R$	$VSWR_1^B$	C_{14}^R	C_{12}^B	C_{12}^R	C_{13}^R	$C_{13}^B = C_{14}^B$
10	0.078	1.04	1.17	33.6	22.9	3.76	4.17	4.52
20	0.039	1.02	1.09	38.5	27.8	3.43	3.65	3.79
40	0.02	1.013	1.04	43.8	33.1	3.23	3.35	3.41
60	0.013	1.01	1.03	47.1	36.4	3.16	3.24	3.27
80	0.01	1.006	1.02	49.5	38.8	3.12	3.19	3.21
100	0.008	1.005	1.02	51.4	40.7	3.10	3.15	3.17
1000	0.0008	1.000	1.00	71.2	60.5	3.02	3.02	3.02

Elements of the scattering matrix of the two-branch hybrid depend on characteristic impedances Z_1 and Z_2 of the two-branch coupler [11]:

$$S_{11} = \frac{Z_1^4 Z_2^4 - \left(Z_2^2 - Z_1^2\right)^2}{q},$$

$$S_{12} = \frac{i 2 Z_1 Z_2^2 \left(Z_2^2 Z_1^2 + Z_2^2 - Z_1^2\right)}{q},$$

$$S_{13} = \frac{i 2 Z_1^2 Z_2 \left(Z_2^2 Z_1^2 - Z_2^2 + Z_1^2\right)}{q},$$

$$S_{14} = \frac{4 Z_2^3 Z_1^3}{q},$$

where

$$q = Z_1^2 Z_2^2 \left(2 Z_2^2 + 2 Z_1^2 + Z_1^2 Z_2^2\right) + \left(Z_2^2 - Z_1^2\right)^2.$$

Impedances Z_1 and Z_2 depend on fabrication tolerances ΔW (deviation of strip width) and Δh (deviation of substrate thickness). The two-branch hybrid is more sensitive to production tolerances than the hybrid ring [5].

Consider the effect of discontinuities that arise in *T*-connections between branches, connecting lines, and input/output lines. In general, all input/output lines at these *T*-connections have different characteristic impedances. Analysis of the effects of discontinuities shows [5] that parameters of the two-branch coupler are more sensitive to them than ring-coupler characteristics.

Different designs of the branch couplers are shown in Figure 7.6. For the sake of downsizing the circuit, low-frequency couplers are given the meander shape [Figure 7.6(c)]. The high-frequency coupler is shown in Figure 7.6(b). It consists of a ring of circumference Λ and four symmetrical input/output lines. Chamfering of sharp corners [Figure 7.6(a)] improves ring-configuration coupler performance.

Simultaneous use of different lines of the branch coupler provides substantially improved characteristics over a broad bandwidth as compared

with conventional branch couplers. Configuration of uniplanar two-branch couplers consisting of a microstrip line, a symmetrical slotline, a nonsymmetrical slotline, and a coplanar line are given in [17].

The branch coupler has the advantage of adjacent output ports which permits combining them in the planar design. For example, a balanced mixer that has the two-branch hybrid and two diodes in output ports 3 and 4 can have one planar output intermediate-frequency (IF) port. Also, the two-branch coupler has a net electrical path length of one wavelength as compared with the ring coupler with 1.5 wavelengths.

If input/output impedances are equal to $z_0 = 50\Omega$, the horizontal arms of the two-branch hybrid [see Figure 7.6(a)] should be realized with characteristic impedance of

$$z_0 \big/ \sqrt{2} = 35.3\Omega,$$

which results in a wide conductor. At X-band and millimeter waves, the width of these lines becomes comparable to their length and causes problems of line intersection. In the ring hybrid, which requires characteristic impedance of arms at

$$z_0 \sqrt{2} = 70.7\Omega,$$

the wide line-width problem of the two-branch hybrid is avoided.

7.3.2. Three-Branch Coupler

Consider the three-branch coupler whose circuit view is shown in Figure 7.8(a). This coupler can be calculated according to Figure 7.8(b). If the three-branch coupler is perfectly matched ($S_{11} = 0$), then it can be shown [5] that

$$Y_3 = \frac{2Y_2^2 Y_1}{1 + Y_1^2}. \tag{7.20}$$

For the ideally matched coupler, using (7.20), the S-matrix can be written as the following

$$[S] = -\frac{1}{1+Y_1^2} \begin{bmatrix} 0 & 0 & Y_1^2-1 & i\,2Y \\ 0 & 0 & i\,2Y_1 & Y_1^2-1 \\ Y_1^2-1 & i\,2Y_1 & 0 & 0 \\ i\,2Y_1 & Y_1^2-1 & 0 & 0 \end{bmatrix}.$$

Similarly to the two-branch coupler, the three-branch coupler has the ideal directivity of type **I**:

$$S_{12} = S_{21} = 0\,.$$

Thus, it is evident that port 2 is isolated and waves reaching ports 3 and 4 have a differential 90° phase shift:

$$\arg\frac{S_{14}}{S_{13}} = \frac{\pi}{2}\,.$$
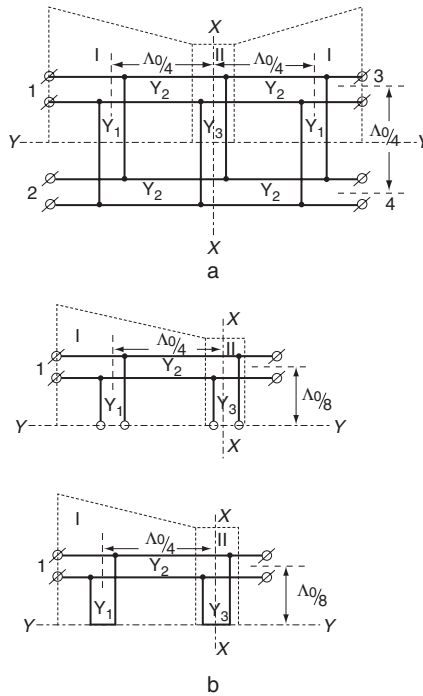
Figure 7.8. Three-branch coupler: basic view of full symmetry coupler (a); circuits for even- and odd-mode (b).

If port 1 is chosen as an input port, then parameters of the three-branch coupler may be defined as

- Insertion loss:

$$C_{13} = 2\log\frac{1}{|S_{13}|} = 20\log\frac{Y_1^2+1}{Y_1^2-1}\,(\text{dB})\;;$$

- Coupling:

$$C_{14} = 20\log\frac{1}{|S_{14}|} = 20\log\frac{Y_1^2+1}{Y_1}\,(\text{dB})\;;$$

- Power split:

$$C_{34} = 20\log\frac{|S_{13}|}{|S_{14}|} = 20\log\frac{Y_1^2-1}{2Y_1}\,(\text{dB})\,.$$

Several remarks on the three-branch coupler are in order. The bandwidth of the three-branch coupler is similar to that of the ring coupler. However, its parameters depend to a great extent on discontinuities and tolerances of line dimensions.

The three-branch coupler has larger bandwidth than the two-branch coupler. Additional branches can expand the bandwidth even further. However, couplers with more than four branches are difficult in microstrip because the end branches require impedances that reach the upper limits of practical realization.

The three-branch coupler with power split regulation is shown in Figure 7.9. It is the three-branch coupler in which two reactances (Y_4) are connected to the center branch. These reactances can be realized as open or short stubs. If port 1 (or port 3) is input, the power split between ports 2 and 4 depends on the stub length. For perfect matching at the mid-frequency band, the characteristic admittances Y_1, Y_2, and Y_3 are given as

$$Y_1 = 1, \quad Y_2^2 - Y_3 = 0.$$

These conditions do not depend on reactances. This three-branch coupler has the ideal directivity of type **III** (see Table 7.2) and an inherent 90° phase difference between the output ports.
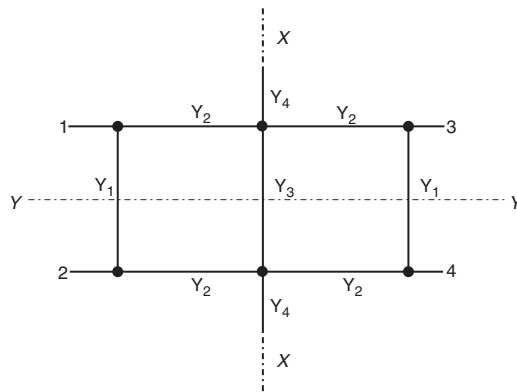
Figure 7.9. Three-branch coupler with power split regulation.

7.4. COUPLED-LINE DIRECTIONAL COUPLERS

7.4.1. $\Lambda/4$ Coupler

One of the most useful structures of directional couplers is the four-port network formed by two coupled lines close enough to each other to be coupled by electric and magnetic fields (Figure 7.10).

The coupled-line directional coupler is a complete symmetry four-port network. Analysis and synthesis of this coupler can be realized through the mirror-reflection method discussed in Chapter 6. A coupler can be represented by independent even and odd modes. The final results are obtained by superposition of the two modes. In the even-mode case currents in both lines are equal and codirectional. In the odd-mode case currents are equal and opposite. We can see (Figure 3.1) that the coupling between lines is caused by the odd mode. According to the mirror-reflection method, it is possible to calculate homogeneous coupled lines with characteristic impedances z_{0e} (even mode) and z_{0o} (odd mode) (the last subscript identifies the mode). It should be noted here that z_{0e} is not equal to z_{0o} because partial capacitances between the lines are different for even and odd modes. The theory of coupled lines was discussed in Chapter 3.

The equivalent circuit of these lines includes the cascade connection of the following two-port networks [Figure 7.10(c, d)]:

1. Step from characteristic impedance z_0 of the input line to characteristic impedance z_{0e} (or z_{0o});
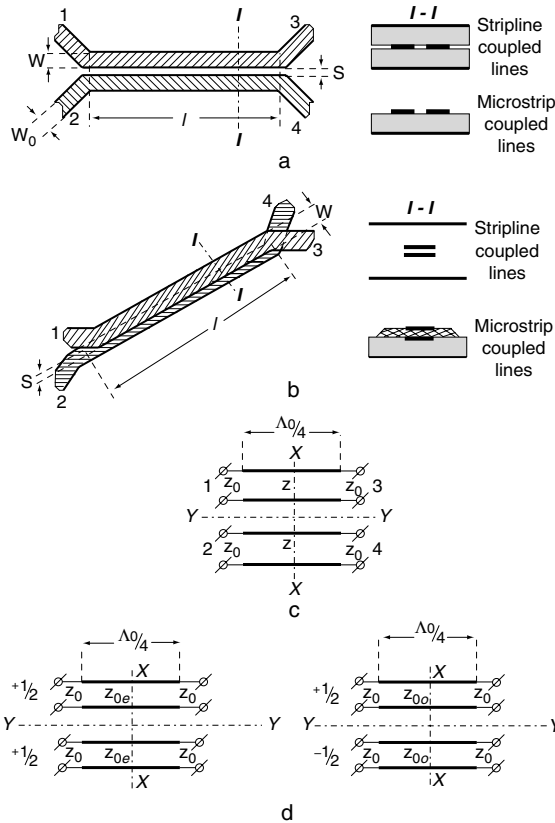
Figure 7.10. Coupled line directional coupler: edge coupled line coupler (a); broadside coupled line coupler (b); equivalent four-port network (c); circuit for even- and odd-mode analysis (d).

2. Line with characteristic impedance z_{0e} (or z_{0o}) with length l in the coupled region;

3. Step from characteristic impedance z_{0e} (or z_{0o}) to the output line characteristic impedance z_0.

The resulting transfer matrices of the equivalent two-port networks for even and odd modes are equal to the product of the transfer matrices of the above component two-port networks in order of energy flow (from left to right). Multiplying these matrices (see Appendix C) and using (6.17), we obtain the following

$$S_{11} = \frac{(z_{0e}z_{0o} - 1)\sin\Theta\left[-\sin\Theta(z_{0e}z_{0o} + 1) + i\cos\Theta(z_{0e} + z_{0o})\right]}{\left[2z_{0e}\cos\Theta + i(1 + z_{0e}^2)\sin\Theta\right]\left[2z_{0o}\cos\Theta + i(1 + z_{0o}^2)\sin\Theta\right]} . \quad (7.21)$$

where $\Theta = 2\pi l/\Lambda_0$ is the electrical length of the coupled lines, and subscript 0 denotes the mid-band operating frequency.

Perfect matching ($S_{11} = 0$) occurs when [see (7.21)]

$$Z_{0e}Z_{0o} = 1 .^{*} \quad (7.22)$$

Equation (7.22) is the ideal matched condition for the coupled line coupler. The scattering matrix of the ideally matched coupler and its frequency characteristics can be derived from (7.22) and [5]

$$[S] = \begin{bmatrix} 0 & S_{12} & S_{13} & 0 \\ S_{12} & 0 & 0 & S_{13} \\ S_{13} & 0 & 0 & S_{12} \\ 0 & S_{13} & S_{12} & 0 \end{bmatrix}, \quad (7.23)$$

where

$$S_{12} = \frac{i(Z_{0e} - Z_{0o})\sin\Theta}{2\cos\Theta + i(Z_{0e} + Z_{0o})\sin\Theta} = \frac{ir\sin\Theta}{\cos\Theta + i\rho\sin\Theta}; \quad (7.24)$$

$$S_{13} = \frac{2}{2\cos\Theta + i(Z_{0e} + Z_{0o})\sin\Theta} = \frac{1}{\cos\Theta + i\rho\sin\Theta}. \quad (7.25)$$

where r and ρ can be defined from (5.20).

For the unitary condition (5.15) for a lossless network, we obtain

$$\left|S_{12}\right|^2 + \left|S_{13}\right|^2 = 1. \quad (7.26)$$

This equation satisfies energy conservation. The quadrature phase difference between output ports 2 and 3 is evidenced by multiple i by which (7.24) differs from (7.25):

$$\arg\frac{S_{13}}{S_{12}} = \frac{\pi}{2}. \quad (7.27)$$

*From this point on, Z_{0e}, Z_{0o} stand for normalized impedances: $Z_{0e} = z_{0e}/z_0$; $Z_{0o} = z_{0o}/z_0$.

Quadrature between output signals does not depend on frequency, or, for fixed frequency, quadrature does not depend on coupled-line length.

Due to full symmetry consideration, we would expect similar operation if we were to drive any port (2, 3, or 4). Signal propagation from port 1 to port 3 on one transmission line produces a coupled signal in the opposite direction—from port 4 to port 2—on the other transmission line. For this reason, this coupler is called *contradictional* or *backward-wave* coupler and corresponds to the directivity of type **II**.

The coupled-line coupler has ideal matching and isolation independent of frequency [see (7.23)], but the coupling and insertion losses [see (7.24) and (7.25)] are changed with frequency. The maximum signal in the coupled port occurs when the length of the coupling structure is $\Lambda_0/4$, where Λ_0 is the mid-band guide wavelength in the coupled lines, which depends on the parameters of the transmission lines, substrate permittivity, and center frequency.

The module of coupling (voltage coupling factor) for the mid-band operating frequency is

$$K = \left|S_{12}\right|_0 = \frac{Z_{0e} - Z_{0o}}{Z_{0e} + Z_{0o}} = \frac{r}{\rho}. \tag{7.28}$$

This equation can be rearranged to give

$$Z_{0e} = \sqrt{\frac{1+K}{1-K}}, \quad Z_{0o} = \sqrt{\frac{1-K}{1+K}}, \quad r = \frac{K}{\sqrt{1-K^2}}, \quad \rho = \frac{1}{\sqrt{1-K^2}}. \tag{7.29}$$

Using (7.29), (7.24) and (7.25) can be rewritten as follows:

$$\left|S_{12}\right|^2 = \frac{K^2 \sin^2 \Theta}{1 - K^2 \cos^2 \Theta}, \tag{7.30}$$

$$\left|S_{13}\right|^2 = \frac{1 - K^2}{1 - K^2 \cos^2 \Theta}. \tag{7.31}$$

Evaluating the first equation at the mid-band frequency and using (7.26), (7.31) gives

$$\left|S_{12}\right|_0^2 = 1 - \left|S_{13}\right|_0^2 = K^2.$$

The following are the working characteristics of the coupled-line coupler with port 1 as the input:

$$C_{12} = 10 \log \frac{1}{K^2} \left[1 + \left(1 - K^2\right) \cot^2 \Theta \right] C_{12}^0 + \Delta C_{12} (\text{dB}), \qquad (7.32)$$

where

$$C_{12}^0 = 10 \log \frac{1}{K^2} (\text{dB}); \quad \Delta C_{12} = 10 \log \left[1 + \left(1 - K^2\right) \cot^2 \Theta \right] (\text{dB}),$$

$$C_{13} = 10 \log \frac{1}{1 - K^2} \left(1 - K^2 \cos^2 \Theta\right) = C_{13}^0 + \Delta C_{13} (\text{dB}),$$

(7.33)

where

$$C_{13}^0 = 10 \log \frac{1}{1 - K^2} (\text{dB}); \quad \Delta C_{13} = 10 \log \left(1 - K^2 \cos^2 \Theta\right) (\text{dB}),$$

$$C_{23} = 10 \log \frac{1 - K^2}{K^2 \sin^2 \Theta} = C_{23}^0 + \Delta C_{23} (\text{dB}), \qquad (7.34)$$

where

$$C_{23}^0 = 10 \log \frac{1 - K^2}{K^2} (\text{dB}),$$

$$\Delta C_{23} = -10 \log \sin^2 \Theta (\text{dB}),$$

where the subscript 0 denotes the mid-band operating frequency.

In above equations, C_{12}^0, C_{13}^0, and C_{23}^0 are the characteristics of the coupled-line directional coupler at the mid-band frequency and ΔC_{12}, ΔC_{13}, and ΔC_{23} are allowed deviations of characteristics as frequency is varied. We can see that at the center frequency, for which $\Theta_0 = \pi/4$, the coupling achieves its minimal value. The theoretical frequency response of the coupling [see (7.32)] is shown in Figure 7.11 for tight and weak coupling. The bandwidth of the quarter-wave coupler is approximately one octave.

Let us consider a typical order of synthesis of a coupled-line directional coupler. In practice, certain values of coupling (C_{12}^0) and coupling flatness (ΔC_{12}) are required. It is then necessary to determine Z_{0e}, Z_{0o} [see
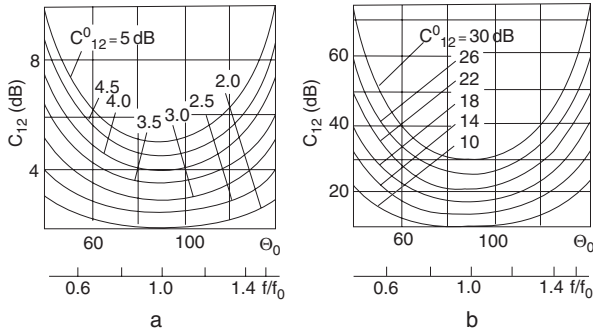
Figure 7.11. Coupling vs. electrical length and relative frequency for coupled line couplers with tight (a) and weak (b) coupling.

(7.29) and (7.32)]. After a transmission line is chosen, width (W) and space (S) dimensions (see Figure 7.10) can be calculated by using their dependence on Z_{0e}, Z_{0o} (see Chapter 3).

The characteristics of coupled-line couplers will be investigated where terminations have reflection coefficients Γ_1, Γ_2, Γ_3, and Γ_4 that are connected correspondingly to ports 1, 2, 3, and 4. In this case, reflection coefficients and voltage transfer coefficients are [5]

$$\Gamma_{1in} = \frac{\Gamma_2\Gamma_3\Gamma_4\left(S_{12}^2 - S_{13}^2\right)^2 - \left(\Gamma_2 S_{12}^2 + \Gamma_3 S_{13}^2\right)}{\Gamma_4\left(\Gamma_2 S_{12}^2 + \Gamma_3 S_{13}^2\right) - 1},$$

$$\frac{U_1}{U_2} = \frac{-1 + \left[\Gamma_2\Gamma_3\Gamma_4\left(S_{12}^2 - S_{13}^2\right)^2 - \left(\Gamma_2 S_{12}^2 + \Gamma_3 S_{13}^2\right)\right] - \Gamma_4\left(\Gamma_2 S_{13}^2 + \Gamma_3 S_{12}^2\right)}{\left(1 + \Gamma_2\right)S_{12}\left[\Gamma_3\Gamma_4\left(S_{12}^2 - S_{13}^2\right) - 1\right]},$$

$$\frac{U_1}{U_2} = \frac{-1 + \left[\Gamma_2\Gamma_3\Gamma_4\left(S_{12}^2 - S_{13}^2\right)^2 - \left(\Gamma_2 S_{12}^2 + \Gamma_3 S_{13}^2\right)\right] - \Gamma_4\left(\Gamma_2 S_{13}^2 + \Gamma_3 S_{12}^2\right)}{\left(1 + \Gamma_3\right)S_{13}\left[\Gamma_2\Gamma_4\left(S_{13}^2 - S_{12}^2\right) - 1\right]},$$

$$\frac{U_1}{U_2} = \frac{1 - \left[\Gamma_2\Gamma_3\Gamma_4\left(S_{12}^2 - S_{13}^2\right)^2 - \left(\Gamma_2 S_{12}^2 + \Gamma_3 S_{13}^2\right)\right] + \Gamma_4\left(\Gamma_2 S_{13}^2 + \Gamma_3 S_{12}^2\right)}{\left(1 + \Gamma_4\right)S_{12}S_{13}\left(\Gamma_2 + \Gamma_3\right)}.$$

All terms containing reflection coefficient Γ_4 of isolated port termination can be neglected, which gives

$$\Gamma_{in} \approx \Gamma_2 K^2 - \Gamma_3\left(1 - K^2\right). \tag{7.35}$$

The ideal matching condition of the first port ($\Gamma_{1in} = 0$) is achieved when

$$\Gamma_3 = \frac{\Gamma_2 K^2}{1 - K^2}. \tag{7.36}$$

For the weak coupling ($K \ll 1$), the input reflection coefficient [see (7.36)] depends mainly on matching Γ_3 of the third port:

$$\Gamma_3 \approx \Gamma_2 K^2. \tag{7.37}$$

For the 3-dB coupler ($K^2 = 0.5$), (7.36) gives

$$\Gamma_2 = \Gamma_3.$$

Therefore, the 3-dB coupled-line coupler is ideally matched when output port terminations are identical.

Figure 7.12(a) shows the $VSWR_1$ of the first port as a function of the reflection coefficient of the third port termination when $|\Gamma_2| = |\Gamma_4| = 0$.

The plot of the $VSWR_1$ as a function of reflection coefficients of output terminations is shown in Figure 7.12(b). As illustrated, the best matching of the 3-dB coupler is realized when the reflection coefficients of loads in ports adjacent to the input are equal.

Let us determine conditions for perfect matching, coupling, transmission losses, and directivity [5]. The results are summarized in Table 7.5. It is evident that in a coupler with mismatched terminations, it is practically impossible to meet the perfect values of all parameters simultaneously. Only the conditions for ideal transmission losses and directivity can be the same.

We can obtain the following with an accuracy sufficient for engineering applications:

$$
\begin{aligned}
C_{12}^0 &\approx 20 \log \left| \frac{1 - \Gamma_2 K^2 + \Gamma_3 \left(1 - K^2\right)}{K\left(1 + \Gamma_2\right)} \right| \text{ (dB)}, \\[2mm]
C_{13}^0 &\approx 20 \log \left| \frac{1 - \Gamma_2 K^2 + \Gamma_3 \left(1 - K^2\right)}{\sqrt{1 - K^2}\left(1 + \Gamma_2\right)} \right| \text{ (dB)}.
\end{aligned}
\tag{7.38}
$$
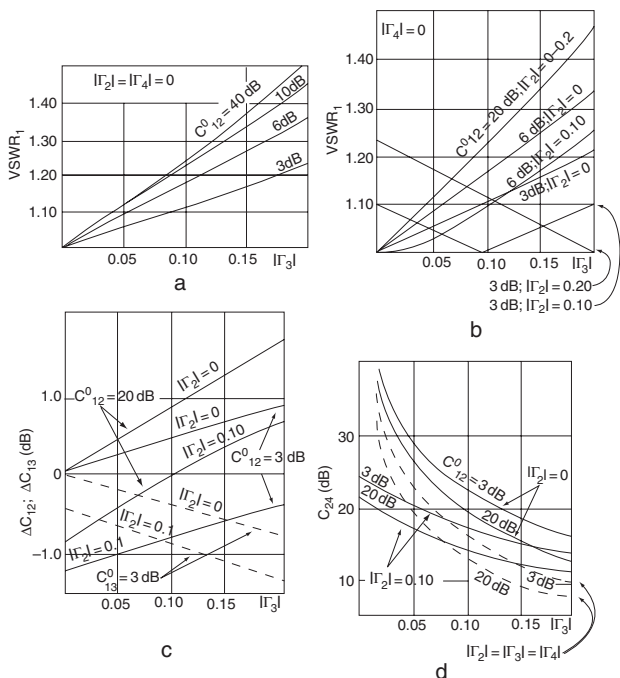
Figure 7.12. Coupled line directional coupler characteristics: matching vs. reflection coefficients for $|\Gamma_2| = |\Gamma_4| = 0$ (a); matching vs. reflection coefficient for $|\Gamma_4| = 0$, $|\Gamma_2| = 0 \ldots 0.2$ (b); insertion loss deviation (ΔC_{13}) (dashed lines) and coupling deviation (ΔC_{12}) (solid lines) versus reflection coefficient $|\Gamma_3|$ with different coupler reflection coefficient $|\Gamma_2|$ and mid-band coupling C_{12}^0 (c); directivity vs. reflection coefficients $|\Gamma_2|$, $|\Gamma_3|$ and mid-band coupling C_{12}^0 (d).

TABLE 7.5. Conditions for Perfect Matching, Coupling, Transmission Losses, and Directivity for the Coupled Line Directional Coupler

Coupling	Arbitrary	Weak	Tight
Ideal matching	$\Gamma_2 K^2 = \Gamma_3 \left(1 - K^2\right)$	$\Gamma_2 = \Gamma_3 \big/ K^2$	$\Gamma_2 = \Gamma_3$
Ideal coupling	$\Gamma_2 \left(1 + K^2\right) = $ $= \Gamma_3 \left(1 - K^2\right)$	$\Gamma_2 = \Gamma_3$	$\Gamma_2 = \Gamma_3 / 3$
Ideal losses	$\Gamma_2 = -\Gamma_3$	$\Gamma_2 = -\Gamma_3$	$\Gamma_2 = -\Gamma_3$
Ideal directivity	$\Gamma_2 = -\Gamma_3$	$\Gamma_2 = -\Gamma_3$	$\Gamma_2 = -\Gamma_3$

For perfect matching ($\Gamma_2 = \Gamma_3 = 0$), we can obtain

$$
\begin{aligned}
C_{12}^0 &\approx 20\log\frac{1}{K}\ (\text{dB}), \\
C_{13}^0 &\approx 20\log\frac{1}{\sqrt{1-K^2}}\ (\text{dB}),
\end{aligned}
\tag{7.39}
$$

which coincide with mid-frequency band parameters of a directional coupler given by (7.32) and (7.33). Figure 7.12(c) shows the dependence of parameters $\Delta C_{12} = C_{12} - C_{12}^0$ (solid lines) and $\Delta C_{13} = C_{13} - C_{13}^0$ (dashed lines) from coefficients $|\Gamma_2|$ and $|\Gamma_3|$ for coupling $C_{12}^0 = 3$ dB and $C_{12}^0 = 20$ dB.

Characteristics of directivity versus reflection coefficients $|\Gamma_2|$ and $|\Gamma_3|$ are plotted in Figure 7.12(d). For a particular C_{12}^0, curves corresponding to different values of $|\Gamma_2|$ diverge in a fanlike pattern as $|\Gamma_3|$ decreases.

Calculations [5] have shown that directivity does not have strong dependence on Θ. For example, for $C_{12}^0 = 20$ dB, $|\Gamma_2| = |\Gamma_3| = |\Gamma_4| = 0\text{--}0.2$, directivity deviates from C_{24}^0 by no more than 0.4 dB as Θ varies from 40° to 140°. Directivity for identical mismatching of ports 2, 3, and 4 is plotted in Figure 7.12(d) (dashed line) for two values of coupling $C_{12}^0 = 3$ dB and $C_{12}^0 = 20$ dB.

Let us define the main parameters of a directional coupler taking into account losses in lines:

- Coupling:

$$
C_{12} = 10\log\frac{1}{|S_{12}|^2} = 10\log\frac{1}{K^2}\left(\frac{8\alpha l + Z_{0e} + Z_{0o}}{4\alpha l + Z_{0e} + Z_{0o}}\right) = C_{12}^0 + \Delta C\ (\text{dB}),\tag{7.40}
$$

where

$$
C_{12}^0 = 10\log\frac{1}{K^2}\ (\text{dB}), \qquad \Delta C = \frac{8\alpha l + Z_{0e} + Z_{0o}}{4\alpha l + Z_{0e} + Z_{0o}}\ (\text{dB});
$$

- Insertion loss:

$$
C_{13} = 10\log\frac{1}{|S_{13}|^2} = 10\log\frac{1}{1-K^2}\left(\frac{8\alpha l + Z_{0e} + Z_{0o}}{4\alpha l + Z_{0e} + Z_{0o}}\right) = C_{13}^0 + \Delta C\ (\text{dB}),\tag{7.41}
$$

where

$$C_{13}^0 = 10\log\frac{1}{1-K^2}\ (\text{dB}),\qquad \Delta C = 10\log\left(\frac{8\alpha l + Z_{0e} + Z_{0o}}{4\alpha l + Z_{0e} + Z_{0o}}\right)(\text{dB});$$

- Matching:

$$VSWR_1 = \frac{1+|S_{11}|}{1-|S_{11}|} = 1;$$

- Isolation:

$$C_{14} = 10\log\frac{1}{|S_{14}|^2} = \infty.$$

Therefore, the presence of loss in the transmission lines does not result in a mismatch of the directional coupler and in a diminishing of its isolation. Coupling and insertion loss vary in the same way as function loss in lines—they change by same quantity ΔC [see (7.40) and (7.41)].

7.4.2. Miniature ($l < \Lambda/4$) Coupler That Shrinks HF/VHF/UHF Designs

In the VHF and UHF range, the classic directional coupler with a coupled-line length of $\Lambda_0/4$ has large dimensions, which makes it difficult to build. Figure 7.13 shows a new microminiature directional coupler [18, 19] comprised of two coupled lines that have a very short geometric length (less than $\Lambda_0/4$).

This length depends on several requirements, including the mid-band frequency, insertion loss, coupling, matching, and directivity.

The main problem of the short coupled-line directional coupler is that its degree of coupling varies with frequency. A special compensation circuit is used to diminish this effect. The secondary line output is electrically connected with series inductor L and shunt resistor R_1 (Figure 7.13). The other end of the secondary line is terminated with resistor R_2, where the value is equal to the impedance of the secondary line. The inductance value depends on the coupling flatness, mid-band frequency, and coupling
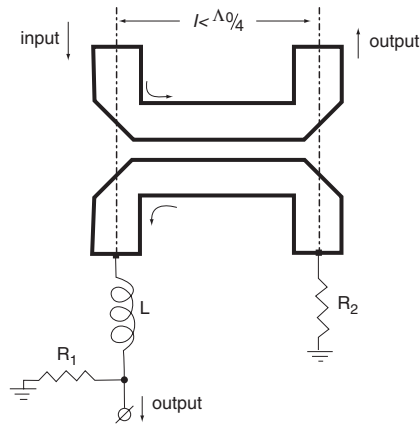
Figure 7.13. Microminiature coupled line directional coupler with compensation circuit.

value. The value of the shunt resistor R_2 depends on the impedance of the secondary line and inductance value.

Figure 7.14(a) illustrates the experimental relationship between inductance (in nanohenries) and coupling flatness ΔC (in decibels) for a frequency of 127 MHz and a bandwidth of 20%, and the relationship between inductance and bandwidth for a coupling line having a length of 2.44 in. and a shunt resistor $R_1 = 62\Omega$. Figure 7.14(b) shows the experimental relationship between coupling (in decibels), center frequency (in megahertz) (or relative length of coupled lines l/Λ_0), and inductance (in nanohenries) for the same directional coupler.

Experiments have shown that for 20% bandwidth, the present microstrip directional coupler with length $l = 0.05\Lambda_0$ (five times less than a traditional directional coupler with $l = \Lambda_0/4$), $L = 180$ nH, $R_1 = 62$ Ω, $f_0 = 120$ MHz has a coupling flatness of +/–0.05 dB, a directivity of more than 23 dB, an insertion loss of less than 0.15 dB, and VSWR of less than 1.15. Tuning of the mid-band frequency (f_0) and coupling (C_0) can be realized by varying the inductance [19].

Unlike traditional $\Lambda_0/4$ directional couplers, the present coupler provides miniature dimensions in HF, VHF, and UHF bands. The level of integration of the coupler is approximately five times greater than in other well-known devices. The coupling flatness in an equally wide band is four times better than in a coupler without the compensation circuit. Tuning of the coupling and the mid-band frequency can be improved because there
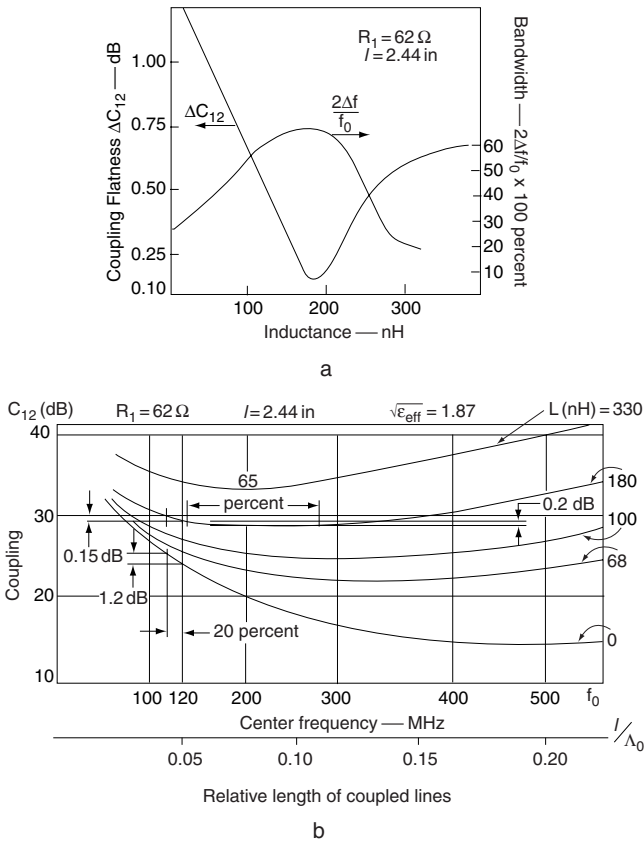
Figure 7.14. An experimental relationship of microstrip directional coupler with compensation network: between inductance L and coupling flatness ΔC_{12} and bandwidth $2\Delta f/f_0 \times 100\%$ for coupling flatness of 0.1 dB (a); between coupling C_{12}, central frequency f_0, and inductance L (b).

is no need to change the configuration or size of the coupled lines. Tuning can be provided simply by varying the inductance value L.

7.4.3. Couplers with Tight Coupling

In many instances, especially in the design of broadband 3-dB directional couplers, the circuits discussed above have some deficiencies. A planar coupled-line directional coupler with tight coupling is difficult to realize because the small gap between coupled lines is difficult to etch. For exam-

ple, a planar 3-dB microstrip directional coupler has a gap of less than 0.5 μinch. Such gap spacing is not realizable because the fabrication tolerances are so tight. A broadside directional coupler [Figure 7.10(b)] has a larger gap, but it requires a very thin dielectric substrate between two coupled lines, which limits the maximum power. In addition, differences in even- and odd-mode velocities can have a significant effect on directional coupler performance.

The noted deficiencies may be overcome by using a tandem interconnection of directional couplers [11, 20, 21]. Why tandem, and not the classic cascade network? A cascade network of directional couplers with directivity of type **I** and fixed tight coupling includes directional couplers with weak coupling. However, if we try to realize the same cascade network for directional couplers with directivity of type **II**, we get a directional coupler with coupling equal to one directional coupler coupling and the frequency band will remove to a high-frequency area.

We get a different picture for a tandem network of directional couplers with directivity of type **II** (Figure 7.15). In Figure 7.15(a) the direct port 3 and coupled port 2 of the left directional coupler are connected to the input port 1 and isolated port 4 of the right directional coupler. This tandem network can be seen as a cascade network of two identical four-port networks with ports 2 and 4 renumbered. In this case, the directional coupler with directivity of type **II** transforms into a directional coupler with directivity of type **I**. This change simplifies calculation of a tandem net-
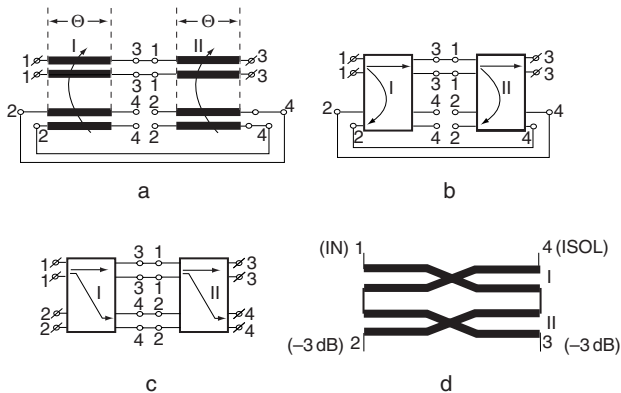
Figure 7.15. Tandem connection of two coupled line couplers: circuit view (a); equivalent connection of two four-port networks (b); two four-port network with new port numeration data (c); tandem of two 8.34 dB coupled line couplers (d).

work by using known correlation with the cascade network of four-port networks. The renumbering of ports by crossing transmission lines is shown in Figure 7.15(c). We will illustrate this transformation and the final results of the connection of two directional couplers with directivity of type **II**.

The scattering matrix of the renumbered directional coupler is

$$[S] = \begin{bmatrix} 0 & 0 & S_{13} & S_{14} \\ 0 & 0 & S_{14} & S_{13} \\ S_{13} & S_{14} & 0 & 0 \\ S_{14} & S_{13} & 0 & 0 \end{bmatrix},$$

where

$$S_{13} = \frac{1}{\cos\Theta + i\rho\sin\Theta} = \frac{\sqrt{1-K^2}}{\sqrt{1-K^2}\cos\Theta + i\sin\Theta},$$

$$S_{14} = \frac{ir\sin\Theta}{\cos\Theta + i\rho\sin\Theta} = \frac{iK\sin\Theta}{\sqrt{1-K^2}\cos\Theta + i\sin\Theta}.$$

The scattering matrix for the mid-frequency band becomes

$$[S]_\Sigma^0 = \begin{bmatrix} 0 & 0 & 2K^2-1 & -2iK\sqrt{1-K^2} \\ 0 & 0 & -2iK\sqrt{1-K^2} & 2K^2-1 \\ 2K^2-1 & -2iK\sqrt{1-K^2} & 0 & 0 \\ -2iK\sqrt{1-K^2} & 2K^2-1 & 0 & 0 \end{bmatrix}.$$

This yields conditions for the 3-dB coupling of the tandem network:

$$|S_{13}| = |S_{14}| = \frac{1}{\sqrt{2}},$$

$$|2K^2-1| = |2K\sqrt{1-K^2}| = \frac{1}{\sqrt{2}},$$

which gives $K = 0.3827$ and $C_{12}^0 = 8.343$ dB.

TABLE 7.6. Relationships Between the Tandem Network Coupling C_{12} and Coupling C_{12}^0 of the Coupled Line Directional Coupler

	C_{12}^0 (dB)			
C_{12} (dB)	$n = 2$	$n = 3$	$n = 4$	$n = 5$
0	3.0	6.0	8.34	10.3
3	8.34	11.7	14.18	16.1
10	15.91	19.4	21.9	23.84

We have arrived at a valuable result: a 3-dB directional coupler can be realized by the tandem connection of two directional couplers with directivity of type **II** and coupling of

$$C_{12}^0 = 8.343 \, \text{dB}.$$

Using the same procedure, we can find the relationship between the tandem network coupling C_{12} and coupling C_{12}^0 of one directional coupler for n cascades (Table 7.6) [22].

Practically, the bandwidth of the tandem network does not depend on the number of cascades. The above results enable us to choose the number of cascades and coupling of every directional coupler for a specified total coupling.

An original design of a 3-dB coupler was presented by Lange [23]: an *interdigital coupler* consisting of several segments of stripline or microstrip line connected by cross wires as shown in Figure 7.16(a). The length of short finger elements is approximately $\Lambda_1/4$ (Λ_1 is the guide wavelength, which corresponds to the highest frequency of the band). The entire length of the center area is equal $\Lambda_2/4$ (Λ_2 is the guide wavelength, which corresponds to the lowest frequency of the band).

The Lange coupler provides tight coupling values with substantially wider gaps than are required for the two coupled-line coupler. The interdigital coupling section compensates for even- and odd-mode phase velocity dispersions over the wide frequency range. For nonhomogeneous microstrip coupled lines, it is difficult to define $\Lambda/4$ precisely, because even- and odd-mode phase velocities are unequal. The Lange coupler is assumed to have infinity isolation of a perfect hybrid and ports that are
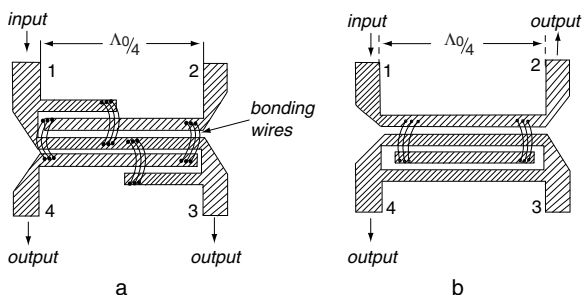
Figure 7.16. Lange directional couplers: original configuration (a); modification (b).

matched perfectly. The signals at output ports 3 and 4 are in quadrature, while port 2 is isolated. The Lange coupler offers an advantage in that both output ports are on the space side, which is very useful for balanced circuit application.

The bonding wires should be as electrically close as possible to short circuit. Their lengths must be kept as short as possible: $l << \Lambda_0/4$, where Λ_0 is the mid-band guide wavelength. Frequently, two or more wires are connected in parallel in order to minimize bondwire inductance. For a given coupling, the spacing between lines in this configuration is much wider than if the same coupling was to be realized in a parallel edge-coupled system. A large benefit to be derived from this coupler is that it can work over an octave of bandwidth or more. The phase difference of the Lange coupler is generally better than +/–2° on nominal 90° relative phase shift. A development of the Lange coupler is shown in Figure 7.16(b). This coupler has fewer coupling lines and straps, but more phase-shift variation over the band.

7.4.4. Multisection Couplers

The bandwidth of the coupled-line directional coupler can be increased by increasing the number of sections with electrical length Θ_0. Multisection couplers may be either symmetrical or asymmetrical.[†] The n-section symmetrical coupler is shown in Figure 7.17(a). Each coupler section is a quarter-wave long at the center frequency. Symmetric couplers have an odd number of sections. Analysis and synthesis of this coupler can be per-

[†]The terms *symmetrical* and *asymmetrical* are used to denote a coupler that has end-to-end symmetry or asymmetry.
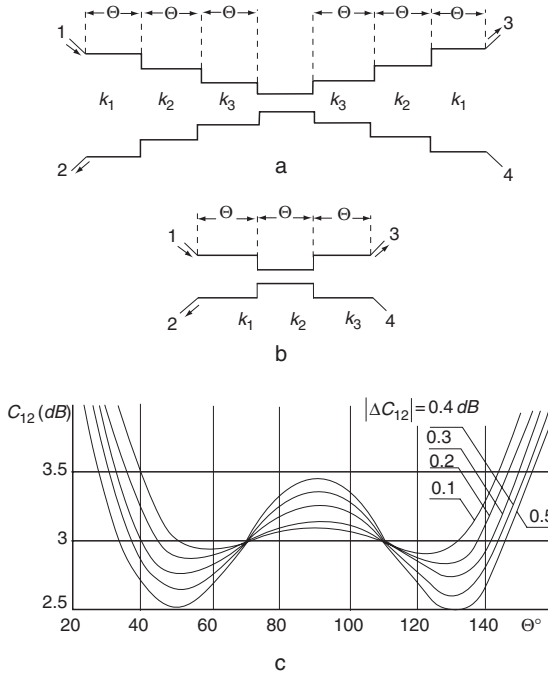
Figure 7.17. Broadband coupled line directional coupler: multi-section (a); three-section (b); coupling vs. electrical length Θ (in degree) for different coupling deviation ΔC_{12} (c).

formed using the theory of filters with step change of characteristic impedance.

A fully symmetrical multisection coupler is calculated by the mirror-reflection method (see Chapter 6). For perfect matching, normalized characteristic impedances of even and odd modes are equal:

$$Z_{0e1}Z_{0o1} = Z_{0e2}Z_{0o2} = Z_{0e3}Z_{0o3} = \ldots Z_{0en}Z_{0on} = 1. \tag{7.42}$$

From (7.28) and (7.42), the module of the coupling coefficient is

$$K_i = \frac{\left(Z_{0e}\right)_i^2 - 1}{\left(Z_{0e}\right)_i^2 + 1}. \tag{7.43}$$

The relative bandwidth of the coupler is

$$W = \frac{f_+ - f_-}{f_0} = 2\frac{f_+ - f_-}{f_+ + f_-},$$

where f_+, f_-, f_0 are the upper, lower, and center frequencies, in between which the coupling is within the amount ΔC_{12}. When calculating directional couplers, we use the frequency bandwidth ratio B:

$$B = \frac{f_+}{f_-}. \tag{7.44}$$

Tables of parameters W, B, and other multisection couplers with different couplings and with Chebyshev and Butterworth frequency characteristics are given in [24, 25]. The bandwidth increases with the number of sections and also with the amount of ripple.

Let us consider in more detail the characteristics of a three-section coupled line directional coupler [Figure 7.17(b)]. According to (7.42), the condition for ideal matching of the three-section coupler is

$$Z_{0e1}Z_{0o1} = Z_{0e2}Z_{0o2} = 1, \tag{7.45}$$

where Z_{0e1} and Z_{0o1} are characteristic impedances of edge sections for the even- and odd-modes, respectively; Z_{0e2} and Z_{0o2} are characteristic impedances of the middle section for the even and odd modes, respectively.

Characteristics of the three-section directional coupler are determined in the same way as those for a one-section $\Lambda_0/4$ directional coupler. A Chebyshev or a Butterworth frequency response of coupling can be obtained with the correct choice of coupling of middle and edge sections. The ripple is equal to half the difference between maximum and minimum coupling in a given bandwidth. The frequency response of the 3-dB three-section coupler with different ripples (ΔC_{12} = +/–0.1, 0.2, 0.3, 0.4, 0.5 dB) is shown in Figure 7.17(c). The bandwidth increases with the amount of ripple.

The symmetrical coupler has a nominal phase of 90° unbalance between output ports. This phase relationship is theoretically independent of the frequency.

The asymmetrical coupler is also built using a series of quarter-wave coupled sections, and it has the highest coupling section at one end [26]. Asymmetrical couplers can have any number of sections. For a given

overall length, the result is a greater bandwidth than in corresponding symmetrical couplers. However, asymmetrical couplers have a phase-frequency dependence, which limits their application. The asymmetrical coupler cannot be used in circumstances where a fixed phase response of the output coupled lines is required. The asymmetrical coupler has a varying phase response as a function of the number of sections. The two-section design has a 180° unbalance between the output ports at the center frequency and varies to each side of 180° as a function of frequency. The three-section coupler is centered at a nominal 90° phase response and varies 0° to 180°over an octave.

7.4.5. Particularities of Microstrip Coupled-Line Directional Couplers

Design of microstrip coupled-line directional couplers is tied to specific difficulties. In such couplers, odd-mode oscillations propagate in air and dielectric substrate, while even-mode oscillations propagate in the dielectric substrate only. This gives rise to the difference between propagation constants for odd and even modes, a difference which grows with increased coupling. In conventional microstrip coupled lines, the odd-mode velocity is greater then the even-mode velocity. As a result, a codirectional propagation (forward direction) appears in the secondary line. In addition, the nonuniform dielectric of the microstrip line increases the difference in dispersion for even and odd modes. Thus, the microstrip coupled-line directional coupler has a low directivity (10 to 15 dB), which drops even further as the coupling becomes weaker or the dielectric permittivity is increased. For example, a 10% difference in phase velocities reduces the directivity of 10-dB and 15-dB couplers to 13 dB and 8 dB, respectively, from the theoretical infinity with equal-phase velocities [27].

One version with overlay dielectric is shown in Figure 7.18(a). This additional dielectric substrate is fixed in the region above the coupled microstrip lines. It serves to match the values of phase velocities for even and odd modes by reducing the odd-mode phase velocity without considerably affecting the even-mode phase velocity. The effective dielectric constant for even and odd modes should be equal to the right amount of overlay thickness. The use of a dielectric overlay also tightens the midband coupling, as compared with a coupled microstrip directional coupler
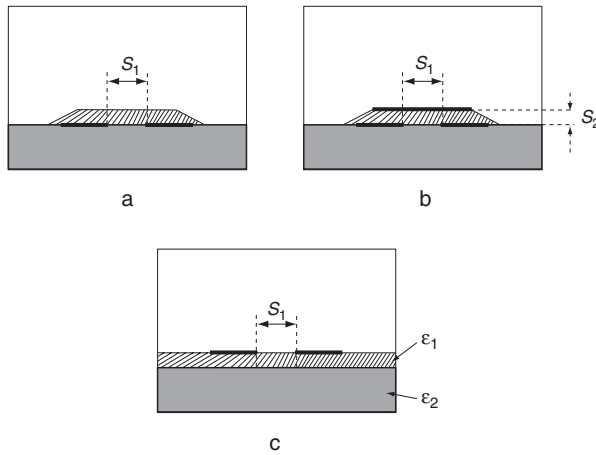
Figure 7.18. Microstrip coupled-line coupler sections: with additional dielectric layer (a); with additional free potential conductor (b); with intermediate dielectric layer (c).

without additional dielectric. Coupling of a compensated coupler depends on the ratio $\varepsilon_{effe}/\varepsilon_{effo}$.

In practice, 4-GHz microstrip directional coupler with dielectric overlay of the same type as the substrate (Duroid 5880, $\varepsilon = 2.2$) provides directivity of 35 dB and losses of 0.1 dB. The same directional coupler without dielectric overlay has directivity of 15 dB and losses of 0.05 dB.

An even better matching of phase velocities is reached with the use of an additional conductor of free potential [Figure 7.18(b)], placed above the coupled lines, separated from them by the additional dielectric substrate.

The length of the conductor is equal to the length of the coupled lines. The conductor increases the capacitance between the coupled lines in the odd mode, while having little or no effect on the capacitance in the even mode. The wider the free conductor, the stronger the additional coupling. However, the width is limited by the value at which the conductor essentially becomes a ground plane. The overlap of the conductor with each of the coupled lines must be equal to at least half the width of the coupled lines.

Let us consider another microstrip directional coupler [Figure 7.18(c)]. In this design, an additional dielectric substrate with small permittivity ε_2 ($\varepsilon_2 < \varepsilon_1$) is placed between the main substrate and the ground plane. This additional substrate reduces the effective dielectric constant for the even mode considerably more than it does for the odd mode.
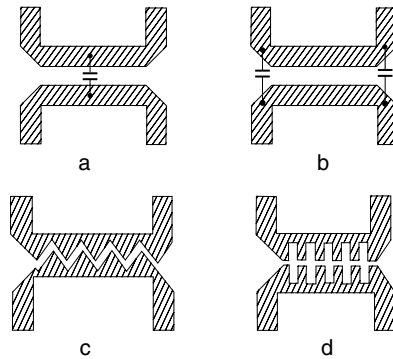
Figure 7.19. Microstrip coupled-line couplers: with additional lumped-element capacitor connected at the midde (a); with additional lumped-element capacitors at the ends (b); with sawtooth shape of coupled lines (c); with periodic step shape of coupled liness (d).
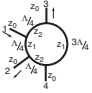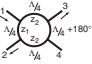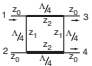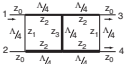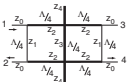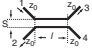
The compensation of difference in phase velocities is achieved by adding lumped-element capacitors connected at the middle [Figure 7.19(a)] or at the ends of the coupled section [Figure 7.19(b)] [28, 29]. These capacitors do not affect the even-mode signal, but affect the odd-mode signal, reducing its phase velocity. The capacitors might be formed either as chip components or as a planar configuration using the interdigital structure (see Chapter 4). These techniques increase directivity, but decrease the overall bandwidth of the coupler.

Another directional coupler design uses a sawtooth shape of coupled lines [Figure 7.19(c)]. The odd-mode currents are concentrated at the surface of the conductor facing the coupled region, while the even-mode currents are concentrated at the outside surface. Thus, the sawtooth shape increases the path of odd-mode currents, having a minimum effect on even-mode currents, thereby again leading to a closer matching of phase velocities. An analogous structure utilizes a periodic step shape [Figure 7.19(d)]. These wiggly-line couplers [Figure 7.19(c, d)] increase the coupling for a given line spacing and slightly increase the loss [30, 31].

The geometrical parameters of sawtooths are defined in [32]. One great advantage of directional couplers (Figure 7.19) is that we retain a totally planar circuit.

The geometric length of the microstrip lines in the coupled region depends on the wavelength, which is a function of the substrate permittivity, geometric dimensions, and mid-band frequency. The length of coupled lines equal to $\Lambda_0/4$ depends on the degree of coupling. On the other

TABLE 7.7. Characteristics of Print Directional Couplers

	Directional Coupler View	Type of Directivity	Phase Balance (deg.)	Coupling (dB)	BW (percent)	Ideal Matching Conditions	Hybrid Equations	Independence from Mismatched Terminations VSWR	Isolation	Coupling	Independence from Losses
Ring coupler of length $3\lambda/2$		2	0 or 180	3 to 6	20	$Y_1^2 + Y_2^2 = 1$	$Y_1 = Y_2 = 1/\sqrt{2}$				
Ring coupler of length λ		2	0 or 180	3	Octave	$Y_1^2 + Y_2^2 = 1$	$Y_1 = Y_2 = 1/\sqrt{2}$	2	1	1	2
Two-branch coupler		1	90	3 to 6	15	$Y_1^2 = Y_2^2 - 1$	$Y_1 = 1;\ Y_2 = \sqrt{2}$				
Three-branch coupler		1	90	3	20	$Y_3 = 2Y_2^2 Y_1 / (1 + Y_1^2)$	$Y_1 = 1;$ $Y_2^2 - Y_3 = 0$	1	2	2	3
Three-branch coupler with power-split regulation		3	90	Variable	20	$Y_3 = 2Y_2^2 Y_1 / (1 + Y_1^2)$	$Y_1 = 1;$ $Y_2^2 - Y_3 = 0$				
$\Lambda/4$ coupled line coupler		2	90	3 to 30	Octave	$Z_{0e} Z_{0o} = 1$					
$3\Lambda/4$ three-stage coupled line coupler		2	90	10 to 30	Two Octave	$Z_{0e1} Z_{0o1} =$ $Z_{0e2} Z_{0e2} =$ $Z_{0e3} Z_{0e3} = 1$		1	2	2	1

hand, the wavelength in microstrip coupled lines depends on the width W of the lines, which is in turn a function of coupling.

Parameters of microstrip directional couplers in the microwave range turn out to be rather sensitive to discontinuities arising in places of connection with input (output) lines and also in places of connection between adjacent sections of a multisection directional coupler. Such discontinuities are of an inductive character. They can be compensated for by increasing the width of the conductor in places of connection.

7.5. COMPARISON OF PRINT DIRECTIONAL COUPLERS

Table 7.7 illustrates the performance and equations of the print directional couplers that are described in this chapter.

REFERENCES

1. Levy, R., "Directional Couplers," in L. Young (ed.), *Advances in Microwave,* Vol. 1, New York: Academic Press, 1966.
2. Matthei, G. L., L. Young, and E. M. T. Jones, *Microwave Filters, Impedance Matching Networks, and Coupling Structures,* Dedham, MA: Artech House, 1980.
3. Altmann, J. L., *Microwave Circuits,* New York: Van Nostrand, 1964.
4. Feldstein, A. L., L. R. Yavich, and V. P. Smirnov, *Waveguide Elements Handbook,* Moscow, Russia: Soviet Radio, 1967.
5. Maloratsky, L. G., and L. R. Yavich, *Design and Calculation of Microwave Elements on Strip-Line,* Moscow, Russia: Soviet Radio, 1972.
6. Maloratsky, L. G., "Understanding the Basics of Microstrip Directional Couplers," *Microwave & RF,* February 2001, pp. 79–94.
7. Tyrrel, W. A., "Hybrid Circuit for Microwaves," *PIRE*, No. 11, 1947.
8. Maloratsky, L. G., "Analysis of a Hybrid Ring," *Telecomm. Radio Eng.,* Washington D.C., Part 2.22,9,92, 1967.
9. Cherne, H. I., and L. G. Maloratsky, "Characteristics of Ring Circuits with Mismatched Loads," *Telecomm. Radio Eng.,* Washington D.C., Vol. 25, No. 3, 1970.

10. Kurzrok, K. M., "Isolation of Lossy Transmission Line Hybrid Circuits," *Trans. IEEE,* Vol. MTT-13, No. 2, 1967.

11. Maloratsky, L. G., *Microminiaturization of Microwave Elements and Devices,* Moscow, Russia: Soviet Radio, 1976.

12. March, S., "A Wide Band Stripline Hybrid Ring," *IEEE Trans. Microwave Theory Tech.,* Vol. MTT-16, June 1968, p. 361.

13. Chien-Hsun Ho, Lu Fan, and Kai Chang, "Broad-Band Uniplanar Hybrid Ring and Branch-Line Couplers," *IEEE Trans. Microwave Theory Tech.,* Vol. 41, December 1993, pp. 2116–2124.

14. Young, L., "Branch Guide Directional Couplers," *Proc. Natl. Electr. Conf.,* Vol. 12, 1956, pp. 723–732.

15. Young, L., "Synchronous Branch Guide Couplers for Low and High Power Applications," *IRE Trans. Microwave Theory Tech.,* Vol. MTT-10, November 1962, pp. 459–475.

16. Levy, R., and L. Lind, "Synthesis of Symmetrical Branch-Guide Directional Couplers," *IEEE Trans. Microwave Theory Tech.,* Vol. MTT-16, February 1968, pp. 80–89.

17. Le Ronde, F. C., "A New Class of Microstrip Directional Couplers," *Proc. IEEE Int. Microwave Symp.,* 1970, pp. 184–185.

18. Maloratsky, L. G., and J. Ide, "Miniature Directional Coupler," U.S. Patent, No. 5,424,694, June 13, 1995.

19. Maloratsky, L. G., "Couplers Shrink HF/VHF/UHF Designs," *Microwave & RF,* June 2000, pp. 93–96.

20. Shelton, J. P., J. J. Wolfe, and R. C. Van Wagoner, "Tandem Couplers and Phase Shifters for Multi-Octave Bandwidth," *Microwaves,* April 1965, p. 14.

21. Carpenter, E., "The Virtues of Mixing Tandem and Cascade Coupler Connections," *IEEE GMTT Int. Microwave Symp.* Washington, D.C., 16-19.

22. Mazepova, O. I., et al., *Print Elements Hand-Book,* Moscow, Russia: Svyaz, 1979.

23. Lange, J., "Interdigital Strip-Line Quadrature Hybrid," *G-MTT Symposium, Digest of Papers,* 1969, pp. 10–13 (see also Lange, J., in *IEEE Trans. Microwave Theory and Tech.,* Vol. MTT-20, November 1972, pp. 777–779).

24. Cristal, E. G., and L. Young, "Theory and Tables of Optimum Symmetrical TEM-Mode Coupled-Transmission-Line Directional Couplers," *Trans. IEEE,* Vol. MTT-13, No. 5, 1965.

25. Young, L., "The Analytical Equivalence of TEM-Mode Directional Couplers and Transmission-Line Stepped-Impedance Filters," *Proc. IEE,* 110, February 1963, pp. 275–281.

26. Levy, R., "General Synthesis of Asymmetric Multi-Element Directional Couplers," *Trans. IRE,* Vol. MTT-11, No. 7, 1963.

27. Young, L., *Parallel Coupled Lines and Directional Couplers,* Dedham, MA: Artech House, 1972.

28. Schaller, G., "Optimization of Microstrip Directional Couplers with Lumped Capacitors," *A.E.V.,* Vol. 31, July–August 1977, pp. 301–307.

29. Mongia, R., I. Bahl, and P. Bhartia, *RF and Microwave Coupled-Line Circuits,* Norwood, MA: Artech House, 1999.

30. Podell, A., "A High-Directivity Microstrip Coupler Technique," *IEEE MTT-S Int. Microwave Symp. Dig.,* 1970, pp. 33–36.

31. Kajfez, D., "Raised Coupler Directivity with Lumped Compensation," *Microwaves,* Vol. 27, March 1978, pp. 64–70.

32. Malherbe, J. A. G., *Microwave Transmission Line Couplers,* Norwood, MA: Artech House, 1988.

Dividers and Combiners

A reciprocal divider can provide an equal or unequal power split between two or more channels [1–4]. Because of their reciprocity, these networks may also be employed to combine a number of oscillators or amplifiers at a single port. Dividers and combiners are used in feed networks in antenna arrays, balanced mixers, high-power transmitters, balanced amplifiers, and test instrumentation.

8.1. *T*- AND *Y*-JUNCTIONS

The simplest printed single-layer three-port divider is analogous to coax and waveguide *T*-junctions. It can have a series or a parallel connection of one input and two outputs. In a series planar connection, the signal splits out of phase; in a parallel connection, it splits in-phase between two outputs.

For improvement of matching, lines can be connected at 120° to each other. Circuits connected in this way are called *Y*-junction. Dividers with equal characteristic impedances are frequently useful. Matching in such dividers is realized with quarter-wave transformers. Various power division ratios can be provided by selecting the appropriate output imped-

ances. The power split is inversely proportional to the output impedance ratio.
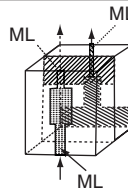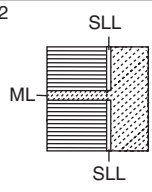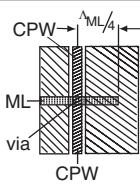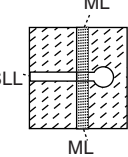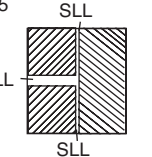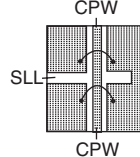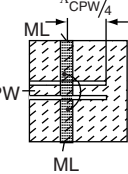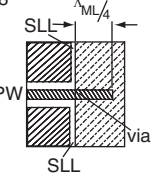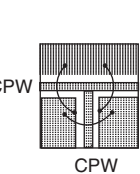
Some useful uniplanar and multilayer *T*-junctions with different input and output transmission lines are illustrated in Table 8.1. Multilayer microstrip *T*-junction is shown in Figure 1 of Table 8.1. An input ML is realized on double substrate and connected with a symmetrical segment that includes two strips. These strips are connected with two output microstrip lines having their ground plane between two dielectric substrates.

Figure 2 of Table 8.1 illustrates the case where the input transmission line is an ML and two output lines are nonsymmetrical slotlines (SLLs) that are realized on two sides of the dielectric substrate. The slotline arms and microstrip arm are connected parallel to each other.

Figure 3 of Table 8.1 shows a *T*-junction between an input ML with quarter-wavelength open stub and two output coplanar waveguides

TABLE 8.1. Uniplanar and Multilayer *T*-Junctions with
Different Input and Output Transmission Lines

(CPW). In the center of the junction, the center conductor of the CPW has a via hole.

The *T*-junction of Figure 4 (Table 8.1) includes an input top slotline open circuit through a nonuniform circular slotline and two output MLs on the bottom substrate side. The microstrip arms and slotline arm are connected in series to each other.

The *T*-junction of three SSLs is displayed in Figure 5 of Table 8.1.

The case in Figure 6 of Table 8.1 shows a *T*-junction that acts as an out-of-phase divider.

Figure 7 of Table 8.1 depicts the CPW-ML *T*-junction with a CPW quarter-wavelength short stub.

Figure 8 of Table 8.1 shows the CPW-slotline *T*-junction with quarter-wavelength ML open stub. In the center of the junction, the center conductor of the CPW has a via hole.

Figure 9 of Table 8.1 illustrates the CPW *T*-junction for in-phase power division. Bridges insure the same potential on each side of the ground plane. Bridges are made by thin wires ($d \approx 25 \ \mu$m).

The simple three-port network structure of *T*- and *Y*-junctions has two significant drawbacks: the absence of isolation between output ports and the imperfect matching of all ports. Theoretically, the reciprocal three-port network without loss cannot be matched at all ports simultaneously. The power dividers/combiners discussed next are free of these disadvantages.

8.2. DIVIDERS AND COMBINERS ON THE DIRECTIONAL COUPLER BASE

8.2.1. Power Dividers

A directional coupler is a reciprocal four-port network, which provides two different amplitude outputs when a signal is applied to its input. This definition of a directional coupler speaks of its possible use for split power from one port between two other ports. Let us consider various dividers/combiners based on directional couplers. The divider based on a ring directional coupler is shown in Figure 8.1(a). Power P_1 flows into port 1 and splits between ports 2 and 3. As a result, powers P_2 and P_3 are dissipated in corresponding terminations R_2 and R_3. A matched ballast
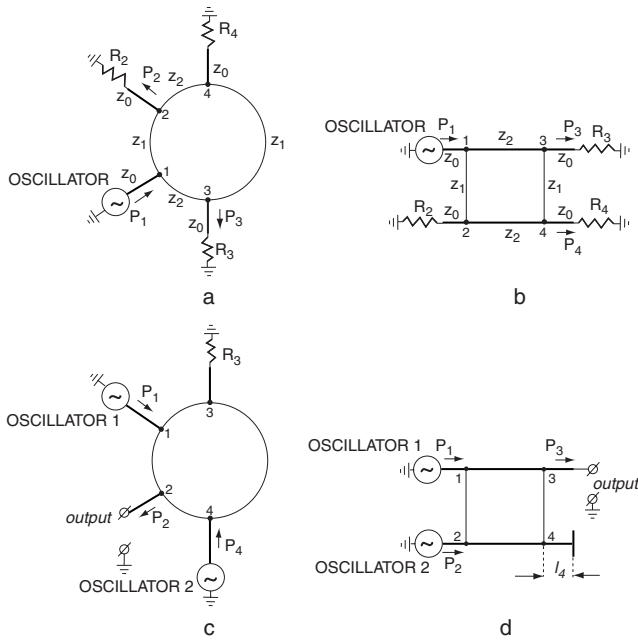
Figure 8.1. Power dividers and combiners: power divider with ring directional coupler (a); power divider with two-branch directional coupler (b); power combiner with ring directional coupler (c); power combiner with two- branch directional coupler (d).

termination R_4 is connected to port 4 to which, theoretically, there is no flow of power. (In practice, there is a significantly diminished power flow.) This termination is "ballast" only from a structural point of view; functionally, it is essential, with a precise optimum value, to ensure the proper performance of the network.

The advantage of a 3-dB directional coupler is its power handling capability (in the range of several hundred watts of CW). The only limitations to power handling are heat generated by internal dissipation losses of the transmission line and the power capability of the ballast external termination.

Let us specify the square of the admittance ratio:

$$\left(\frac{y_1}{y_2}\right)^2 = \left(\frac{Y_1}{Y_2}\right)^2 = m.$$

Then, using (7.2), we obtain

$$y_1 = y_0 \sqrt{\frac{m}{m+1}}, \quad y_2 = y_0 \sqrt{\frac{1}{m+1}}. \tag{8.1}$$

Substituting (8.1) in (7.1), we obtain the scattering matrix of the ring divider

$$[S] = \begin{bmatrix} 0 & -i\sqrt{\dfrac{m}{m+1}} & -i\sqrt{\dfrac{1}{m+1}} & 0 \\ -i\sqrt{\dfrac{m}{m+1}} & 0 & 0 & -i\sqrt{\dfrac{1}{m+1}} \\ -i\sqrt{\dfrac{1}{m+1}} & 0 & 0 & i\sqrt{\dfrac{m}{m+1}} \\ 0 & -i\sqrt{\dfrac{1}{m+1}} & i\sqrt{\dfrac{m}{m+1}} & 0 \end{bmatrix}. \tag{8.2}$$

As can be seen from (8.2), the energy of the source connected to one of the ports of the ring divider is distributed between the adjacent ports according to the square of the admittances ratio m:

$$\frac{P_2}{P_3} = \frac{|S_{12}|^2}{|S_{13}|^2} = m,$$

where P_2 and P_3 are signal powers in ports 2 and 3 when the ring is energized from port 1.

If the power split for the two-branch divider shown in Figure 8.1(b) is specified at

$$m = \frac{P_3}{P_4} = \frac{|S_{13}|^2}{|S_{14}|^2} = \frac{1}{Y_1^2} = \frac{1}{Y_2^2 - 1},$$

then the normalized admittances are equal such that

$$Y_1^2 = \frac{1}{m}, \quad Y_2^2 = \frac{m+1}{m}. \tag{8.3}$$

The square of the admittance ratio is

$$\frac{Y_1^2}{Y_2^2} = \frac{1}{m+1}.$$

The scattering matrix of a two-branch divider is

$$[S] = -\frac{m}{\sqrt{1-m^2}} \begin{bmatrix} 0 & 0 & i & {1}/{\sqrt{m}} \\ 0 & 0 & {1}/{\sqrt{m}} & i \\ i & {1}/{\sqrt{m}} & 0 & 0 \\ {1}/{\sqrt{m}} & i & 0 & 0 \end{bmatrix}.$$

From (8.1) and (8.3) we can define normalized admittances of ring and two-branch dividers (see Table 8.2). For $m > 3$, it is difficult to realize the corresponding ratio of admittances; therefore, the maximum practical power split used is $m = 3$.

The important advantage of the branch dividers is achieving good input matching because reflected signals from identical outputs are absorbed in a ballast termination. In addition, the branch dividers/combiners are effective for planar fabrication of balanced circuits because the output ports from the network are on one side.

In this respect, directional couplers have an advantage over T- and Y-junctions: in directional couplers, the split coefficient m is proportional to the square of the ratio of admittances, which gives more room for increasing m. However, a decrease in admittance and a corresponding decrease in the width of the conductor lead to increased losses. In this case, unequal losses take place on different segments of a directional coupler which results in deviation from the specified m, mismatching, and a decrease in isolation.

8.2.2. Power Combiners

Ring and branch directional couplers can be used as combiners of a number of coherent oscillators at a single port. Due to the reciprocity of divid-

TABLE 8.2. Normalized Admittances of Ring and Two-Branch Dividers

Circuit	Power Split		
	$m = 1$	$m = 2$	$m = 3$
Ring coupler	$Y_1 = Y_2 = \dfrac{1}{\sqrt{2}}$	$Y_1 = \sqrt{\dfrac{2}{3}}; Y_2 = \dfrac{1}{\sqrt{3}}$	$Y_1 = \dfrac{\sqrt{3}}{2}; Y_2 = \dfrac{1}{2}$
Two-branch coupler	$Y_1 = 1; Y_2 = \sqrt{2}$	$Y_1 = \dfrac{1}{\sqrt{2}}; Y_2 = \sqrt{\dfrac{3}{2}}$	$Y_1 = \dfrac{1}{\sqrt{3}}; Y_2 = \dfrac{2}{\sqrt{3}}$

ers, relationships obtained for them are also true for combiners. However, the combining mode has a series of particulars. To get lossless combining, the input signals should be coherent and of equal amplitude.

Combining the powers P_1 and P_4 of two oscillators is realized in a ring combiner, as shown in Figure 8.1(c). Ballast termination R_3 is connected to the ring combiner. From the analysis of the scattering matrix (8.2), it follows that signals from two in-phase oscillators are in phase at port 2 and out of phase at port 3. Power flowing into port 3 is zero when

$$P_1 \left|S_{13}\right|^2 = P_2 \left|S_{43}\right|^2 .$$

The main condition for high-efficiency power combining in the common termination is the equality of different oscillators' frequencies and phases. These conditions can be satisfied by the mutual synchronization of oscillators using signals that leak through because of the imperfect coupler isolation. The coupler's imperfect isolation is caused by the mismatched terminations and manufacturing tolerances (see Chapter 7). Due to the uncontrolled variations of these parameters, it is difficult in practice to ensure constant coupling between oscillators. Thus, additional tuning is required to provide the optimum synchronizing signal that maximizes efficiency. The part of such a tuning element can be played by a variable reactive termination connected to the ballast port. An example of this circuit is shown in Figure 8.1(d). In this circuit, equal quadrature signals of two identical-frequency oscillators connected to ports 1 and 2 of a 3-dB

two-branch coupler are combined. In the ideal case, the combined power appears only on port 3, while port 4 is isolated. If any of the above conditions (equal powers, phase quadrature, and equal frequencies) are not satisfied, then an unbalanced signal appears in port 4.

A specified coupling between oscillators can be realized in the network. Due to the specially introduced mismatching element (short or open segment l_4 of adjustable length), the unbalanced signal is reflected from the end of line l_4 and travels into the two oscillators for mutual synchronization. Another possibility is to use an additional synchronizing oscillator connected to port 4.

A coupled-line directional coupler (Chapter 7) can be used for broadband power division or combining. The edge-coupled-line printed coupler cannot be manufactured for a power division $m < 10$ because of etching tolerances. For the ratio $1 < m < 10$, the broadside coupled-line coupler can be used. The 3-dB broadband Lange directional coupler is used for equal power division ($m = 1$). The scattering matrix of the ideally matched coupled-line divider or combiner can be derived from [4]

$$[S] = \begin{bmatrix} 0 & S_{12} & -iS_{12}\sqrt{m} & 0 \\ S_{12} & 0 & 0 & -iS_{12}\sqrt{m} \\ -iS_{12}\sqrt{m} & 0 & 0 & S_{12} \\ 0 & -iS_{12}\sqrt{m} & S_{12} & 0 \end{bmatrix}, \qquad (8.4)$$

where

$$S_{12} = \frac{i(Z_{0e} - Z_{0o})\sin\Theta}{2\cos\Theta + i(Z_{0e} + Z_{0o})\cos\Theta}, \qquad \Theta = \frac{2\pi l}{\Lambda}$$

is electrical length of the coupled lines, Λ is the guide wavelength, Z_{0e} is normalized characteristic impedance for the even mode, Z_{0o} is normalized characteristic impedance for the odd mode, and

$$\sqrt{m} = \frac{|S_{13}|}{|S_{12}|} = \frac{2}{(Z_{0e} - Z_{0o})\sin\Theta} \ .$$

The disadvantages of couplers used for dividers or combiners are the complexity of the circuit, the significant dependence of parameters of the circuit on frequency, and the need for additional ballast terminations.

The advantages of these couplers are convenience of adjustment with a ballast output and good electrical characteristics (high isolation, good matching, low loss, and equal power split).

8.3. IN-PHASE QUARTER-WAVELENGTH POWER DIVIDERS/COMBINERS

8.3.1. Brief History

In-phase quarter-wavelength power dividers and combiners are important components widely used in various applications such as feed networks in antenna arrays, balanced power amplifiers, mixers, phase shifters, vector modulators, and combiners.

The simplest quarter-wavelength multiport divider, known as the Wilkinson divider [5, 6], provides matching of all ports, low loss, in-phase split, and high isolation between output ports. Historically, this device has been reported earlier [7–11]. It was also described in [9], together with the so-called Gysel-type combiner [12], based on a conventional hybrid ring ("rat race") (see Chapter 7 and [13, 14]).

Over the past 40 years, several different circuit configurations of in-phase quarter-wavelength dividers/combiners have been developed. They have specific connection lines (type, impedance, and length), quantity of outputs/inputs, and stages. These modifications, which provide wide bandwidth and arbitrary power-division ratios, are briefly summarized in Table 8.3.

8.3.2. Equal Power-Split Ratio Divider

The well-known Wilkinson power divider/combiner in Figure 8.2(a) consists of two transmission lines, which have a physical length $l = \Lambda_0/4$ relative to the mid-band frequency of the divider (Λ_0 is the guide wavelength). The lumped resistor R_2 is connected between outputs of the two quarter-wavelength lines. If the signal flows into port 3, it is split equally between

TABLE 8.3. Characteristics of In-Phase Quarter-Wavelength Dividers/Combiners

Parameters	Simplest In-Phase Quarter-Wavelength Divider/Combiner [5–11]	Modified Dividers/Combiners
Bandwidth	Narrow	Wide [15–19]
Power	Low	High [7–12]
Power ratio	Equal	Unequal [20]
Number of outputs/inputs (N)	Binary ($N = 2^n$)	Any N [5, 6, 10, 21–24]
Type of transmission lines	Regular	Irregular or coupled [16, 17, 25, 26]
Type of isolating resistor	For maximum isolation	For specified isolation [27] and switchable [24, 28]

ports 1 and 2. In this case, due to symmetry, points B and C are equipotential; therefore, there is no dissipation on resistor R_2. If the signal flows into port 1, it gets to point C in two ways: through lumped resistor R_2 and through two quarter-wave segments. Thus, these two parts of the input signal are out of phase at point C. With certain values (with respect to characteristic impedance z_0) of R_2 and characteristic impedances z_1 of quarter-wave segments, the two parts of the input signal are equal in amplitude and, therefore, cancel each other out at point C. In this way, isolation of ports 1 and 2 is ensured, as half of the input power travels into port 3 and the other half is dissipated on R_2.

The power-handling capability of the Wilkinson divider is determined by the power-dissipation capacity limits of the internal lumped-element resistor R_2. Typically, the CW input power is several watts and is also a function of the impedance match between the divider and external systems.

Let us consider in more detail the equal power-split divider.

The mirror reflection method (see Chapter 6) will be applied to the Wilkinson divider/combiner [Figure 8.2(a)]. Accordingly, the equivalent three-port network [Figure 8.2(b)] is split into two two-port networks, symmetrical relative to the *YY*-axis and operating with even mode [Figure 8.2(c)] and odd mode [Figure 8.2(d)].
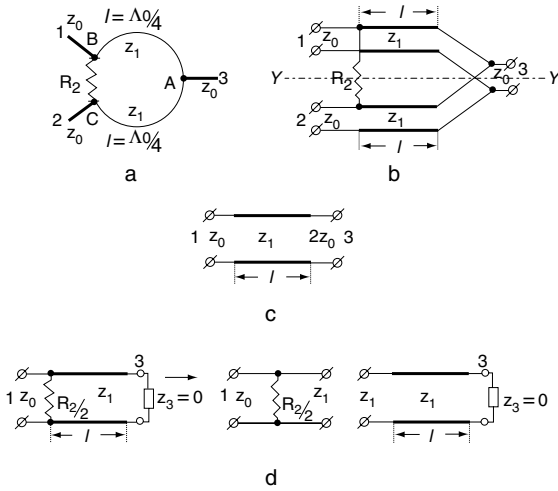
Figure 8.2. Wilkinson equal-split power divider: basic view (a); equivalent three- port network (b); even-mode excitation model (c); odd-mode excitation model (d).

The normalized classical transfer matrices of even-mode and odd-mode two-ports are given by [29]

$$
[A]^{++} = \begin{bmatrix} \sqrt{2}\cos\Theta & i\dfrac{\sin\Theta}{\sqrt{2}\,Y_1} \\[2ex] i\sqrt{2}\,Y_1\sin\Theta & \dfrac{\cos\Theta}{\sqrt{2}} \end{bmatrix},
$$

$$
[A]^{+-} = \begin{bmatrix} \sqrt{\dfrac{1}{Y_3}}\cos\Theta & i\dfrac{\sqrt{Y_3}}{Y_1}\sin\Theta \\[2ex] \dfrac{Y_2}{\sqrt{Y_3}}\cos\Theta + i\dfrac{Y_1}{\sqrt{Y_3}}\sin\Theta & \sqrt{Y_3}\cos\Theta + i\dfrac{Y_2\sqrt{Y_3}}{Y_1}\sin\Theta \end{bmatrix},
$$

(8.5)

where $Y_1 = z_0/z_1$ is the normalized admittance of line segments of length l, z_o is the characteristic impedance of the input (output) lines, $\Theta = 2\pi l/\Lambda$ is the electrical length of line segments, Λ is the guide wavelength, and $Y_2 = 2z_0/R_2$ is twice the normalized admittance of resistor R_2 and is the normalized admittance of the short-circuit segment (it will be assumed henceforth that $Y_3 = \infty$).

The elements of the three-port scattering matrix at its center frequency may be found by means of (8.5) and Appendix C:

$$\hat{S}_{33} = \frac{1 - 2Y_1^2}{1 + 2Y_1^2},$$

$$\hat{S}_{11} = \hat{S}_{22} = \frac{1}{2}\left(\frac{1 - 2Y_1^2}{1 + 2Y_1^2} + \frac{1 - Y_2}{1 + Y_2}\right), \tag{8.6}$$

$$\hat{S}_{12} = \frac{1}{2}\left(\frac{1 - 2Y_1^2}{1 + 2Y_1^2} - \frac{1 - Y_2}{1 + Y_2}\right).$$

It follows from this that perfect matching of all divider ports

$$\left(\hat{S}_{11} = \hat{S}_{22} = \hat{S}_{33}\right)$$

and perfect isolation between the first and second ports $\left(\hat{S}_{12} = 0\right)$ are obtained if

$$Y_1 = \frac{1}{\sqrt{2}}, \quad Y_2 = 1,$$

or

$$z_1 = z_0\sqrt{2}, \quad R_2 = 2z_0. \tag{8.7}$$

The scattering matrix of the ideally matched Wilkinson divider at the center frequency is

$$\left[\hat{S}\right] = -i\begin{bmatrix} 0 & 0 & \dfrac{1}{\sqrt{2}} \\ 0 & 0 & \dfrac{1}{\sqrt{2}} \\ \dfrac{1}{\sqrt{2}} & \dfrac{1}{\sqrt{2}} & 0 \end{bmatrix}.$$

Differing from no less reciprocal T-junctions, the Wilkinson divider can be matched at all ports simultaneously because this three-port network uses a lossy element (resistor R_2).

The Wilkinson power divider is a network with outputs whose phase relationship is 0°. This characteristic is a necessity, for example, in phased arrays. Another advantage of the Wilkinson divider is its superior amplitude balance as compared with a 3-dB directional coupler.

Using (8.6) and conditions (8.7), we can find [29] the frequency response of the Wilkinson divider parameters: matching, insertion loss, and isolation:

$$VSWR_1 = VSWR_2 = \frac{1 + \left|\hat{S}_{11}\right|}{1 - \left|\hat{S}_{11}\right|} = \frac{\sqrt{64t^4 + 80t^2 + 9} + 1}{\sqrt{64t^4 + 80t^2 + 9} - 1},$$

$$VSWR_3 = \frac{1 + \left|\hat{S}_{33}\right|}{1 - \left|\hat{S}_{33}\right|} = \frac{\sqrt{9 + 8t^2} + 1}{\sqrt{9 + 8t^2} - 1},$$

$$C_{13} = C_{23} = 20\log\frac{1}{\left|\hat{S}_{13}\right|} = 20\log\frac{\sqrt{8 + \cos^2\Theta}}{2} \quad (\text{dB}),$$

$$C_{12} = 20\log\frac{1}{\left|\hat{S}_{12}\right|} = 20\log\frac{\sqrt{64t^4 + 80t^2 + 9}}{2\sqrt{2t^2 + 1}} \quad (\text{dB}),$$

(8.8)

where $t = \tan 2\pi l/\Lambda$.

The maximum isolation theoretically goes to infinity. However, the real divider characteristics deviate from the ideal, due to manufacture tolerances, losses, discontinuities, and mismatching of the terminations, as well as the physical quality of the resistor. The influence of these different factors on the parameters of the divider will be examined. In particular, the frequency dependencies quoted above can be used to describe the divider parameters at a fixed frequency when the section lengths deviate from nominal (when $l/\Lambda_0 \neq 0.25$).

The normalized admittances Y_1 and Y_2 can deviate from their nominal values, as given by (8.7). If one of the conditions in (8.7) is satisfied (e.g.,

$R_2 = 2z_0$), then, from (8.6) and (8.8), the dependencies of parameters of the divider on admittance Y_1 will be given by

$$
\left.
\begin{aligned}
VSWR_1 &= VSWR_2 = \frac{\left|2\left(1+2Y_1^2\right)\right| + \left|1-2Y_1^2\right|}{\left|2\left(1+2Y_1^2\right)\right| - \left|1-2Y_1^2\right|}, \\[2mm]
VSWR_3 &= \frac{\left|\left(1+2Y_1^2\right)\right| + \left|1-2Y_1^2\right|}{\left|\left(1+2Y_1^2\right)\right| - \left|1-2Y_1^2\right|}, \\[2mm]
C_{13} &= C_{23} = 10\log\left|\frac{1+2Y_1^2}{2Y_1}\right| \quad (\text{dB}), \\[2mm]
C_{12} &= 20\log\left|\frac{2\left(1+2Y_1^2\right)}{1-2Y_1^2}\right| \quad (\text{dB}).
\end{aligned}
\right\}
\tag{8.9}
$$

The influence of the resistance R_2 (with $Y_1 = 1/\sqrt{2}$) on the parameters may be found similarly:

$$
\left.
\begin{aligned}
VSWR_1 &= VSWR_2 = \frac{\left|2\left(1+Y_2\right)\right| + \left|1-Y_2\right|}{\left|2\left(1+Y_2\right)\right| - \left|1-Y_2\right|}, \\[2mm]
VSWR_3 &= 1, \\[2mm]
C_{13} &= C_{23} = 3.01\,\text{dB}, \\[2mm]
C_{12} &= 20\log\left|\frac{2\left(1+Y_2\right)}{Y_2-1}\right| (\text{dB}).
\end{aligned}
\right\}
\tag{8.10}
$$

According to (8.9) and (8.10), the admittance Y_1 influences all the divider parameters, while Y_2 only affects the matching of the first and second ports and the amount of isolation (C_{12}). The input return loss (of port 3) and insertion losses are independent of R_2.

Resistive losses in the quarter-wave segments of the divider will be characterized by the normalized loss αl (see Chapter 7). When $\alpha l < 0.1$, under conditions (8.7), divider parameters:

$$VSWR_1 = VSWR_2 = \frac{2\left(\alpha^2 l^2 + 2\sqrt{2}\ \alpha l + 2\right)}{\alpha^2 l^2 + 4\sqrt{2}\ \alpha l + 4},$$

$$VSWR_3 = \frac{2\alpha l + 1}{\alpha l + 1},$$

$$C_{13} = C_{23} = 20\log\left(1.5\alpha l + \sqrt{2}\right)(\text{dB}),$$ \quad (8.11)

$$C_{12} = 20\log\frac{3\alpha^2 l^2 + 8\sqrt{2}\ \alpha l + 8}{2\left(\alpha^2 l^2 + \sqrt{2}\ \alpha l\right)}(\text{dB}).$$

If αl is in the range 0.001 to 0.1 Nep, then $VSWR_1 = VSWR_2 \leq 1.002$, $VSWR_3 = 1.09$, $C_{13} = C_{23} \leq 3.08$ dB, and $C_{12} \geq 29.7$ dB. Such influence only needs to be taken into account when designing a complicated feeder system with a large number of dividers (combiners).

Let us consider the effect on the divider operation if the terminations connected to ports 1, 2, and 3 are mismatched. The divider parameters are found [30] to be (see Table 8.4)

$$VSWR_k = \frac{1 + \left|\Gamma_{in\,k}\right|}{1 - \left|\Gamma_{in\,k}\right|},$$

$$C_{ik} = 10\log\left|\frac{P_i}{P_k}\right|(\text{dB}).$$ \quad (8.12)

If the termination of the third port is matched ($\Gamma_3 = 0$), we obtain perfect isolation ($C_{12} = \infty$) and matching of the first and second ports ($VSWR_1 = VSWR_2 = 1$) regardless of the amount of mismatch in the terminations of ports 1 and 2.

However, such mismatch influences the mismatching of the third port. The curves of Figure 8.3 show how the divider parameters depend on the purely real termination factors. If the output ports 1 and 2 are loaded with terminations of nearly identical, reflection coefficients ($\Gamma_1 = \Gamma_2$), the input match (Γ_{3in}) degrades according to the magnitude of the reflection coefficients: $|\Gamma_{3in}| = |\Gamma_1| = |\Gamma_2|$.

TABLE 8.4. Reflection Coefficients and Power Transmission Coefficients of the In-Phase Quarter-Wavelength Dividers/Combiners

Transmission from		
Port 1	Port 2	Port 3
$\Gamma_{in\,1} = -\dfrac{\Gamma_3}{2 + \Gamma_2\Gamma_3}$	$\Gamma_{in\,2} = -\dfrac{\Gamma_3}{2 + \Gamma_1\Gamma_3}$	$\Gamma_{in\,3} = -\dfrac{\Gamma_1 + \Gamma_2}{2}$
$\dfrac{P_1}{P_2} = \dfrac{\left\|2 + \Gamma_2\Gamma_3\right\|^2 - \left\|\Gamma_3\right\|^2}{\left(1 - \left\|\Gamma_2\right\|^2\right)\left\|\Gamma_3\right\|^2}$	$\dfrac{P_2}{P_1} = -\dfrac{\left\|2 + \Gamma_1\Gamma_3\right\|^2 - \left\|\Gamma_3\right\|^2}{\left(1 - \left\|\Gamma_1\right\|^2\right)\left\|\Gamma_3\right\|^2}$	$\dfrac{P_3}{P_1} = \dfrac{4 - \left\|\Gamma_1 + \Gamma_2\right\|^2}{2\left(1 - \left\|\Gamma_1\right\|^2\right)}$
$\dfrac{P_1}{P_3} = \dfrac{\left\|2 + \Gamma_2\Gamma_3\right\|^2 - \left\|\Gamma_3\right\|^2}{2\left(1 - \left\|\Gamma_3\right\|^2\right)}$	$\dfrac{P_2}{P_3} = \dfrac{\left\|2 + \Gamma_1\Gamma_3\right\|^2 - \left\|\Gamma_3\right\|^2}{2\left(1 - \left\|\Gamma_3\right\|^2\right)}$	$\dfrac{P_3}{P_2} = \dfrac{4 - \left\|\Gamma_1 + \Gamma_2\right\|}{2\left(1 - \left\|\Gamma_2\right\|^2\right)}$
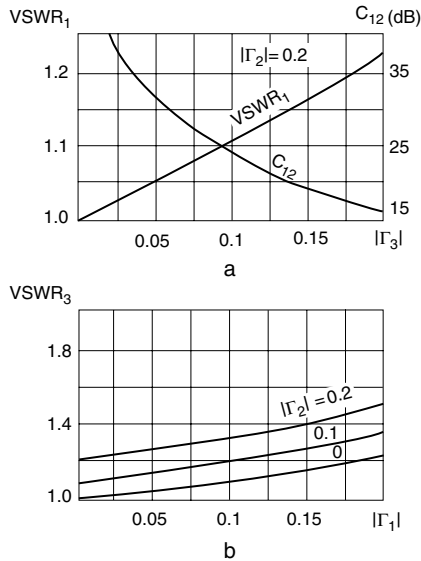
Figure 8.3. Characteristics of power divider as a function from: $|\Gamma_3|$ (a); $|\Gamma_1|$ and $|\Gamma_2|$ (b).

When laying out the divider ports 1 and 2, discontinuities may appear at points where transmission lines with different impedances (z_1 and z_0) are connected. These discontinuities can be taken into account in the divider equivalent circuit by introducing an impedance Z_4 shunting the first and the second ports. On performing calculations similar to the above, for the divider with discontinuities, we obtain

$$VSWR_1 = VSWR_2 = VSWR_3 = \frac{\left|2+Y_4\right| + \left|Y_4\right|}{\left|2+Y_4\right| - \left|Y_4\right|},$$

$$C_{13} = C_{23} = 20\log\left|\frac{2+Y_4}{\sqrt{2}}\right| \quad (\text{dB}),$$

$$C_{12} = \infty \quad (\text{dB}).$$

The isolation between the first and the second ports thus remains perfect whatever the degree of their mismatch, provided that it is identical for each port.

8.3.3. Power Combiner with Specified Isolation

In some applications a specified value of isolation is required. For example, for combining power of oscillators, specified isolation provides mutual synchronization of the oscillators [4, 25, 27].

This combiner with specified isolation between ports 1 and 2 can be realized as shown in Figure 8.4(a). In this circuit, the value of the isolation resistor is $R \neq 2z_0$ and the coupling between ports 1 and 2 becomes dependent on the value of R. The influence of the resistance R (with $Y_1 = 1/\sqrt{2}$) on the parameters may be found from [27]

$$\left.\begin{aligned} VSWR_1 &= VSWR_2 = \frac{\left|2(1+Y) + (1-Y)\right|}{\left|2(1+Y) - (1-Y)\right|} \\[2mm] C_{12} &= 20\log\left|\frac{2(1+Y)}{Y-1}\right| \quad (\text{dB}) \end{aligned}\right\}, \qquad (8.13)$$

where $Y = 2z_0/R$ is twice the normalized admittance of isolation resistor R.
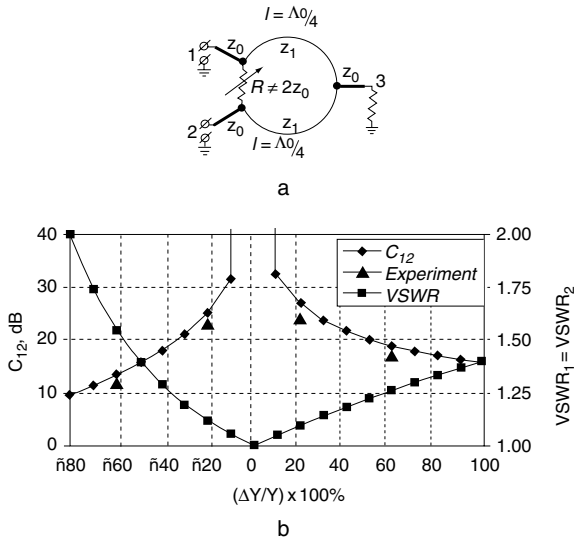
Figure 8.4. Power combiner with specified isolation: schematic (a); characteristics as function from isolating resistor admittance variation (b).

Input return loss at port 3 and insertion loss are independent of R. Theoretical and experimental characteristics of isolation C_{12} and matching $VSWR_1 = VSWR_2$ [see (8.13)] versus admittance deviation $\Delta Y/Y \times 100\%$, are shown in Figure 8.4(b).

In the circuit [Figure 8.4(a)] with the specified isolation and ideal matching of port 3, ports 1 and 2 are mismatched. For the normal functioning of oscillators, good matching of the ports 1 and 2 is required. For the perfect matching of ports 1 and 2 for a specified isolation, it is necessary that

$$Y_1 = \frac{1}{\sqrt{2Y}},$$

that is,

$$z_1 = z_0 \sqrt{2 \frac{z_0}{R}} \ (\Omega).$$

8.3.4. Broadband Dividers/Combiners

N-Section Network

Dr. Seymour Cohn [15] described an in-line power divider consisting of a number of quarter-wavelength sections with resistive terminations at the end of each section, as shown in Figure 8.5(a).

Let us consider the *n*-section broadband divider [Figure 8.5(a)] with equal terminations z_0 (characteristic impedances of input/output lines). The power divider can be represented by an equivalent symmetrical with respect to a *YY*-plane three-port network [Figure 8.5(b)].
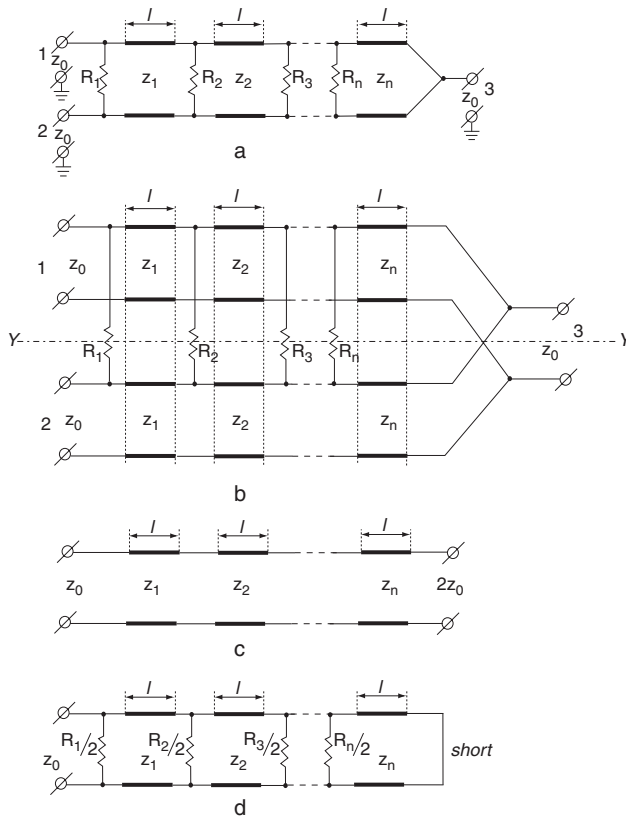

Figure 8.5. Broadband *n*-section power divider: total view (a); equivalent circuit (b); even-mode two-port (c); odd-mode two-port (d).

The three-port network can be represented by equivalent two-port networks [Figure 8.5, (c, d)] for even and odd modes (see Chapter 6). The circuit in Figure 8.5(c) can be interpreted as a step connection between active terminations with $R = 2z_0/z_0 = 2$. In this case, the main parameters of the multisection power divider are dependent solely on the module of the input (output) reflection coefficient of the impedance transformer:

$$\left| S_{11}^{++} \right| = \left| S_{22}^{++} \right| = \left| \Gamma \right|.$$

Based on the above, we can use the well-known theory of impedance transformers [31] to calculate the broadband power dividers. In particular, let us determine the number of sections (n) necessary for the realization of the permissible reflection coefficient

$$\left| \Gamma \right|_{\max} = \left| S_{33} \right|_{\max} = \left| S_{22}^{++} \right|_{\max} = \left| S_{11}^{++} \right|_{\max}$$

and the relative bandwidth W_B for the specified Chebyshev frequency response

$$n = \frac{arcch\left[\dfrac{\sqrt{1-\left|S_{33}\right|_{\max}^2}}{2\sqrt{2}\left|S_{33}\right|_{\max}} \right]}{arcch\left[\dfrac{1}{\sin\left(\dfrac{\pi W_B}{4}\right)} \right]},$$

and the Butterworth (maximally flat) frequency response

$$n = \frac{\log\left[\dfrac{2\sqrt{2}\left|S_{33}\right|_{\max}}{\sqrt{1-\left|S_{33}\right|_{\max}^2}} \right]}{\log\left[\cos\dfrac{\pi}{2}\left(1-\dfrac{W_B}{2}\right) \right]},$$

where

$$W_B = 2\frac{\Theta_B - \Theta_{-B}}{\Theta_B + \Theta_{-B}} = 2\frac{\dfrac{\Lambda_{-B}}{\Lambda_B} - 1}{\dfrac{\Lambda_{-B}}{\Lambda_B} + 1}, \quad \Theta = 2\pi l \Big/ \Lambda$$

is the electrical length of segments; Θ_B and Θ_{-B} are upper and lower band-edge Θ; and Λ_B and Λ_{-B} are upper and lower band-edge wavelength, respectively.

As the number of sections increases, the bandwidth of the divider/combiner also increases. Power dividers with bandwidths from one octave up to one decade have been designed.

Coupled-Line Divider/Combiner

Consider a simple in-phase coupled-line divider/combiner [Figure 8.6(a)] [25], in which the isolating resistor is connected through the coupled lines and is dc isolated from the in-phase transfer path. Figure 8.6(c) represents the equivalent interconnection of three fractional lines with self-imped-ance z_{10} (conductor 1-ground plane), self-impedance z_{20} (conductor 2-ground plane), and mutual impedance z_{12} (between conductors 1 and 2). All three lines are assumed to have identical electrical length Θ and form a quarter-wavelength impedance transformers. Considering, the simplest case of symmetrical coupled lines ($z_{10} = z_{20} = z$), the resulting characteristic impedance of the quarter-wavelength transformer is

$$z_{0e} = \frac{z(z + z_{12})}{2z + z_{12}}. \tag{8.14}$$

Because only the value z_{0e} is specified for in-phase impedance trans-formation between $R_L^{(2)}$ and z_0 at ports 1 and 2

$$z_{0e} = \sqrt{2z_0 R_L^{(2)}},$$

there exists some freedom in choosing of fractional impedances z and z_{12}. This freedom can be used for the optimization of the odd-mode decompo-sition circuit [Figure 8.6(d, e)] as a result of being short-circuited at the axis of symmetry YY in Figure 8.6(a) to provide maximum isolation between ports 1 and 2.
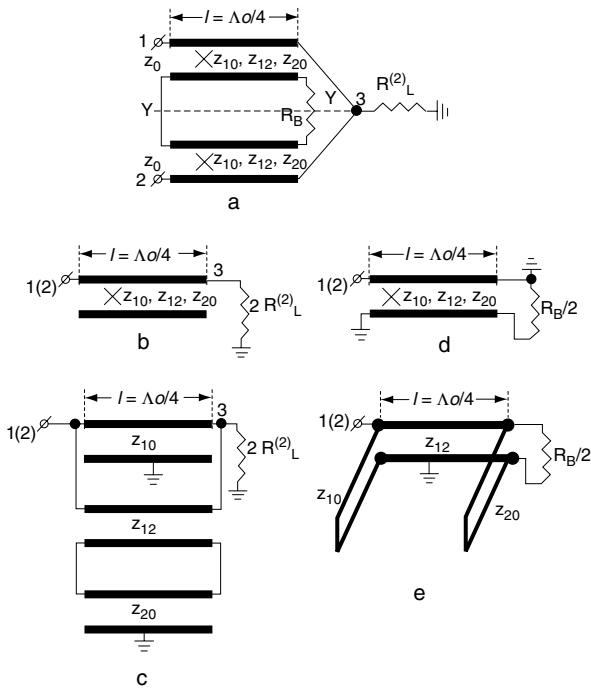
Figure 8.6. Two-way coupled-line power combiner/divider: total view (a); even mode circuit (b); even-mode equivalent schematic with uncoupled lines (c); odd-mode circuit (d); odd-mode equivalent schematic with uncoupled lines (e).

Let us consider, for example, the simplest case when the load impedance at port 3 is equal to

$$R_L^{(2)} = \frac{z_0}{2},$$

for which the even-mode impedance $z_{0e} = z_0$ provides full matching independent of frequency ($\Gamma_{0e} = 0$). The odd-mode impedance z_{0o} should be optimized to provide the minimum odd-mode reflection coefficient (Γ_{0o}). It can be obtained by analysis of the circuit in Figure 8.6(d, e):

$$\Gamma_{0o} = \frac{-k^2 - C\,ctg\Theta + iC^2}{k^2 - C\,ctg^2\Theta + 2C\,ctg\Theta + iC^2}, \tag{8.15}$$

where

$$k = \frac{z}{z + z_{12}} = \frac{z_{0e} - z_{0o}}{z_{0e} + z_{0o}}$$

is the voltage coupling coefficient between the coupled lines, $C = 1 - k^2$, $\Theta = 2\pi l/\Lambda_0$ is electrical length of coupled lines, and Λ_0 is the guide wavelength at the center frequency. Some results of the calculation are shown in Figure 8.7. Because of $\Gamma_{0e} = 0$, the reflection coefficient at ports 1 and 2 is equal to $\Gamma_{0o}/2$.

The isolation between ports 1 and 2 is defined as

$$ISO = 20\log\left|\frac{2}{\Gamma_{0o} - \Gamma_{0e}}\right|(\text{dB}). \tag{8.16}$$

A significantly broader bandwidth of this type of coupled-line combiner is achieved in two or more stage devices [25]. A schematic of a two-way, two-stage combiner is shown in Figure 8.7. Consider the practical case, when

$$R_L^{(2)} = R_{B1} = R_{B2} = z_0 = 50\,\Omega\left(\Gamma_{0e} \neq 0\right).$$

The results of numerical optimization using software GENESYS v. 8.1 (Eagleware Corporation) are shown in Table 8.5. Typical characteristics are illustrated in Figure 8.8 for $F_{max}/F_{min} = 2.33$.
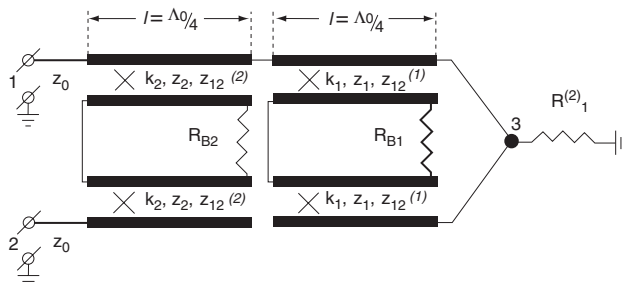

Figure 8.7. Two-way, two-stage coupled-line power combiner/divider.

TABLE 8.5. Parameters of Two-Way Two-Stage Divider/Combiner with Symmetrical Coupled Lines

F_{max}/F_{min}	$z_1(\Omega)$	$z_{12}(\Omega)$	k_1	$z_2(\Omega)$	$z_{12}(\Omega)$	k_2	$|\Gamma_{0e}|$	ISO (dB)
1.5	146.87	45.3	0.764	83.85	126.6	0.398	0.018	56
2.0	145.47	42.6	0.773	86.97	117.1	0.426	0.050	42
2.33	144.30	40.6	0.780	88.94	112.4	0.442	0.074	36
2.5	143.88	39.3	0.786	90.28	108.2	0.455	0.086	34
3.0	142.61	36.1	0.798	93.56	99.23	0.485	0.118	30

8.3.5. Unequal Power-Split Ratio Divider

Unequal power-split ratio power dividers (combiners) are frequently employed in array antennas and different types of receivers.

The unequal power-split ratio divider is described in [20]. It consists (see Figure 8.9) of two branches of different impedances, z_2 and z_3, that
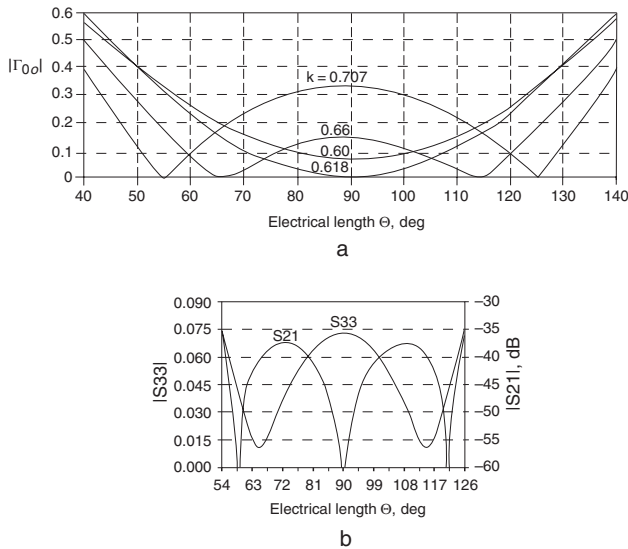

Figure 8.8. Frequency response of coupled line power divider: for odd-mode reflection coefficient (a); for two-stage divider reflection coefficient and isolation (b).
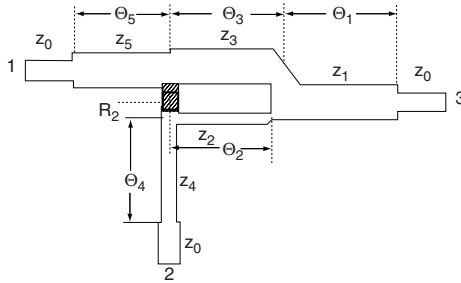
Figure 8.9. Microstrip Wilkinson power divider with unequal power-split ratio.

realize the desired power division. These two branches have an electrical length of 90° at the center frequency of the divider. For a microstrip divider $\Theta_2 \neq \Theta_3$ because $\varepsilon_{eff2} \neq \varepsilon_{eff3}$. Quarter-wave output transformers match the outputs/inputs of the divider to the characteristic impedance z_0. This unequal power-split ratio divider has normalized impedances and lumped resistor [20] determined by

$$m = \frac{P_1}{P_2},$$

$$z_1 = z_0 \left(\frac{\sqrt{m}}{1+m} \right)^{\frac{1}{4}}, \quad z_2 = z_0 \left[m^{\frac{3}{8}} \left(1+m\right)^{\frac{1}{4}} \right],$$

$$z_3 = z_0 \left[\frac{\left(1+m\right)^{\frac{1}{4}}}{k^{\frac{5}{8}}} \right], \quad z_4 = z_0 m^{\frac{1}{4}}, \quad z_5 = \frac{z_0}{m^{\frac{1}{4}}},$$

$$R_2 = z_0 \left[\frac{\left(1+m\right)}{\sqrt{m}} \right].$$

A power divider with unequal division ratios provides matched input and matched in-phase outputs with theoretically perfect isolation between the output ports.

8.3.6. Lumped Element Divider

The Wilkinson power divider is relatively large for low-frequency applications. Let us substitute Λ/4 segments of the divider with equivalent
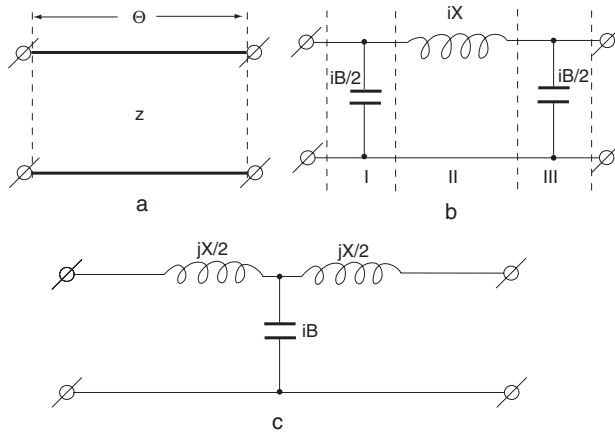
Figure 8.10. The segment of the transmission line (a) and its π-section (b) and *T*-section (c) equivalent.

lumped-element circuits. A short segment of transmission line of characteristic impedance z and electrical length Θ [Figure 8.10(a)] is equivalent to a π-section circuit [Figure 8.10(b)] or a *T*-section circuit [Figure 8.10(c)]. The classic non-normalized transfer matrix of π-section, including cascade connection of the three simplest two-port networks [**I**, **II**, and **III**; see Figure 8.10(b)], is [see Chapter 5, (6.1), and Appendix C]

$$[a]_\pi = [a]_I [a]_{II} [a]_{III} = \begin{bmatrix} 1 - X\dfrac{B}{2} & iX \\ i\dfrac{B}{2}\left(2 - X\dfrac{B}{2}\right) & 1 - X\dfrac{B}{2} \end{bmatrix}. \tag{8.17}$$

The section of the uniform line of characteristic impedance z and geometric length l without losses has a non-normalized transfer matrix (see Appendix C):

$$[a] = \begin{bmatrix} \cos\Theta & iz\sin\Theta \\ i\dfrac{\sin\Theta}{z} & \cos\Theta \end{bmatrix}. \tag{8.18}$$

Comparing (8.17) and (8.18), we obtain

$$1 - X\frac{B}{2} = \cos\Theta, \tag{8.19}$$
$$X = z\sin\Theta.$$

Therefore,

$$\frac{B}{2} = \frac{1 - \cos\Theta}{z\sin\Theta} = Y\tan\left(\frac{\Theta}{2}\right). \tag{8.20}$$

For the quarter-wavelength segments of the Wilkinson divider [from (8.19) and (8.20)], the equivalent lumped elements of the π-section [Figure 8.10(b)] are

$$X = z, \quad \frac{B}{2} = \frac{1}{z} \quad \text{or} \quad L = \frac{z}{2\pi f_0}, \quad C = \frac{1}{2\pi f_0 z}. \tag{8.21}$$

The equivalent lumped-element circuit can be used for each quarter-wavelength segment. The π-section equivalent can be realized with meander-line inductor and two capacitors in each section. Capacitors of two
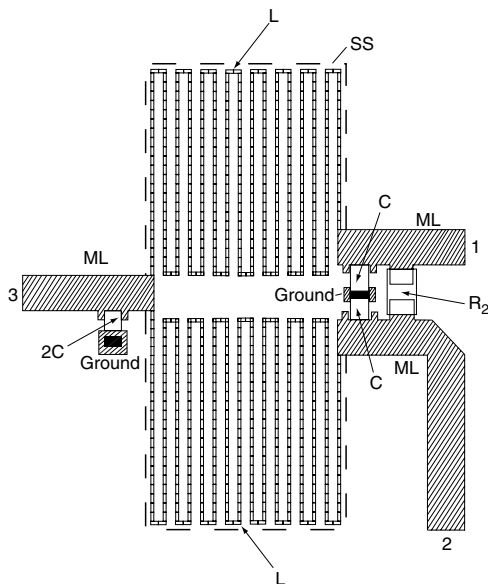

Figure 8.11. Low-frequency lumped element power divider/combiner.

segments at the input of the power divider may be replaced by a single capacitor of twice the value.

One version of a lumped element divider was constructed on a 0.005-in. Kapton substrate ($\varepsilon = 3.45$), designed to operate on a frequency of 100 MHz. Figure 8.11 shows the layout of the lumped-element divider. A combination of suspended stripline (SS) inductors and microstrip input/output lines offers certain advantages. The SS structure provides a low parasitic capacitance between the meander line and ground. This divider occupied an area of 1.5 in^2—a factor of 10 reduction as compared to the conventional distributed Wilkinson divider. The measured performance parameters of this divider in bandwidth of 30% were: return losses at all ports better than 20 dB, isolation between output ports of 22 dB, and losses of 0.1 dB.

8.4. *N*-WAY DIVIDERS/COMBINERS

8.4.1. Chain-Like Dividers/Combiners Based on Directional Couplers

Power combining of more than two oscillators can be realized by a chain-like connection of ring combiners in which each consecutive ring combiner acts as a load for the preceding one, as shown in Figure 8.12. Characteristic admittances of different segments of a ring coupler are determined in accordance with Table 8.2, while admittances of ballast and output termination are equal to each other.

Power combining of more than two oscillators can be realized, for example, by the network displayed in Figure 8.13. This network ensures power combining of four oscillators using three two-branch combiners. These combiners are interconnected by line segments l_1 and l_2. Line segments of length l_i ($i =$ I, II, III) performing the same functions as segment l_4 [Figure 8.1(d)] are connected to port 4 of each two-branch combiner. Analysis of elements of the scattering matrix [27] leads to the following conclusion. Scattering matrix elements S_{15}, S_{25}, S_{35}, and S_{45}, which characterize voltage transmission coefficients from the corresponding oscillator to the load, are independent of mismatching of ports 4_I, 4_{II}, and 4_{III}. Reflection coefficients Γ_I, Γ_{II}, and Γ_{III} of the adjustable segments connected to these ports determine only the coupling between oscillators. The
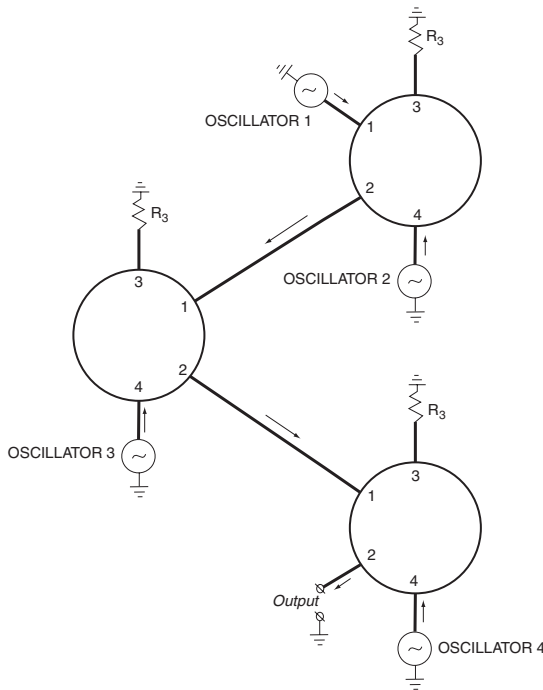
Figure 8.12. Combiner using ring directional couplers for combining power of four oscillators.

mutual synchronization can be regulated by varying reflection coefficients Γ_I, Γ_{II}, and Γ_{III}. Mutual coupling between oscillators from different pairs (e.g., between oscillators connected to ports 1 and 3) does not depend on terminations in ports 4_I and 4_{II} and is determined only by the mismatching of termination in port 4_{III} (Γ_{III}).

Based on the above, we can recommend the following procedure for adjustment of a combiner in Figure 8.13. First, using an adjustable segment connected to port 4_I, we establish a mutual synchronization of the pair of oscillators connected to the first branch coupler. The same is done for the pair of oscillators connected to the second branch coupler using the adjustable segment connected to port 4_{II}. Then, using the adjustable element connected to port 4_{III}, we establish the mutual synchronization of all four oscillators.

The given network also can be used for splitting the power of one source at port 3_{III}.
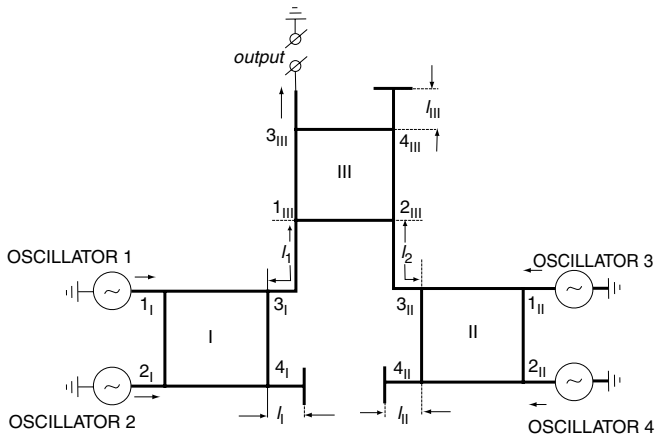
Figure 8.13. Combiner using two-branch directional couplers for four oscillators.

8.4.2. Networks Based on Wilkinson Dividers

In multichannel dividers and combiners, the connection of several Wilkinson dividers is used as shown in Figure 8.14. The best parameters of such a circuit are attained when the distance between dividers is $l = \Lambda_0/2$ (where Λ_0 is the guide wavelength relative to the center frequency of the divider).

Figure 8.14. Four-way divider/combiner.

Modules of scattering matrix elements of this circuit are [27]

$$
\left.
\begin{aligned}
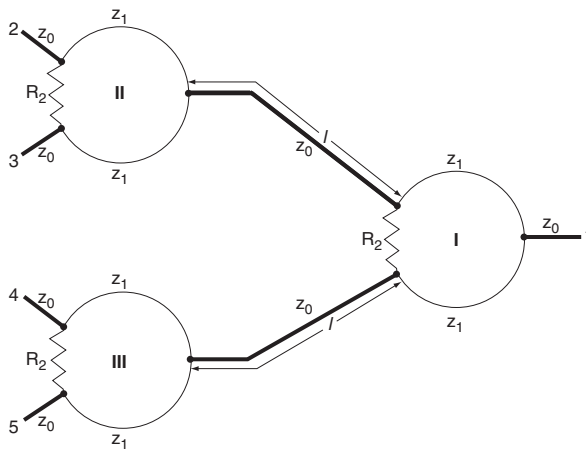|S_{11}| &\approx \left|\frac{\cos^2\Theta}{8+\cos^2\Theta}\right|\sqrt{\frac{288+\cos^2\Theta}{8+\cos^2\Theta}}, \\[2mm]
|S_{12}| &\approx \left|\frac{4}{8+\cos^2\Theta}\right|, \\[2mm]
|S_{22}| &\approx \left|\frac{1}{\sqrt{64t^4+80t^2+9}}\,\frac{\sqrt{\left(9\cos^2\Theta+4\right)^2+72\sin^2 2\Theta}}{8+\cos^2\Theta}\right|, \\[2mm]
|S_{24}| &\approx \frac{8}{8+\cos^2\Theta}\left|\sqrt{\frac{2t^2+1}{64t^4+80t^2+9}}\right|.
\end{aligned}
\right\}
\tag{8.22}
$$

Figure 8.15(a) shows the circuit's frequency characteristics, as well as the frequency response of the single divider (dashed lines) for comparison. These characteristics show that the matching of input/output ports of a three-divider network is more sensitive to frequency change than the matching of a single divider. The obtained frequency characteristics of an ideal connection may be interpreted as characteristics of a nonideal connection working at a fixed frequency, in which lengths of segments deviate from the nominal values. Thus, the required production tolerances of length l are stricter for the three-divider connection.

From (8.22) it follows that insertion losses of the circuit in Figure 8.14 are equal to double the losses of a single divider. The isolation between input ports of different power dividers ($C_{24} = C_{25} = C_{34} = C_{35}$) is equal to the sum of isolation between output ports of a single divider and the insertion losses of the three-divider connection C_{12}.

In practice, characteristics of the three-divider connection differ from the ideal characteristics due to production tolerances, losses in transmission line, and mismatching of terminations. Production tolerances of the dielectric constant of the substrate, of line widths of the divider, and of substrate thickness cause a deviation of admittance Y_1 from the nominal value

$$
\left(Y_1 = \frac{1}{\sqrt{2}}\right).
$$
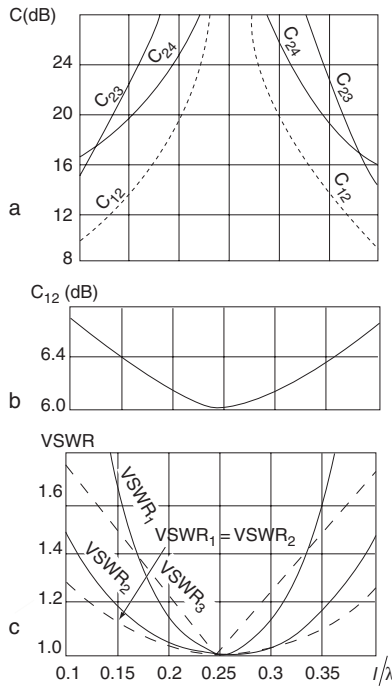
Figure 8.15. Frequency response of isolation (a), insertion loss (b), and matching (c) of three power dividers (solid lines) and single power divider (dotted lines).

The influence of Y_1 on the parameters of the three-divider connection can be seen from the following relationships [27]:

$$|S_{11}| \approx \left| \frac{1 - 2Y_1^2}{1 + 2Y_1^2} \right|^3,$$

$$|S_{12}| \approx \frac{2Y_1^2 \left(3 + 4Y_1^2 + 12Y_1^4 \right)}{\left(1 + 2Y_1^2 \right)^4},$$

$$|S_{22}| = |S_{33}| \approx \left| \frac{1 - 2Y_1^2}{1 + 2Y_1^2} \right| \left| \frac{1}{2} - \frac{Y_1^2 \left(3 + 4Y_1^2 + 12Y_1^4 \right)}{\left(1 + 2Y_1^2 \right)^4} \right|,$$

$$|S_{24}| \approx \left| \frac{2Y_1^2 \left(1 - 2Y_1^2 \right)}{\left(1 + 2Y_1^2 \right)} \right|.$$

A comparison of this network with the single divider shows that the degree of mismatch of all ports of the connection is less sensitive to the variation of Y_1 than the degree of mismatch of ports of the single divider. Dependencies of parameters of the three-divider connection on the deviation of R_2 from the nominal value, when

$$Y_1 = \frac{1}{\sqrt{2}} \text{ and } l_1 = \frac{\Lambda_1}{2},$$

are determined by the following relationships:

$$|S_{11}| = 0, \quad |S_{12}| = \frac{1}{2}, \quad |S_{22}| = |S_{24}| = \frac{1}{4}\left|\frac{1 - Y_2}{1 + Y_2}\right|.$$

Comparing the characteristics of the three-divider connection and parameters of a single divider [27], we conclude that the matching of output ports of the three-divider connection ($VSWR_2$) is more sensitive to the deviation of $VSWR_1$ from the nominal value than that of a single divider. Isolation between any two output ports of the three-divider connection ($C_{24} = C_{23}$) is greater than the isolation between output ports of a single divider by 6.02 dB.

In sum, in the three-divider connection Y_1 influences all parameters, while Y_2 influences only the matching and isolation of output ports. Moreover, matching and isolation turn out to be more sensitive to Y_1 than to Y_2.

The described circuit of the three-divider connection can be used as an elementary module for the design of dividers/combiners with a bigger number of channels.

Let us consider dividers with an odd number of three or more output ports. In the basic three-way divider, the power level at each of the three output ports is 4.77 dB below that of the input power level. Planar microwave power dividers are shown in Figure 8.16(a, b). The divider in Figure 8.16(a) [21] is obtained by using two sections of three transmission lines and four isolation resistors. The characteristic impedances of the input and three output ports are 50Ω. The characteristic impedances of transmission lines of the two sections are $z_1 = 114.0Ω$ and $z_2 = 65.8Ω$, and the resistances are $R_1 = 65Ω$ and $R_2 = 200Ω$. At the 5-GHz frequency range, the isolation characteristic between ports 2 and 3 and 1 and 2 is more than 28 dB, the isolation between ports 1 and 3 is more than 20 dB, and VSWR is less than 1.3 in 1.5:1 bandwidth. In a microstrip realization, the 114Ω
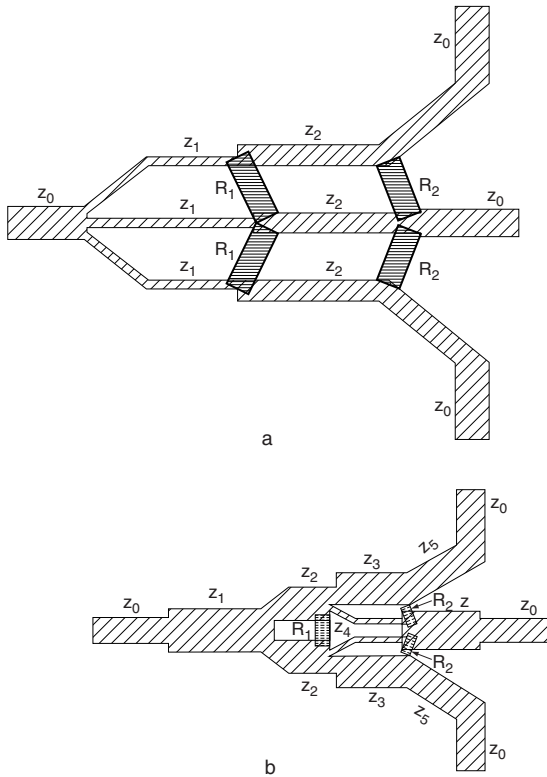
Figure 8.16. Layouts of three-way power dividers: with three transmission lines (a); recombinant circuit (b).

transmission lines are very narrow and substantially increase the insertion loss (~0.5 dB).

The other divider in Figure 8.16(b) requires a maximum line impedance of 80Ω, and only three isolation resistors [22]. The first section provides equal power split. The second section in a corporate feed is designed to provide a 1:2 unequal power split (–1.77 dB, –4.77 dB) and the two lower power arms are recombined into a single center arm using an equal combiner. In this recombinant divider, the characteristic impedances of transmission lines are $z_0 = 50\Omega$, $z_1 = 36\Omega$, $z_2 = z_3 = z_5 = z_6 = 40\Omega$, and $z_4 = 80\Omega$. The isolation resistors are $R_1 = 50\Omega$, $R_2 = 100\Omega$. At the 5.0-GHz frequency range over 1.5:1 bandwidth, isolation exceeds 20 dB and insertion loss is less than 0.3 dB.
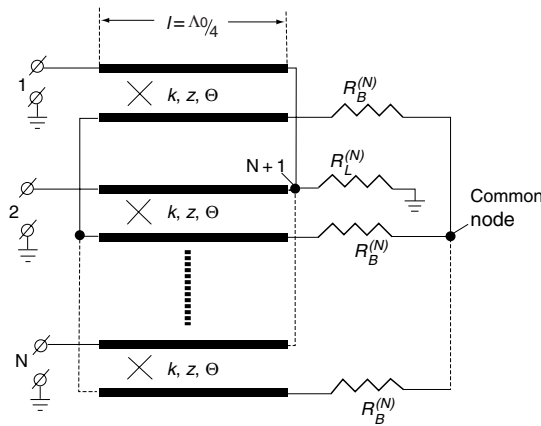
Figure 8.17. Coupled line *N*-way power divider/combiner.

8.4.3. *N*-Way Coupled-Line Combiner

A two-way coupled-line power combiner [Figure 8.6(a)] can be considered as a result of the specific interconnection of two identical 90° directional couplers and can also be extended to an *N*-way in-phase combiner/divider, as shown in Figure 8.17 [25]. In this case, *N* identical 90° directional couplers are interconnected in the same manner. The resulting circuit in Figure 8.30 has the same circular symmetry as the circuit in Figure 8.7, or the Wilkinson-type combiner and, in this case, there is additional freedom: *N* identical coupled lines can be chosen as symmetrical or non-symmetrical. For the particular case of symmetrical coupled lines ($z_{10} = z_{20} = z$), (8.14) is valid. If the load resistance is equal to

$$R_L^{(N)} = \frac{z_0}{N},$$

(8.15) is also valid. In the common case, the isolation between any two ports 1…*N* is equal to

$$ISO = 20 \log \left| \frac{N}{\Gamma_{0o}^{(N)} - \Gamma_{0e}^{(N)}} \right| \ (\text{dB}), \tag{8.23}$$

where values $\Gamma_{0o}^{(N)}$ and $\Gamma_{0e}^{(N)}$ should be defined for proper N. For the case considered above, when

$$R_L^{(N)} = \frac{z_0}{N},$$

we have

$$\Gamma_{0e}^{(N)} = 0 \text{ and } \Gamma_{0o}^{(N)} = \Gamma_{0o}$$

from (8.15). Expression (8.23) is a result of the same circular symmetry as for the circuit in Figure 8.7 and can be used for any values of Γ_{0e} and Γ_{0o}, depending on the chosen ratio

$$\frac{R_L^{(N)}}{z_0}.$$

TABLE 8.6. Normalized Impedance Values for Different Dividers/Combiners

	Power Split				
Divider	$m = 1$	$m = 2$	$m = 3$	$m = 10$	$m = 100$
Wilkinson	$Z_1 = Z_2 = \sqrt{2}$ $\overline{R}_2 = 2$	$Z_1 = 2.060$ $Z_2 = 0.612$ $\overline{R}_2 = 2.121$	$Z_1 = 2.630$ (Difficult to realize) $Z_2 = 0.385$ $\overline{R}_2 = 2.309$	N/A	N/A
Ring	$Z_1 = Z_2 = \sqrt{2}$	$Z_1 = \sqrt{\frac{3}{2}}$ $Z_2 = \sqrt{3}$	$Z_1 = \frac{2}{\sqrt{3}}$ $Z_2 = 2$	N/A	N/A
Two-branch	$Z_1 = 1$ $Z_2 = \frac{1}{\sqrt{2}}$	$Z_1 = \sqrt{2}$ $Z_2 = \sqrt{\frac{2}{3}}$	$Z_1 = \sqrt{3}$ $Z_2 = \sqrt{\frac{3}{2}}$	N/A	N/A
Coupled line	$Z_{0e} = 2.414$ $Z_{0o} = 0.414$	$Z_{0e} = 1.931$ $Z_{0o} = 0.518$	$Z_{0e} = 1.732$ $Z_{0o} = 0.577$	$Z_{0e} = 1.365$ $Z_{0o} = 0.732$	$Z_{0e} = 1.060$ $Z_{0o} = 0.905$

TABLE 8.7. Parameters of Different Dividers/Combiners

Divider/ Combiner	Power Division (m)	Bandwidth	Matching	Isolation	Phase Balance	Application for Balanced Amplifiers	Size
T-Junction	1…2	Broadband	Pure	No	In-phase	No	Very small
Wilkinson	1…2	Broadband	Good	Yes	In-phase	Yes	Small
Ring	1…3	Narrowband	Good	Yes	In-phase–out-of-phase	No	Large
Branch	1…3	Narrowband	Good	Yes	Quadrature	Yes	Moderate
Coupled line	1…100	Broadband	Good	Yes	Quadrature	Yes	Small

8.5. COMPARISON OF DIFFERENT DIVIDERS/COMBINERS

Using (8.1) and (8.4), normalized impedance values for different dividers having isolation of output ports are listed in Table 8.6. The power split m ≥ 3 is difficult to realize in Wilkinson, ring, and branch dividers. The limiting factor here is the impossibility of manufacturing narrow printed conductors of high impedance segments. In addition, an increase in impedance and a corresponding decrease of the conductor width lead to increased losses (see Chapter 2). Table 8.7 illustrates comparison of different dividers/combiners.

REFERENCES

1. Montgomery, C. G., R. H. Dicke, and E. M. Purcell, *Principles of Microwave Circuits,* New York: McGraw-Hill, 1948.
2. Ishii, T. K., *Microwave Engineering,* New York: The Ronald Press Company, 1966.
3. Matthaei, G. L., L. Young, and E. M. T. Jones, *Microwave Filters, Impedance Matching Networks and Coupling Structures,* New York: McGraw-Hill, 1964.
4. Maloratsky, L. G., "The Basics of Print Reciprocal Dividers/Combiners," *Microwave Journal,* September 2000, pp. 108–124.

5. Wilkinson, E. J., "An N-Way Hybrid Power Divider," *IRE Trans.*, Vol. MTT-8, 1960, pp. 116–118.

6. Wilkinson, E. J., "Power Divider," U.S. Patent, No. 3,091,743, Cl. 333-9, 1963.

7. Model, Z. I., and V. M. Katushkina, "Hybrid Combiners of High Power VHF Transmitters," *Proc. of Leningrad Politechnic Institute, Radiophisics,* Vol. 194, 1958.

8. Katushkina, V. M., and Z. I. Model, "N-Way Power Combiners of VHF-UHF Transmitters," *Electrosvyaz,* Vol. 7, July 1959, pp. 17–25.

9. London, S. Y., "Independent Operation of High Power VHF Amplifiers on Common Load," *Problems of Radio-Electronics,* Series X, Techniques of Communication, Vol. 6, 1959, pp. 87–96.

10. London, S. Y., "An *N*-Way Power Combiner," Patent USSR, Cl. $21a^4 9_{01}$, No. 132674, 1960, Patents Publication Bulletin, No. 10, 1960.

11. Katushkina, V. M., and Z. I. Model, "Power Combiner of VHF-UHF Transmitters," Patent USSR, $Cl.21a^4 9_{01}$, No. 142346 (Priority April 1957), Publication Bulletin, No. 21, 1961.

12. Gysel, U. H., "A New *N*-Way Power Divider/Combiner Suitable for High Power Applications," *IEEE International Symposium Digest*, Vol. MTTS-5, 1975, pp. 116–118.

13. Tyrrel, W. A., "Hybrid Circuit for Microwaves," *PIRE*, No. 11, 1947.

14. March, S., "A Wide Band Stripline Hybrid Ring," *IEEE Trans. Microwave Theory Tech.,* Vol. MTT-16, June 1968, p. 361.

15. Cohn, S. B., "A Class of Broadband Three-Port TEM-Mode Hybrids," *IEEE Trans. Microwave Theory Tech.,* Vol. MTT-16, February 1968, pp. 110–116.

16. London, S. Y., "A New Broadband Coupled-Line *N*-Way Power Combiner/Splitter," *Applied Microwave & Wireless,* May 2001, pp. 28–38.

17. London, S. Y., "Broadband Coupled-Line Power Combiner/Divider," U.S. Patent, Int. Cl. H01P 5/12, No. 6,121,853, 2000, and No. 6,472,950, 2002.

18. Shor, A., "Broadbanding Techniques for TEM *N*-Way Power Dividers," *IEEE MTT-S Digest,* 1988, pp. 657–659.

19. Linckelmann, G., "Shaltung zum Aufteilen oder Zusammenfuhren von Hochfrequenzleistung," Deutshes Patentamp, DE 27 33 888 C2, Int. Cl.H03H007/48, 1983.

20. Parad, L. I., and R. L. Moynihan, "A Split-Tee Power Divider," *IEEE Trans. Microwave Theory Tech.,* Vol. MTT-13, January 1965, pp. 91–95.

21. Nobuo, N., E. Maekawa, and K. Ono, "A New *n*-Way Hybrid Power Dividers," *IEEE Trans. Microwave Theory Tech.,* Vol. MTT-25, No. 12, December 1977, pp. 1008–1012.

22. Goldfarb, M. E., "A Recombinant, In-Phase Power Divider," *IEEE Trans. Microwave Theory Tech.,* Vol. 39, No. 8, August 1991, pp. 1438–1440.

23. Adel, A., and M. Saleh, "Planar Electrically Symmetric *N*-Way Hybrid Power Dividers/Combiners," *IEEE Trans. on Microwave Theory Tech.*, Vol. MTT-28, June 1980, pp. 555–563.

24. KMW Inc., "Switchable *N*-Way Power Divider/Combiner," *Microwave Journal,* October 1996.

25. Maloratsky, L. G., and S. Y. London, "Quarter-Wavelength *N*-Way Power Dividers/Combiners: Historical Aspects and New Modifications," *Microwave Journal*, September 2003, pp. 194–202.

26. Mussener, K. M., "Bruckenschaltung mit Lastausgleichswiderstanden," Earopaisches Patentanmeldung, Int. Cl. H03H007/48, No. 0 344 458, A1, 1989.

27. Maloratsky, L. G., *Microminiaturization of Microwave Elements and Devices,* Moscow, Russia: Soviet Radio, 1976.

28. Kim, et al., "Switchable *N*-Way Power Divider/Combiner," U.S. Patent No. 5,872,491, February 1999.

29. Maloratsky, L. G., "Analysis of a Six-Pole Ring-Type Power Divider," *Telecomm., Radio Eng.,* Vol. 27, No. 9, Washington, D.C., 1972, pp. 100–104.

30. Maloratsky L. G., and L. R. Yavich, *Design and Calculation of Microwave Elements on Strip-Line,* Moscow, Russia: Soviet Radio, 1972.

31. Feldstein, A. L., and L. R. Yavich, *Synthesis of Microwave Two- and Four-Port Networks,* Moscow, Russia: Svyaz, 1971.

This Page Intentionally Left Blank

CHAPTER 9

Filters

RF and microwave filters suppress unwanted signals and separate signals of different frequencies. RF and microwave receivers and transmitters require numerous miniature filters for such functions as preselection in the case of a receiver front end, suppression of mixer spurious products, and suppression of transmitter parasitic signals, providing access to the passband and stopband characteristics in multiplexers.

9.1. CLASSIFICATION

Filters can be classified into five different categories of characteristics:

1. Frequency selection:
   - Lowpass frequency (LPF),
   - Highpass frequency (HPF),
   - Bandpass frequency (BPF),
   - Bandstop frequency (BSF);
2. Filter response:
   - Chebyshev,
   - Butterworth,
   - Other (elliptical, Bessel, Gaussian, and so forth);

3. Percentage bandwidth:
    *   Narrowband (0%–20%),
    *   Moderate band (10%–50%),
    *   Wideband (over 50%);
4. Type of elements:
    *   Distributed elements,
    *   Lumped elements;
5. Construction types:
    *   Stepped impedance,
    *   Parallel coupled line,
    *   End-coupled line,
    *   Interdigital,
    *   Comb-line,
    *   Hairpin,
    *   Irregular line.

In addition, there are some different types of filters which are not considered in this book: active, electromechanical, with piezoelectric (surface-acoustic wave), monolithic crystal, magnetostrictive resonators, ceramic-resonator, and YIG-tuned.

The lowpass and highpass characteristics have the cutoff frequency, defined by the specified insertion loss in decibels, at which the passband ends. The LPF transfers energy to the load at frequencies lower than the cutoff frequency with minimal attenuation and reflects an increasing fraction of the energy back to the source as the frequency is increased above the cutoff frequency. The HPF transfers energy to the load at frequencies higher than the cutoff frequency with minimal attenuation and reflects an increasing fraction of the energy back to the source as the frequency is decreased below the cutoff frequency.

The bandpass and bandstop filter characteristics have two cutoff frequencies, or band-edge frequencies, which are defined by the specified insertion loss in decibels. In the BPF, energy is transferred to the load in a band of frequencies between the lower and upper cutoff frequencies. In the BSF energy transfers to the load in two frequency bands: from dc to the lower bandstop cutoff and from the upper bandstop cutoff to infinite frequency.

The most popular solutions for the filter transfer function are the Chebyshev and Butterworth responses [1–9]. Butterworth function filters have

no ripples—insertion loss is flat in the frequency band (thus, the popular name "maximally flat") and rises monotonously with changing frequency. The insertion loss for this response may be expressed as

$$a = 10 \log \left[1 + h^2 \left(\frac{\omega}{\omega_c} \right)^{2n} \right] (\text{dB}),$$ (9.1)

where

$$h = \sqrt{10^{0.1a_r} - 1}$$

is the ripple factor, a_r is the passband attenuation ripple in decibels, ω is the desired angular frequency, ω_c is the cutoff angular frequency, and n is the order of the filter (the number of reactive elements required to obtain the desired response). The Butterworth filter phase response is nonlinear about the cutoff region, with group delay that increases slightly toward the band edges.

A Chebyshev function filter provides the sharpest possible rise of the insertion loss with frequency for a maximum specified passband insertion loss ripple (small changes in the attenuation characteristic of a passband). Since increased ripple results in better selectivity, this approximation offers a compromise between passband ripple and selectivity. The Chebyshev function produces greater rejection amplitude response than the Butterworth function, but has a slight ripple in the passband and greater phase shift and time- or group-delay variations. The phase response of the Chebyshev filter tends to be poor, with a rapid increase in the group-delay variations at the band edges. For the Chebyshev response, the insertion loss may be expressed by the following formula:

$$a = 10 \log \left[1 + h^2 C_n^2 \left(\frac{\omega}{\omega_c} \right) \right] (\text{dB}),$$ (9.2)

where

$$C_n \left(\frac{\omega}{\omega_c} \right)$$

is the Chebyshev polynomial of the first kind and of the order n. In most applications Chebyshev responses are preferred because of higher rejection, but at the cost of slight ripple in the passband.

The elliptic function approximation is equiripple in both the passband and the stopband. The elliptic filter provides a much steeper stopband shape for a given value n, and greater losses as compared to the Butterworth and Chebyshev filters. The price for this performance is paid in stopband ripple levels. A Bessel response is maximally flat in phase within the passband and relative equal-ripple response, but this filter sacrifices somewhat in the sharpness of its rolloff region.

9.2. FILTER SYNTHESIS

The general synthesis of filters proceeds from tabulated lowpass filter prototypes. The lowpass prototype filter synthesis has been most popular and consists of the following steps.

The first step is the design of a prototype lowpass filter with the desired passband characteristics. Lumped-element lowpass filters consist of a ladder network of series inductors and shunt capacitors. Normalization in impedance and frequency is used. The synthesized lowpass filter, normalized for a system impedance of 1Ω, with a cutoff frequency of 1 radian/s, has series inductors in henries and shunt capacitors in farads. These values are referred to as prototype, or g, values.

The design procedure for LPF consists of calculation of the filter order based upon a maximum attenuation in the stopband, a minimum level of ripples in the passband, and the cutoff frequency.

The order of the Chebyshev lowpass filter prototype is equal to

$$n = \frac{\cosh^{-1}\left(\sqrt{\dfrac{A_{max}-1}{A_{min}-1}}\right)}{\cosh^{-1}\left(\dfrac{\omega_p}{\omega_s}\right)}, \tag{9.3}$$

where

$$A_{max} = 10^{a_{max}/10}$$

is the maximum attenuation in the stopband above a certain limiting frequency ω_s (normalized stopband angular frequency),

$$A_{min} = 10^{a_{min}/10}$$

is the minimum level of ripples in the passband attenuation in the passband, ω_p is normalized angular passband frequency, and α_{max} and α_{min} are attenuation in decibels.

The order of the Butterworth lowpass filter prototype is

$$n = \frac{\log\left(\sqrt{\dfrac{A_{max} - 1}{A_{min} - 1}}\right)}{\log\left(\dfrac{\omega_p}{\omega_s}\right)}. \tag{9.4}$$

Also, microwave filters can be synthesized using stepped impedance elements [6, 10].

The second step of filter synthesis is the transformation of the lowpass lumped-element filter prototype to the required filter type (LPF, HPF, BPF, or BSF). Equations for frequency and element transformations are given in [1, 8].

The third step is the practical design of a microwave filter.

Because of the limited scope of this book, we will consider RF and microwave LPFs and BPFs only.

9.3. LPFs

In the case of LPF, all frequencies below a set frequency are selected, and all frequencies above this same set frequency are unwanted.

9.3.1. Stepped-Impedance LPF

TEM structures of stripline and microstrip lines are ideal for LPFs. A waveguide LPF is not possible because waveguides have low cutoff frequencies. The design of a microwave LPF closely follows the idealized lumped-element circuit.
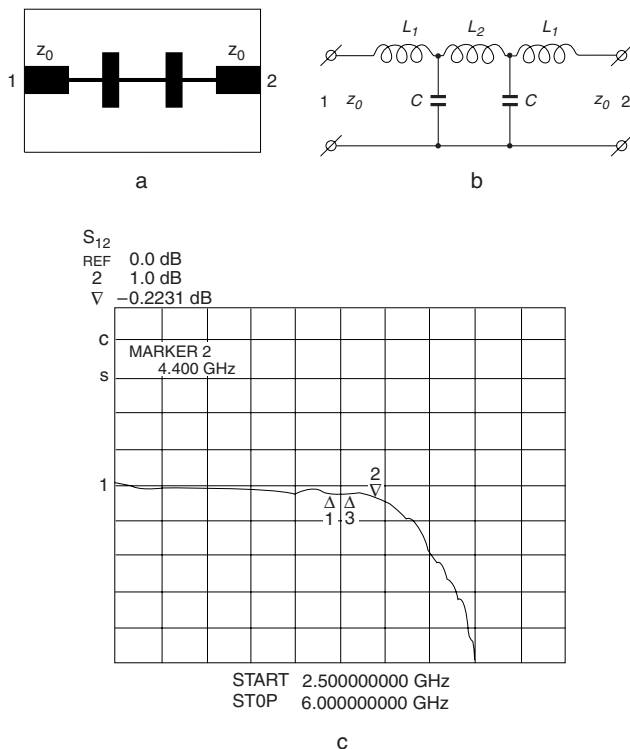
Figure 9.1. Stepped impedance microstrip LPF: layout of 5th order filter (a); equivalent circuit (b); insertion loss frequency response (c)

Figure 9.1 illustrates the relationship between a microwave lowpass filter and a low-frequency lowpass filter prototype. A short section of a high-impedance transmission line can approximate a series inductance. A short section of a low-impedance transmission line can approximate a shunt capacitor.

Let us consider a section of transmission line of characteristic imped-ance z and length l (electrical length $\Theta = 2\pi l/\Lambda$) [see Figure 8.10(a)]. The π-section equivalent circuit of the line is shown in Figure 8.10(b). If the length of a high-impedance section is less than $\Lambda/8(\Theta < \pi/4)$, from (8.19) we have the following: for the prototype $X = \omega l$, where $\omega = 1$, and for a real section

$$X = z\sin\Theta = z\sin\frac{\omega_c l}{\upsilon},$$

where υ is the velocity of signal propagating along the line, and ω_c is the band edge in the microwave filter. Thus,

$$L = z \sin\left(\frac{\omega_c l}{\upsilon}\right). \qquad (9.5)$$

Likewise, for shunt capacitors in the *T*-section [Figure 8.10(c)], we have

$$C = Y \sin\left(\frac{\omega_c l}{\upsilon}\right). \qquad (9.6)$$

If we connect π- and *T*-sections, or cascade the equivalent high- and low-impedance transmission lines using these elements as basic building blocks, we obtain a lowpass filter. The filter selectivity increases with the number of sections. A shorter section electrical length provides a broader stopband.

The input can be either a shunt capacitor or a series inductor. Shunt capacitances should be realized by sections having the lowest possible characteristic impedance, while series inductances should be realized by sections with the highest possible impedance. However, one has to keep in mind the etching tolerance. The narrower high-impedance lines have greater sensitivity to the etching factor. For the low-impedance line, the line width must not allow any transverse resonance to occur at the operating frequency.

The width steps are significant discontinuities (see Chapter 4) that can be reduced by using thinner dielectric substrates. However, for higher Q, we have to use thicker substrates.

It accounts for the electrical length of the microstrip junction and the parasitic effects of the discontinuity, primarily a small shunt capacitance. The experimental characteristics of a microstrip fifth-order lowpass filter that uses a Duroid substrate ($\varepsilon = 2.2$) with thickness of 30 mil are shown in Figure 9.1(c). Insertion losses of this filter are less than 0.15 dB, VSWR is less than 1.1 in the frequency range up to 4.3 GHz, and the second harmonic ($f = 8.6$ GHz) attenuation is greater than 32 dB.

Microstrip line has a relatively low Q-factor, and if a lower loss LPF is required, higher Q transmission lines are more suitable. The layout of a stepped-impedance lowpass filter realized on a combination of microstrip and suspended striplines is shown in Figure 9.2 [11]. This design uses

series high-impedance SS inductive elements and low-impedance shunt microstrip capacitive elements. This combination of two different lines allows a very large impedance ratio and, therefore, very good stopband performance, in addition to small size. The capacitive element is formed with the ground plane metallization of the PCB bottom side under the low-impedance line. The PCB is supported in these areas by a housing pedestal [see Figure 9.2(b)]. The inductor element is realized by meander SS in order to minimize size.

The measured insertion loss and rejection characteristics are shown in Figure 9.2(c) for an 11-order LPF fabricated on a 10-mil TLE-95 (from
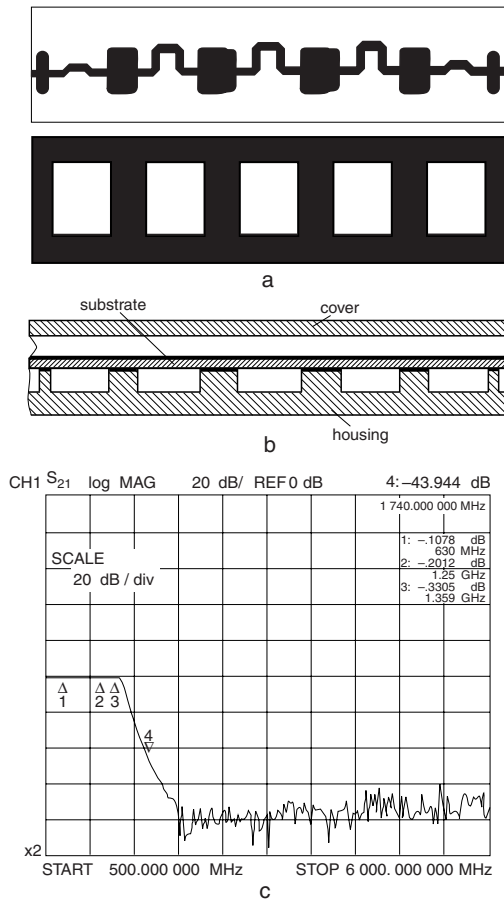
Figure 9.2. Stepped impedance microstrip-suspended stripline LPF: filter layout (top and bottom sides) (a); filter assembly (side view) (b); insertion loss frequency response (c).

"Taconic") substrate. This filter provides an insertion loss of less than 0.3 dB, a VSWR of less than 1.2 in the frequency range up to 1.1 GHz, and attenuation of more than 70 dB in the frequency range between 2.0 and 5.0 GHz.

9.3.2. Lumped-Element LPF

At lower frequencies, lumped-element LPFs are more practical. Lumped-element filters exceded distributed filters in size and spurious-free rejection characteristics. Lumped-element LPF can be realized based on lumped-element capacitors and print planar inductors (see Chapter 4). Circuit elements in this filter must be much smaller than the wavelength in the transmission line. Therefore, the application of lumped-element filters is limited by the extremely small dimensions required.

Real lumped-element filters are designed in the range of up to 2 GHz. We have to remember that at high frequencies, lumped elements have a low Q-factor, and filters have higher losses than distributed element filters. Lumped-element filters require the fabrication of high-Q inductors. Unfortunately, parasitic capacitances, as well as series resistance, limit the usefulness of lumped inductors. The performance of lumped-element filters is usually limited by the conductor loss of the inductive elements.

A miniature LPF (Figure 9.3) was designed at VHF range. This Chebyshev LPF was realized with three single-layer spiral series inductors (see Chapter 4) and four shunt ceramic capacitors. Ground connections of the shunt capacitors were achieved by built-in vias. LPF was fabricated on the G-10 dielectric substrate with a 65-mil thickness. The parasitic capacitances to ground in the spiral can be significant for filter design. Therefore, in this design there is no ground on the bottom side of the spiral inductors [see Figure 9.3(b)]. This LPF operates at a frequency of around 110 to 140 MHz, with a bandpass loss less than 0.6 dB [Figure 9.3(c)] and input and output return loss greater than 20 dB. It provides second- and third-harmonic attenuation at greater than 30 dB and 65 dB, respectively.

9.3.3. Irregular-Line LPF

Filters with irregular lines (see Chapter 3) in UHF and *L*-frequency ranges have small physical dimensions and low cost [12, 13]. One cascade of this
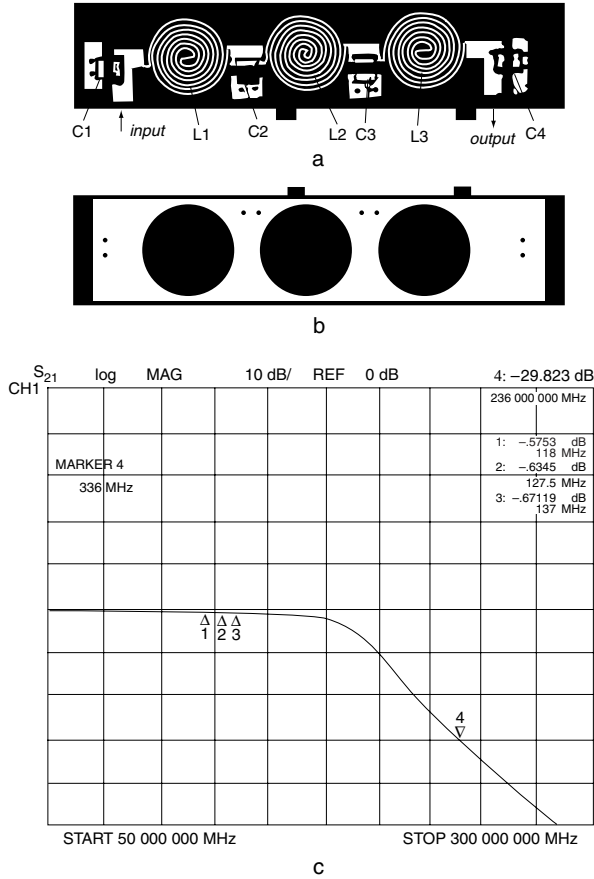
Figure 9.3. Lowpass filter with single-layer inductors: top PCB view (a); bottom PCB view (b); insertion loss frequency response (c).

filter and its classic transfer matrix $[a]$ is shown in Table 3.3, row 5. Electrical length Θ of this cascade is small; therefore, $\tan(\Theta/2) \approx \Theta/2$ (when $k_m = 0.8$–1.0), and the non-normalized classic transfer matrix becomes

$$
[a] = \begin{bmatrix} 1 & iZ\dfrac{\Theta}{2}\left(1 - k_m\right) \\[2mm] i\dfrac{\Theta}{Z} & 1 - \left(1 - k_m\right)\dfrac{\Theta^2}{4\left(1 - k_m\right)} \end{bmatrix}. \tag{9.7}
$$

The relationships between parameters Z, Θ and prototype parameters L, C are

$$\left.\begin{array}{l} Z\Theta = \omega Ll = 2\omega L_o l\left(1-k_m\right) \\ \dfrac{\Theta}{Z} = \omega Cl \end{array}\right\}, \tag{9.8}$$

where C and L are capacitance and inductance per unit length, L_0 is self-inductance per unit length of an isolated conductor of irregular lines, and l is the physical length of irregular lines.

Using (9.8), we can rewrite (9.7) as follows:

$$\left[a\right] = \begin{bmatrix} 1 & i\omega L_o l \\ i\omega Cl & 1+\left(i\omega L_o l\right)i\omega Cl \end{bmatrix}. \tag{9.9}$$

Matrix (9.9) describes the circuit of Figure 9.4(a) with parallel capacitance Cl and series inductance $L_0 l$. A lowpass filter based on irregular lines can be realized by a cascade connection of such circuits [see Figure 9.4(b)], with parameters chosen to meet the required characteristics of the prototype. This lowpass ladder network can be optimized by the known method [1]. The first step is to use the prototype ladder network of Figure 9.4(c), where parameters correspond to the required frequency characteristic of the insertion losses:

$$a = 10\log\left\{1+h^2 P^2\left(\Omega\right)\right\} \ (\text{dB}),$$

where $P(\Omega)$ is the extremum polynomial (Butterworth, Chebyshev, and so forth), $\Omega = \omega/\omega_c$ is the normalized frequency, and ω_c is the cutoff frequency.

The relationships between g_i and the real parameters of LPF are

$$g_1 = \omega_c C_1 R, \quad g_2 = \omega_c L_2 R, \quad g_3 = \omega_c C_3 R, \quad g_4 = \omega_c L_4 R \ \ ...,$$

where $C_1 = (Cl)_1$, $L_2 = (L_0 l)_2$, $C_3 = (Cl)_3$, $L_4 = (L_0 l)_4$ ...

From tabulated parameters of g_i [1], we can find elements of LPF:

$$\left(Cl\right)_1 = \dfrac{g_1}{\omega_c R}, \quad \left(L_o l\right)_2 = \dfrac{g_2 R}{\omega_c}, \quad \left(Cl\right)_3 = \dfrac{g_2}{\omega_c R}, \quad \left(L_o l\right)_4 = \dfrac{g_4 R}{\omega_c} \quad ... \tag{9.10}$$
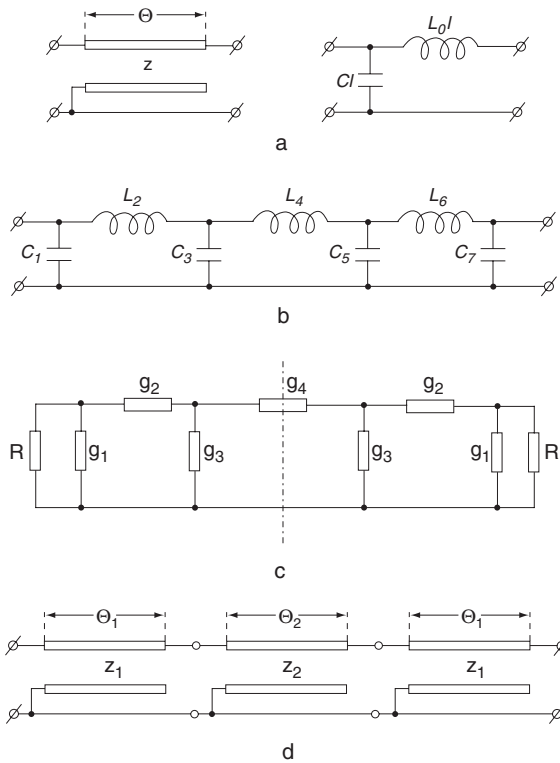
Figure 9.4. LPF with irregular lines and equivalent circuit of irregular lines with horizontal isolation of one port (a); LPF ladder network (b); prototype LPF ladder network (c); ladder LPF with irregular lines (d).

Parameters g_i are given for $\omega_c = 1$ rad/sec, $R = 1\Omega$, different values of prototype cascades n ($i = 1, 2, 3, \ldots, n$), and different values of real LPF cascades m ($j = 1, 2, 3, \ldots, m$). Relationships between Z, Θ, and Cl, Ll are

$$Z_j = \sqrt{(Ll)_j / (Cl)_j}, \quad \Theta_j = \omega\sqrt{(Ll)_j (Cl)_j}, \tag{9.11}$$

where Z_j and Θ_j are characteristic impedance and electrical length, respectively, of the jth cascade of LPF.

From (9.8), (9.10), and (9.11), we can find relationships between normalized filter parameters and parameters of the lowpass filter prototype for all cascades (except for two, which are near the axis of symmetry),

$$\frac{Z_j}{R} = \sqrt{\frac{g_{2j}}{g_{2j-1}}} \sqrt{2(1-k_m)},$$

$$\frac{\Theta_j}{\Omega} = \sqrt{g_{2j}g_{2j-1}} \sqrt{2(1-k_m)},$$

and for two cascades near the axis of symmetry,

$$\frac{Z_j}{R} = \sqrt{\frac{g_{2j}}{g_{2j-1}}} \sqrt{(1-k_m)},$$

$$\frac{\Theta_j}{\Omega} = \sqrt{g_{2j}g_{2j-1}} \sqrt{(1-k_m)}.$$

The multipliers

$$\sqrt{2(1-k_m)} \quad \text{and} \quad \sqrt{(1-k_m)}$$

influence the contraction of electrical length and the decrease of characteristic impedance. For example, if $k_m = 0.9$, the length of the irregular line cascade decreases by a factor of 2.2.

9.4. BPFs

BPFs are important components in different systems. They provide frequency selectivity and affect receiver sensitivity.

9.4.1. Integration Index

The integration quality of the BPF is characterized by the following parameters: volume V (cubed inches or cubed centimeters), minimum of dissipated losses in the bandwidth A_0 (in decibels), bandwidth ($\Delta f/f_0$) 100%, and number of sections n. The relationship between these parameters is described by the *integration index* (or *integration factor*) [6]:

$$G = \frac{V}{n}\frac{a_o}{n}\frac{\Delta f}{f_o}100 \left(dB \times cm^3\right)$$

$$= 0.061\frac{V}{n}\frac{a_o}{n}\frac{\Delta f}{f_o}100 \left(dB \times in^3\right) \qquad (9.12)$$

$$= 0.061 A_o V_1 \left(dB \times in^3\right),$$

where a_o is loss of BPF and $V_1 = V/n$ is the average volume of one BPF resonator; V is the total volume of BPF, including resonators, package, screens, heat sink out, and so forth:

$$A_o = \frac{a_o}{n}\frac{\Delta f}{f_o}100 = \frac{a_o}{n}\frac{1}{Q}100 \;\; (dB), \qquad (9.13)$$

where a_0/n is in decibels.

Parameter A_o is a function of resonator Q-factor. Figure 9.5(a) illustrates the relationship between A_o and Q-factor for Chebyshev (1) and Butterworth (2) frequency responses of BPF. For $\Delta f/f_0$ 100% = 1%, from (9.13), a_0/n can be interpreted as the average loss in the BPF resonator of 1% bandwidth. This average loss as a function of bandwidth and Q-factor are shown in Figure 9.5(b) for Chebyshev and Figure 9.5(c) for Butterworth frequency characteristics [6]. We can see that these curves are hyperbolas. The rightmost flat parts of the curves are typical characteristics of broadband elements, while the leftmost sharp parts correspond to narrowband elements, which have more losses and more sensitivity to tolerances. One of the problems of BPF design is that the passband loss is inversely proportional to the passband bandwidth.

The BPF with a minimum integration index G is the optimum filter. Parameter G and average losses for different popular BPFs at the S-band are given in Figure 9.6. All BPFs have $G > 0.1$, which indicates the limit of combining the smallest physical dimensions with the best electrical characteristics. It is important to keep in mind that the integration index varies linearly with frequency.

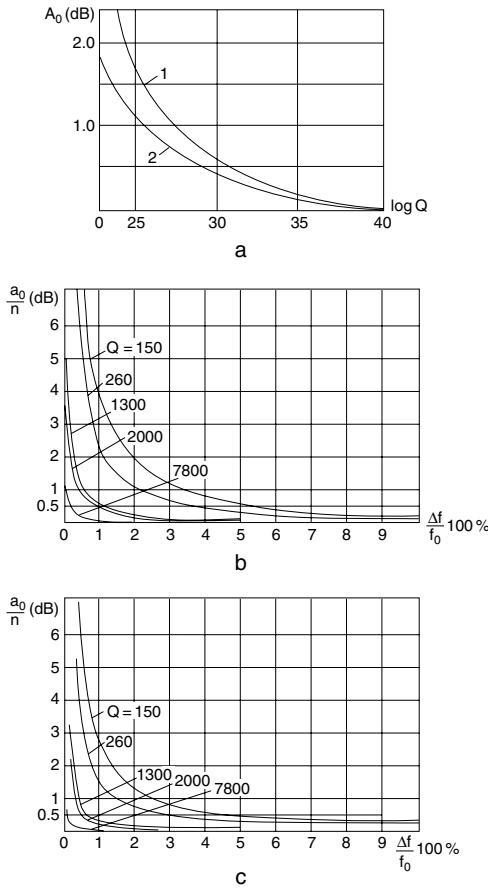Let us consider the most popular configuration of printed circuit bandpass filters and its new modifications.

Figure 9.5. Bandpass filter characteristics: relationship between losses and Q-factor for Chebyshev (1) and Batterworth (2) frequency responses (a); average losses vs. bandwidth and Q-factor for Chebyshev frequency response (b); average losses vs. bandwidth and Q-factor for Batterworth frequency response (c).

9.4.2. Parallel Coupled-Line BPF

The typical planar bandpass filter (Figure 9.7) consists of a cascade of parallel coupled half-wavelength-long printed resonators that are open circuited at both ends [1, 2, 7, 11, 12, 14–16]. The resonators are positioned parallel to each other, so that adjacent resonators are coupled along a length equal to the quarter-wavelength of the center frequency of the filter.
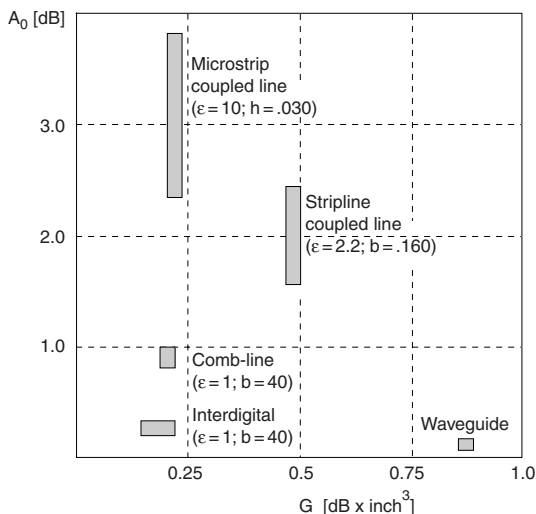
Figure 9.6. Losses and integration factor for different BPF configurations.

We have to remember that for microstrip resonators, wavelength in the line depends on ε_{eff}

$$\left(\Lambda = \lambda \Big/ \sqrt{\varepsilon_{eff}} \right),$$

which in turn varies with cross-sectional physical dimensions (W, S, h). Therefore, for resonators with different cross-sectional dimensions, the lengths will also be different. Conventional microstrip coupled resonators typically have Q on the order of 200.
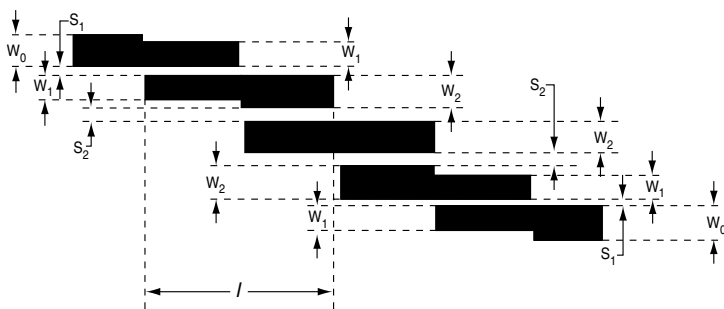

Figure 9.7. Parallel-coupled line bandpass filter.

Parallel-coupled microstrip bandpass filters are small in size and easy to fabricate due to the absence of short circuits. The disadvantages of these filters are parasitic bandwidths, the difficulty of obtaining a narrow band, and the radiation from open ends.

The open end of a strip conductor emits some radiation that can be seen as either adding to capacitance or increasing the effective length of the resonator (see Chapter 4). The open-edge effect on both ends of each resonator increases the electrical length of the resonator and decreases the operating frequency of the filter. Parasitic reactances of opened resonators can be compensated for by shortening resonator lengths by Δl_i.

Resonator length has to equal

$$l_i = l_i' - \Delta l_i,$$

where l_i' is the calculated length of the ideal resonator without radiation.

Most coupled-line filter designs involve gaps between coupled lines, which can be just several thousandths of an inch wide. Physical parameters that are critical to filter performance are coupled-line width, gaps between coupled lines, trace thickness, ground-plane spacing, and the dielectric constant of the substrate material. For example, as the bandwidth is increased, the gaps become smaller, which may increase production difficulties and the tolerance effect.

Tighter tolerances are available at a higher cost. Typical PCB on the PTFE material has etching tolerance of ±1 mil, dielectric constant ±2%, and dielectric thickness ±1 mil. Due to the functional etching tolerances, changes in resonator width produce the opposite changes in the gap. For instance, overetching a filter would typically result in narrower traces with a correspondingly wider gap between the resonators. Since characteristic impedance of coupled lines increases with decreasing line width and decreases as the gap increases (see Figure 3.4), the two effects partially compensate for each other, and the influence of etching tolerances can usually be neglected.

For BPF with a bandwidth above 5%, the spacing of the end resonators to external lines becomes very small and the etching tolerance may be significant. The dielectric constant tolerance on real substrate material has the most dramatic effect on filter performance: It shifts the filter passband, especially in narrow bandwidth circuits.

The spacing of the ground planes affects filter bandwidth and pass-band insertion loss. The tolerance of this spacing especially influences the wide bandwidth design.

Let us consider a parallel coupled-line BPF that includes $n+1$ cascade-connected two-ports. Every two-port is transformed from a four-port network with identical coupled lines with diagonal ports 2 and 3 opened [Figure 5.5(b)]. Matrices for this two-port network were given in Chapter 5. This two-port network can also be represented by a two-port with a cascade connection of two segments of transmission line with electrical length Θ and an impedance inverter with transformer coefficient k. Comparing the results of Chapter 5 and the parameters of the impedance inverter, we can obtain the following results for even-mode and odd-mode characteristic impedances of the ith cascade of BPF [1, 2, 6]:

$$
Z_{0e}^{(i)} = Z_0 \left[1 + \frac{Z_0}{k_{i-1,i}} + \left(\frac{Z_0}{k_{i-1,i}} \right)^2 \right],
$$

$$
Z_{0o}^{(i)} = Z_0 \left[1 - \frac{Z_0}{k_{i-1,i}} + \left(\frac{Z_0}{k_{i-1,i}} \right)^2 \right].
$$
(9.14)

In these equations, index i varies between $i = 1$ and $i = n + 1$. A two-port network with $n + 1$ cascades corresponds to the lowpass filter prototype with n cascades.

The relationship between (9.14) and terminating g-values of the lowpass prototype structure may be written as [2, 6]

$$
\frac{Z_0}{k_{i-1,i}} = \frac{\pi}{\omega_p} \left(\frac{f_p - f_{-p}}{f_p + f_{-p}} \right) \left(\frac{1}{g_{i-1}g_i} \right)^{1/2},
$$
(9.15)

where g-values can be defined from [1]. The g-values of the edge elements of the prototype lowpass filter are described by

$$
g_0 = \frac{\pi}{\omega_p} \left(\frac{f_p - f_{-p}}{f_p + f_{-p}} \right),
$$

$$
g_{n+1} = \frac{\pi}{k\omega_p} \left(\frac{f_p - f_{-p}}{f_p + f_{-p}} \right),
$$
(9.16)

where $k = 1$ in all cases, except for an even number of cascades in a Chebyshev LPF prototype.

Thus, we have a relationship between prototype parameters and characteristic impedances of the even and odd modes of cascaded coupled resonators. The last stage of the synthesis procedure for a BPF is calculating the physical dimensions of all coupled lines for the chosen transmission line (see Chapter 2).

Taking into account fabrication tolerances, we have to reserve a bandpass 20% greater and a bandstop 10% smaller than the specified values. Besides, the specified values of ripples in bandpass should be reduced by 50% for the Butterworth response and by 70% for the Chebyshev response. The minimum attenuation in bandstop should be increased by 20%. These corrections create a sufficient margin for meeting requirements on a filter with all possible production tolerances.

9.4.3. Wiggly Coupled-Line BPF: Useful "Zig-Zag"

There are some problems associated with the coupled-line BPF design. Theoretically, the first spurious response of a coupled-line BPF occurs at three times the center frequency. This is true in pure TEM-mode media such as stripline filters. In a practical microstrip parallel-coupled BPF, a spurious mode occurs at approximately twice the passband frequency due to the different even-mode and odd-mode propagation velocities of the coupled resonators.

The large imbalance between the effective dielectric constants and the related phase velocities for the even and odd modes can lead to some limitations in the application of microstrip coupled lines. Two methods can be used to resolve this problem: equalizing the phase velocities and providing different lengths for even and odd modes [16]. However, all of these methods increase the loss and cost and provide imperfect attenuation for higher-order modes. Also, as with many microelectronic circuit components, the required physical size of a conventional microstrip BPF limits circuit miniaturization.

The microstrip wiggly coupled-line BPF [Figure 9.8(a)] [17] improves the performance of conventional microstrip BPFs. This filter is comprised of microstrip coupled lines (1) and open-circuited microstrip lines (2). The coupled-line resonators *cd* and *ga* have physical length equal to $\Lambda_0/4$, where Λ_0 is the center-guided wavelength at the microstrip coupled lines.
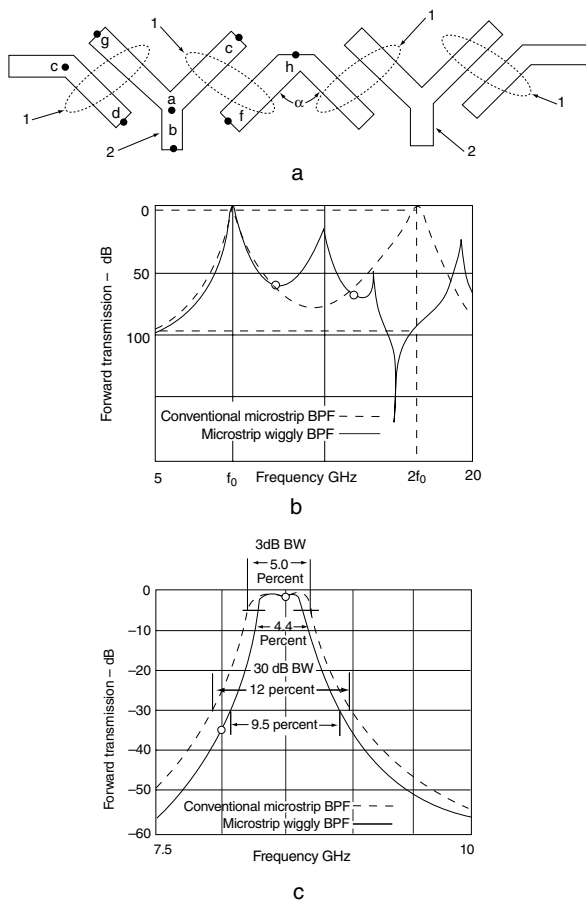
Figure 9.8. The novel microstrip wiggly coupled-line BPF: total view (a); simulation results compare the second-harmonic attenuation (b); simulation results of bandpass responses for microstrip conventional and wiggly coupled-line BPF's (c).

Generally, the banding angle, α, between different coupled resonators is substantially less than 180° to reduce the overall physical length of the filter. In many applications, this angle should be between 25° and ~100°. Angles smaller than 25° are more difficult to implement, while angles larger than 100° do not provide a length-reduction benefit for this filter.

The open-circuited line 2 is formed with a physical length equal to the guided quarter-wavelength of an input signal's second harmonic to provide good second-harmonic signal attenuation. Good third-harmonic attenuation can be realized if the physical length *ab* of open-circuited line

2 is equal to the guided quarter-wavelength of the input signal's third harmonic. The length of the open-circuited line 2 may vary, depending on the characteristics required.

The open-circuited line 2 does not significantly increase signal loss because the open-ended line input impedance is very high for the main frequency signal. Also, the open-circuited line 2 is located at the minimum EM-field position of the resonators.

For the line *cd* coupled to the line *ag*, the electrical phase, φ_1, of the signal in the open end, *d*, and the phase of radiation signal, φ_{1rad}, from the open end *d*, relative to open end *c*, can be calculated by:

$$\varphi_1 = \varphi_{1rad} = arctg \frac{2Z \sin \Theta_1 \cos \Theta_1}{\cos^2 \Theta_1 - Z \sin^2 \Theta_1} - \frac{\pi}{2},$$

where Z is the normalized impedance of the line,

$$\Theta_1 = \frac{2\pi l_1}{\Lambda}$$

is the electrical length of the line, and l_1 is the physical length of the line.

Parameter Θ_1 for the quarter-wavelength input line *cd* is equal to $\pi/2$, therefore making

$$\varphi_1 = \varphi_{1rad} = -\frac{\pi}{2}.$$

For the line *fh,* the electrical phase, φ_2, of the signal in the open end is

$$\varphi_2 = \varphi_1 = -\frac{\pi}{2}.$$

However, the phase of the radiation signal is equal to $\varphi_{2rad} = -\varphi_2 = -\varphi_{1rad}$. Therefore, resonators that contain open-circuited lines reduce free-space radiation due to the phase cancellation of fields at the ends *d* and *f*.

The total physical length of the microstrip wiggly coupled-line filter [Figure 9.8(a)] is approximately 20% less than that of a conventional coupled line filter because the half-wavelength resonators that contain open-circuited lines are banded. As discussed earlier, the reduction in length depends on the banding angle, α.

Figure 9.8(b, c) illustrates simulated frequency responses of the microstrip wiggly coupled-line four-pole BPF as compared with a con-

ventional microstrip four-pole BPF (Figure 9.7). The simulated data for the microstrip wiggly filter is signified with a solid line, while the conventional filter data is identified with a dashed line. As illustrated in Figure 9.8(b), the microstrip wiggly coupled line BPF provides significantly improved second-harmonic attenuation of 95 dB, while the conventional BPF provides second-harmonic attenuation of only 3.9 dB. Bandpass losses for the microstrip wiggly BPF are less than 2 dB [Figure 9.8(c)]. The 30-dB attenuation level of the microstrip wiggly BPF is 9.5%, as compared with 12% in the conventional filter. The 3-dB level is 4.4% using the wiggly filter, as compared with 5% for the conventional BPF.

Three different microstrip wiggly BPFs are shown in Figure 9.9. To improve frequency response, radial stubs [Figure 9.9(c)] can be used instead of regular stubs. Figure 9.9(d) illustrates comparison of frequency responses for three different microstrip wiggly coupled-line BPFs. The
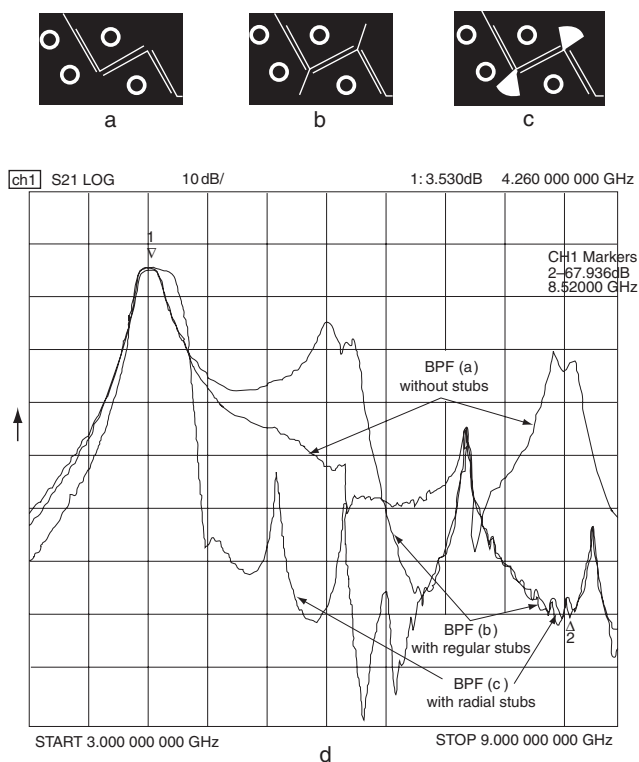
Figure 9.9. Microstrip wiggly coupled line BPFs: without stubs (a); with regular stubs (b); with radial stubs (c); experimental insertion loss frequency response for three BPFs (d).

substrate material for the filters in these experiments was TLE-95 from "Taconic" with a thickness of 0.010 in. and a dielectric constant of 2.95. Performance measurements of the microstrip filter indicated that attenuation of the second harmonics was 68 dB.

9.4.4. End-Coupled BPF

A basic end-coupled microstrip or stripline BPF [Figure 9.10(a)] [1] consists of a series of half-wavelength-long strip resonators spaced by capacitive gaps. An advantage of this filter is constant, narrow width. The long and narrow end-coupled filters can fit into a long metal housing, which has a higher cutoff frequency for undesired waveguide modes. Therefore, it is possible to build high-frequency microstrip filters. However, the end-coupled BPF becomes extremely long as the frequency is decreased. Its length is two times greater than the length of the parallel coupled filter. This may create difficulties in fabrication on hard ceramics, such as alumina. It may also lead to an increased number of defects in production due to breakage, which raises the filter's cost.

Resonators in an end-coupled BPF are close in length. The distances between the centers of the gaps are equal to:

$$l = \frac{\Lambda_0}{2} = \frac{\lambda_0}{2\sqrt{\varepsilon_{eff}}}.$$

The reactive loading of the resonators causes the electrical length of every resonator to be slightly less than $\Lambda_0/2$. This shortening increases with increasing bandwidth. The equivalent circuit of a gap was illustrated in Figure 4.1(b). The space depends on the type of transmission line, physical dimensions, and dielectric constant (see Chapter 4).

The number of resonators is calculated by (9.3) for the Chebyshev frequency response, and by (9.4) for the Butterworth response. These filters have a spurious response at $2f_0$.

An end-coupled single-layer BPF provides only a narrow bandpass. Medium-band and wideband filters require a tighter coupling. Filters based on a two-layer configuration of suspended stripline [Figure 9.10(b)] [15, 18] provide a compact structure with wide passbands. In this circuit, every resonator is replaced by a double-strip structure on the two sides of the dielectric substrate. The capacitances are formed by the coupled ends
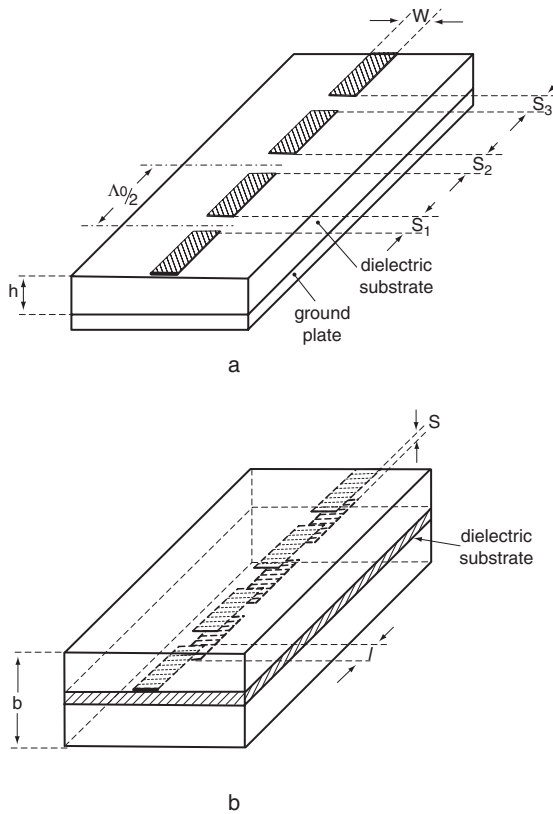
Figure 9.10. End-coupled bandpass filters: microstrip configuration (a); suspended stripline configuration (b).

of strip resonators placed on different sides of the dielectric substrate. In contrast to end-coupled BPF [Figure 9.10(a)], a wide range of coupling coefficients is possible. Therefore, this design produces compact filters with low losses in a wide passband.

9.4.5. Interdigital BPF

An interdigital filter is constructed from an array of quarter-wave long coupled lines by alternately short- and open-circuiting opposite ends of each conductor (Figure 9.11). Interdigital filters are usually designed for fixed frequencies. A typical construction is realized by stripline suspending resonators in an air-filled metal case. Microstrip interdigital filters are
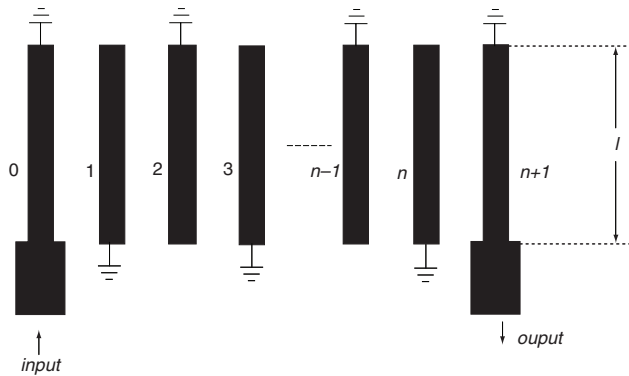
Figure 9.11. Interdigital bandpass filter.

compact, but suffer from severe asymmetry of the filter response due to the effect of coupling between nonadjacent resonators.

Coupling between resonators is realized by fringing fields. Coupled-stripline self- and mutual capacitances [1] are the starting point for the determination of the resonator widths and spacing. The mutual coupling between the resonators causes the resonator width to be less than the width of uncoupled lines. The resonator impedance should be approximately 60Ω if the input and output lines have impedances at 50Ω [19].

Interdigital filters achieve good electrical characteristics (low losses and narrow or wide passbands). The integration index of these filters is equal to $G = 0.14$–0.2 (decibel $\times$ cubed inch) at the S-band (see Figure 9.6). The bandwidth of interdigital filters can vary between 1% and 70%. The filter has the maximum attenuation in the areas of even harmonics. All interdigital filters have the nearest spurious response at $3f_0$ because the resonators are a quarter-wavelength long using the grounding.

While this type of filter construction is very solid and reliable, it is expensive due to the required machining and extremely tight tolerances. It is difficult in practice to build a shorted resonator of exactly the desired quarter guide wavelength.

9.4.6. Comb-Line BPF

Comb-line BPF [1, 7, 20–23] [Figure 9.12(a)] consists of set of parallel grounded resonators that are short-circuited at one end, with a lumped capacitance between the other end and ground. The original comb-line

C_0 C_1 C_2 C_3 C_{n-1} C_n C_{n+1}

0   1   2   3   n-1   n   n+1 l

input   output

a

W_0 W_1 W_2 W_3 W_{n-1} W_n W_{n+1}

via b

S_{01} S_{12} S_{23} $S_{n-1,n}$ $S_{n+1,n}$

b
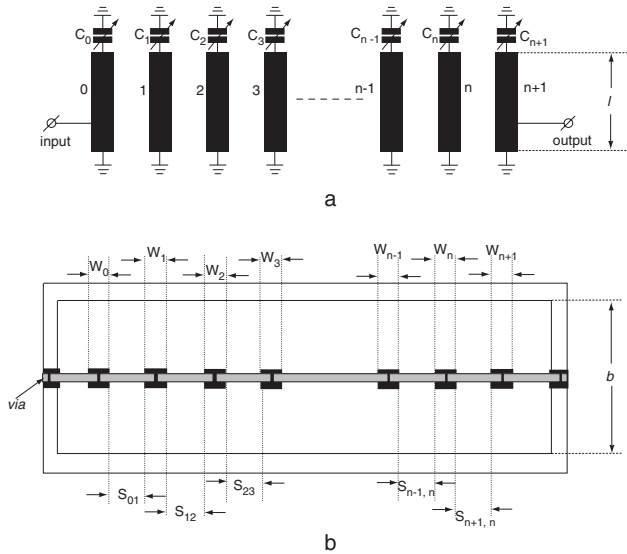
Figure 9.12. Tunable print comb-line bandpass filter: plane view (a); cross section of suspended stripline resonators (b).

filters used stab-line construction, which included machined rectangular bars or round-road center resonators between metallic ground planes. A comb-line filter with these capacitors and stab-line resonators has very low losses. However, the machined stab-line round-rod filter is expensive and large.

Progress in transmission lines and dielectric materials resulted in major advances in comb-line filter miniaturization and unit cost reduction. A comb-line filter can be realized on the different print transmission lines. SS provides high Q-factor, stability over a wide temperature range, high impedance range, and low cost (see Chapter 2). In the high-Q SS, the parallel strips are printed on both sides of the dielectric substrate in a symmetrical configuration [see Figure 9.12(b)]. Plated through-holes (vias) provide electrical connection between the top and bottom conductors.

SS resonators are placed between two parallel ground planes. Adjacent SS resonators are coupled by the fringing fields between resonators. The typical length of the comb-line filter resonators is between $l = \Lambda_0/16$ and $l = \Lambda_0/8$, where Λ_0 is the center guided wavelength at the resonator. For this resonator length, magnetic coupling predominates (see Chapter 3). The minimum practical length of the resonators is limited by a decreased Q-factor. Practical Q-factor is dependent on ground-plane spac-

ing (base), frequency, ground surface finish, plating material of PCB, and SS structure.

The short length of resonators results in a compact structure with excellent stopband performance. For example, when resonator length is $l = \Lambda_0/8$, then the second passband will appear at over four times the operating frequency, and when length $l = \Lambda_0/16$, the second passband will be located at over eight times the operating frequency. The minimum resonator length could be limited by the decrease of the unloaded Q-factor of the resonator. Comb-line filter trade offs for different resonator lengths have been described in [23].

The bandwidth of comb-line filters is a function of the ground-plane spacing, b, to the wavelength ratio (b/Λ_0) and spacing, S, between resonators. The bandwidth is greater for greater b/Λ_0 and S. A bandwidth of comb-line filters from 2% to 50% can be obtained. Positioning the resonator closer together provides wider bandwidth if necessary.

The spacing, b, between two ground planes (cover and housing) defines resonator impedances and lengths, as well as the maximum power rating and Q-factor. In practice, impedances of resonators are equal to 70 to 140Ω at frequencies $f \leq 1$ GHz. A larger base leads to higher power and Q-factor; however, it also leads to the unfavorable increase in resonator lengths and housing height.

The loading capacitance for each resonator (see Figure 9.12) is [1]

$$C_{\Sigma} = Y_i \frac{\cot \Theta_0}{\omega_0}, \tag{9.17}$$

where Y_i is the admittance of the ith resonator when $(i-1)$th and $(i+1)$th resonators are shorted, and $\Theta_0 = 2\pi l/\Lambda_0$ is the electrical length at the center frequency.

Usually, capacitors are also used to adjust for a range of center frequencies or as tunable elements to compensate for production tolerances, which becomes especially critical for narrow bandwidth. For low frequencies, the Q of capacitors is higher than the Q of resonators. However, at microwave frequencies and for greater capacitor values, the Q-factor of capacitors can be lower than that of the resonators and dominates when filter losses are calculated. Commercially available air trimmer capacitors from Johanson and Voltronics provide high Q-factor, high voltage rating, and precise mechanical tuning. The trimmer capacitor can be positioned head on to the resonator or perpendicularly to the resonator.
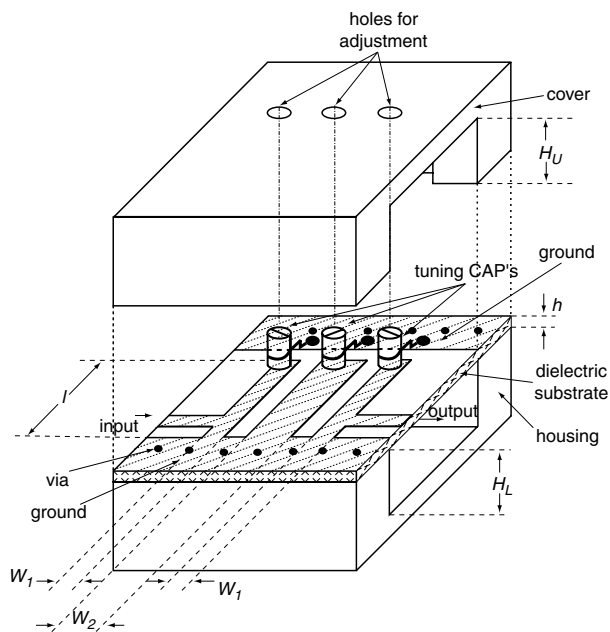
Figure 9.13. Three-pole tunable comb-line BPF with suspended stripline resonators and tuning capacitors.

Figure 9.13 shows three-pole tunable comb-line SS BPF with vertical mounted trimmer capacitors. Table 9.1 illustrates experimental results of the tunable comb-line filters with two, three, and five SS resonators hav-

TABLE 9.1. Experimental Results of the Tunable Comb-Line Filters

BPF	Two Poles	Three Poles	Five Poles
Parameters	—	—	—
Insertion loss @ 1030 MHz (dB)	1.2	2.1	3.4
Bandwidth @ 3-dB level (MHz)	41.0	29.0	25.0
Return loss (dB)	20.3	23.5	20.7
Second-harmonic rejection @ 2060 MHz (dB)	—	—	94.8
Third-harmonic rejection @ 3090 MHz (dB)	—	—	94.6

ing length Λ/12 and air trimmer capacitors Giga-Trim (Johanson) with capacitance range of 0.4 to 2.5 pF [22]. In the tuning frequency band 962 to 1213 MHz, the filter bandwidth remains approximately constant.

The comb-line filter compared with the interdigital filter is compact due to shorter resonators and is closer together. The interdigital filters have the advantages of a broad stopband, a relatively symmetrical frequency response, and greater-percentage bandwidths than their comb-line counterparts.

9.4.7. Hairpin BPF

At UHF and lower microwave frequencies, parallel-coupled BPF with half-wavelength resonators is very long. In the miniature hairpin structure (see Figure 9.14), the half-wavelength resonators are folded into a U-shape. The line between two bends tends to shorten the physical length of the coupling sections. The coupled section is less than a quarter-wavelength [24]. The reduction of the coupled-line lengths reduces the coupling between resonators.

The interdigital or comb-line filters require the grounding of resonators, leading to higher production costs. The hairpin filter does not require any ground connection. Open-circuit resonators reduce free-space radiation due to phase cancellation of fields at the ends. The radiation decreases with decreasing space between the folded lines of the hairpin (see Chapter 4). However, when this space is small, self-resonator coupling causes a decrease in filter bandwidth and in the center frequency and an increase in losses. When the space between the lines is changed, the lengths of uncoupled lines of resonators must also be changed, which affects the resonant frequencies of the resonators. A reasonable spacing is
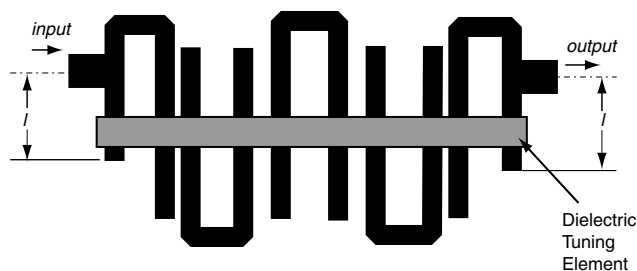
Figure 9.14. Hairpin bandpass filter.

two to three times the inter-resonator spacing, or five times the substrate thickness. Microstrip narrowband hairpin filters require quite large resonator spacing in order to achieve the desired narrowband.

The center frequency can be adjusted by the special dielectric plate (see Figure 9.14) placed near the symmetry plane. At high frequencies, there are two problems: the decrease of the length-to-width ratio (folding of resonators is difficult) and the influence of the bend discontinuities. Therefore, hairpin filters are useful for low-frequency applications.

In the microstrip hairpin BPF, a spurious mode occurs at approximately twice the passband frequency due to the different even- and odd-mode propagation velocities of coupled resonators. To resove this problem, the length l (see Figure 9.14) of the input/output lines should be approximately $\Lambda_0/8$.

REFERENCES

1. Matthaei, G. L., L. Young, and E. M. T. Jones, *Microwave Filters, Impedance Matching Networks and Coupling Structures*, New York: McGraw-Hill, 1964.
2. Cohn, S., "Parallel-Coupled Transmission-Line Resonator Filters," *IRE Trans. Microwave Theory Tech.*, Vol. MTT-6, April 1958, pp. 223–231.
3. Zverev, A. I., *Handbook of Filter Synthesis*, New York: John Wiley & Sons, 1967.
4. Young, L., *Microstrip Filters Using Parallel Coupled Lines,* Dedham, MA: Artech House, 1972.
5. Mongia, R., et al., *RF and Microwave Coupled-Line Circuits,* Norwood, MA: Artech House, 1999.
6. Mazepova, O. I., et al., *Stripline Elements Handbook*, Moscow, Russia: Sviaz, 1979.
7. Helszajn, J., *Microwave Planar Passive Circuits and Filters,* New York: John Wiley & Sons, 1994.
8. Hunter, I., *Theory and Design of Microwave Filters,* New York: The Institute of Electrical Engineers, 2001.
9. Hong, J.-S., and M. J. Lancaster, *Microstrip Filters for RF/Microwave Applications,* New York: Wiley-Interscience, 2001.

10. Feldshtein, A. L., and L. R. Yavich, *Synthesis of Microwave Two-Ports and Four-Ports,* Moscow, Russia: Svyaz, 1965.

11. Maloratsky, L. G., "Reviewing the Basics of Suspended Striplines," *Microwave Journal,* October 2002, pp. 82–90.

12. Maloratsky, L. G., "Design Regular- and Irregular-Print Coupled Lines," *Microwave & RF,* September 2000, pp. 97–106.

13. Zelyah, E. V., et al., *UHF and VHF Miniature Devices*, Moscow, Russia: Radio and Svyaz, 1989.

14. Maloratsky, L. G., and L. R. Yavich, *Design and Calculation Microwave Stripline Elements*, Moscow, Russia: Soviet Radio, 1972.

15. Maloratsky, L. G., *Microminiaturization of Microwave Elements and Devices*, Moscow, Russia: Soviet Radio, 1976.

16. Riddle, A., "High Performance Parallel Coupled Microstrip Filters," *IEEE MTT-S Digest,* 1988, pp. 427–430.

17. Maloratsky, L. G., "Improve BPF Performance with Wiggly Coupled Lines," *Microwave & RF*, April 2002, pp. 53–62.

18. Sturdivant, R., "A Capacitively Coupled BPF Design Using a Suspended Substrate Stripline," *Microwave Journal*, November 1993, pp. 71–74.

19. Rhea, R. W., *HF Filter Design and Computer Simulation*, Atlanta, GA: Noble Publishing, 1994.

20. Matthaei, G. L., "Comb-Line Band-Pass Filter of Narrow or Moderate Bandwidth," *Microwave Journal,* August 1964, pp. 428–439.

21. Kurzrok, R. M., "Tunable Comb-Line Filter Using 60 Degree Resonators," *Applied Microwave & Wireless,* Vol. 12, November 2000, pp. 98–100.

22. Maloratsky, L. G., "Assemble a Tunable *L*-Band Preselector," *Microwave & RF*, September 2003, pp. 80–88.

23. Wenzel, R. J., "Synthesis of Combline and Capacitively Loaded Interdigital Filters of Arbitrary Bandwidth," *IEEE Trans. on MTT-19,* August 1971, pp. 678–686.

24. Gysel, U. H., "New Theory and Design for Hairpin-Line Filters," *IEEE Trans. Microwave Theory Tech.*, Vol. MTT-22, May 1974.

This Page Intentionally Left Blank

CHAPTER 10

Diode Control Devices

10.1. PIN DIODE PARAMETERS

Diode control devices (switches, attenuators, and limiters) utilize PIN diodes. A PIN diode is a semiconductor device that operates as a variable resistor at RF and microwave frequencies. Equivalent circuits of a PIN diode for reverse and forward biases are shown in Figure 10.1 [1–6]. In these circuits,

- R_F is the series resistance under forward bias.
- C_j is the junction capacitance.
- L_P is the package inductance.
- C_P is the package capacitance.
- R_R is the parallel resistance at zero or reverse bias.

    With reverse bias, the PIN diode exhibits very high resistance, but when forward bias is applied across the PIN diode, resistance is very low. It makes the PIN diode attractive for switches and attenuators.
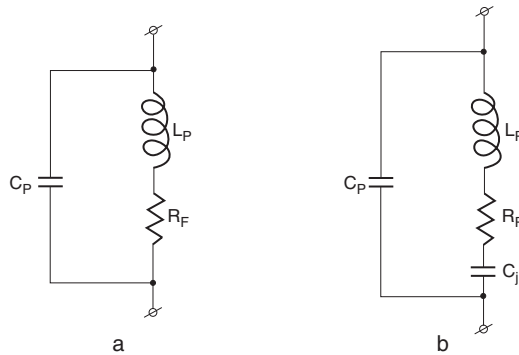
Figure 10.1. Equivalent PIN diode circuits for forward (a) and reverse (b) biases.

The frequency at which the reactance of C_j is numerically equal to the geometric mean of the forward and reverse resistance is

$$f_c = \frac{1}{2\pi C_j \sqrt{R_F R_R}}.$$

(10.1)

This cutoff frequency determines diode efficiency for switch devices. Diode capacitance limits signal control circuit performance at high frequencies. For good linearity and low distortion, the minimum signal frequency should be $10 \times f_c$. At frequencies below f_c, the PIN diode rectifies the signal like a simple PN junction diode. Typically, f_c can be in the range of 0.05 MHz to 30 MHz.

Another parameter of a diode is the *diode quality factor* [7]:

$$K = \frac{\sqrt{A_{iso}} - 1}{\sqrt{A_{ins}} - 1} = \left(\frac{f_c}{f}\right)^2,$$

(10.2)

where

$$A_{iso} = 10^{a_{iso}/10}, \; a_{iso}$$

is the diode isolation in decibels;

$$A_{ins} = 10^{a_{ins}/10}, \; a_{ins}$$

is the diode insertion loss in decibels;

f is the operating frequency; and A_{iso} and A_{ins} are attenuations (not a decibel notation) numerical ratios of input to output power. The diode quality factor decreases with increasing frequency.

The maximum RF power that a PIN diode can handle is limited by two factors. The first is the power dissipation capability that is determined by the maximum junction temperature (at which the device can operate with full reliability) and the thermal resistance of the diode and packaging. The second factor is the breakdown voltage that the device can be subjected to without causing damage to the junction. The amount of maximum RF power is usually much larger than the power dissipation in the diode because PIN diodes are usually operated in a reflective mode. The breakdown voltage of PIN diodes must exceed the value of reverse bias plus twice the peak RF voltage to prevent nonlinear loss.

Another important PIN diode parameter is the *switching time*. The switching time of a PIN diode is determined by the characteristics of the diode and by the bias wave forms supplied to the diode. The transition for the PIN diode from nonconduction to conduction is bounded by the transit time of a charge carrier across the diode's *I*-layer thickness. Reverse-to-forward switching time, T_{RF}, decreases as the forward current, I_F, increases it.

The transition for the PIN diode from conduction to nonconduction is determined by the amount of charge that is stored in the PIN diode's *I*-layer and by the rate at which this charge is removed. This transition time, T_{FR}, is approximated by

$$T_{FR} \approx \tau \ln\left(1 + \frac{I_F}{I_R}\right) \text{ (sec),}$$

where τ is the diode minority carrier lifetime, and I_R is the peak reverse-bias current (immediately following the bias polarity change).

Real PIN diode-switching speed from one position to another is in the range of 5 ns to a few microseconds. They are faster than ferrite switches and electromechanical switches, which take from 20 ms to 100 ms to switch.

The PIN diode is a nonlinear element, so it will generate harmonics, intermodulation, and cross-modulation distortion in switching circuits. In order to minimize intermodulation distortion, the carrier lifetime of the diode must be much longer than the period of the lowest operating

frequency. For some applications we have to specify the required distortion [8].

10.2. SWITCHES

10.2.1. Classification

Switches can be classified according to seven types of characteristics:

1. Number of input/output channels:
   - Single-pole, single-throw (SPST),
   - Single-pole, double-throw (SPDT),
   - Double-pole, double-throw (DPDT),
   - Multithrow;
2. Type of connection with the transmission line:
   - Series,
   - Shunt,
   - Series-shunt,
   - Tee,
   - Stub;
3. Number of stages;
   - Single (one stage),
   - Two stages;
4. Maximum power:
   - Low,
   - High;
5. Input matching in the isolated state:
   - Reflective,
   - Nonreflective;
6. Configuration of elements:
   - Lumped elements,
   - Distributed elements,
   - Combination of lumped and distributed elements;
7. Bandwidth:
   - Narrowband,
   - Broadband.
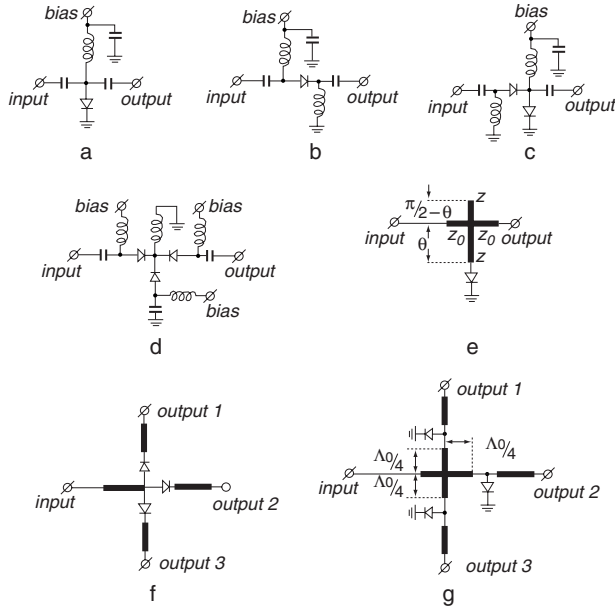
Figure 10.2. Basic configurations of switches: SPST shunt (a); SPST series (b); SPST series-shunt (c); SPST TEE stub (d); SPST stub (e); SP3T series (f); SP3T shunt (g).

10.2.2. Basic Configurations

Basic configurations of PIN diode switches are shown in Figure 10.2. The main equations for different switches in Figure 10.2 are given in Table 10.1 [9].

Let us consider the simplest shunt SPST switch [Figure 10.2(a)] that can be represented by parallel complex diode normalized admittance $Y = G + iB$. From Appendix C (Table C.3), the scattering matrix coefficients of this circuit are

$$S_{11} = \frac{-Y}{2+Y}, \qquad S_{21} = \frac{2}{2+Y}. \tag{10.3}$$

Attenuation (insertion loss) in the circuit of Figure 10.2(a) is

$$A = |T_{11}|^2 = \frac{1}{|S_{21}|^2} = \left(1 + \frac{Y}{2}\right)^2. \tag{10.4}$$

TABLE 10.1. Isolation and Insertion Loss for Different Types of PIN Diode Switches

Type of Circuit	Isolation (dB)	Insertion Loss (dB)
Series	$10\log\left[1+\left(\dfrac{X_c}{2z_0}\right)^2\right]$	$20\log\left[1+\dfrac{R_F}{2z_0}\right]$
Shunt	$20\log\left[1+\dfrac{z_0}{2R_F}\right]$	$10\log\left[1+\left(\dfrac{z_0}{2X_c}\right)^2\right]$
Series-shunt	$10\log\left[\left(1+\dfrac{z_0}{2R_F}\right)^2+\left(\dfrac{X_c}{2z_0}\right)^2\left(1+\dfrac{z_0}{R_F}\right)^2\right]$	$10\log\left[\left(1+\dfrac{R_F}{2z_0}\right)^2+\left(\dfrac{z_0+R_F}{2X_C}\right)^2\right]$
Tee	$10\log\left[1+\left(\dfrac{X_c}{z_0}\right)^2\right]+10\log\left[\left(1+\dfrac{z_0}{2R_F}\right)^2+\left(\dfrac{X_c}{2R_F}\right)^2\right]$	$20\log\left[1+\dfrac{R_F}{z_0}\right]+10\log\left[1+\left(\dfrac{z_0+R_F}{2X_c}\right)^2\right]$

Therefore,

$$1 + \frac{Y}{2} = \sqrt{A}$$

or

$$Y = 2\left(\sqrt{A} - 1\right). \tag{10.5}$$

The admittance Y varies as the bias on the diode is varied. Microwave power incident on the switch is reflected back and is partly dissipated in the PIN diode. As can be seen from (10.4), the attenuation does not depend on frequency and is a function of the normalized diode admittance. However, when a real diode is used, the attenuation is frequency-dependent because a real diode contains reactance elements (see Figure 10.1).

According to the principle of the conservation of energy, the normalized dissipated power [from (10.3)] is

$$A_{dis} = \frac{P_{dis}}{P_{in}} = 1 - |S_{11}|^2 - |S_{21}|^2 = \frac{4Y}{(2+Y)^2}. \tag{10.6}$$

where P_{in} is the incident power.

Dissipated losses are

$$a_{dis} = 20 \log \frac{2\sqrt{Y}}{2+Y} \ (\text{dB}). \tag{10.7}$$

Figure 10.3 shows the plot of power distribution versus resistance R_F (for $B \ll 1$) in a shunt SPST single diode switch where (P_{dis}/P_{in}) is the normalized dissipated power, (P_{ref}/P_{in}) is the normalized reflected power, and (P_{out}/P_{in}) is the normalized output power. The dissipated power will be at its maximum (50%) when the normalized resistance $R_F = (1/G) = 0.5$. For example, for a 50Ω input line, maximum dissipated power will occur when R_F is equal to 25Ω.

From (10.5) and (10.6), the normalized dissipated power is

$$A_{dis} = \frac{2\left(\sqrt{A} - 1\right)}{A}. \tag{10.8}$$
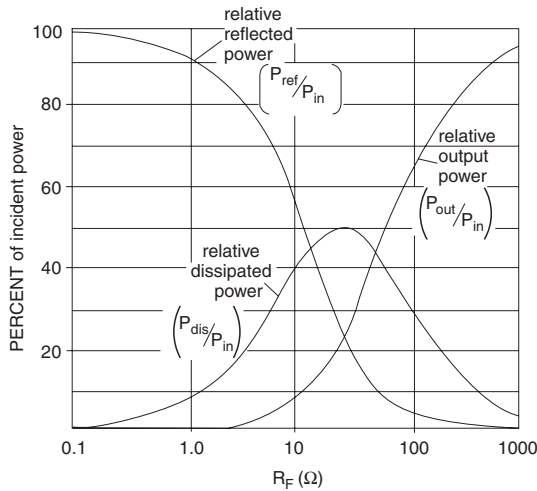
Figure 10.3. Power distribution in a shunt SPST single diode switch as a function of R_F.

Let us consider two different states of this SPST switch. In the ON state, when the diode is zero or reverse biased, we have $Y = G << 1$. From (10.6), we have

$$A_{dis} = \frac{P_{dis}}{P_{in}} \approx G, \qquad (10.9)$$

and from Appendix C, we have

$$|\Gamma|^2 = |S_{11}|^2 \approx \frac{G^2}{4}. \qquad (10.10)$$

According to (10.4),

$$A \approx 1 + G. \qquad (10.11)$$

Therefore, in the ON state from (10.9) and (10.10), for $Y = Y_R << 1$, we obtain

$$|\Gamma|^2 << A_{dis}.$$

This means that for the above conditions, the dissipated power is much greater than the reflected power (see also the right-side region of the plot in Figure 10.3).

Using the same procedure, we can get relationships for the OFF state when the diode is forward biased ($Y = G \gg 1$) (left side of Figure 10.3). In this case, the reflected power is much higher than the dissipated power; therefore [see (10.6)], the isolation is

$$A_{iso} \approx \frac{G^2}{4},$$

$$a_{iso} = 10 \log A_{iso} = 10 \log \frac{G^2}{4} \quad \text{(dB)}. \tag{10.12}$$

In this full reflection mode, return loss (RL) may be computed from the following equation:

$$RL = -20 \log \left| \frac{1}{2R_F/z_0 + 1} \right| \text{(dB)},$$

where z_0 is the impedance of the input line. The full reflection mode of the shunt switch can be used in phase shifters (Chapter 11).

Let us consider the series SPST single diode switch [Figure 10.2(b)]. In the ON state when the diode is forward biased, the equivalent circuit represents a low series resistance R_F. In this case, insertion loss is a function of the diode resistance. In the OFF state, the diode is at zero or reverse biased, and it presents a high series impedance. In this state, maximum isolation depends on the capacitance of the PIN diode.

From Appendix C, for a series configuration, coefficients of the scattering matrix become

$$S_{11} = \frac{Z}{Z+2}, \qquad S_{21} = \frac{2}{Z+2}. \tag{10.13}$$

The attenuation in this switch [Figure 10.2(b)] is

$$A = \frac{1}{|S_{21}|^2} = \left(\frac{Z+2}{2}\right)^2 .$$

(10.14)

Therefore,

$$\frac{Z+2}{2} = \sqrt{A}$$

or

$$Z = 2\left(\sqrt{A} - 1\right).$$

(10.15)

According to the principle of the conservation of energy [(5.8) and (10.13)], the normalized dissipated power is

$$A_{dis} = \frac{P_{dis}}{P_{in}} = \frac{4Z}{(Z+2)^2},$$

(10.16)

and dissipated losses are

$$a_{dis} = -20\log \frac{2\sqrt{Z}}{Z+2} (\text{dB}).$$

(10.17)

From (10.15) and (10.16), we can obtain:

$$A_{dis} = \frac{2\left(\sqrt{A} - 1\right)}{A}.$$

(10.18)

This equation is the same as (10.8) for the shunt configuration. The shunt diode switches are commonly used for devices with high isolation and are capable of handling higher power because heat dissipation in a shunt diode (which has one grounded end) is much better than for a diode in a series-type switch due to good heat sinking. The series diode switches are commonly used in broadband circuits.

The series-shunt configuration [Figure 10.2(c)] of the switch provides the ON state when the series diode has a low impedance and the shunt diode has a high impedance. In the OFF state, the series diode has a high

impedance and the shunt diode has a low impedance. Formulas for the isolation and the insertion loss of series-shunt configuration are given in Table 10.1.

A comparison of shunt, series, and series-shunt configurations shows that the isolation of a series-shunt switch is more than twice (in decibels) that for a series or shunt switch. A series-shunt configuration requires a bias current from both positive and negative sources. This would significantly increase dc power dissipation.

A *TEE-configuration* switch is shown in Figure 10.2(d), and equations for the isolation and the insertion loss are given in Table 10.1. In the ON state of the switch, the two series diodes are in the low-impedance state and the shunt diode is in the high-impedance state. In the OFF state the series diodes are in the high-impedance state, and the shunt diode is in the low-impedance state.

In a *stub circuit* [see Figure 10.2(e)], the PIN diode is connected with the main transmission line through the transforming stub with characteristic impedance z and electrical length $\Theta \leq \pi/2$. In the OFF state of the switch, the diode has a high impedance, which transforms (through the stub) to the junction as the high active conductivity. In the ON state of the switch, input capacitance appears in the junction area. This capacitance can be compensated for by an additional open-circuited stub [see Figure 10.2(e)]. The electrical length of this stub should be equal to $\pi/2 - \Theta$, and the sum of the electrical lengths of the two stubs should be $\pi/2$.

Multithrow switches can be of series, shunt, or series-shunt configuration. Figure 10.2(f) shows a single pole, three-throw (SP3T) switch using series-mounted diodes. This configuration is useful for design of wideband switches. Figure 10.2(g) illustrates SP3T switch using shunt-mounted diodes. In the shunt configuration, the shunt diodes must be mounted a quarter-wavelength from the common junction to minimize reactive loading of the open port by the closed port. Therefore, the bandwidth of the SP3T switch is limited. The series SP3T switch can control less power than one using shunt diodes.

10.2.3. Multiple-Diode Switch

Multiple-diode switches can be used when the maximum isolation requirements are greater than what can be obtained by the above basic circuit configurations. A simple connection of two diodes with a zero dis-
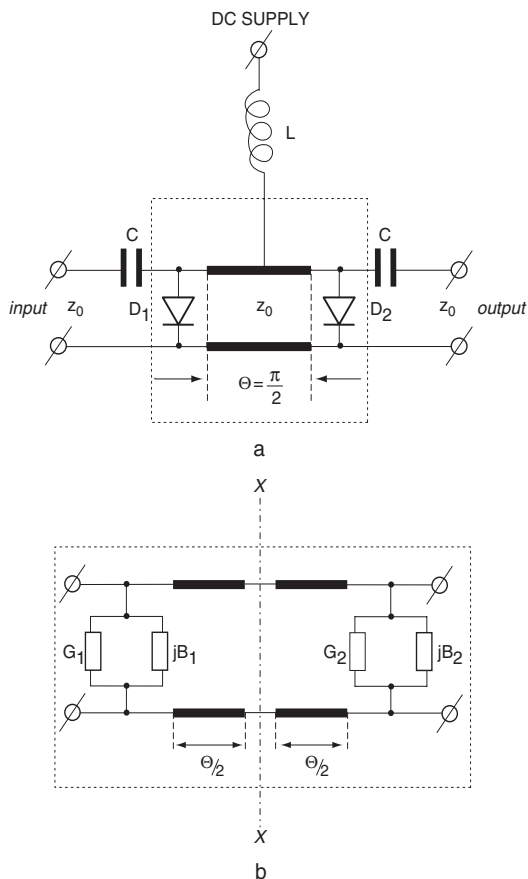
Figure 10.4. Two-diode shunt-iterated SPST switch: schematic (a); equivalent circuit (b).

tance between them will only increase the attenuation by a maximum 6 dB (as compared with the isolation of a single diode) and will increase the insertion loss. However, if diodes are spaced at approximately quarter-wavelength intervals, as shown in Figure 10.4, the overall attenuation can be increased, and the insertion loss may also decrease.

Figure 10.4 illustrates a two-diode shunt-iterated SPST switch and its equivalent circuit. Transfer matrix [T] of this equivalent circuit is the product of the individual matrices (see Appendix C) of the shunt element Y_1 (first diode susceptance for diode OFF or admittance for diode ON), of the uniform line with electrical length $\Theta = 2\pi l/\Lambda_0$, and of the shunt

element Y_2 (second diode susceptance for diode OFF or admittance for diode ON):

$$[T] = [T]_I [T]_{II} [T]_{III} \qquad (10.19)$$

$$= \frac{1}{4} \begin{bmatrix} 2+Y_1 & Y_1 \\ -Y_1 & 2-Y_1 \end{bmatrix} \begin{bmatrix} e^{i\Theta} & 0 \\ 0 & e^{-i\Theta} \end{bmatrix} \begin{bmatrix} 2+Y_2 & Y_2 \\ -Y_2 & 2-Y_2 \end{bmatrix}$$

$$= \frac{1}{4} \begin{bmatrix} (2+Y_1)(2+Y_2)e^{i\Theta} - Y_1 Y_2 e^{-i\Theta} & \vdots & Y_2(2+Y_1)e^{i\Theta} + Y_1(2-Y_2)e^{-i\Theta} \\ -Y_1(2+Y_2)e^{i\Theta} - Y_2(2-Y_1)e^{-i\Theta} & \vdots & -Y_1 Y_2 e^{i\Theta} + (2-Y_1)(2-Y_2)e^{-i\Theta} \end{bmatrix}$$

For diode OFF,

$$Y_1 = z_0 i\omega C_{j1}, \ Y_2 = z_0 i\omega C_{j2};$$

for diode ON,

$$Y_1 = \frac{z_0}{R_{F1}}, \quad Y_2 = \frac{z_0}{R_{F2}};$$

z_0 is impedance of input/output lines and the transmission line between diodes.

For diodes OFF, the ideal matching condition is

$$|S_{11}| = \left| \frac{T_{21}}{T_{11}} \right| = 0, \quad |T_{21}| = 0.$$

From (10.19), we obtain

$$|T_{21}| = \left| \frac{1}{4} \left[Y_1(2+Y_2)e^{i\Theta} + Y_2(2-Y_1)e^{-i\Theta} \right] \right| = 0. \qquad (10.20)$$

From (10.20), we can obtain the ideal matching condition:

$$\Theta = \tan^{-1} \frac{Y_1 + Y_2}{Y_2 - Y_1 Y_2 - Y_1}. \qquad (10.21)$$

For identical diodes ($Y_1 = Y_2 = Y$),

$$\Theta = \tan^{-1}\left(\frac{2}{Y}\right). \tag{10.22}$$

For real PIN diodes with $C_j \neq 0$, there is an additional phase shift of the propagation wave in the switch. In this case, the optimum spacing between diodes that provides the minimum insertion loss should be less than a quarter-wavelength ($\Theta < 90°$). This spacing depends on C_j and the operating frequency. In other words, it is possible to compensate for the parasitic capacitance C_j by correction of the spacing between diodes. For example, for two diodes with $C_j = 1$ pF at frequency 1 GHz, optimum spacing is $81°$ ($l/\Lambda_0 = 0.225$). The insertion loss of the shunt diode switch also may be reduced by making the dc high-impedance conductor length shorter than $\Lambda_0/4$ to realize the parallel resonance of this equivalent inductance and the diode junction capacitance.

Using (10.19) for the ON diode mode (when $Y = 1/R_F$), we find the relationships between the isolation of the two-diode shunt-iterated switch and both the spacing between PIN diodes and resistance of the diodes under forward bias:

$$a_{iso} = 20\log\frac{1}{|S_{21}|}\,(\text{dB}) = 20\log|T_{11}|\,(\text{dB})$$

$$= 20\log\frac{1}{4}\left|(2+Y_1)(2+Y_2)e^{i\Theta} - Y_1 Y_2 e^{-i\Theta}\right|\,(\text{dB}).$$

For identical diodes with $R_{F1} = R_{F2} = R_F$ (or $Y_1 = Y_2 = Y$), we obtain

$$a_{iso} = 20\log\frac{1}{4}\left|(2+Y)^2 e^{i\Theta} - Y^2 e^{-i\Theta}\right|\,(\text{dB})$$

$$= 10\log\left|\frac{Y^4}{4}\sin^2\Theta + Y^3\sin^3\Theta + Y^2\sin^2\Theta + Y^2 + 2Y + 1\right|\,(\text{dB}). \tag{10.23}$$

The maximum isolation occurs at the spacing of $l = \Lambda_0/4$ ($\Theta = \pi/2$). For this spacing, from (10.23), we obtain

$$a_{iso} \approx 10\log\frac{Y^4}{4} = 10\log\frac{Y^2}{4} + 10\log\frac{Y^2}{4} + 10\log 4\,(\text{dB}).$$

For $R_F = 1/Y << z_o$, isolation is

$$a_{iso} \approx 10\log\frac{Y^4}{4} = 10\log\frac{Y^2}{4} + 10\log\frac{Y^2}{4} + 10\log 4 \text{ (dB)}. \qquad (10.24)$$

Comparing (10.24) with (10.12), we can see that the isolation of the two shunt-iterated diodes separated by a spacing of $l = \Lambda_0/4$ is double that of a single device, plus 6 dB [10 log 4 (dB)] extra. The isolation of the n-diode shunt-iterated SPST switch is

$$a_{iso} = n10\log\frac{Y^2}{4} + (n-1)6 \text{ (dB)}. \qquad (10.25)$$

Figure 10.5 illustrates the frequency response of the isolation in a very broad frequency range [10]. The characteristics are given for two, three, and four series-iterated diodes with the spacing of $l = \Lambda_0/4$, frequency 10 GHz, characteristic impedance of 50Ω and $C_j = 0.03$ pF. In the low-frequency range, the isolation depends on the frequency characteristic of C_j. The influence of spacing variation here is less than that at high frequencies. At extremely low frequencies, spacing $l << \Lambda_0$ and the switch looks like a cascade connection of series-iterated diodes with no spacing between them. In this region, the isolation depends on R_R.

The multiple-diode switch can be reflective or nonreflective. The reflective switch reflects incident power back to the source when in the isolated state. In the nonreflective switch (or "matched switch"), input and output shunt diodes connect in series with resistors. Resistor value is equal to impedance of input/output lines. These resistors provide absorption of the RF energy when the switch in the isolated state. In this circuit, the maximum RF power is limited to the power dissipation capabilities of the resistor. Compromise between maximum dissipation power and input matching is possible when the resistor value is different from the switch input/output impedance.

10.2.4. Transmit-Receive Switch

An SPDT transmit-receive TX/RCV antenna switch is a network used in transceiver applications whose function is to connect the single antenna to the transmitter in the transmit mode and to the receiver in the receive mode. The circuit of the TX/RCV switch consists of a PIN diode D_1 con-
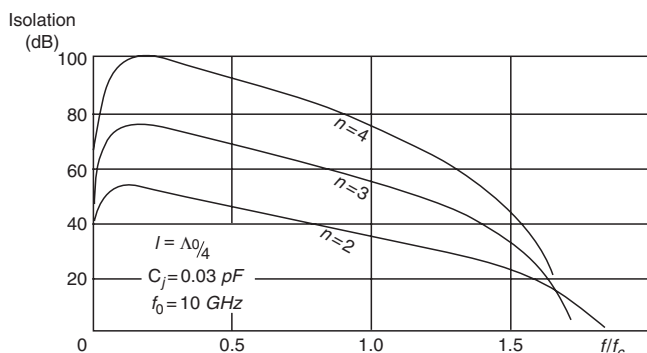
Figure 10.5. Isolation vs. frequency for two-, three-, and four-diode series-iterated switches with spacing $\Lambda_0/4$ at frequency 10 GHz.

nected in series with the transmitter and a shunt PIN diode D_2 placed a quarter-wavelength away from the TX/RCV antenna in the direction of the receiver section [see Figure 10.6(a)]. When the switch is in the transmit mode, each diode becomes forward biased. The series diode appears as a low impedance to the signal heading toward the antenna, and the shunt diode effectively shorts antenna terminals of the receiver to prevent overloading. In receive mode, the quarter-wavelength section (with characteristic impedance z) transforms the short circuit formed by the shunt diode into an open circuit at the common junction. This section narrows the bandwidth to approximately 20%. The OFF transmitter is isolated from the antenna by the high capacitive reactance of the series diode.

The insertion loss of the transmitter and the isolation of the receiver depend on the diode resistance. In order to protect the receiver from high power, a high transmitter isolation (more than 20 dB) is required, but in receive mode such high isolation is not necessary. In this circuit, both transmitter insertion loss and receiver isolation depend on the forward resistance, R_F, of the diode employed. In the narrowband, greater than 30-dB isolation and less than 0.3-dB insertion loss can be expected for a diode R_F at 1.0Ω or less. To minimize insertion loss in the receiver port, the distance from the series diode D_1 to the common junction should be at the absolute minimum.

At VHF, UHF, and the *L*-band, in order to save board space, the quarter-wavelength section can be realized by an equivalent lumped-element π-circuit (see Figure 8.10). Figure 10.6(b) shows a switch configuration that consists of two PIN diodes and a lumped π-circuit (equivalent to a
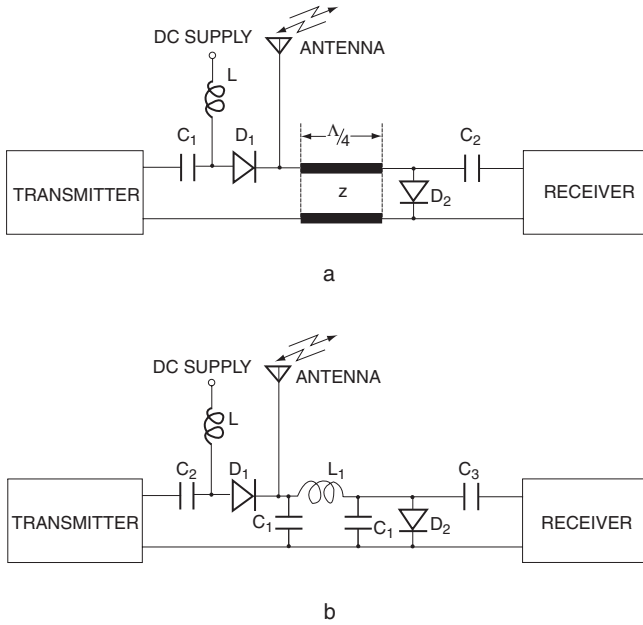
Figure 10.6. Transmit-receive switch: with quarter-wavelength section (a); with lumped element π-section (b).

quarter-wavelength transmission line section with impedance z). The π-circuit has parameters

$$L_1 = \frac{z}{2\pi f_0}, \quad C_1 = \frac{1}{z 2\pi f_0}.$$

10.3. ATTENUATORS

Analog and digital attenuators can be built using PIN diodes. A PIN diode acts as a variable resistor controlled by dc current. The main difference between an attenuator and a switch is that in a switch attenuation changes abruptly between the two levels a_{ins} and a_{iso}, while in an attenuator the change is continuous. Linearity of resistance with bias makes the PIN diodes attractive for attenuation applications. Digital attenuators can provide a linear attenuation versus a digital step.

A variable attenuator is characterized by attenuation range, return loss, attenuation flatness, frequency range, and input power. Attenuators can be reflective or nonreflective.

10.3.1. Reflective Attenuators

The insertion loss (attenuation) for different circuits is given in Table 10.1. Attenuation is achieved by reflection and partly by dissipation in the PIN diode. As can be seen, the attenuation is not dependent on frequency and is a function of the ratio of the transmission line impedance to the diode resistance. Real diodes have reactance elements (see Figure 10.1); therefore, the attenuation characteristics become frequency dependent. For some applications the poor matching at the input/output of reflective attenuators cannot be tolerated. For these cases, nonreflective attenuators can be built.

10.3.2. Nonreflective Attenuators

The basic circuits of nonreflective (absorptive) diode attenuators are shown in Figure 10.7. In the bridged TEE-attenuator circuit [Figure 10.7(a)], the required attenuation is provided by absorbing RF power in the PIN diodes D_1 and D_2. PIN diodes are used as current controlled variable resistors. The design equations of this attenuator are

$$a = 20\log\left(1 + \frac{z_0}{R_{F1}}\right)\ (\text{dB}),$$

$$z_0^2 = R_{F1}R_{F2}\ (\Omega^2),$$

where R_{F1} and R_{F2} are resistances of the two diodes with the forward bias. The resistances of the two series resistors [Figure 10.7(a)] are equal to the input/output characteristic impedances z_0.

The π-attenuator circuit is shown in Figure 10.7(b). The design equations of this circuit are

$$a = 20 \log \left(\frac{R_{F1} + z_0}{R_{F1} - z_0} \right) \text{ (dB),}$$

$$R_{F1} = R_{F2} \text{ (}\Omega\text{),}$$

$$R_{F3} = \frac{2 R_{F1} z_0^2}{R_{F1}^2 - z_0^2} \text{ (}\Omega\text{).}$$

Unlike the bridged TEE-attenuator, the π-attenuator has a rather complicated bias network (two different biases). Both lumped-element structures are very compact and are used at relatively low frequencies up to 1 GHz. Also, in these circuits the impedances at both RF ports remain constant, while the overall attenuation can be varied over a range of less than 1 dB to greater than 20 dB.

Nonreflective distributed attenuators are useful in the microwave frequency range. Figure 10.7(c, d) illustrates some distributed configurations of variable attenuators. In the attenuator of Figure 10.7(c), two PIN diodes are connected with a quadrature hybrid, such as a branch hybrid, Lange coupler, and so forth (see Chapter 7). In this circuit, the power incident on port 1 divides equally between ports 3 and 4 and passes to the two PIN diodes D_1 and D_2 connected in parallel with the loads. The diodes must be spaced equally from ports 3 and 4. The purpose of the loads is both to make the attenuator less sensitive to individual diode differences and to increase the power handling by a factor of 2. Because the incident power
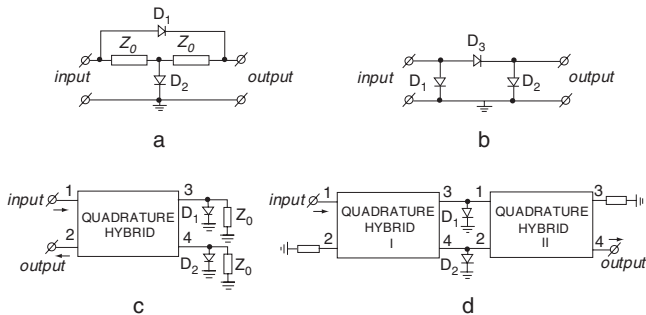
Figure 10.7. PIN diode attenuators: TEE-circuit (a); π-circuit (b); quadrature hybrid matched attenuator (c); matched attenuator with two quadrature hybrids (d).

is divided into two paths, this attenuator is capable of handling twice the power of the simple diode configuration. Resistances of the loads are equal to the characteristic impedances of the output lines. PIN diodes are used as mismatched elements.

The amount of reflected power from the diodes depends on the bias voltage. Powers reflected at ports 3 and 4 combine in port 2. Ideally, the reflected signal does not pass through to port 1; therefore, this port has good matching. Using the results for the two-branch 3-dB coupler or for the 3-dB coupled-line directional coupler (see Chapter 7), we can see that for perfect hybrids and diodes with identical S-parameters, input matching (at port 1) of this nonreflective attenuator depends only on the mismatching of the isolated port. From Chapter 7 we can find the maximum attenuation, the insertion loss, and the mismatching of this circuit for real conditions (mismatching of loads, losses in transmission line, fabrication tolerances, and discontinuities).

A nonreflective attenuator with two quadrature hybrids is shown in Figure 10.7(d). This attenuator consists of two shunt PIN diodes D_1 and D_2 located between two quadrature hybrids. The first hybrid splits the input power from input port 1 to ports 3 and 4, which are connected to the PIN diodes. When the PIN diodes are zero biased, or reverse biased (equivalent open circuit), nearly all input power divides between ports 1 and 2 of the second quadrature hybrid. This hybrid combines input signals to output port 4. Whenever the diodes draw bias current, they absorb a portion of the input power, while reflecting some of the input power back to ports 3 and 4 of the first hybrid. The reflected power is combined with and absorbed into the 50Ω termination in port 2 of the first hybrid. Unlike the single-hybrid attenuator [Figure 10.7(c)], this attenuator ensures good input/output VSWR and decreases ripple, dependency of attenuation on hybrid directivity, and variation of attenuation with frequency.

10.3.3. Switched Channel Attenuators

The switched attenuator structure is shown in Figure 10.8. The basic form of the switched attenuator [see Figure 10.8(a)] [11] has an attenuator pass (7, 5, 8) and reference pass (bypass) (6). The attenuator includes an input transmission line 1 and an output transmission line 2. Both lines have characteristic impedances Z_0. These transmission lines are connected to the attenuator pass and bypass line through two SPDT switches 3 and 4,
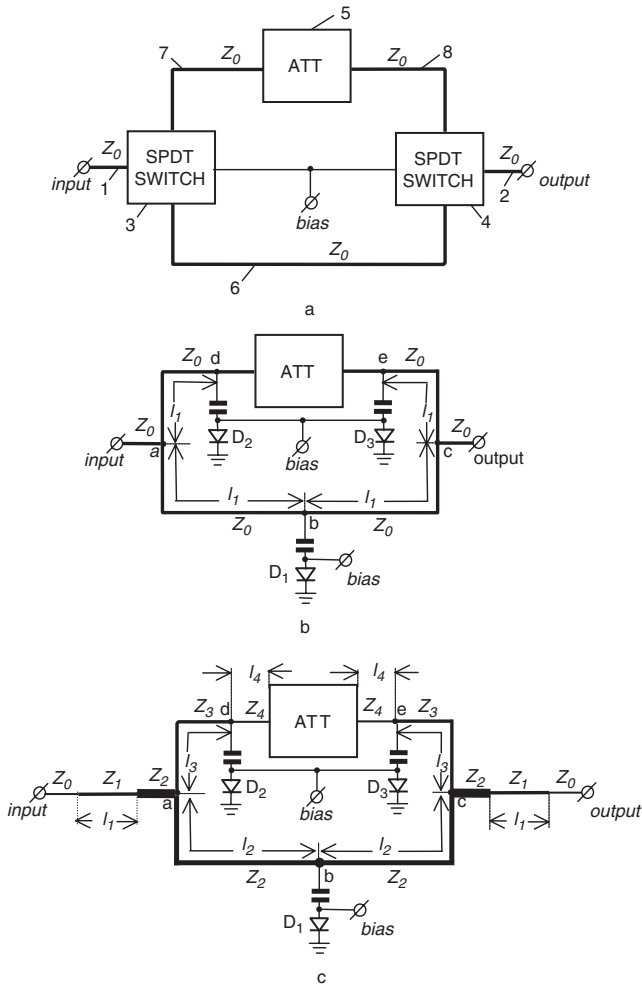
Figure 10.8. Switched attenuators: with two SPDT switches (a); with SPST switches (b); with SPST switches and different impedance transmission lines (c).

which switch an input and output to the attenuator path or to the bypass line. The bypass and attenuator path lines have the same impedances Z_0.

Figure 10.8(b) illustrates a switched channel attenuator with shunt PIN diodes [12]. The PIN diodes operate as SPST switches that are ON when reverse-biased and OFF when current flows through the diodes (forward biased). The bypass section includes a shunt diode D_1 located at the center of a half-wavelength transmission line *abc*. When the diode D_1 is forward

biased, an RF signal is not permitted to flow through the bypass section
abc. When the diode D_1 is reverse-biased, the RF signal is permitted to
flow through this bypass section. Within attenuation section *adec*, two
shunt PIN diodes, D_2 and D_3, are disposed a distance l_1 of one quarter-
wavelength from junctions *a* and *c*, respectively. When the diodes D_2 and
D_3 are reverse biased, the RF signal passes through the attenuation section
and is attenuated according to the insertion loss value of the attenuator
cell (ATT). When the diodes D_2 and D_3 are forward biased, the RF signal
does not pass through the attenuator cell. Properly actuating or biasing
diodes D_1, D_2, and D_3 allows the direction of the RF signal exclusively and
selectively through either the attenuator cell or the bypass section.

The insertion of the bypass and the attenuator pass of the net-
works in Figure 10.8(a, b) are identical. In practical application of the step
attenuators, insertion losses of the bypass and isolation of the attenuator
pass are accordingly more critical than insertion losses of the attenuator
pass and isolation of the bypass. For many applications, the primary
design concern is to minimize bypass losses.

The microstrip switched channel attenuator [Figure 10.8(c)] includes
the bypass and the attenuator pass with different transmission line imped-
ances: low impedance of the bypass line and high-impedance transmis-
sion line of the attenuator pass. The input and output of the switched
attenuator are connected with low-impedance transmission lines and
transformers, which provide input and output matching. The *T*- or π-resis-
tive circuit of the attenuator pass is matched with the high-impedance
input and output transmission lines.

From a power division of the *T*-junctions [*a* and *c* of Figure 10.8(c)] in
proportion to the ratio of admittances, we have

$$\frac{Y_2}{Y_3} \left(Y_2 = \frac{1}{Z_2}, Y_3 = \frac{1}{Z_3} \right).$$

If $Z_2 < Z_3$ and $Z_2 < Z_0$, we can obtain the desired minimum insertion losses
at the bypass.

The insertion losses of the bypass depend on the power division of the
input and output junctions *a* and *c*, transmission line losses, and PIN
diode losses. To minimize bypass losses, the junctions *a* and *c* are realized
with the unequal power division: The bypass RF signal power should be
greater than the attenuator path RF signal power. In this case, the trans-
mission-line impedance of the bypass should be less than the transmis-

sion-line impedance of the attenuator path. Therefore, at the bypass mode, the bypass losses are less and influence of the attenuator pass is less than in the conventional network [Figure 10.8(b)]. Mismatching between the bypass line and input (output) transmission lines can be avoided by additional quarter-wavelength transformers with length l_1 and impedance Z_1 [see Figure 10.8(c)].

For the shunt PIN diode switches (with diodes D_1, D_2, and D_3), the isolation is

$$a_{iso} = 20\log\left[1+\left(\frac{Z_0}{2R_F}\right)\right] \text{ (dB)}, \tag{10.26}$$

and the insertion loss is

$$IL = 10\log\left[1+\left(\frac{Z_0}{2X_C}\right)^2\right] \text{ (dB)}, \tag{10.27}$$

where Z_0 is the characteristic impedance of the input/output transmission lines, R_F is the PIN diode resistance at under forward bias, $X_C = 1/i\omega C_j$, and C_j is the diode junction capacitance at under zero or reverse bias. It can be seen from (10.26) and (10.27) that isolation is a function of the diode's forward resistance R_F, and the insertion losses are primarily dependent on the junction capacitance C_j. To minimize insertion loss through the bypass section, the PIN diode D_1 needs to have the low junction capacitance C_j. The PIN diodes D_2 and D_3 must exhibit the low forward resistance R_F to maximize isolation of the attenuator path. With respect to the attenuation section, higher insertion losses of the diodes D_2 and D_3 with moderate junction capacitances should be compensated by correction of the resistive network attenuation.

In practical high-power microstrip attenuator networks, errors of the attenuation steps are observed due to parasitic capacitance between high-power resistors of the attenuator cell and underlying ground plane. These parasitic shunt capacitances and the PIN diode junction capacitance C_j can be compensated for by a series inductance between each PIN diode and the resistive network. This inductance can be realized by an additional high-impedance [Z_4 in Figure 10.8(c)] short microstrip line that is coupled to the diode section and the resistive network. The combination of this series inductance and two shunt capacitances (diode junction capacitance and total resistors capacitance) forms a matched three-element low-pass

filter. If the length l_4 of the high impedance (Z_4) microstrip line is less than the eighth wavelength, the equivalent series inductance can be obtained from

$$\omega L_4 \approx Z_4 \, \omega_c l_4 \Big/ v,$$

where v is the velocity of signal propagation along the line and ω_c is the band edge of the LPF frequency characteristic.

The practical 1-GHz attenuator [Figure 10.8(c)] has been built using a microstrip line based on the dielectric substrate with thickness of 25 mil and dielectric constant of 10.2. The circuit includes diodes D_2, D_3 with junction capacitance 0.9 pF, series resistance 0.32Ω, and diode D_1 with junction capacitance 0.5 pF, and series resistance 0.75Ω. The input and output transmission lines with impedance $Z_0 = 50\Omega$ are connected to transmission lines having low impedance $Z_2 = 30\Omega$ by quarter-wavelength transformers with impedance $Z_1 = 38.7\Omega$. At the attenuator pass, the 50Ω quarter-wavelength transmission lines l_3 are coupled to lines with imped- ance Z_2 and short transmission lines l_4 having impedance $Z_4 = 83.3\Omega$.

The π-circuit resistor attenuator cell with input/output impedance $Z_{in} = Z_{out} = 83.3\Omega$ provides the necessary attenuation of the attenuator path and good input/output matching. The 1-GHz attenuator provides the insertion loss of the low-loss path (bypass) at 0.25-dB maximum and the input/out- put return loss at 20 dB minimum. At the attenuator path the return loss is 20 dB minimum.

10.4. LIMITERS

Limiters are primarily used to protect power-sensitive components and devices (for example, LNA and mixer) from nearby high-power sources. A diode limiter is a power-sensitive variable attenuator that uses the non- linear properties of a diode to provide an impedance mismatch when a sufficient amount of RF power is incident on the device. The output power is reduced to the level protecting receivers from high-power leak- age.

Practically any varactor or PIN diode can be used in a limiter. The basic design for limiters is the same as for PIN diode switches. The main difference between the two designs is the rectification transients.
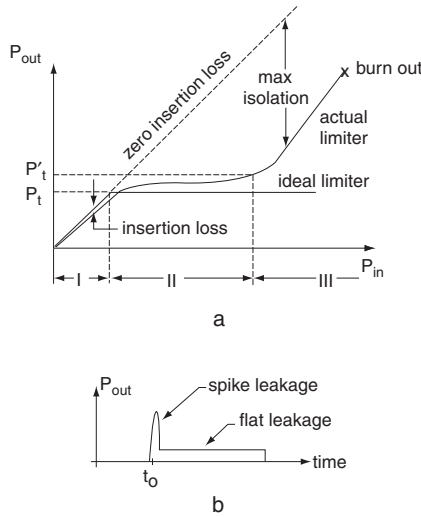
Figure 10.9. Limiter characteristics: typical transfer characteristic for an ideal and practical limiter (a); transmitter power pulse vs. time (b).

Figure 10.9(a) shows a typical plot of the output power (P_{out}) versus input power (P_{in}) for an ideal limiter. This plot has three operating regions. In the first linear region (**I**), signals below a threshold power (P_t) pass through the limiter with minimum losses. In the second compression region (**II**), when input power levels exceed the diode threshold level ($P_t < P < P_{t'}$), the output power tends to remain constant with increase of input power. The 1-dB compression is usually used to mark the onset of the compression region. For an input power beyond the maximum level of isolation $P_{t'}$, the output power starts to rise again (region **III**), until the diode reaches its burnout temperature.

Figure 10.9(b) illustrates spike leakage. After the spike leakage is complete, the limiter transmits a constant power. The spike leakage would be for a nanosecond rise-time signal.

There are three types of limiter configuration [Figure 10.10(a–c)]. In practice, limiters are based on shunt configurations, which can handle a higher power.

In a *passive* (*self-bias*) *limiter* [Figure 11.10(a)], output power depends on the variable diode resistance. Limiter diodes are turned on by the RF signal itself. A passive limiter is a self-activating switch that is activated by high-level incident power. When the self-rectified bias is increasing (with increasing of P_{in}), diode impedance is decreasing. The
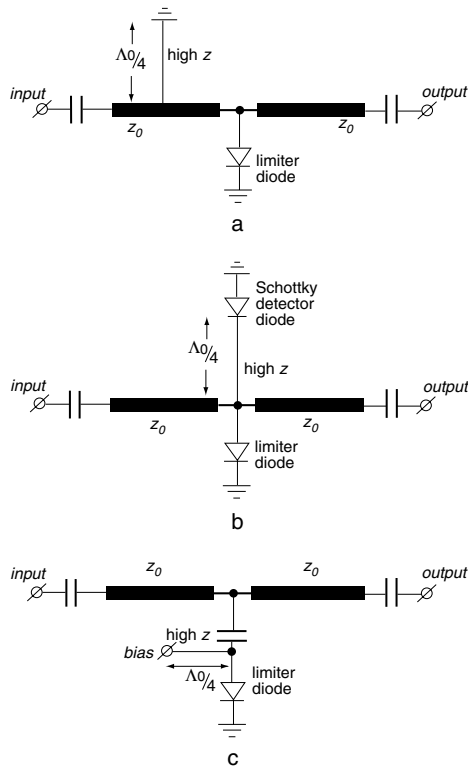
Figure 10.10. Limiter configurations: passive (self bias) (a); quasi-active (b); active (c).

speed of this process depends on the diode lifetime (20–200 ns). This relatively slow process leads to a high dissipation power on the diode: its maximum is approximately 50% of input power (see Figure 10.3). After this, diode impedance becomes very low, the rectified current increases rapidly, and the output power saturates. This process causes spike leakage power nearly equal to the incident power level [Figure 10.9(b)]. The amplitude and length of this spike depend on the rise time of the input pulse and the lifetime of the diode. The maximum signal RF power that a limiter diode can handle is limited by either the diode's breakdown voltage or its power-dissipation capability.

The *active limiter* [Figure 10.10(c)] works on separate current sources. One of the uses of the limiter is in the sensitive time control (STC) systems, where it also provides the passive limiting mode [13].
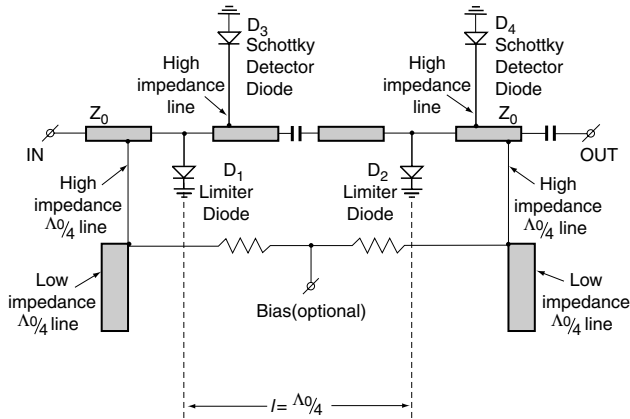
Figure 10.11. *X*-band two-stage limiter.

The *quasi-active limiter* [Figure 10.10(b)] uses a high-power Schottky barrier diode detector that supplies dc current to the limiter diode. The Schottky diode rectification process is much faster than limiter diode self-bias. The limiter diode is turned on primarily by the external bias current from the Schottky detector diode, which is sensitive to the incident signal.

Figure 10.11 shows a two-stage limiter with limiter diodes D_1 and D_2 and two Schottky detector diodes D_3 and D_4. The Schottky diodes D_3 and D_4 are coupled (–20 dB) with the main 50Ω transmission line through high-impedance (~120Ω) conductors. Diodes D_3 and D_4 detect the incident microwave power and rapidly apply self-rectified current to the limiter diodes D_1 and D_2, causing a rapid increase in attenuation. The first Schottky diode D_3 starts activating the first high-power limiter diode D_1 at 15-dBm incident power. Diode D_1 is used as a prelimiter of the high-incident microwave power. The right type of Schottky diode (barrier diameter, breakdown voltage, or package) should protect this diode against burnout.

The second low-power limiter diode D_2 has a faster response and, therefore, provides protection during the initial stages of pulse rise time. For example, the limiter diode with a lifetime of 10 to 20 ns reaches the 10-dB isolation point in about 4 ns [14]. Thus, the second limiter diode is the first ON. At the end of the pulse, the process reverses, and the limiter diodes "recover" the high impedance to the first limiter diode D_1, reducing the turn-on time. The first limiter diode absorbs either an equal or a greater amount of power than the second diode, depending upon the elec-

trical spacing of two diodes and diode resistance. The spacing between two limiter diodes should be $\Lambda_0/4$ or $3\Lambda_0/4$.

The bias injection port is provided to drive the limiter diodes during the isolation test mode and can also be used during the regular high-isolation mode.

The parasitic reactances of the limiter diodes can be compensated for by choosing the optimum spacing and characteristic impedance of the transmission line between them.

The diode package for the microstrip limiter includes two bonding wires (straps), which are equivalent to inductances. The values of these inductances (~0.1 nH) depend on the widths and lengths of the straps [see (4.3)]. These inductances, in conjunction with limiter diode junction capacitance (0.1 pF), or with an additional chip capacitor, form a matched three-element low-pass filter. This filter provides broadband matching and flat leakage characteristics.

REFERENCES

1. White, J., *Microwave Semiconductor Engineering*, New York: Van Nostrand Reinhold, 1982.
2. Garver, R. V., *Microwave Control Devices*, Dedham, MA: Artech House, 1978.
3. Watson, H. A., *Microwave Semiconductor Devices and Their Circuit Applications*, New York: McGraw-Hill, 1969.
4. Mortenson, K. E., and J. M. Borrego, *Design Performance and Application of Microwave Semiconductor Control Components*, Dedham, MA: Artech House, 1972.
5. Hiller, G., "Design with PIN Diodes," Application Note, Alpha Industries, Inc.
6. "Application of PIN Diodes," Application Note, 922, Hewlett Packard, 1997.
7. Malsky, I. V., and B. V. Sestroretsky (eds.), *Microwave Devices with Semiconductor Diodes*, Moscow, Russia: Soviet Radio, 1969.
8. Gaverly, R., and G. Hiller, "Distortion in PIN Diode Control Circuits," *IEEE Trans. Microwave Theory Tech.*, Vol. MTT-35, May 1987, p. 492.

9. Hiller, G., Design with PIN Diodes, M/A-COM Catalog, No. AG312, 1995.

10. Visblat, A. V., *Microwave Semiconductor Switch Devices*, Moscow, Russia: Radio and Svyaz, 1987.

11. Koul, S. K., and B. Bhat, *Microwave and Millimeter-Wave Phase Shifters*, *Volume II: Semiconductor and Delay Line,* Norwood, MA: Artech House, 1991.

12. Kyriakos, C. S., J. B. Ledebur, L. G. Maloratsky, and C. E. Steen, "High-Power Precision 1 dB Step Attenuator," U.S. Patent No. 6,472,948, October 29, 2002.

13. Niehenke, E. C., T. E. Steigerwald, and A. E. Lisenbardt, "New Limiters Protect Low-Noise FET Amps," *Microwaves & RF*, February 1984, pp. 89, 90, 92, 95, 96.

14. Semiconductors and MMICs, Alpha Co., Catalog, 1996.

This Page Intentionally Left Blank

CHAPTER 11

Phase Shifters

RF and microwave phase shifters have many applications in various equipment. For example, they play a very important role in phased-array antennas. Changing the phase of each array element allows the main antenna beam to be steered. Phase shifters utilize diodes, FETs, ferrites, transmission line segments, and hybrids. The final choice of a phase shifter network depends on the required bandwidth, insertion loss, switching speed, power handling accuracy, and resolution. A choice between analog and digital control must also be made.

11.1. DIODE PHASE SHIFTERS

The general principle of the diode *digital phase shifter* is that either the signal is switched between two networks that have a fixed phase difference or the phase shift of a single network is controlled by switching elements in or out of the network. The switching elements are usually PIN diodes with varied resistance values from approximately 10,000Ω to less than 1Ω (see Chapter 10). The high-speed PIN diodes make it very popular for high-speed, current-controlled phase shifters. In MMIC design the switching elements are often realized with FETs.

Analog phase shifters are devices whose phase shift changes continuously as the control input. The most commonly used semiconductor control elements in analog phase shifters are varactor diodes. Varactor diodes operating in a reverse-biased condition provide a junction capacitance that varies with applied voltage and can be used as an "electrically variable" capacitor in tuned circuits. The variable capacitance of a varactor diode is a nonlinear function of voltage; therefore, the drive voltage is too distorted for a linear relationship between dc voltage and phase. The varactor capacitance changes rapidly (in less than a nanosecond) with voltage around zero volt bias; therefore, the continuous phase shifters generate harmonics and increase losses for higher-incident power levels at a low bias voltages. The dc voltage has to be larger than the RF voltage to control the phase shift.

Varactor continuous phase shifters can achieve a large amount of phase shift and high speed and require fewer diodes than digital phase shifters, but at the cost of decreased accuracy, relatively narrow band, and low input power levels (less than 1W).

11.1.1. Switched-Line Phase Shifters

In the switched-line phase shifter [Figure 11.1(a)] two (or several) lines of different lengths are switched by two single-pole, double-throw PIN diode switches. When the PIN diodes D1 and D2 are ON while PIN diodes D3 and D4 are OFF, the reference transmission line **I** is in the circuit. When the diodes D3 and D4 are ON, the transmission line **II** is in the circuit. By switching a signal between two lines of different lengths, it is possible to realize a specific phase shift. The difference in physical length Δl between these two stages gives the phase shift

$$\Delta \varphi = \frac{2\pi \Delta l}{\Lambda},$$

where Λ is the guide wavelength. The resulting phase shift varies linearly with frequency.

Because the phase shift in the switched-line configuration is well defined by differences in the line length only, this phase shifter is useful in devices without adjustments, and it is very stable over time and temperature.
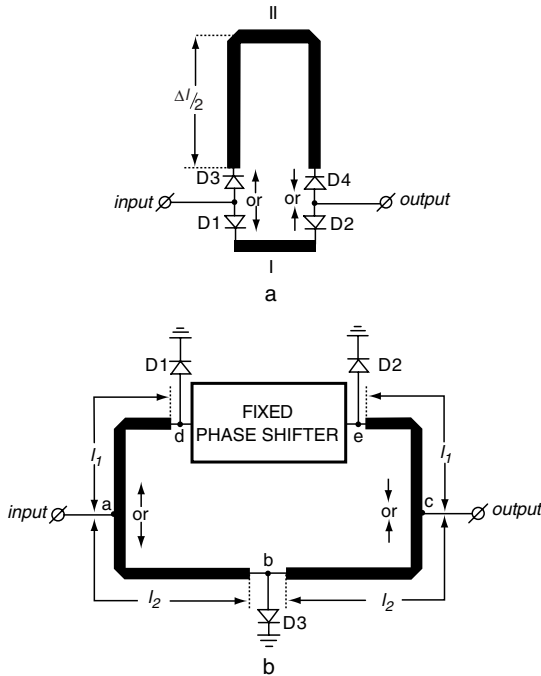
Figure 11.1. Switched-channel phase shifters: with switching of transmission lines (a); with fixed phase shifter (b).

The isolation per switch in the OFF state must be greater than 20 dB to avoid phase error. Insertion loss of the switched-line phase shifter is equal to the loss of the single-pole, double-throw switches plus line losses. Because of the unequal transmission line paths, the loss depends on the phase shift. A practical problem in this phase shifter is that of insertion loss resonances [1]. These resonances appear where the effective length of the off-diode mode (electrical length of the line plus the equivalent lengths of the capacitive off-diodes) is equal to $n\lambda/2$ ($n = 1, 2, \ldots$). At resonant frequencies there are large phase errors and insertion loss spikes. Therefore, the length of the two lines should be chosen with this effect taken into account.

Switched-line digital phase shifters providing a certain phase increment can be made by a series connection of individual switched-line phase shifters. Switched bit phase shifters are generally used where there are requirements for very high switching speeds and moderate-to-high power handling capability. If the number of stages is n for a phase shifter

giving up to φ_{max} degrees of phase shift, then the smallest phase increment $\Delta\varphi$ is given by

$$\Delta\varphi = \frac{\varphi_{max}}{2^n}.$$

Multibit switched line phase shifters can be used to vary phase shift up to 360°. Figure 11.2 illustrates the 4-bit switched-line phase shifters consisting of a cascade of digital phase shifters and covering 180° in nominal steps of 22.5°. PIN diodes or FET devices may be used as switching elements.

The problem with multibit phase shifters is a large variation in the return loss across the phase states. Also, more bits add insertion loss and accumulate phase error. The mismatch effect limits the phase resolution and accuracy of the phase shifter. The only solution is to provide good return loss of each individual bit.

The other device is a switch-channel circuit with a fixed phase shifter [Figure 11.1(b)]. This switchable phase shifter includes a reference pass (bypass) *abc* and fixed phase shifter pass *adec*. The bypass line has one diode section D3, which is located at the center *b* of the half-wavelength transmission line $l_{abc} = 2l_2 = \Lambda_0/2$. When this diode is forward biased, signal flows through the fixed phase shifter pass, and when it is reverse
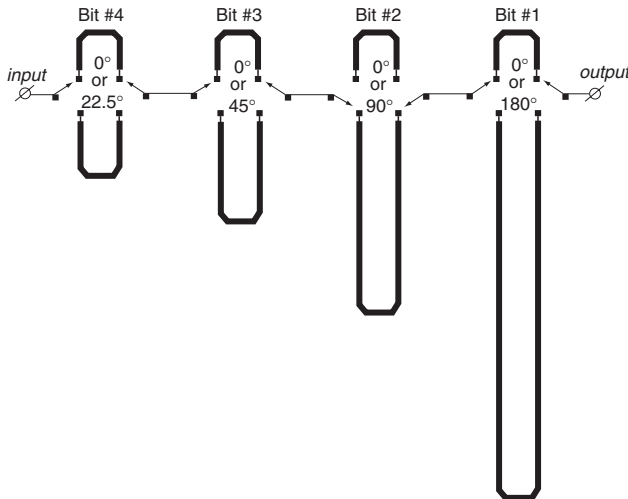
Figure 11.2. 4-bit phase shifter.

biased, signal passes through the bypass line. The fixed phase shifter is connected to the input and output by diode sections D1 and D2, which are at a distance of a quarter-wavelength ($l_1 = \Lambda_0/4$) from the junctions *a* and *c*. When these diodes are forward biased, signal flows through the bypass line, and when they are reversed biased, signal passes through the *adec* pass and has a fixed phase shift.

11.1.2. Loaded-Line Phase Shifters

In the loaded-line phase shifter Figure 11.3(a), the transmission line is loaded by variable susceptances *iB* and *–iB*. Adjacent loading susceptances are equal and are switched into either a capacitive or an inductive state. The shunt capacitive element electrically lengthens a transmission line, while an inductive element shortens it, and switching from an inductive to a capacitive element produces an increase in electrical length (or corresponding phase shift). Susceptance can be switched between two states with a PIN diode switch. Usually only one control signal for switching is required for this phase shifter, since the loads can be biased simultaneously.

The susceptances are spaced about a quarter-wavelength apart ($\Theta = 90°$) to improve input matching: reflections from the reactive elements cancel out at the input terminal of the phase shifter. Using the results in Chapter 10 [see (10.19)] for $Y = iB$ ($G = 0$), we can obtain the voltage transmission coefficient:

$$
\begin{aligned}
\frac{1}{S_{12}} &= \left[e^{i\Theta}\left(1+iB\right) - \frac{i}{2}B^2\sin\Theta \right] \\
&= \left(\cos\Theta - B\sin\Theta\right) + i\left(\sin\Theta + B\cos\Theta - \frac{B^2}{2}\sin\Theta \right),
\end{aligned}
\tag{11.1}
$$

where *B* is the normalized shunting susceptance.

Comparing (11.1) with the corresponding matrix coefficient of the equivalent regular line (see Appendix C), we obtain the phase shift of the loaded-line phase shifter:

$$
\cos\varphi = \cos\Theta - B\sin\Theta.
\tag{11.2}
$$
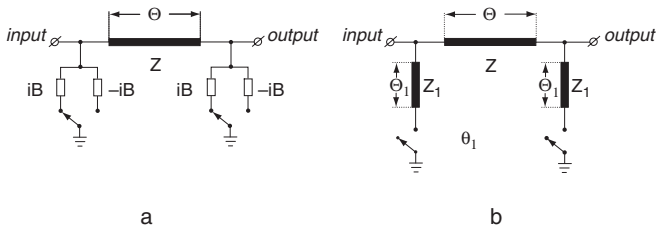
Figure 11.3. Loaded-line phase shifter: with capacitive and inductance elements (a); with short-circuited stubs (b).

For two distinct values of B_1 and B_2, we have

$$\cos\varphi_1 = \cos\Theta - B_1 \sin\Theta,$$
$$\cos\varphi_2 = \cos\Theta - B_2 \sin\Theta,$$

and the required phase shift is

$$\Delta\varphi = \varphi_1 - \varphi_2.$$

The lumped-element loaded-line phase shifter [Figure 11.3(a)] provides small dimensions for relatively low frequencies, where compact design could be achieved with the lumped-element equivalent of the transmission line. For higher frequencies, the loaded-line phase shifter with short-circuited stubs [Figure 11.3(b)] can be used.

The loaded-line phase shifter can be used for high-power and narrowband devices for small amounts of phase shift (generally 45° or less). For a specified phase error and VSWR, the smaller the phase shift, the larger the bandwidth. For example, within a phase shift error of +/–2° and a VSWR of 1.5, a 22.5° phase shift is reported at nearly an octave bandwidth, whereas for a 45° phase shift, the bandwidth reduces to about 25%.

The extremely high-power capability of this phase shifter is due partly to the use of shunt-mounted switch PIN diodes, plus the fact that the diodes are never in the direct path of the full microwave power. The limiting factor of the highest power-handling capability is the linear operating range of the PIN switches.

11.1.3. High-Pass/Low-Pass Phase Shifters

High-pass/low-pass phase shifters are shown in Figure 11.4(a, b). This type of phase shifter consists of three elements associated in a *T*-network
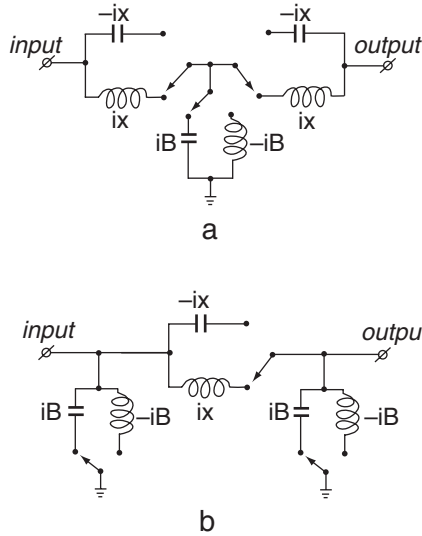
Figure 11.4. Switched-element phase shifters: with high-low pass *T*-circuit (a); with high-low pass *π*-circuit (b).

[Figure 11.4(a)] or a *π*-network [Figure 11.4(b)]. A phase shift of these lumped-element phase shifters results from the difference between the phase of two filters (high-pass or low-pass). This circuit provides phase delay in the low-pass mode and phase advance in the high-pass mode.

These phase shifters use SPDT switches to switch the signal between a high-pass filter and a low-pass filter. The three switches are controlled in synchronization.

For the *π*-circuit [1, 2, 3],

$$\Delta\varphi = \tan^{-1}\left(\frac{2B}{B^2 - 1}\right),$$

$$X = \frac{2B}{1 + B^2}.$$

X and *B* can be expressed in terms of phase shift as

$$X = \sin\left(\frac{\Delta\varphi}{2}\right),$$

$$B = \tan\left(\frac{\Delta\varphi}{2}\right).$$

For the *T*-circuit,

$$\Delta\varphi = 2\tan^{-1}\left(\frac{2X}{X^2 - 1}\right),$$

$$B = \frac{2X}{1 + X^2}.$$

X and B can be expressed in terms of phase shift as

$$X = \tan\left(\frac{\Delta\varphi}{4}\right),$$

$$B = \sin\left(\frac{\Delta\varphi}{2}\right).$$

The high-pass/low-pass phase shifter provides wide bandwidth (over an octave) and can be realized much smaller than the other types because lumped elements are typically used instead of transmission lines. This phase shifter is suited to low frequencies, particularly in the VHF and UHF bands. The cutoff frequencies of the two filter networks must be outside of the phase shift band. A disadvantage of this approach is that the circuit requires three diodes per stage and usually requires two control signals. Also, the amplitude difference varies with frequency, since the band-edge slopes of the two filters are rolling in opposite directions.

11.1.4. Reflection-Type Phase Shifters

The reflection-type phase shifters use either a circulator or a hybrid and require minimum diodes per stage. Figure 11.5 shows a reflection phase shifter of the circulator type. The basic principle is that the reflection coefficient S_{22} of the reflection circulator load becomes the transmission coefficient S_{31} of the circuit. The phase shift of this phase shifter is

$$\Delta\varphi = \frac{2\pi\Delta l}{\Lambda},$$

where Δl is twice the transmission line length.

To minimize phase error, it is very important to have good matching between the circulator and the terminating impedance. The finite isolation
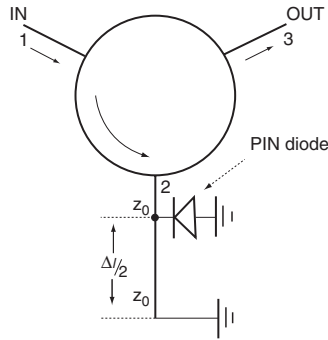
Figure 11.5. Reflection circulator-type phase shifter.

is caused by internal reflections in the circuit. It has been reported by Garver [2, 4] that a circulator having 20-dB isolation gives +/−22.8° maximum phase error and 30-dB isolation gives +/−7.2° maximum phase error. This type of phase shifter is usually more expensive (circulator cost).

Figure 11.6(a, b) illustrates two configurations of reflection-type phase shifters with different hybrids. In the circuit of Figure 11.6(a), separating the incident and reflected signals is realized by a quadrature hybrid, such as the 3-dB branch-line or Lange coupler (see Chapter 7). The input signal is divided into two quadrature components with equal amplitudes on the output ports. These two signals are reflected from the identical terminations (controlled loads) in the two output ports and recombined in phase on the normally decoupled port. In the ideal case, there is no reflected signal on the input port (see Chapter 7). This circuit provides a signal phase shift of between 0° and −180°. The terminations can be either short or open or have another impedance.

Switching the diodes ON or OFF positions the total path length for both reflected signals by twice the electrical length between diodes and grounds, producing a phase shift of $\Delta\varphi$ at the output.

The reflection phase shifter that uses the in-phase–out-of-phase hybrid, such as the hybrid ring (see Chapter 7), is shown in Figure 11.6(b). In this configuration, a 90° line section is added to one of its output ports. Using the results of Chapter 7, we can find the main characteristics of the different reflection phase shifters (see Table 11.1). The two-branch hybrid and hybrid ring have a bandwidth limited to about 10%. The broadest bandwidth (up to an octave) can be realized by the coupled-line hybrid.
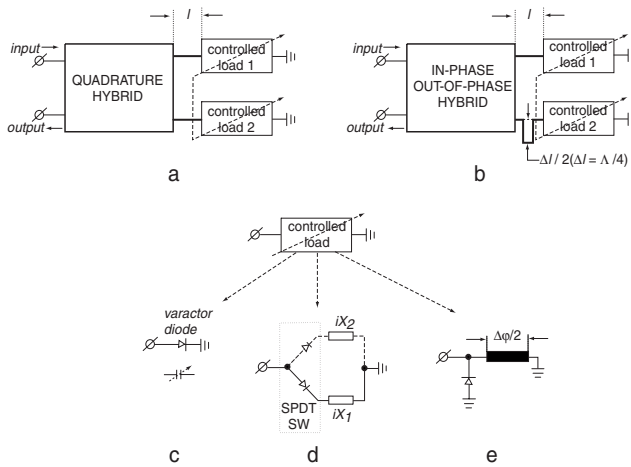
Figure 11.6. Reflection hybrid type phase shifters: with quadrature hybrid (a); with in-phase–out-of-phase hybrid (b); controlled load with varactor diodes (c); controlled load with two reactances (d); controlled load with regular line (e).

If the output reflection coefficients are equal, then the input port is perfectly matched. This is true even for such drastic output conditions as open or short circuits. Insertion losses are limited by losses of the hybrid and the forward and reverse resistances of the diodes. The bandwidth of these phase shifters depends on the bandwidth of the coupler as well as

TABLE 11.1. Transition and Reflection Coefficients of the
Reflection Phase Shifters

PARAMETERS			
Transmission Coefficient	$-i\dfrac{\Gamma_3 + \Gamma_4}{2 + \Gamma_3 - \Gamma_4}$	$-i\dfrac{\Gamma_2 + \Gamma_3}{2 + \Gamma_2 - \Gamma_3}$	$-i\dfrac{\Gamma_2 + \Gamma_3}{2 + \Gamma_2 - \Gamma_3}$
Reflection Coefficient	$\dfrac{\Gamma_3 - \Gamma_4}{2}$	$\dfrac{\Gamma_3 - \Gamma_2}{2}$	$\dfrac{\Gamma_3 - \Gamma_2}{2}$

the reflection circuits. The phase shift depends on the reactance values of the two controlled loads. The different types of controlled loads are shown in Figure 11.6(c–e). The controlled loads should be very similar, which is easily achieved with the fabrication of a phase shifter on the same die.

A continuous variation of phase shift can be realized by using varactor diodes [Figure 11.6(c)]. These diodes are in effect capacitors, the value of which depends upon the reverse voltage. The output signal is that reflected from the two varactor diodes. In the ideal case, the magnitude of the diode reflection coefficient is fixed at unity. The phase varies from zero (zero capacitance) to $-180°$ (maximum capacitance). As a result, the output signal phase is varied continuously by changing the bias voltage on the varactor diodes. In practice, the phase-shift range is limited by the capacitance ratio of the varactor diodes; the maximum phase shift that can be achieved is limited to around $160°$. When more phase shift is desired, several identical stages should be cascaded.

The control load with two reactances and the SPDT switch is shown in Figure 11.6(d). Figure 11.6(e) illustrates control load using a regular transmission line with an electrical length equal to $\Theta = \Delta\varphi/2$.

The hybrid reflection phase shifter requires only one control signal, because the loads can be biased simultaneously. In comparison with the circulator-type phase shifter, the reflection phase shifter with hybrids can handle up to twice the average or peak power when using the same diodes, but requires twice as many diodes.

11.2. FERRITE PHASE SHIFTERS

Ferrite phase shifters are based on a variation of the propagation constant of the transmission line built on a magnetized ferrite substrate. Varying the magnetic field applied to a ferrite will change the permeability, causing the corresponding phase shift.

To minimize physical dimensions, the center conductor of the microstrip or stripline has a meandered configuration (Figure 11.7) [3, 5–7]. This meander line consists of tightly coupled quarter-wave-length at the center frequency. It provides circularly polarized magnetic field in the ferrite medium and is used for nonreciprocal phase shifters.
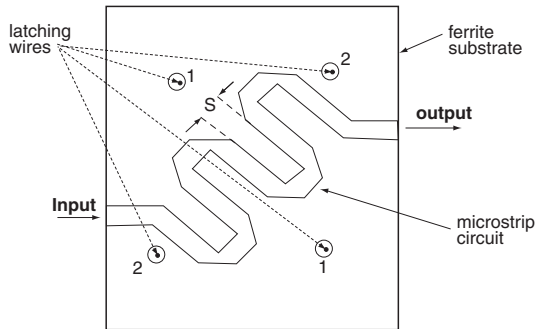
Figure 11.7. Digital latching control phase shifter.

The space *S* between adjacent lines is approximately equal to substrate thickness. The smaller gap between the adjacent meander conductors results in a higher maximum differential phase shift. The total number of meander legs is determined by the total desired phase shift.

If the ferrite substrate is magnetized along the direction of the meander lines (i.e., perpendicular to the RF magnetic field), a nonreciprocal differential interaction is obtained if the direction of the magnetization is reversed. When the ferrite substrate is magnetized in a direction perpendicular to the meander lines (i.e., parallel to the RF magnetic field), there is a minimum interaction between the ferrite and the RF magnetic field.

Two holes (one on either side of the meander line) are drilled in the substrate and latching wires are passed through the holes (Figure 11.7). Reversing the polarity of the pulse changes the direction of magnetization.

The slotline and the coplanar waveguide produce elliptically polarized RF magnetic fields and can be used for nonreciprocal phase shifters with a magnetized ferrite substrate [3, 8, 9]. The dc magnetic field is oriented in the plane of the ferrite substrate, but perpendicular to the direction of propagation.

In reciprocal phase shifters, the meander line is also used to reduce dimensions. To minimize nonreciprocal effects, the meandered conductors must be separated by at least five times the ground plane spacing ($S > 5h$) and the length of each section is not equal to a quarter wavelength.

The reciprocal ferrite phase shifter (Figure 11.7) operates by switching between two orthogonal states of magnetization, one parallel and the other perpendicular to the direction of propagation. Ferrite substrate can be magnetized circumferentially in its plane by means of the current pulse

applied to a control wire that is passed through the hole in the substrate (see Figure 11.7).

Ferrite phase shifters have good performance: lower loss and higher power than diode phase shifters. For example, ferrite phase shifters can have losses of less than 1 dB at 44 GHz, while diode phase shifters typically have 1-dB losses at 5 GHz and several decibel losses at 44 GHz [7]. The disadvantages of ferrite phase shifters are greater size and weight, higher cost, more sensitive to temperature variation, and slower speeds (by a few microseconds to tens of microseconds). The switching time for PIN diodes is less than 1 μs.

Another type of phase shifter is a composite ferrite-dielectric-substrate device [10–12]. The phase shift is obtained by the relative change in the dielectric constant of the ferroelectric material (Ba-Sr)TiO$_3$ due to the change in the dc biasing voltage. The dielectric constant can be modulated under the effect of an externally applied electric field perpendicular to the direction of propagation of a microwave signal. These ferroelectric phase shifters are reciprocal devices. Ferroelectric can generally handle high peak power levels and low switching times (typically 100 ns). The use of ferroelectric materials in the microwave frequency range has been limited due to the high losses of these materials and high electric field necessary to bias the structure in order to obtain substantial dielectric constant change [12].

11.3. DIFFERENTIAL PHASE SHIFTERS

11.3.1. Schiffman 90° Phase Shifter

The basic Schiffman phase shifter [13, 14] is shown in Figure 11.8(a). It consists of two separate sections, one of which (**I**) is a reference uniform line. The other (**II**) is a pair of equal length parallel coupled lines directly connected to each other at one end. The coupled section has the length L of one-quarter wavelength at the central frequency.

The matching condition for the output impedance of coupled sections is

$$z_0 = \sqrt{z_{0e} z_{0o}},$$

where z_{0e} and z_{0o} are even-mode and odd-mode impedances, respectively.
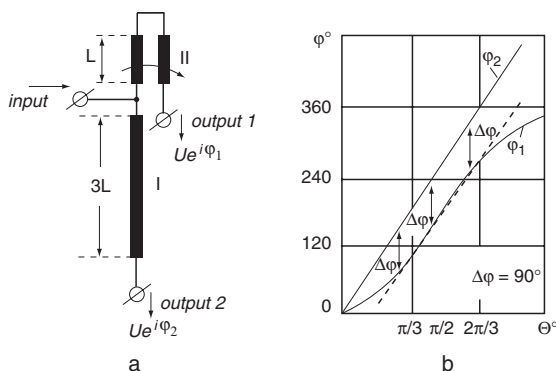
Figure 11.8. Schiffman 90-degree phase shifter: basic view (a); frequency response of phase shift (b).

The phase-shift function is determined by the phase difference of signals transmitted through the coupled section **II** and the reference line **I**:

$$\Delta\varphi = \arg S_{12}^{II} - \arg S_{12}^{I},$$

where S_{12}^{I} and S_{12}^{II} are the scattering matrix elements of two-ports **I** and **II**, respectively.

The phase shift of the coupled-line section is determined by [11]

$$\cos\varphi_1 = \frac{\left(\dfrac{z_{0e}}{z_{0o}}\right) - \tan^2\Theta}{\left(\dfrac{z_{0e}}{z_{0o}}\right) + \tan^2\Theta},$$

where $\Theta = 2\pi L/\Lambda$ is the electrical length of the coupled-line section. This section provides in an octave band a nearly constant phase shift $\Delta\varphi = 90°$, compared to a uniform line **I** with electrical length 3Θ [see Figure 11.8(b)]. For $z_{0e}/z_{0o} = 4$, phase shift is equal $90°$ within $+/-4.8°$ for frequency ratio 2.27:1. With a smaller value of z_{0e}/z_{0o}, bandwidth and phase error become reduced.

For multioctave operation, some authors [14–16] use coupled-line sections interconnected in a cascade in place of the single coupled-line section. It is a cascade of coupled sections of equal lengths (one quarter-wavelength at the central operating frequency) and different coupling coefficients.

Schiffman phase shifters can be used to achieve flat relative-phase differences between output ports, but these require implementing a long reference line (3Θ) and equal even-mode and odd-mode characteristics. In the microstrip Schiffman phase shifter, the even-mode and odd-mode phase velocities in the coupled-line section are not equal, and the above formulas are not applicable. For equalizing the two mode velocities, several techniques have been considered in Chapter 7.

11.3.2. Irregular-Line 180° Phase Shifter

The 180° ferrite-core phase shifters and transformers are widely used at RF and lower microwave frequencies. They offer advantages in size and bandwidth. The RF signals at the input and output ports of the transformer may be in-phase or out-of-phase.

Ferrite-core phase shifters have the following disadvantages. They are impossible to achieve with the printed-circuit designs favored at high frequencies. Frequency limitations arise from core loss, parasitic elements, and length of the winding. Permeability and dielectric constant of transformer material can vary dramatically with temperature and frequency. Transformer cores saturate, resulting in a reduction in bandwidth and power-handling capability.

The above disadvantages can be eliminated in print phase shifters without cores. The 180° phase shifter that uses a diagonally connected irregular line (see Table 3.3) is shown in Figure 11.9(a) [17]. This differential phase shifter includes a regular transmission line (1) and irregular coupled lines (2). The irregular lines (without ground plane) contain two parallel broadside coupled conductors (3, top, and 4, bottom) located on the two sides of a thin dielectric substrate (5). Unlike a conventional transformer, the irregular line has strong magnetic coupling of two broadside conductors without special cores. The strong magnetic coupling allows for the small length of the irregular lines (see Chapter 3). This effect is intensified by the elimination of the ground plane from the area (6) directly below the coupled lines.

Coupled lines have a short-circuit connection between the end of line 3 (7) and the end of line 4 (8). This short-circuit connection [by (19)] is also dc connected to the ground plane (9) of the regular line (1). The ground plane (9) is located on the base dielectric substrate (10).
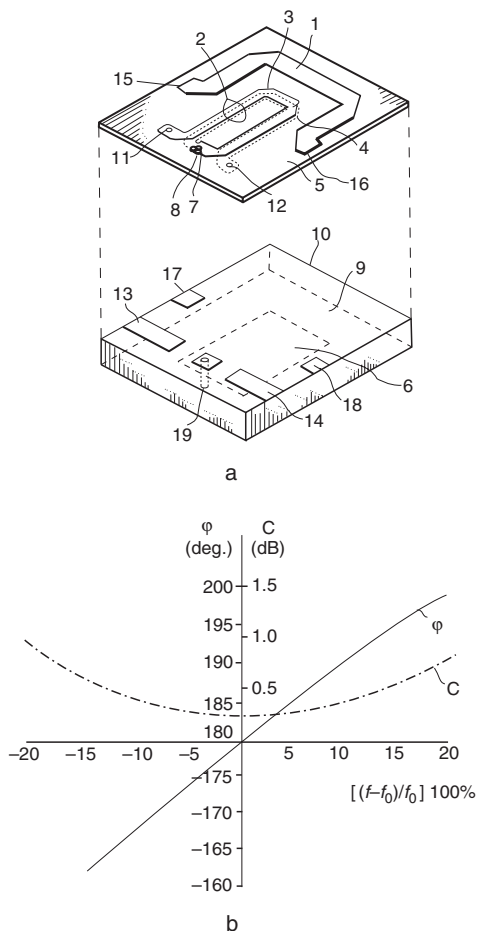
Figure 11.9. Printed 180-degree differential phase shifter: isometric view (a); dependence of phase shift (in degree) and loss (in dB) on relative detuning (in percent) (b).

Input (11) [see Figure 11.9(a)] and output (12) of coupled lines are electrically interconnected with corresponding input (13) and output (14) on the base dielectric substrate. Input (15) and output (16) of the regular line (1) are electrically interconnected with corresponding input (17) and output (18).

The electrical length Θ_n of the irregular lines is equal to the electrical length Θ_r of the regular line:

$$\Theta_n = \Theta_r,$$

where

$$\Theta_n = \frac{2\pi l_n}{\Lambda_n} \ \text{ and } \ \Theta_r = \frac{2\pi l_r}{\Lambda_r},$$

$$\text{and } \Lambda_n \text{ and } \Lambda_r$$

are wavelengths in the irregular and regular lines, respectively. The physical length of the irregular lines $l_n = (0.02\text{--}0.08)\Lambda_n$ depends on the coefficient of magnetic coupling k_m (see Table 3.3). The physical length l_r of the regular line is equal to $(0.02\text{--}0.08)\Lambda_r$. In general, wavelengths Λ_n and Λ_r are not equal, and for the equalization of the electrical lengths of both sections, it is necessary that $l_n = (\Lambda_n/\Lambda_r)l_r$.

Figure 11.9(b) shows the dependence of a phase shift (in degrees) and loss (in decibels) on relative detuning (in percent) for the 180° differential phase shifter (with length of coupled lines $l_r = 0.055\Lambda_r$), which was designed on a thin Kapton dielectric with a thickness of 0.003 in. (with center frequency equal to 120 MHz). The uniform microstrip line is printed on the same Kapton substrate, which is connected with the base dielectric substrate made of Duroid 5880 material. It can be seen that this gives a phase shift equal to 180° +/–5°.

REFERENCES

1. White, J. F., *Microwave Semiconductor Engineering,* New York: Van Nostrand Reinhold, 1982.
2. Garver, R.V., *Microwave Control Devices,* Dedham, MA: Artech House, 1978.
3. Koul, S. K., and B. Bhat, *Microwave and Millimeter Wave Phase Shifters,* Norwood, MA: Artech House, Vol. 1, 1991; Vol. 2, 1992.
4. Garver, R. V., "Broad-Band Diode Phase Shifters," *IEEE Trans. Microwave Theory Tech.* Vol. MTT-20, May 1972, pp. 314–323.
5. Roome, G. T., and H. A. Hair, "Thin Ferrite Devices for Microwave Integrated Circuits," *IEEE Trans. Microwave Theory Tech.,* July 1968, pp. 411–420.
6. Hansson, E. R. B., S. Aditya, and M. S. Larsson, "Planar Meander-Line Ferrite-Dielectric Phase Shifter," *IEEE Trans. Microwave Theory Tech.,* Vol. MTT-29, March 1981, pp. 209–215.

7. Hord, W. E., "Microwave and mm-Wave Phase Shifter," *Microwave Journal,* September 1989, pp. 95–112.

8. Gupta, K. C., et al., *Microstrip Lines and Slotlines,* Norwood, MA: Artech House, 1996.

9. Wen, C., "Coplanar Waveguide: A Surface Strip Transmission Line Suitable for Non-Reciprocal Gyromagnetic Device Applications," *IEEE Trans. Microwave Theory Tech.,* December 1969.

10. Das, S., "HTS Ferroelectrics Form High-Power Phase Shifters," *Microwave and RF,* December 1994, pp. 137–144.

11. Varadan, V. K., et al., "A Novel Microwave Planar Phase Shifters," *Microwave Journal,* April 1995, pp. 244–254.

12. DeFlaviis, F., N. G. Alexopoulos, and O. M. Stafsudd, "Planar Microwave Integrated Phase Shifter Design with High Purity Ferroelectric Material," *IEEE Trans. on Microwave and Techniques,* Vol. 45, No. 6, June 1997, pp. 963–969.

13. Schiffman, B. M., "A New Class of Broadband Microwave 90-Degree Phase Shifters," *IRE Trans. Microwave Theory Tech.,* Vol. MTT-6, April 1958, pp. 232–237.

14. Schiffman, B. M., "Multisection Microwave Phase Shift Network," *IEEE Trans. Microwave Theory Tech.,* Vol. MTT-14, April 1966, p. 209.

15. Meschanov, V. P., et al., "A New Structure of Microwave Ultrawide-Band Differential Phase Shifter," *IEEE Trans. Microwave Theory Tech.* Vol. 42, No. 5, May 1994, pp. 762–765.

16. Schiek, B., and J. Kohler, "A Method for Broadband Matching of Microstrip Differential Phase Shifters," *IEEE Trans. Microwave Theory Tech.,* Vol. MTT-25, August 1977, pp. 666–671.

17. Maloratsky, L. G., "Design Regular- and Irregular-Print Coupled Lines," *Microwave & RF,* September 2000, pp. 97–106.

CHAPTER 12

Circulators and Isolators

12.1. INTRODUCTION

Circulators and isolators are *N*-port nonreciprocal devices providing one-way sequential transmission of power between their ports. In these devices, there is very little loss of power in the forward direction, while the reflected power is absorbed in the termination. Circulators and isolators are used in various systems, for example, where a transmitter and a receiver are connected with a common antenna system or where the operation of an oscillator should not be affected by signals reflected from the mismatched load. Circulators have found another common application as the coupling elements in reflection amplifiers, such as parametric amplifiers or a tunnel-diode amplifiers.

In most cases circulators and isolators use ferrite materials. However, there are some new conceptions of nonreciprocal nonferrite devices that will be considered in this chapter.

Properties of a three-port circulator can be expressed in terms of the scattering matrix. For perfectly matched clockwise circulation, when

power through the circulator flows in accordance with the port sequence 1 $\rightarrow 2 \rightarrow 3 \rightarrow 1$,[*] the scattering matrix is given by

$$[S] = \begin{bmatrix} 0 & 0 & 1 \\ 1 & 0 & 0 \\ 0 & 1 & 0 \end{bmatrix}, \tag{12.1}$$

and for the counterclockwise circulation (direction $1 \rightarrow 3 \rightarrow 2 \rightarrow 1$), the scattering matrix is

$$[S] = \begin{bmatrix} 0 & 1 & 0 \\ 0 & 0 & 1 \\ 1 & 0 & 0 \end{bmatrix}. \tag{12.2}$$

Equations (12.1) and (12.2), for a lossless circulator, meet the unitary conditions [see (5.7)]. Correspondingly, the perfect circulation can be realized in a lossless network.

The resonance frequency is determined by the atomic makeup of ferrite material and by the net applied magnetic field. The nonreciprocal action in ferrite component is realized when the frequency offset between the applied signal and the resonance frequency gets the specified value. The direction of circulation can be reversed by inverting the direction of the magnetic field.

Ferrite circulators and isolators should be optimized to meet the following parameters for most applications: insertion loss, isolation, VSWR, bandwidth, temperature range, and size. The losses are the most important characteristic of ferrite devices. The variation of losses with magnetic field is shown in Figure 12.1. We can see that the losses have two high-loss domains, **I** and **II,** that should be avoided. In region **II** the losses are caused by a ferrimagnetic resonance. Ferrimagnetic resonance occurs when a rotating RF magnetic field has the same direction and frequency as the precessing electrons in the ferrite material. At the longer wavelength the resonance characteristic shifts to the region of lower magnetic fields [see Figure 12.1(b)]. In region **I** the losses are caused by a low magnetic field that is not sufficient to fully saturate or align the individual magnetic domains of the ferrite material. The low-loss operation is still

---

[*]The direction of circulation of the circulator (when viewed from the top or circuit side of the device) is shown by an arrow marked on the device.
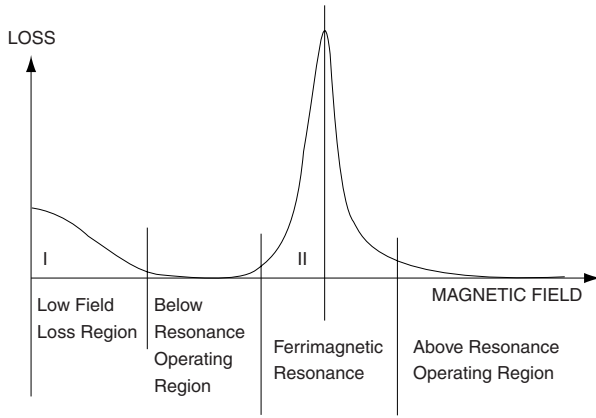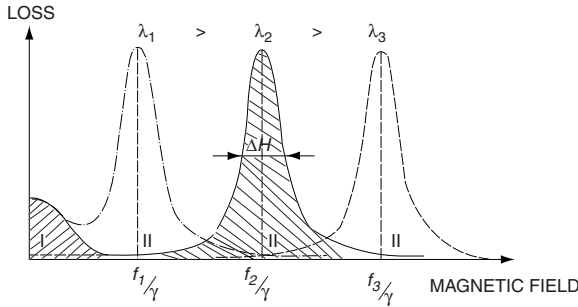
Figure 12.1. Regions of ferrite device operation: basic regions (a); regions of operation vary with wavelength (b).

possible in the *below-resonance* and *above-resonance* regions, as shown in Figure 12.1(a).

Above-resonance circulators and isolators can be designed to operate from 50 MHz to approximately 3.0 GHz. Below-resonance devices are generally available above 500 MHz. Above-resonance devices can cover the bandwidth up to 40% with insertion loss less than 0.5 dB. The octave-bandwidth can be achieved in below-resonance devices with less than 0.4-dB loss.

Generally, there are two kinds of circulators/isolators: distributed element devices and lumped element devices. We will consider both of these classes separately.

12.2. DISTRIBUTED FERRITE DEVICES

12.2.1. Ferrite Circulators

In distributed ferrite circulators the electromagnetic resonance occurs in the ferrite resonator consisting of one or two ferrite discs attached to the center of the *Y*-junction. The input RF signal propagating along one of the branches of the junction excites the circumferential waves in ferrite discs that have opposite directions of propagation. The constructive interference of counterpropagating waves creates the standing waves known as the spatial harmonics of ferrite discs. Exactly one wavelength of the basic spatial harmonic fits the perimeter of the ferrite resonator at the operation frequency of the circulator. The azimuthal position of the nodes of spatial harmonics with respect to the input port depends on the strength of the biasing magnetic field applied perpendicularly to the planes of disc resonator(s). In the absence of a magnetic field, the standing-wave pattern is symmetrical with respect to the input port, and energy is transferred equally into the other two ports. The presence of an axial magnetic field across the ferrite material changes the effective permeability seen by the rotating waves [1, 2]. The circulation condition is met when the biasing magnetic field turns the standing-wave pattern by 30°, so that the node of spatial harmonics meets the isolation port.

The center frequency, bandwidth, and isolation of circulators and isolators are functions of circuit geometry, type of ferrite, and the strength of the biasing magnetic field.

Figure 12.2 shows various configurations of print resonators used in circulators. The most popular resonators are junction circulators in the shape of disks [Figure 12.2(a)] or triangles [Figure 12.2(b)]. In a triangular resonator, the input/output lines may be connected to the corners or the midpoints of the sides of the triangle [see Figure 12.2(b)]. In [3, 4], it is shown that the insertion loss of the triangular junction is about 17% lower than the loss in a disk-type junction.

A WYE resonator [Figure 12.2(c)] is formed by attaching three open-circuited stubs to the central junction. In this resonator, the input/output lines may be connected either to the corners of the junction or directly to the stubs.

Figure 12.2(e) illustrates various types of slow-wave structures.
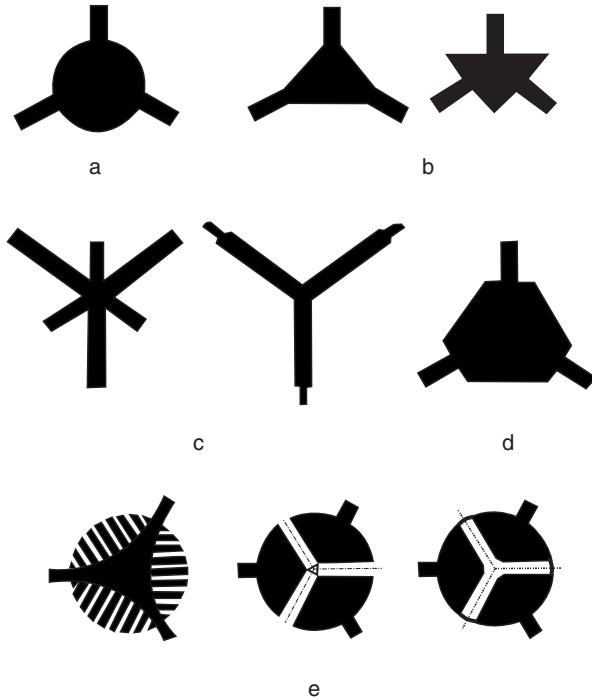
Figure 12.2. Center conductor geometries: disc (a); triangle (b); *WYE* (c); hexagonal (d); delay slow-wave structure (e).

The mentioned resonators are formed on ferrite inserts which may be used in combination with dielectric rings, triangular prisms, and so forth. Such combination allows widening bandwidth and improved the heat dissipation, which in turn increases the allowed maximum power. In this case, a ceramic with a high thermal conductivity is used as a dielectric.

If an enhanced isolation is necessary, the required isolation can be realized by simply cascading the circulators. One should remember, however, that it increases the overall insertion losses and adds to the number of parts.

12.2.2. Ferrite Isolators

An isolator is a two-port device that transfers the forward power from input to output with little attenuation and dissipates the power propagat-

ing in the reverse direction. The typical application includes the coupling of an RF or microwave generator with a load. The advantage is that almost all the entire power from the generator can be delivered to the load while the reflection from a mismatched load does not flow back to the generator. This allows the elimination of the variation in output power and frequency pulling with load mismatch.

The two most commonly used isolators are the *junction isolator* and the *resonance isolator.*

A junction isolator can be realized by terminating one of the ports of a three-port circulator with a matched load. A high power rating can be achieved by using two terminations connected in parallel or by utilizing special high-power print terminations. The power rating depends on the mismatch of the output port. For example, if the VSWR = 1.5, then 4% of the power reflects back to the isolator and is dissipated in termination, and for VSWR = 2.0, almost 11% of power is reflected back to termination.

In the isolator shown in Figure 12.3(a), the stub of length $\Lambda_0/8$ is connected to the main line so that currents in the stub and in the main line are in quadrature. A ferrite disc is placed at the junction, where the magnetic field is polarized circularly. Compensation for the reactance of the stub is obtained by using an additional stub of the length $3/8\Lambda_0$. The diameter of the ferrite disc d_F should be equal to $(2–3)W$ [see Figure 12.3(a)]. The resonance isolator operates by biasing the ferrite material at the resonance. For broadband operation, the ferrite material should have a relatively wide resonance curve (see Figure 12.1). Significant advantages of a resonance isolator with stubs are the simple design and relatively small size of the ferrite disc. The bandwidth of such isolators is 10% to 15%.

The stripline resonance isolator with a comb-type slow-wave structure [Figure 12.3(b)] consists of two rectangular ferrite plates and a center conductor with a "comb" of open-circuited stubs. To ensure broadband matching (about 40%), the stubs should gradually increase in length from 0 to $0.125\Lambda_0$. Circular polarization is developed in the vertical plane at a distance of $\Delta_1 \approx 0.02\Lambda_0$ from the bases of the stubs [see Figure 12.3(b)]. The step of the comb-type structure is $\Delta \leq b/3$ (b is the stripline height) and the width of the stub is equal to the gap between the stubs.

A *field-displacement isolator*, also known as *edge-side mode* or *peripheral mode* [5, 6], is shown in Figure 12.4. This microstrip isolator combines a transmission-line segment with a composite substrate made of ferrite and absorbing materials. The concentrations of RF energy are dif-
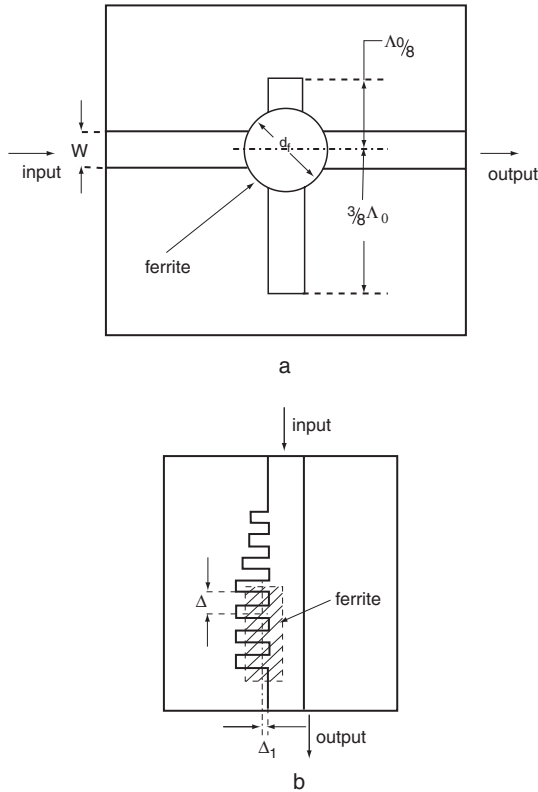
Figure 12.3. Ferrite isolators: with reactance stubs (a); comb-type slow-wave structure (b).

ferent at the left and right sides of the transmission line. The signal travel-ing in the forward direction concentrates at the side of the conductor adjacent to the conductor in the ferrite and is transmitted with minimum attenuation. A signal traveling in the opposite direction shifts to the other side of the conductor and meets the absorption material which introduces the attenuation of microwave energy. The field-displacement isolators have an ultra broadband (more than an octave). The bandwidth can be fur-ther increased using a multilayer ferrite structure [see Figure 12.4(a)] [7]. The ferrite layer next to the absorption material having the highest mag-netic saturation M_{Smax} corresponds to the highest frequency f_{max} of the bandwidth, while the ferrite layer on the opposite side should have the lowest magnetic saturation M_{Smin}, which corresponds to f_{min}. The input/out-put matching of isolator can be realized by using a multistep [Figure 12.4(b)] or taper-type [Figure 12.4(a)] junction.
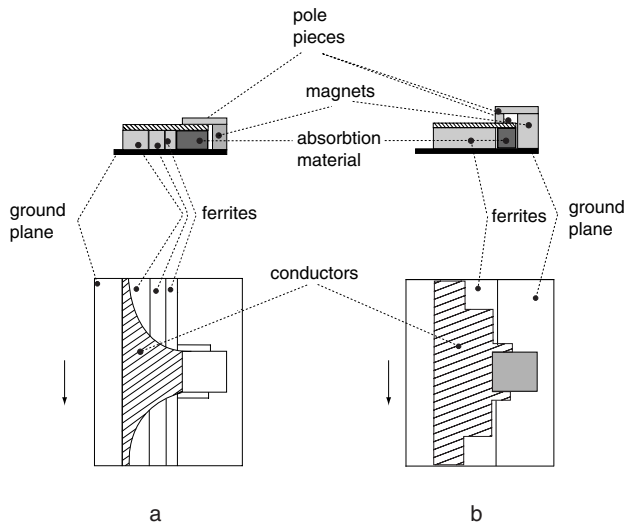
Figure 12.4. Field-displacement isolators: with multilayer ferrite and taper conductor (a), with stepped conductor (b).

Let us consider the problem of circulator/isolator matching. The ferrite junction has a low impedance. For matching to standard 50Ω lines, the impedance-transforming network should be introduced in each of circulator/isolator input/output. Quarter-wavelength transformers are commonly used for these purposes. The length of a transformer can be shortened by using dielectric materials with high permittivity and by meandering the line. Bandwidth greater than an octave can be obtained by using multiple quarter-wavelength sections.

Stubs of length $\Lambda_0/8$ can also provide the matching of L-band circulators/isolators [7].

12.3. LUMPED-ELEMENT FERRITE CIRCULATORS AND ISOLATORS

The distributed circulators operating at low frequencies have comparably large dimensions. The miniaturization of circulators and isolators operating in VHF, UHF, and low microwave frequency ranges may be achieved by using lumped-element circuits, slow-wave structure, and so forth. The sizes of such devices are small because the dimensions of ferrite discs do

not depend on operating frequency. It should be noted, however, that the ferrite sites affect the power rating: The smaller the diameter, the lower the power rating. One of possible way of decreasing the ferrite diameter is to use a slow-wave structure. The utilization of slow-wave structures enables the reduction of the ferrite diameter by a factor of 2.

The circulator with a lumped-element design (Figure 12.5) was proposed by Konishi [8] and others [9–12]. It consists of a ferrite disk with three pairs of center conductors wound on it and insulated from each other in the areas of crossover. The thickness of the insulation layer should be minimized to ensure that all the strips are close to the ferrite. The crossover points should have low parasitic capacitance.

The RF magnetic fields of the coil are oriented by 120° with respect to each other. Since the diameter of the ferrite disk is much less than the wavelength, only the RF magnetic field exists inside the ferrite. The thickness of the ferrite disc in the element circulator approximately equals one-tenth of the disk diameter. The lumped constant capacitors connected in shunt or in series to the terminals provide the storage of electrical energy.

In common lumped-element circulators/isolators the inductances are formed by the junction inductor in connection with the separate capacitors. Such a design leads to the increase in size and fabrication cost. In order to keep the circulator sites small, it is desirable for a lumped circuit element to act both as a capacitor and inductor simultaneously.
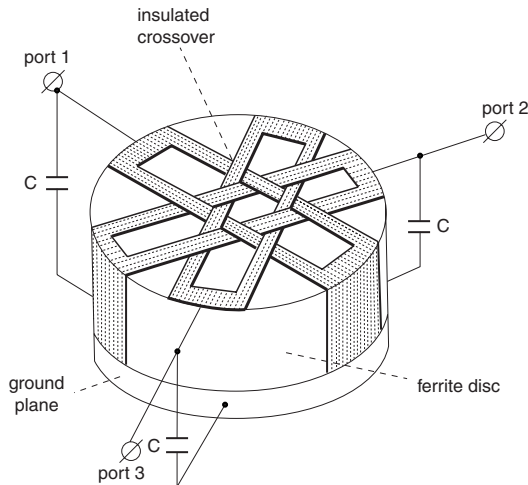
Figure 12.5. Lumped element circulator.

Figure 12.6(a) illustrates a compact lumped-element circulator [13] comprising a set of three spiral strip inductors, which simultaneously serve as capacitances with the bottom metal ground plane. The print inductors are connected with input/output ports by high-impedance strip conductors. Both conductors and inductors have a common junction point located at the center of the circuit. The entire circuit is printed on the top surface of a ferrite substrate. A portion of each inductor is interrupted by
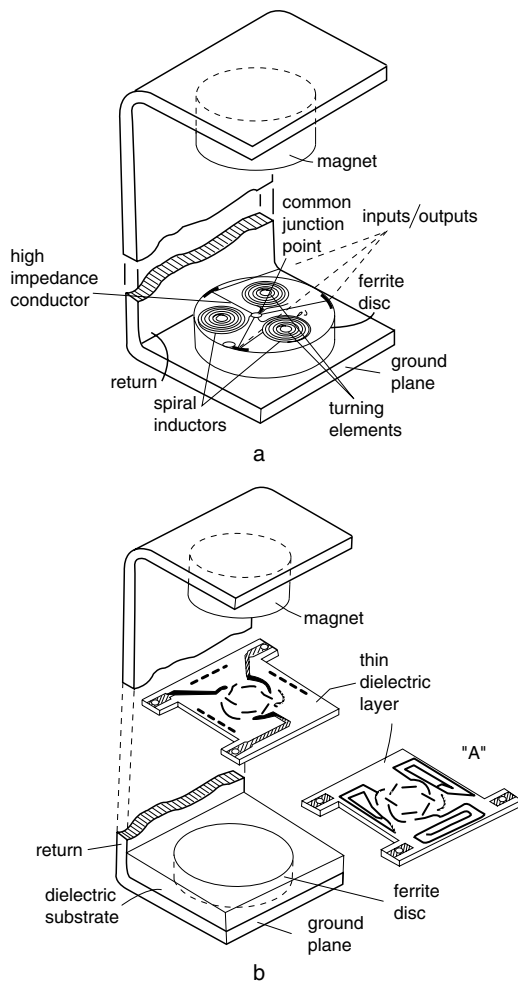
Figure 12.6. Isometric view of lumped element circulator: with circular spirals (a); using crossover print conductors and print spirals (b).

gaps to allow the tuning of the lumped element. Since the inductors also act as capacitors, with both *L* and *C* being as a single entity, such lumped-element circulators eliminate the need for separate capacitors.

Another modification of this idea is illustrated in Figure 12.6(b) [13]. The ferrite substrate is placed inside a dielectric substrate having higher dielectric constant than the ferrite. Each of the three inductances is composed of the two-layer junction inductor connected in series with an additional single-layer inductor. The latter is printed on the thin dielectric layer and positioned directly above the dielectric substrate. The three capacitors are formed of the spiral conductors and ground plane separated by the dielectric substrate. (The high dielectric constant of ceramic enables the decreasing of the size of the capacitors.) View "A" shows the pattern of the bottom side of thin dielectric layer.

In summary, lumped-element circuits allow a reduction in the size and cost of low-frequency RF circulators and isolators. In addition, the lumped-element circulators can be used at relatively high-power levels without generating harmonics and intermodulation products, because such devices operate in the above-resonance range.

12.4. FERRITE AND MAGNET SYSTEMS

The substrate material used in nonreciprocal devices is ferrite or a combination of ferrite and dielectric. The size of the substrate is determined by the operation frequency, effective permeability, dielectric constant of substrate, and the impedance of the system in which the circulator should be incorporated. Circulators and isolators with large bandwidths (>20%) and low operating frequencies will require large substrates. Narrowband devices with simpler matching circuits and devices operating at higher frequencies will use smaller substrates. At the same operation frequency, above-resonance circulators or isolators will allow smaller ferrite discs than the below-resonance devices. This is because effective permeability of ferrite is higher above than below the resonance.

The operating frequency, power level, temperature range, and insertion loss affect the selection of ferrite material. The analysis of the various ferrite materials used in circulators and isolators is given in several existing sources (see, for example, [14]).

The electrical performance of a ferrite device strongly depends on the static magnetic field applied to the ferrite. The characteristics of permanent magnets commonly used in circulators are given in [3]. The required magnetic field is provided by the ceramic, rare earth, or metal permanent magnets. The magnets are initially magnetized up to saturation and then de-Gaussed to the specified level as part of the factory tuning procedure.

The required intensity of the external magnetic field depends on the frequency of operation, the mode of operation (above- or below-resonance), the type of ferrite material, and the shape of the ferrite insert. The utilization of magnets with high-energy product allows decreasing the number of magnet sites. In addition to its strength, the field should also have a certain orientation. The devices incorporating thin ferrite plates or disks are especially sensitive to the field orientation. The deviation of the external magnetic field from the normal to the plane of the ferrite insert introduces a change in the effective demagnetization factor and leads to an increase of losses. This deviation from the normal should not exceed $3°$ to $5°$.

The saturation magnetization of the ferrite and the magnetic field of the magnets change with temperature variations. If no measures are taken, the center frequency and bandwidth will change with temperature. To avoid the alteration of electrical performance, the magnetic system should incorporate magnetic materials that provide thermal stabilization. The steel alloy composed of 29% to 32% nickel in iron (that of Carpenter or Simond) is used for such purposes.

The temperature-compensating elements can be inserted in the magnetic circuit in two ways. The first way is when the compensators are placed under the magnets. In this case the temperature-compensating disc is in "series" with the magnetic circuit, thus providing a negative $\Delta H_e/\Delta T$ (decreasing magnetic field with increasing temperature). The second way is when the compensating element short-circuits the magnet. Correspondingly, the compensator acts as a shunt providing a positive compensation $\Delta H_e/\Delta T$ (increasing magnetic field with increasing temperature). In the series configuration the entire flux passes through the temperature-compensating disk, while in the shunt configuration, a fraction of the flux passes through the compensator.

Let us consider the *three-dimensional tandem nonreciprocal circuit* to simplify the magnet system in cascaded circulators/isolators (Figure 12.7) [15]. In this circulator the permanent magnet is located between the

ground plane portions of two *C*-shaped magnetic circuit elements. Figure 12.7(b) represents a vertical cross-sectional view of the tandem circuit, where a tandem-connected circuit is comprised of housing, two magnetic circuit elements (each having a shield portion and a return portion), a ground plane, two ferrites, a permanent magnet, a dielectric film, and a dielectric substrate. Each ferrite is located inside a dielectric substrate flush with its upper and lower surfaces. As shown in Figure 12.7(a), each junction, including the center conductors, is printed on the dielectric film. The dielectric film has a *C*-like shape bent around the ferrites and centered around the permanent magnet. The vertical portion of the film is used to connect the top and bottom print circuits. This vertical portion can also be used to install an additional element, such as an amplifier, between the tandem-connected circuits. The magnetic circuit can be modified to accommodate multijunction devices [15].

The three-dimensional devices described above have a better integration level in the horizontal plane. They also provide a lower cost and higher quality as compared with the traditional multijunction circulators.

The circulators and isolators can be realized in a very popular drop-in configuration [Figure 12.8(a, b)]. The tab leads in drop-in devices are extensions of the center conductor itself. The tabs provide good contact with the integrated circuit and tension-free solder joint. The bottom of the unit should be mounted on a flat surface to ensure proper grounding. Drop-in-type ferrite devices in a flange configuration are frequently screwed into place (see Figure 12.8).

The design of drop-in ferrite circulators can be aided by the relatively new direct-bond copper (DBC) technique [16], which will be described in Chapter 14. In DBC drop-in circulators, metal conductors and tabs on ferrite material provide easy interconnection to other MICs. The comparison of DBC with thin-film and thick-film microstrip devices shows that the DBC microstrip circulator has the lowest insertion loss.

The microstrip circulator or isolator, having no special leads [Figure 12.9(a, b)], can be installed directly in the integrated module. Such a small device allows for its incorporation into integrated circuits where there is not enough room for other types. The interconnection between the microstrip circulator (or isolator) and adjacent microstrips can be realized using copper or gold ribbon, wires that may be soldered, welded, or bonded to the adjacent microstrip lines to avoid an electrical discontinuity. The ribbon width should be slightly smaller than the strip widths of
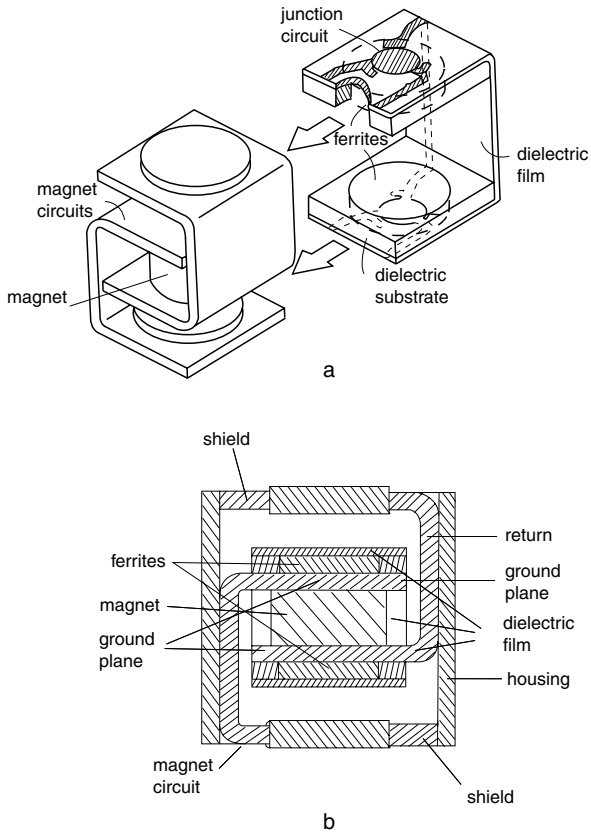
Figure 12.7. Three-dimensional two-junction circulator with one magnet: isometric view (a); vertical cross-section view (b).
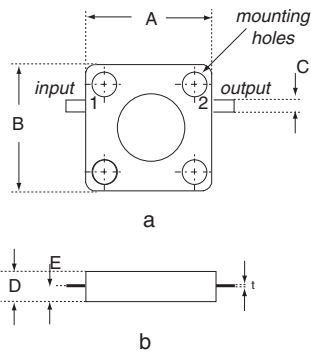
Figure 12.8. Drop-in isolator: top view (a); side view (b).
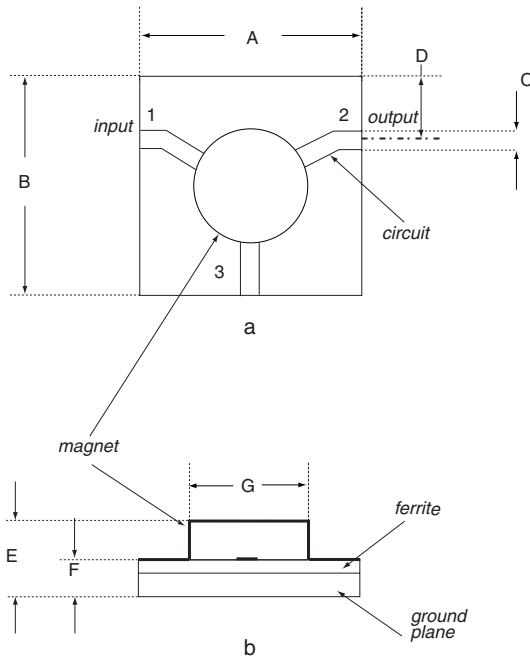
Figure 12.9. Miniature ferrite circulator with printed circuit on ferrite substrate: top view (a); side view (b).

the input/output ports of the ferrite device and the outside strip lines. In general, low-frequency microstrip circulators have a single magnet placed on the ground plane. At higher frequencies ($f > 7$ GHz), an additional magnet is used on the circuit side.

High-power ferrite devices feature some peculiarities. An increased average power level will increase the dissipated power. This will in turn increase the operating temperature and lead to a degradation in performance such that some convection or cooling features will be required. The power dissipated in the circulator is proportional to the insertion loss. The average power rating will also depend on the resultant mismatch at the circulator output port. The peak power is the amount of power that can be handled by the circulator without creating a voltage breakdown. In below resonance type devices, the high power level at the peak also causes an increase in the insertion loss due to the nonlinear effects of the ferrite material. The peak power threshold depends on the junction geometry, bandwidth, and ferrite material properties. The nonlinear effect in a ferrite can be used for the generation of harmonics at microwaves. In such

applications the ferrites can be operated at much higher power levels than crystal diodes.

12.5. HIGH-ISOLATION CIRCULATOR NETWORK

The conventional ferrite circulators when properly matched usually offer isolation in the range of 30 to 35 dB when properly matched. Isolation, however, degrades considerably when the circulators are connected to the loads, deviating from the ideal matching. It is, however, possible to maintain high isolation by using an additional compensation network.

Figure 12.10 illustrates one possible option for the compensation network. A first coupling element is connected to a variable phase shifter to provide a sample of the input signal. An output of the variable phase shifter is connected to a variable attenuator joining a combiner. The variable phase shifter and variable attenuator provide the variation of phase and amplitude of the input signal sample. The combiner sums the input signal sample with the parasitic reflection signal. A second coupling element is connected to the combiner output to provide a sample of the sum product to an amplitude compensation block. This block and the phase comparator generate the driving signals for the compensation network to change the magnitude and phase of the sample input signal in such a way that the amplitude of the sampled signal is the same as that of the mismatched signal, but is 180° out of phase from this parasitic signal. As a result, the parasitic leakage signal will be compensated for by the input signal sample, and the circulator will have higher isolation.
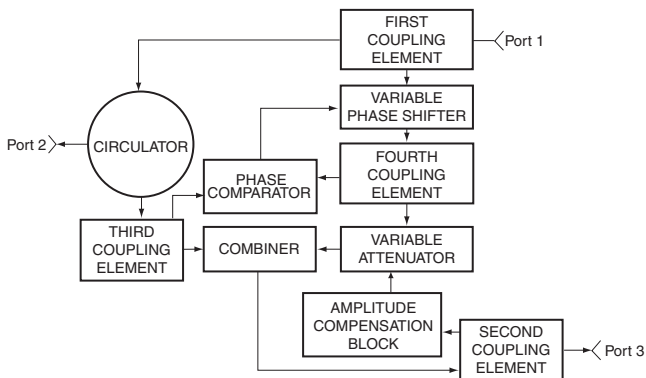
Figure 12.10. High isolation circulator with compensation network.

12.6. NONFERRITE NONRECIPROCAL DEVICES

The common ferrite nonreciprocal devices are not capable of insuring small losses in a wide frequency band or providing high isolation when they are connected to real mismatched loads.

Emerging new principles and technologies offer the possibility of fabricating of nonreciprocal devices without using ferrites. Several designs utilizing an active circulator have been described in [17–19].

Figure 12.11 shows a nonferrite four-port circuit that realizes a nonreciprocal transmission of FM signals [20]. This device includes several (k) tracking filters (1). The input of each filter is connected to a corresponding output of frequency modulator (3) through a delay line (2) of the modulating signal. The other delay lines (4) are connected between each pair of consecutive tracking filters to introduce a delay in the RF signal. Some of the RF delay lines (4) are followed by the leads which act as the outputs (6, 7, 8) for the device. An FM signal going into the input port (5) passes through the chain of alternating filters and RF delay lines before getting the port (6). The modulating signal originating in the frequency modulator (3) passes through the delay lines (2). The parameters of each delay line are set to ensure that the modulating signal is in-phase with the RF signal arriving at the input of the corresponding tracking filter when the signal flows in the forward direction (marked by the arrow). With such a setting all filters between input (5) and output (6) are tracking in phase, and the signal passes through to the output (6) with minimal losses. The same happens with signals propagating from 6 to 7 and from 7 to 8.

The RF signal does not pass in the reverse direction because of the mismatch between the modulating and RF signals increasing along the chain. The calculations assuming that the bandwidth of each tracking filter is 4 times greater than the frequency of modulation and that the deviation of the FM signal is 20 times greater than the side bandwidth have revealed that for the chain of six tracking filter-delay line pairs, the isolation will be exceed 65 to 80 dB. The isolation can be further increased by increasing the number of tracking filters in the chain and by increasing the ratio of frequency deviation to the bandwidth of the filters. To ensure full isolation between ports (for example, between ports 5 and 7) a delay equal to half the period of modulation is introduced between the RF signal at the output (6) and the first tracking filter of the next chain (6–7). Besides the mentioned isolation property, the described nonreciprocal device also pro-
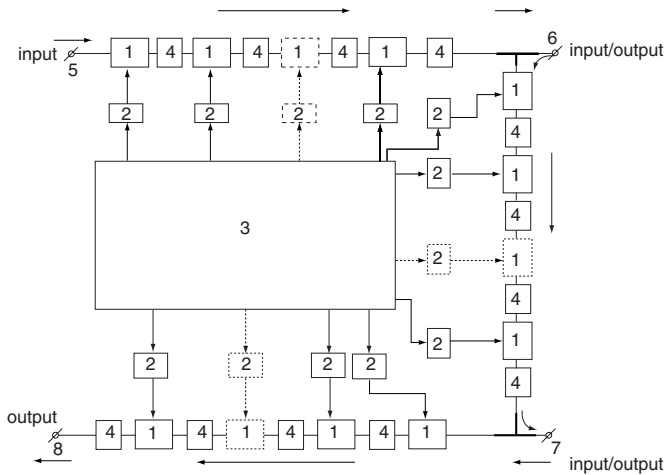
Figure 12.11. Four-port non-reciprocal circuit with tracking filters: (1) tracking filter, (2) delay line for modulating signal; (3) frequency modulator; (4) delay line for RF FM signal.

vides a high phase selectivity of FM signals against the background of various interference.

REFERENCES

1. Bosma, H., "On Stripline Circulation at UHF," *IEEE Trans. on Microwave Theory Tech.,* Vol. MTT-12, January 1964, pp. 61–72.
2. Fay, C. E., and R. L. Comstock, "Operation of the Ferrite Junction Circulator," *IEEE Trans. on Microwave Theory Tech.,* Vol. MTT-13, 1965, pp. 15–27.
3. Helszajn, J., *Microwave Planar Passive Circuits and Filters*, New York: John Wiley & Sons, 1994.
4. Helszajn, J., and D. S. James, "Planar Triangular Resonators with Magnetic Walls," *IEEE Trans. on Microwave Theory Tech.,* 1978, pp. 95–100.
5. Hines, M., "Reciprocal and Nonreciprocal Modes of Propagation on Ferrite Stripline and Microstrip Devices," *IEEE Trans. on Microwave Theory Tech.,* Vol. MTT-19, No. 5, 1971, pp. 442–451.
6. Scloemann, E., and R. E. Blight, "Broad-Band Stripline Isolators," *IEEE Trans. on Microwave Theory Tech.,* Vol. MTT-34, No. 12, December 1986.

7. Vambersky, M., V. Abramov, and V. Kazancev, *Design of Ferrite Non-Reciprocal Devices,* Moscow, Russia: Radio and Svyaz, 1982.

8. Konishi, Y., "Lumped Element *Y*-Circulator," *IEEE Trans. Microwave Theory Tech.,* Vol. MTT-13, November 1965, pp. 852–864.

9. Dun, V. E., and R. W. Roberts, "Miniature VHF and UHF Circulators Use Lumped Element Design," *Microwaves,* December, 1963, pp. 46–47.

10. Deutsch, J., and B. Weiser, "Resonance Isolator and *Y*-Circulator with Lumped Elements at VHF," *IEEE Trans. Magn.,* Vol. MAG-2, September 1966, pp. 278–282.

11. Knerr, R. H., "A Thin-Film Lumped Element Circulator," *IEEE Trans. Microwave Theory Tech.,* Vol. MTT-17, December 1969, pp. 1152–1154.

12. Helszajn, J., and McDermott, "The Inductance of a Lumped Constant Circulator," *IEEE Trans. Microwave Theory Tech.,* Vol. MTT-18, January 1970, pp. 50–52.

13. Kurian, T., and L. G. Maloratsky, "Compact Lumped Constant Non-Reciprocal Circuit Element," U.S. Patent #5,164,687, November 1992.

14. Linkhart, D. K., *Microwave Circulator Design,* Norwood, MA: Artech House, 1989.

15. Kurian, T., and L. G. Maloratsky, "Compact Tandem Non-Reciprocal Circuit," U.S. Patent #5,185,587, February 1993.

16. Yoshikawa, Y., et al., "Drop-In Ferrite Circulators Fabricated by Direct-Bond Copper Technique," *3rd Asia-Pacific Microwave Conference Proceedings,* Tokyo, Japan, 1990.

17. Tanaka, S., N. Shimommura, and K. Ohtake, "Active Circulators: The Realization of Circulators Using Transistors," *Proc. IEEE,* Vol. 53, No. 3, 1965, pp. 260–267.

18. Bahl, I. J., "The Design of a 6-Port Active Circulator," *IEEE MMT-S Int. Microwave Symposium Digest*, 1988, pp. 1011–1014.

19. Katzin, P., et al., "6 to 18 GHz MMIC Circulators," *Microwave Journal,* May 1992.

20. Vinitsky, A. S., and L. G. Maloratsky, "Non-Reciprocal Frequency-Modulation Device," Patent USSR, No. 585610, cl. H 04 B 1/38, January 27, 1977.

This Page Intentionally Left Blank

Microwave Integrated Subassemblies

RF and microwave passive and active components form different subsystems and systems. In this chapter we will consider several examples of microwave integrated subassemblies using passive components and control devices that have been described in this book.

13.1. *L*-BAND MULTIFUNCTIONAL TRANSMIT/RECEIVE MODULE

A schematic view of a multifunctional TX/RCV module is presented in Figure 13.1(a). An *L*-band transmitter and receiver are connected to a single antenna through an LPF. This network provides three different modes: transmit mode, receive mode, and self-test mode.

During the transmit mode, the switch should have sufficient isolation in the receiver port to protect the receiver front end from damage. Therefore, switch diodes D1, D2, and D4 [see Figure 13.1(a)] become forward-biased (low-impedance state). The series PIN diode D1 appears as a low impedance to the transmitter signal heading towards the antenna, and the shunt diodes D2 and D4 effectively short the antenna terminal of the receiver to prevent overloading. The insertion loss of the transmitter and
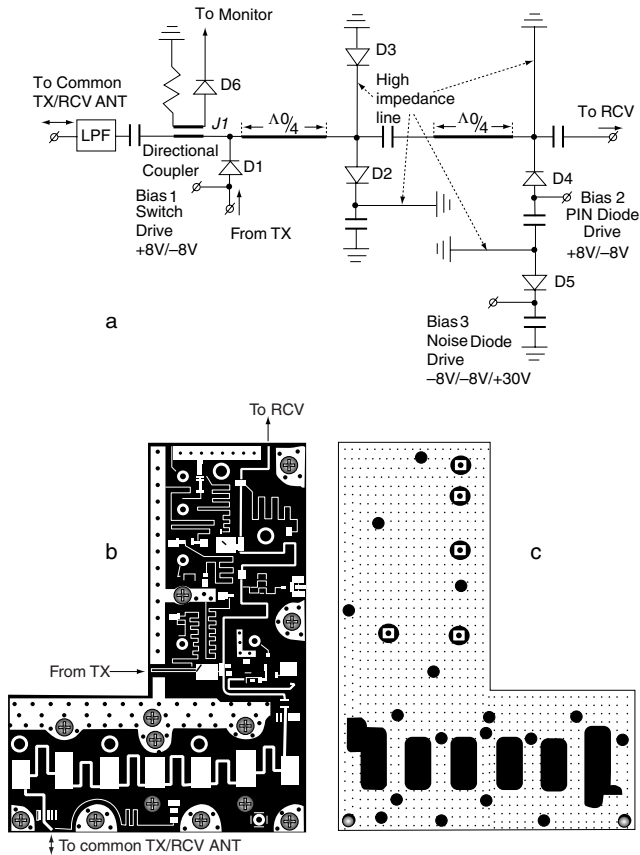
Figure 13.1. Multifunctional RF transmit/receive module (used in Rockwell Collins DME system): schematic (a); PCB top side (b); PCB bottom side (c).

isolation of the receiver depend on the diode resistance (see Chapter 10). The quarter-wavelength section [see Figure 13.1(a)] transforms the short circuit formed by the shunt diode D2 into an open circuit at the common junction $J1$. In order to protect the receiver from high power, high transmitter isolation is required, but in the receiver mode, such high isolation is not necessary.

In receive mode, the PIN diodes D1, D2, and D4 become reverse biased and present high impedances, which create isolation of the transmitter from the antenna and low insertion loss between the common antenna and receiver. The OFF transmitter is isolated from the common antenna by the high capacitive reactance of the series diode D1. To mini-

mize insertion loss on the receiver port, the distance from the series diode D1 to the common junction should be at an absolute minimum.

The limiter diode D2 and Schottky detector diode D3 provide the limiter function for strong parasitic outside signals during receive mode. This quasi-active limiter (see Chapter 10) uses the Schottky detector diode D3, which supplies dc current to the limiter diode. These two diodes are RF-isolated from each other, but they are dc coupled by the high impedance transmission line. The limiter diode D2 is turned on primarily by the external bias current from the Schottky detector diode D3, which is sensitive to the incident signal. The Schottky detector–driven limiter provides protection from fast rice or nanosecond-wide pulses with low threshold and leakage levels.

The self-test mode is realized by a noise source network (noise diode D5 and drive PIN diode D4) and monitor circuit (Schottky detector diode D6 and coupled-line directional coupler). In the noise-test mode for testing the RCV, drive PIN diode D4 is forward biased, while the noise diode is pulsed at the voltage required to generate noise for testing the receiver. As a result, the noise signal is generated by diode D5 coupled through diode D4 and applied to the receiver. The possible failure situation when diode D1 and (or) diode D2 are opened should be controlled by the power

TABLE 13.1. Experimental Characteristics of the
Multifunctional Transmit/Receive Module

	TX Mode				RCV Mode			
Freq. (MHz)	Insertion Loss (dB)	Isolation (TX to RCV) (dB)	TX Port Return Loss (dB)	Ant. Port Return Loss (dB)	Insertion Loss (dB)	Isolation (RCV to TX) (dB)	RCV Port Return Loss (dB)	Ant. Port Return Loss (dB)
962	—	—	—	—	1.1	12.3	19.1	24.6
1025	0.85	48.8	21.6	22.6	—	—	—	—
1090	0.8	51.1	29.1	34.2	1.3	11.9	16.7	16.9
1150	0.8	43.8	20.4	20.3	—	—	—	—
1213	—	—	—	—	1.3	11.6	24.2	21.4

monitor during transmit mode. Therefore, the self-test mode is realized by a combination of noise-injection and monitoring of output transmitter power.

Figure 13.1(b, c) illustrates PCB of the multifunctional TX/RCV module using microstrip line with 10-mil dielectric thickness. Experimental characteristics of this subassembly versus frequency are listed in Table 13.1.

The LPF uses series high-impedance SS inductive elements and low-impedance shunt microstrip capacitive elements [1] (see Chapter 9). The 11-section LPF provides low insertion loss at 0.3 dB in the passband and high rejection for the harmonics of the transmitter to help in preventing interference to the equipment (second harmonic attenuation is greater than 70 dB).

13.2. ELECTRICALLY TUNABLE *L*-BAND PRESELECTOR

The electrically tunable preselector [2–4] is a key element in the receivers of communication, avionics, and radar systems. For example, avionics distance measurement equipment (DME) requires a very low noise preselector with a tracking filter regime in the 962–1213-MHz frequency range. The passband of the tunable filter should be at 20 MHz, securing 10 times the reduction of noise and interference. Narrowband RF and microwave preselectors are required to prevent large off-channel signals from overdriving the receiver front end. To minimize the receiver input noise figure, the tunable BPF is separated by an LNA into two filters. The first two-pole filter before LNA prevents undesirable signals from over-driving the LNA. The second three-pole filter after LNA provides selectivity against receiver image and spurious frequencies. The three-pole BPF placed after LNA has a negligible effect on the overall preselector input noise figure.

To reduce size, loss, and cost, and to improve stopband performance, the comb-line bandpass filter was used (see Chapter 9 and [4]).

The electrically tunable BPF [Figure 13.2(a)] consists [4] of the SS resonators, which are grounded at one end, high Q-factor GaAs varactor diodes, and lumped-element loading capacitors between the other end of each resonator and the ground plane. SS (see Chapter 2) provides high Q-factor ($Q \approx 500$), stability over a wide temperature range and high imped-

ance range [1]. The tunable BPF was realized with reverse-biased varactor diodes D_1, D_2, D_3, D_4, and D_5, which were used as tuning elements to adjust comb-line BPF at the full frequency range.

Preselector selectivity depends on filter Q-factor. The total quality factor of the tunable BPF is taken as the combination of the resonator, loading capacitor, and varactor diode Q-factors. For a low-loss L-band comb-line filter, the Q-factor of varactor diodes is an extremely important parameter. The Q-factor of the best varactor diodes is lower than that of the SS resonators and loading capacitors, and it dominated when filter losses were calculated.

To increase Q, GaAs varactor diodes can be used. GaAs abrupt varactor diodes MA46617 (from "M/A-COM") with $Q = 210$ at 1 GHz are used as variable capacitors. For these diodes, the total capacitance ratio $C_{T0}/C_{T45} = 4.4$–6.9, where C_{T0} and C_{T45} are the varactor capacitances at 0 and 45 volts, respectively. Parameters of these diodes (junction capacitance, capacitance ratio, Q-factor, and breakdown voltage) determine the performance of the tuning filter. When the varactor diode bias is changed, the capacitance of the varactor diode tunes resonant electrical length and the center frequency of the filter resonator. The tuning voltage for every varactor diode is generated by the microprocessor.

For a 25% tuning range, we can use varactor diodes and shunt capacitors C_1, C_2, C_3, C_4, and C_5. To allow for biasing, capacitors C_6, C_7, C_8, C_9, and C_{10} are added [see Figure 13.2(a)]. These capacitors provide an RF short for the varactors and an open circuit for the biases.

The preselector is based on combination of suspended stripline and microstrip line. These two transmission lines offer certain advantageous features with respect to each other [1]. The microstrip design of the LNA offers advantages regarding heat removal and integration, since a good ground connection (with minimum reactance) is usually required for such devices. The LNA consists of a discrete MGA-85563 (from "HP") [5] and operates from +3-VDC bias supply and draws a nominal current of 15 mA. The RF layout of the LNA is shown in Figure 13.2(b). All of the ground pins of the MMIC LNA are connected to the RF ground plane on the backside of the microstrip line by means of the vias that are placed near the package terminals. Multiple microstrip vias minimize ground path inductance.

The inductor L_1 placed in series with the input of the LNA is all that is necessary to match the input to the 50Ω two-pole BPF output. The dc
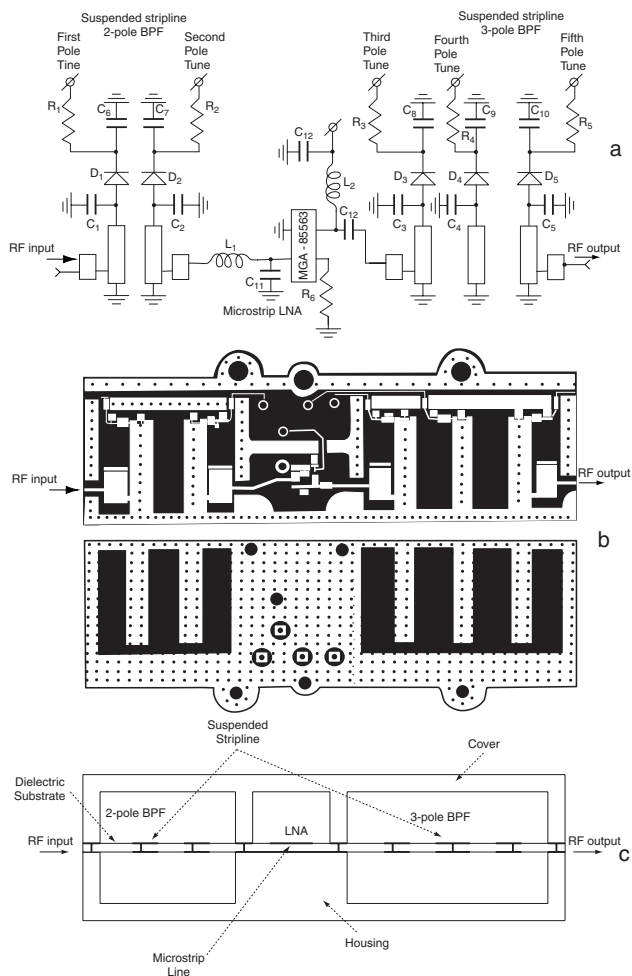
Figure 13.2. Electrically tunable *L*-band preselector (used in Rockwell Collins DME system): schematic view (a); top and bottom PCB view (b); side view (c).

blocking capacitor C_{12} is used at the output of the MMIC to isolate the device from three-pole BPF.

The input/output network provides transition from the microstrip line LNA to the SS BPF. For low-frequency application ($f \leq 1$ GHz), the straight connection between microstrip and SS can be used. This connection includes the step between center conductors of two lines and ground plane step to provide 50Ω impedance for both lines. For higher-frequency
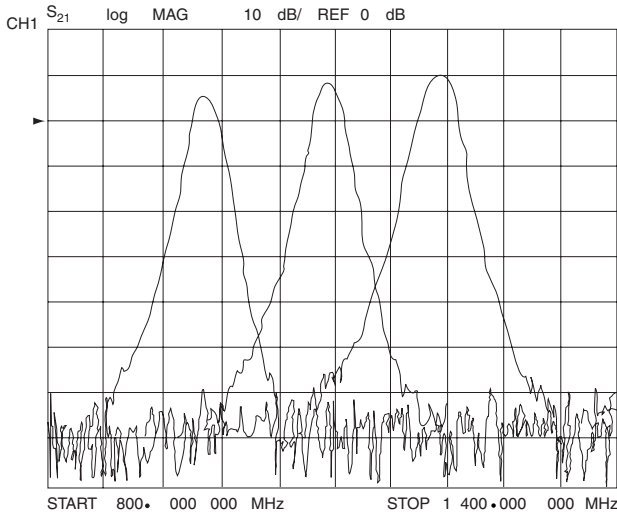
Figure 13.3. Tunable preselector frequency response.

applications, the special transition between these two lines [1] can be used.

The preselector (Figure 13.2) was fabricated on 10-mil dielectric substrate TLE-95 (from "Taconic"). The PCB was suspended over a silverplated aluminum machined housing. The depth of the housing and cover was 0.200 in. Two parallel internal walls prevent RF leakage from the input to the output of the preselector and improve isolation from the output to the input. The total dimensions of the preselector are 5.000 in. × 2.000 in. × 0.500 in. The layout of the preselector is shown in Figure 13.2(b). Figure 13.3 illustrates the frequency response of the tunable preselector for various varactor tuning voltages. As the filter tunes from 962

TABLE 13.2. Experimental Characteristics of the *L*-Band Preselector

Frequency (MHz)	3-dB BW (MHz)	Input Return Loss (dB)	Input Noise Figure (dB)	Gain (dB)
962	18.1	23.7	4.6	4.5
1090	20.8	20.6	3.8	6.0
1213	24.4	26.3	4.0	7.0

MHz to 1213 MHz, 3-dB bandwidth varies from 18.1 to 24.4 MHz. Table 13.2 summarizes the performance of the preselector in Figure 13.2.

The preselector input matching is good with a return loss of better than –18 dB; the total preselector gain is around 4.5 dB. The increase in preselector insertion loss at the low end of the tuning range is due to the decrease in the electrical length of the SS resonators and as a result of the decreased resonator quality factor.

13.3. SWITCHABLE BALANCED AMPLIFIER

The balanced amplifier is normally used where it is important to present good noise performance, input match, and high output power. This amplifier requires at least one divider and one combiner. The input splitter divides the input power equally between two output ports. The output combiner recombines the output signals from amplifiers or other devices.

Disadvantages of existing balanced amplifiers include low reliability, low efficiency, average power limitation, moderate bandwidth, and high distortion if one of the amplifiers fails. The combiner output power is reduced further as the power from the remaining operational (active) amplifier is divided between the isolation resistor and the output port. In this case, the output power of the conventional network drops not by 3 dB, but by 6 dB. Half of the output power of the still-functioning amplifier will be dissipated in the isolation resistor. The average power handling capability of the conventional Wilkinson power divider depends upon the average power rating of the isolation resistor (see Chapter 8). This condition alone drives the need for an isolation resistor with power-handling capacity of at least one-half of the maximum output of a single amplifier. This results in excessive heat dissipation in the isolation resistor, limiting power capabilities, especially in high-power applications.

Higher-power resistors have a larger surface area and greater parasitic capacitance between resistor and ground plane. The required tuning circuitry for compensation of this parasitic capacitance is sometimes limited in bandwidth. The cost of a high-power resistor and its installation with a heat sink may be high.

During the failure mode, the reflected signal from the failed amplifier creates mismatching of the driver amplifier (before balanced amplifier) because half the reflection power will appear at the driver amplifier out-
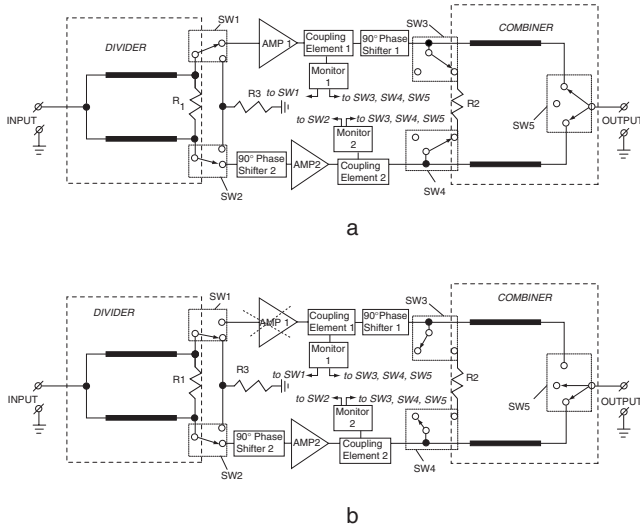
Figure 13.4. High efficiency balanced amplifier: full power mode (a); failure mode (b).

put. In the event of an *N*-way power combiner, when a failed state occurs in *M* power amplifiers, the efficiency of the combiner is $\eta = (1 - M/N)$. As the number *M* of the failed amplifiers is increased, the efficiency is decreased.

There are generally known configurations with a plurality of low-power amplifiers in order to maximize efficiency when some amplifiers have failed [6–8]. In these amplifiers, as the number of nonoperative channels increases, additional degradation of the impedance matching among the operative channels is inevitable; as a result, the divider/combiner characteristics will suffer accordingly.

Figure 13.4(a) illustrates a novel high-efficiency balanced amplifier [9], which includes the Wilkinson power divider and two SPDT switches: SW1 and SW2. During the full-power operating mode, switches SW1 and SW2 electrically connect amplifiers, AMP1 and AMP2, to the power divider. Besides, during this mode, switches SW3 and SW4 electrically connect the power combiner's inputs to the isolating resistor R2, while SW5 still connects the quarter-wavelength lines to the output of the combiner.

Now consider the failure mode [Figure 13.4(b)] separately at the input and output sides of the balanced amplifier.

- *Input side:* Switch SW1 (or SW2) connects additional resistor R3 to one power divider output. The value of the grounded resistor R3

should be equal to the impedance of the divider outputs. Monitors 1 and 2 represent monitoring the output power of both amplifiers AMP1 and AMP2 and provide driver signals for switches SW1 and SW2. In the event that output power of the amplifier AMP1 drops [see Figure 13.4(b)], monitor 1 fixes minimum (or zero) power, and the control circuit forms a driver signal for switching switch SW1 to provide a connection between the divider top output and resistor R3, as well as the disconnection of this output from the AMP1.

At the same time, the control circuit in monitor 2 provides a driver signal to SW2 to connect the divider second output to AMP2 and disconnect of this output from the grounded resistor R3. Therefore, balanced amplifier input power is divided equally between the active amplifier AMP2 and grounded resistor R3. The input power of AMP2 will be the same as in the full-power operating mode. Reflected signal from the failed amplifier does not appear at the balanced amplifier input because the failed amplifier channel is removed from operation.

•   *Output side:* Monitor 1 forms a driver signal to provide opened switch position for switches SW3 and SW4 (R2 is disconnected at both sides). Switch SW5 disconnects the top quarter-wavelength line from the combiner's top output. As a result, maximum power from the active AMP2 will be at the output terminal of the balanced amplifier in contrast to the conventional balanced amplifier with an additional 3-dB loss of active amplifier power. The analog procedure of switching operation takes place only if amplifier AMP2 fails.

The novel switchable balanced amplifier provides a greater average power rating and high efficiency and can be realized with low-power isolating resistors with low cost, small size, and lower parasitic capacitance.

13.4. HIGH-ACCURACY HIGH-POWER WHISPER/SHOUT ATTENUATOR

This section describes novel attenuators for aircraft traffic alert and collision avoidance systems (TCAS). On aircraft, a small four-element TCAS antenna array capable of four directional beams is typically used. The four directional beams provide some, but not sufficient, segregation in space. For further segregation, a process called whisper/shout is used.

Whisper/shout essentially varies TCAS transmitter power levels and correspondingly varies the TCAS receiver threshold level to segregate responding transponders in relation to the distance from the protected aircraft. A TCAS whisper/shout step attenuator is required to attenuate a 1.03-GHz transmitted signal in excess of 1-kW peak power, monotonically from 0 dB to 31 dB in 1.0 +/–0.5–dB increments.

A common step attenuator has a number of individual attenuators, or attenuator cells, selectively connected in series. Each attenuator cell attenuates an input signal by a predetermined value, which is typically measured in decibels (see Chapter 10). A step attenuator may be designed to include n attenuator cells having attenuation values of 2^k (dB), where $k =$ 0, 1, 2, …, n. An individual switch pair is provided for each attenuator cell. By opening and closing the switches, it is possible to select any given value of attenuation up to the sum of the attenuation of all of the attenuator cells.

Figure 13.5(a) shows a high-power step attenuator [10], which consists of five single-step attenuator cells of increasing levels of attenuation. Each cell includes a high power T- or π-resistive network that is selected to provide the desired attenuation and to equalize the input/output impedance of the attenuator cell with the input/output impedance of the step attenuator. Each single-step attenuator cell consists of a pair of SPDT PIN diode switches. These switches are directed at input signal either through an attenuator cell or through a bypass line (reference pass), which bypasses the attenuator cell. It is possible to select any given value of attenuation between 0 dB and 31 dB (in 1-dB steps) as desired.

One problem with a step attenuator is that significant losses are incurred in the switches and transmission lines even when the input signal does not pass through the attenuator cells. To resolve this problem, another type of step attenuator has been developed, shown in Figure 13.5(b), which includes a common bypass line 1. When attenuation is desired, switches are positioned as shown in Figure 13.5(b) to direct the input signal through the attenuator cells. When no attenuation is desired, switches 3 and 4 are positioned to direct the input signal through the common bypass line 1. This arrangement reduces the insertion losses because the nonattenuated input signal does not pass through all of the switches and attenuator cells.

However, such an arrangement does not address step error, which is also present in known step attenuators. Step error occurs when the differ-
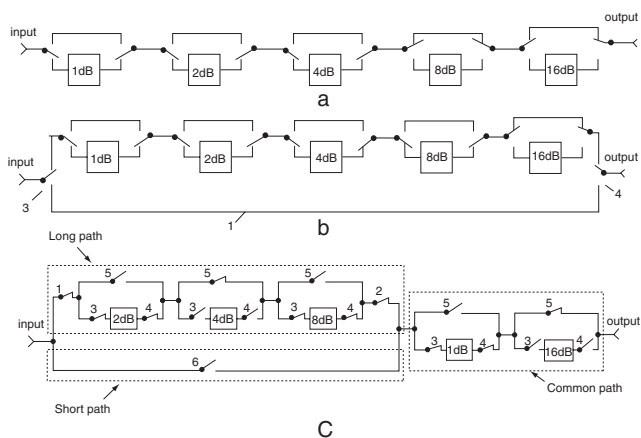
Figure 13.5. Step attenuator block diagram: with five attenuator cells (a); with five attenuator cells and common bypass line (b); with short, long, and common path (c).

ence between two attenuation levels is too small to differentiate between the levels. For instance, if the step error between attenuation levels 1 dB apart is more than +/–0.5 dB, it will be difficult to tell which attenuation level is desired. To minimize the 1-dB step error to less than +/–0.5 dB, the bypass line 1 [Figure 13.5(b)] should be insulated from the line having the attenuator cells to a level of at least 70 dB. This may be accomplished by including a multiple diode switch (see Chapter 10 and [11–13]). However, the multiple diode network requires more area and increases the insertion losses in the attenuation such that the insertion loss through the switches is greater than 1.5 dB. Therefore, the first 1-dB step is difficult to attain.

Figure 13.5(c) illustrates the novel whisper/shout attenuator network [14]. This step attenuator has a long path and short pass in parallel with each other and also a common path. A plurality of attenuation cells of 2 dB, 4 dB, and 8 dB are disposed in series between long-path input switch 1 and long-path output switch 2. Each attenuator cell has an attenuator cell input switch 3 and an attenuator cell output switch 4 (see Chapter 10). An attenuator cell bypass switch 5 is disposed along the attenuator cell bypass line and permits the signal to selectivity bypass the attenuator cell with which it is associated. The short path includes SPST switch 6. The common path includes a plurality of attenuator cells (1 dB, 16 dB) connected in series with each other. In this attenuator, the signal may be attenuated from 0 to 31 dB in 1-dB steps with good accuracy.

Because attenuator cells providing 1 dB and 16 dB of attenuation are disposed within a common path, isolation requirements between the long and short paths are reduced at 17 dB when compared with the conventional step attenuator shown in Figure 13.5(b). This permits size reduction and simplified construction. Furthermore, the short path SPST switch 6 can be realized with less isolation than isolation of switches that are used in the conventional step attenuator [Figure 13.5(b)]. For the step attenuator [Figure 13.5(c)], isolation between the short path and the long path should be 50 to 55 dB. This isolation level can be realized by a two-diode switch (see Chapter 10) in the short-path network.

The miniature microstrip L-band step attenuator requires a substrate having a high dielectric constant and a minimum thickness. Parasitic capacitances between the pads of the electronic components (such as diodes, capacitors, resistors, and the like) and the ground plane are a point of concern when using microstrip attenuators. Such parasitic capacitances cause additional losses, narrow the band of available frequencies, and require high manufacturing tolerances. To eliminate these problem, the pads of electronic components have no underlying ground. Alternately, the grounded housing should be far from the printed circuit board. The reduction in parasitic capacitance also reduces the need for additional tuning and matching elements.

A 1-GHz high-power precision step attenuator (Figure 13.6) has been built according to the block diagram of Figure 13.5(c). The microstrip 1-GHz step attenuator provides pulse power at 1.6 kW and attenuation in 1-dB steps with an increment error of +/–0.35 dB and a minimum insertion loss of 1.1 dB.

13.5. *C*-BAND MULTICHANNEL RECEIVER

Figure 13.7 illustrates the PCB of a three-channel C-band receiver for an avionics microwave landing system (MLS). Three antenna inputs are connected to three bandpass filters and switches. A common junction of three switch outputs is connected to a directional coupler for coupling with noise source for receiver self-test. A common preselector includes two-stage LNA, limiter/AGC and BPF. When one antenna channel is opened, the shunt PIN diode of this channel is reverse biased so that the received signal is applied to the front-end circuits. At the same time two other PIN
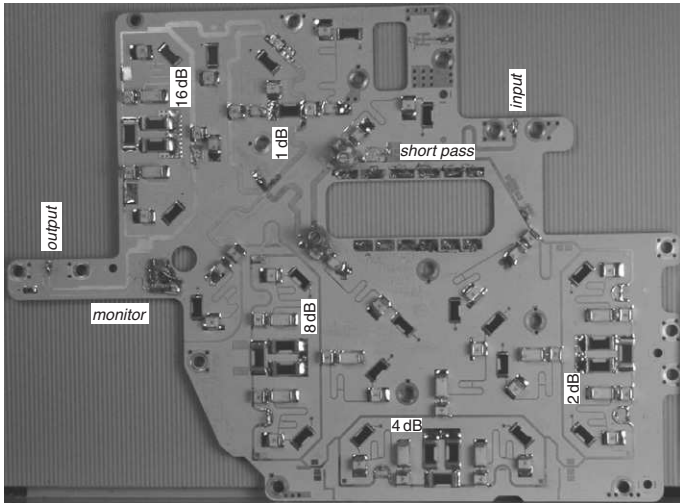
Figure 13.6. *L*-band step attenuator ASSY (used in Rockwell Collins TCAS).

diodes are forward biased. This allows a signal from only one antenna to be used.

The *C*-band subassembly utilizes a combination of low-loss SS to minimize input N.F. and a microstrip line to minimize size. BPF1, BPF2, BPF3, SW1, SW2, and SW3 utilize SS. All front-end circuitry is assembled in a microwave cavity. LNA1, AGC/Limiter, LNA2, BPF4, mixer, and self-test network (STN) are based on microstrip line. The three identical suspended stripline filters BPF1, BPF2, and BPF3 protect the receiver
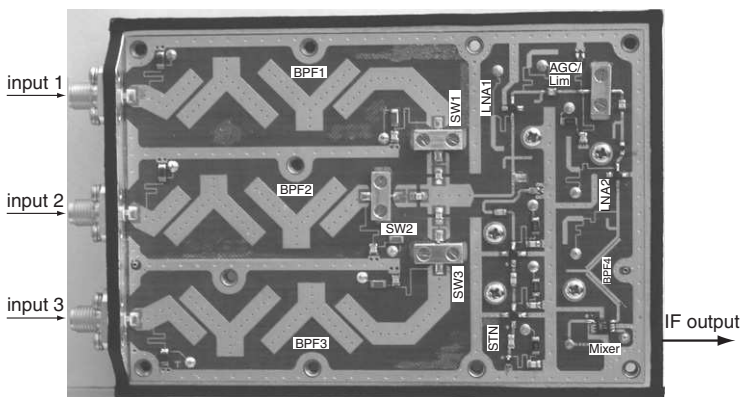
Figure 13.7. *C*-band receiver ASSY (used in Rockwell Collins MLS).

from strong prasitic signals. The fourth microstrip filter, BPF4, between LNA2 and mixer, provides additional protection from parasitic signals. All wiggly coupled-line BPFs have excellent attenuation of the second harmonic (see Chapter 9).

The antenna single-pole, three-throw switch includes three shunt PIN diodes connected through quarter-wavelength suspended striplines to a common junction (see Chapter 10). The AGC/Limiter network is used to protect the LNA2 and mixer from extraneous high-power input signals. The quasi-active limiter (see Chapter 10) includes a limiter diode and a Schottky detector diode. This module provides input N.F. less than 2.5 dB, isolation between receiver channels greater than 25 dB, and input return loss better than –15 dB.

13.6. SINGLE ANTENNA RADIO ALTIMETER TX/RCV

Well-known frequency modulated continuous wave (FM-CW) radio altimeters use two antennas: one as a transmitter and the second as a receiver. Two-antenna FM-CW radio altimeters have several disadvantages that may be eliminated with a single antenna system.

The novel single antenna FM radio altimeter [15] includes a transmitter for generating a continuous wave signal with a constant FM modulation period below a critical altitude and an interrupted continuous wave signal with a variable FM modulation period above a critical altitude.

Figure 13.8 illustrates an RF TX/RCV block [15] of the single antenna radio altimeter. The single TX/RCV antenna is connected through an LPF and a ferrite circulator to the transmitter and receiver. The circulator provides coupling of the transmitter and receiver to the common antenna and isolation between the transmitter and receiver. The subassembly in Figure 13.8 was designed using a combination of microstrip and suspended stripline. The transition between the SS and microstrip line is described in [1].

FM signal with 0.5W CW power passes through the directional coupler, circulator, and LPF to the single TX/RCV antenna. The microstrip directional coupler with 15-dB coupling provides LO power for a mixer. A drop-in circulator (from "REC") provides 20-dB isolation between the TX and the RCV networks. The LPF, using a combination of microstrip and suspended stripline (see Chapter 9 and [1]), has less than 0.2-dB insertion loss and greater than 35-dB attenuation for the second harmonic.
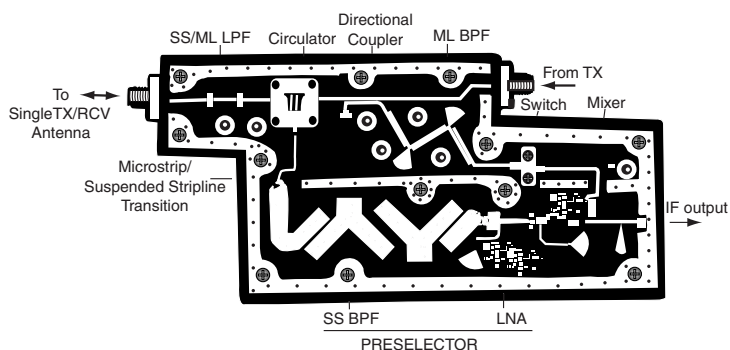
Figure 13.8. Single antenna radio altimeter transmitter/receiver block.

The LO signal passes through the microstrip wiggly BPF and SPST switch, which switches on the LO power during the CW mode and during the ICW mode in the receiving half-period. The double-balanced mixer ALY-4 (from "Mini-Circuits") has electrical performance optimized over the altimeter frequency range with a low-conversion loss of 5.7 dB.

In the receiver network, the SS BPF [1] shows the following electrical characteristics: the insertion losses are less than 0.4 dB and the second harmonic attenuation is greater than 60 dB. The receiver LNA provides 0.8-dB input N.F. and 20-dB gain.

This TX/RCV block, with a combination of SS and microstrip elements, is effective for simultaneously providing frequency selectivity, low transmitter losses, low noise figures, and small dimensions.

REFERENCES

1. Maloratsky, L. G., "Reviewing the Basic of Suspended Striplines," *Microwave Journal,* October 2002, pp. 82–98.
2. Hunter, I. C., and J. D. Rhodes, "Electrically Tunable Microwave Bandpass Filters," *IEEE Trans. on Microwave Theory and Tech.*, Vol. 30, September 1982, pp. 1354–1360.
3. Kurzrok, R. M., "Tunable Combline Filter Using 60 Degree Resonators," *Applied Microwave & Wireless*, Vol. 12, November 2000, pp. 98–100.
4. Maloratsky, L. G., "Assemble a Tunable *L*-Band Preselector," *Microwaves & RF,* September 2003, pp. 80–88.

5. Hewlett Packard, Technical Data, "3-Volts, Low Noise Amplifier for 0.8–6 GHz Application," 1998.

6. Blum, R. G., "Microwave High Power Combiner/Divider," U.S. Patent No. 5,410,281, 1995.

7. KMW, Inc., "Switchable *N*-Way Power Divider/Combiner," *Microwave Journal,* October 1996.

8. Kim, D. Y., I. Chang, "Switchable *N*-Way Power Divider/Combiner," U.S. Patent No. 5,872,491, February 1999.

9. Maloratsky, L. G., "High Efficiency Balanced Amplifier," patent pending, 2003.

10. Dosdall, C. L., and J. R. Troxel, "Calibrated High Power Radio Frequency Step Attenuator," U.S. Patent No. 6,144,265, November 7, 2000.

11. Koul, S. K., and B. Bhat, *Microwave and Millimeter Wave Phase Shifters, Volume II: Semiconductor and Delay Line Phase Shifters,* Norwood, MA: Artech House, 1991.

12. Garver, R. V., *Microwave Diode Control Devices,* Dedham, MA: Artech House, 1978.

13. White, J. F., *Microwave Semiconductor Engineering,* New York: Van Nostrand Reinhold, 1982.

14. Kyriakos, C. S., J. B. Ledebur, L. G. Maloratsky, C. E. Steen, "High-Power Precision 1 dB Step Attenuator," U.S. Patent No. 6,472,948, October 29, 2002.

15. Maloratsky, L. G., "An Aircraft Single-antenna FM Radio Altimeter," *Microwave Journal,* May 2003, pp. 196–210.

This Page Intentionally Left Blank

Design and Fabrication Technology

The RF and microwave design field is inherently exciting because of its combination of art, science, and intuition [1]. The designer has to have knowledge in different areas such as electronics, physics, mathematics, technology, and mechanical processes.

The main goals of integrated circuit design are to achieve the right level of integration and good electrical performance and provide cost-effective solutions. Module design permits us to confine all RF elements and devices within an enclosed module to ease integration and manufacturing requirements. By integrating more than one element in one module, assemblies are produced that exhibit superior microwave performance in a reduced package size at a lower-system cost than a collection of discrete elements. Better performance is the result of eliminating excess line lengths, some connectors, and multiple mismatches.

14.1. RF/MICROWAVE PACKAGES

The main functions of the packages are mechanical support, protection from the environment, power and signal distribution, and thermal stabilization. The simplest two-layer design is the stripline package. There are

different types of stripline packages [3]: sandwich package, channelized chassis, box and cover, and caseless package. The caseless stripline package (no chassis) is useful when drop-in components are to be used. The package is assembled by placing the ground-plane laminates together with the thin dielectric material between them. In this case, the unit is not reparable. There are different types of RF/microwave packages: metal package, ceramic package, plastic package, and multilayer package.

14.1.1. Metal Packages

The main purposes of the metal package are to provide mechanical strength, electric shielding, germetization, and heat sinking in the case of high-power applications. The packages have to protect the internal circuit from moisture and humidity, dust, salt spray, and so forth. In order to protect the circuit, certain methods of sealing can be used: conductive epoxy, solder, gasket material, or metallization tape.

For microwave applications, the factors critical in housing design are: low cost, light weight, vibration and temperature cycling, resistance to shock, and low loss. Usually, microwave modules consist of microelectronics circuits inside a hermetically sealed metal package. One of the main considerations in choosing the right housing material is the coefficient of thermal expansion (CTE). The housing CTE must be closed to the CTE of the MIC substrate material. Table 14.1 shows CTEs for different housing materials. Conventional thermal dissipation materials such as aluminum and copper have CTE values much higher than the MIC substrate material.

The coefficient of thermal expansion of Kovar (an iron-nickel-cobalt alloy) is very close to that of ceramic $[(6–7) \times 10^{-6}/°C]$. However, this material is extremely heavy and has poor thermal conductivity. In this case, a two-piece base design is a reasonable solution. For example, an aluminum housing, offering light weight, low cost, and good thermal conductivity, can be used with Kovar carrier (base) to compensate for the CTE mismatch between the substrate and the housing. The surface of the aluminum housing is silver plated for high conductivity and protection from oxidation. Silver-plating the housing cuts the loss by up to 10%.

For microstrip circuits, the radiated power is carried by the surface waves and radiation waves. For the shielded microstrip circuit (Table 2.1)

TABLE 14.1. Characteristics of Different Housing Materials

Characteristics	Housing Material		
	Al	Cu	Kovar
CTE $\times 10^{-6}/°C$	22.9	16.5	4.4–5.2
Density (gm/cm^3)	2.7	8.96	8.2
Thermal resistivity (°C – cm/W)	0.46	0.25	5.94
Electrical resistivity (Ω-cm)	2.1×10^{-5}	1.72×10^{-6}	$(4.5\text{-}8.5) \times 10^{-5}$

these waves change into the higher-order modes. Fitting a microstrip circuit into a housing may be looked upon as a dielectrically loaded cavity resonator [see Figure 14.1(a)] with the following inner dimensions: a is the width, l is the length, and H is the housing height [2]. These dimensions should be selected in a way such that the waveguide modes are below cutoff.

In this shielded microstrip line, longitudinal parasitic waveguide modes can exist. The wavelength of the parasitic mode is

$$\Lambda = \lambda_0 \left[\frac{\varepsilon_2}{1 - \left(\dfrac{h}{H} \right)\left(1 - \dfrac{\varepsilon_2}{\varepsilon_1} \right)} - \left(\frac{\lambda_0 N}{2a} \right)^2 \right]^{\frac{1}{2}}, \qquad (14.1)$$

where ε_1 is the dielectric constant of substrate material, ε_2 is the dielectric constant of the medium above the substrate, and N is a positive integer.

A resonance can occur if the length of the resonator is

$$l = \frac{M\Lambda}{2}, \qquad (14.2)$$

where M is a positive integer.

From (14.1) and (14.2), for $\varepsilon_2 = 1$ (air between substrate and cover), we obtain the following

$$\Lambda = \frac{2l}{M} = \frac{\lambda_0}{\sqrt{p^2 - \left(\dfrac{\lambda_0 N}{2a}\right)^2}}, \tag{14.3}$$

where

$$p = \left[1 - \left(\frac{h}{H}\right)\left(1 - \frac{1}{\varepsilon_1}\right)\right]^{-\frac{1}{2}}.$$

From (14.3) we have

$$p = \left(\frac{\lambda_0}{2}\right)\sqrt{\left(\frac{M}{l}\right)^2 + \left(\frac{N}{a}\right)^2}.$$

The parasitic modes appear in this resonator if

$$H = \frac{h\left(1 - \dfrac{1}{\varepsilon_1}\right)R}{R - 1}, \tag{14.4}$$

where

$$R = p^2 = \left(\frac{\lambda_0}{2}\right)^2\left[\left(\frac{M}{l}\right)^2 + \left(\frac{N}{a}\right)^2\right].$$

From (14.4) it is possible to obtain the condition of absence of parasitic modes:

$$R - 1 < 0; \quad R < 1$$

or

$$\lambda_0^2 < \frac{4}{\left[\left(\dfrac{M}{l}\right)^2 + \left(\dfrac{N}{a}\right)^2\right]} \tag{14.5}$$

or

$$\lambda_0 < \lambda = \frac{2}{\sqrt{\left(\dfrac{M}{l}\right)^2 + \left(\dfrac{N}{a}\right)^2}}. \tag{14.6}$$

Equation (14.6) is known as the condition for wave propagation in a waveguide with dimensions $l \times a$. In this case, it can also be considered the condition for the absence of parasitic modes in a waveguide of cross-section $a \times H$ or $l \times H$. If (14.6) is not satisfied, parasitic modes can arise, and the height H must be chosen to suppress these modes. Figure 14.1(b) illustrates the resulting graphs of unfavorable H versus λ_0 for housing dimensions of $a = 24$ mm, $l = 30$ mm, and dielectric substrate with a dielectric constant of 9.8 and THK of 0.5 mm. The narrower the MIC channel, the higher the cutoff frequency of waveguide modes. The top cover and walls essentially redistribute the field of the more theoretical
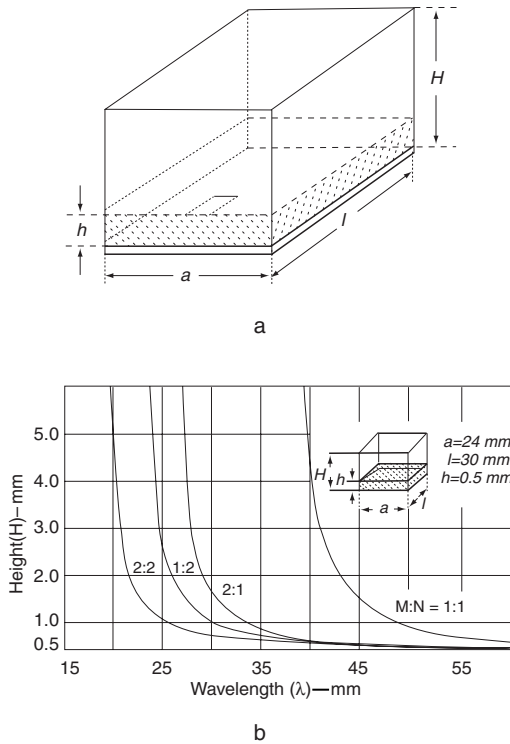
Figure 14.1. Selection of housing dimensions: housing with microstrip circuit (a); unfavorable housing height vs. wavelength and different parasitic modes (b).

microstrip and understandably have an influence on the effective dielectric constant (Figure 2.3) and characteristic impedance (Figure 2.5).

There are other known ways of reducing the effect of the housing on the characteristics of MIC. For example, RF absorption material can be placed on the inside surface of the cover plate in order to suppress the high modes. Another approach is using a metal diaphragm, which is attached to the top cover of the housing.

Suspended stripline structures are generally housed in a metallic box in order to provide isolation from other elements. The metallic box has to have a groove to suspend the dielectric substrate. The dimensions of the housing must be chosen so as to avoid propagation of undesired waveguide modes.

14.1.2. Ceramic Packages

Ceramic packages provide low weight, low cost, reduced waveguide box resonance, and can easily integrate signal lines and vias. The package of ceramic construction is based on a metallized alumina substrate, ceramic cover, and sealed with an epoxy preform. The thermal coefficient of expansion of all materials is closely matched to minimize thermal stresses. In a multilayer ceramic package, on each layer passive components are deposited, and via holes for interlayer interconnects are drilled or punched.

14.1.3. Plastic Packages

Plastic packages have been widely used because of their low manufacturing cost. Plastic packages are not hermetic and are also susceptible to cracking during temperature cycling in humid environments. The implementation of plastic packages reduces the overall cost and weight compared to a hermetically sealed ceramic package. Metal-injection molding involves mixing metal powders and binders and then injection molding to the desired shape. Then, the binders are removed and the housing is sintered at temperatures close to 1,000°C to produce a solid single-piece structure. Plastic packages are used to house predominantly low-frequency (typically below 2 GHz) devices. The typical injection-molded plastic package process is described in [4, 5].

14.2. THREE-DIMENSIONAL DESIGN

High-density RF and microwave modules can be fabricated in a three-dimensional configuration [6–8]. Such a configuration can consist of various combinations of multilayer, horizontal-vertical, and flexible structures. Three-dimensional structures provide the freedom to design in all axes. A typical three-dimensional configuration includes a multilayer structure combined with vertical passive elements, vias, transitions, connectors, coupling elements, shielding metal walls, and so forth.

14.2.1. Horizontal-Vertical Configuration

Examples of horizontal-vertical design are described in Chapter 12 (Figure 12.7) and [6]. High density interconnections between different layers of a multilayer structure can be obtained by building flexible printed circuits. Flexible circuits are based on polyamide Kapton ($\varepsilon = 3.45$, $\tan\delta = 0.002$), polyester Mylar ($\varepsilon = 3.35$, $\tan\delta = 0.0115$),[*] and epoxy substrates. Dielectric flexible substrate must be thin (0.5–2 mil). Flexible circuits are available in three basic types: single layer, double layer, and multilayer. It is sometimes necessary to add a section of rigid board material to a flexible circuit to stiffen the flex.

14.2.2. Multilayer Structures

Multilayer techniques are used for microwave and RF integrated circuits to significantly increase the density of modules, reduce weight, improve reliability, and reduce system cost. The other reason for employing multilayer configuration is that several circuit functions are difficult to realize in a single-layer planar structure, for example, baluns and tight coupling directional couplers (see Chapter 7). Multilayer configuration also provides integration of RF, analog, digital circuitry, and printed antennas in single modules.

Traditional designs use separate digital and RF subassemblies with special connections (cables, connectors, feed-through filters, and so forth). The modern multilayer boards can incorporate both RF and periph-

*Kapton and Mylar are registered trademarks of DuPont.

eral components such as a digital board. For example, PTFE material inserts for circuits integrated into an RF-4 multilayer PCB for low frequency and digital circuits.

There are two different design approaches for transition between layers: electromagnetic coupling and direct contact. For the stripline, print ground planes can provide decoupling or shielding between different layers. Interconnections between layers can be achieved with plated through holes or vias, which provide vertical electrical signal connections. The via [Figure 4.7(a)] is used in series with the signal line when changing layers. This design is effective in that it is a low inductance connection. Unlike traditional transmission lines, vias do not have ground planes to support well-guided electromagnetic waves. A method for modeling and analyzing vias in multilayer integrated circuits is presented in [7].

Via holes are formed by laser drilling, followed by metallization and via fillets. To produce a plated via hole, a hole must have good sidewall texture and surface roughness, via placement accuracy, repeatability, and via hole size. The diameter of a plated-through-hole should be approximately five times greater than the board thickness [9]. Such a diameter is large enough to allow for reliable plated-through metallization, but is still smaller than the width of the connecting line. The smallest via diameter that can be laser drilled and reliably plated through is at least 0.01 in. in diameter. Therefore, the strip width should be no less than 0.012 in. A via hole exhibits increasing radiation due to the increased electrical length of the via at high frequencies.

Instead of via holes, a slot in the ground plane can act as the connection between layers. This practice eliminates the need for ohmic contact, which is sometimes difficult to ensure.

The air-bridge structure is used in MICs to bridge a signal over to other conductors, like, for example, in the spiral inductors [see Figure 4.2(g)]. The values of width W_B, span l_B, thickness h_B, and height h_B have been determined as a compromise between electrical and mechanical requirements. With the thickness of two to three microns, the air bridges must not be damaged during handling.

In the multilayer construction, dielectric-substrate characteristics are very important. The most critical parameter is the Z-axis coefficient of thermal expansion (CTE). Higher CTE will limit the total number of layers that can be stacked in a multilayer assembly. A high Z-axis CTE can result in poor reliability of plated through-holes in multilayer boards

thicker than 0.03 in. A material with low CTE minimizes residual stresses during cladding. Dielectric material RT 6002 with good CTE of 24 ppm/°C is recommended for multilayer RF boards [10].

Multilayer design is very useful for multichannel dividers and combiners. One version of an N-way divider/combiner was shown in Chapter 8 and [11]. This network utilizes N quarter-wavelength transmission lines. Isolation between divider N output ports is realized by resistors R_I connected between output of transmission lines and common node. This multichannel network presents a serious packaging problem. In practice, the devices are difficult to realize in a planar structure when $N > 2$ as the resistors to be connected to a floating common node [12] (see Figure 8.17). The N-way planar circuits are subject to signal crossover and cross-coupling, which adversely affects the isolation and mismatching characteristics. Also, this crossover configuration limits the power-handling capability of the high-power divider/combiner. The size of this network increases drastically as the number of ports increases.

To overcome these limits, the multilayer design can be used. Figure 14.2 represents a multilayer three-dimensional design [11]. The input connection of quarter-wavelength transmission lines and floating common node are realized by vias in multilayer construction. In Figure 14.2(a, b) two microstrip dividers are connected back to back. Input 5 is connected to stripline, and outputs 1, 2, 3, and 4 are connected to microstrip lines. Figure 14.2(c, d) represents a multilayer six-way divider with all stripline input/outputs with similar connection between layers by vias. This multilayer three-dimensional design is considerably more compact than a traditional planar design.

A multilayer structure can be realized by Low Temperature Cofired Ceramics (LTCC) technology (see Section 14.3.1). LTCC technology is a low-cost process for fabrication of multilayer ceramic structures with easy-to-integrate divider circuit components like via holes and thick film resistors.

In multilayer structures, a combination of different print transmission lines is possible. For a multilayer design with various transmission-line types, special transitions between these lines are necessary. These transitions have to provide very low return loss, wide bandwidth, and very high transmission efficiency. Let us consider useful transition circuits.

Figure 1 of Table 14.2 illustrates a transition between two striplines using a slot resonator in the common ground plane for coupling. A transi-
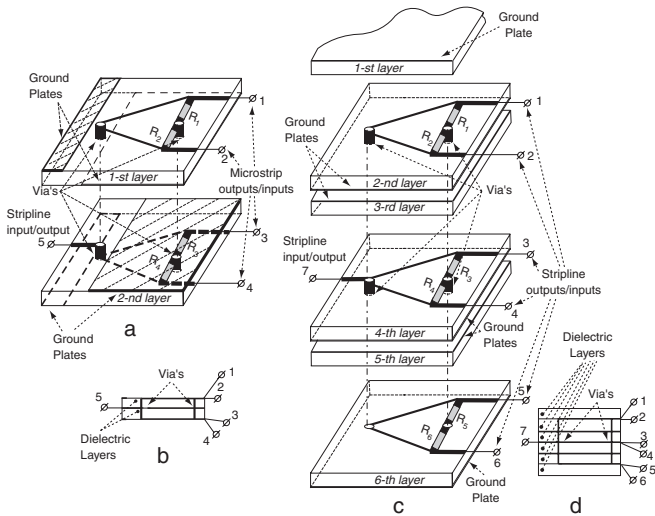
Figure 14.2. Multi-layer divider: 4-way microstrip/stripline divider (a, b); 6-way stripline divider (c, d).

tion between microstrip line and stripline (Figure 2 of Table 14.2) is also realized by means of a slot in the common ground plane.
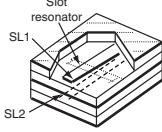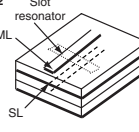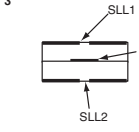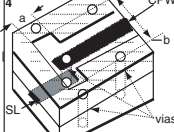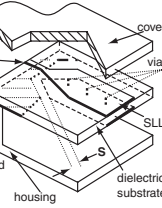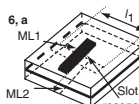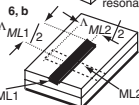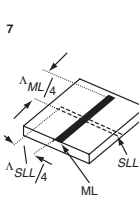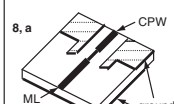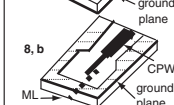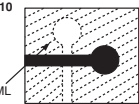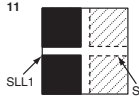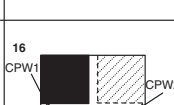
In Figure 3 of Table 14.2, two slotlines, SLL1 and SLL2, are coupled by a stripline (SL) [13].

Figure 4 of Table 14.2 illustrates the SL-CPW transition [14, 15]. The center conductors of the two lines and also ground planes are connected by via holes. The dimensions *a* and *b* are chosen for optimum matching.

A transition between SSL and microstrip line ML is shown in Figure 5 of Table 14.2 [16]. The top conductors of the ML and SS are placed on the same side of a single dielectric substrate and share the same top ground plane (cover). The bottom conductor of the SS has no connection with the microstrip bottom ground plane, which is connected with the bottom SS ground plane (housing). Improvement in bandwidth and size reduction can be carried out by adjusting the transition-line shape and dimension *S* (see Figure 5 of Table 14.2).

Figure 6(a) of Table 14.2 illustrates aperture transition for back-to-back microstrip lines ML1 and ML2 with a coupling slot printed on the common ground plane. Total transmission can be reached if the orientation angle of the slot is properly chosen. The length (l_1) of the slot resonator required for transition is between one-fourth and one-third of the

TABLE 14.2. Different Types of Print Transition Circuits

	STRIPLINE (SL)	MICROSTRIP (ML)	SLOTLINE (SLL)	COPLANAR WAVEGUIDE (CPW)
STRIPLINE (SL)	1	2	3	4
MICROSTRIP (ML)	5	6, a / 6, b	7	8, a / 8, b
SLOTLINE (SLL)	9 See #3	10	11	12
COPLANAR WAVEGUIDE (CPW)	13 See #4	14	15	16

microstrip guide wavelength [17]. The bowtie slot increases the bandwidth up to 50% [18]. The opened MLs are extended a certain distance beyond the slot, so that their extenuation may act as a tuning stub. This tuning stub can be realized as a radial stub or delta stub to enhance the transition bandwidth. In addition, its length is reduced as compared with a rectangular microstrip case.

A transition between two proximity-coupled open-ended MLs in a double-layer planar structure is shown in Figure 6(b) of Table 14.2. In this transition, the open-circuited ML1 is printed on the top dielectric substrate and crossed at a right angle by another open-circuited ML2 that is printed on the bottom substrate. These two lines are extended a certain distance beyond the cross junction to provide tuning stubs. The coupling

is maximal when the length of each stub is equal to half the wavelength in the corresponding line [19]. For this transition, the dielectric constant of the substrate has a strong effect on coupling.

A transition between a slotline and ML is shown in Figure 7 of Table 14.2 [19–21]. An ML on one side of the substrate and a slotline etched into the microstrip ground plane have equal characteristic impedances, cross each other at a right angle, and extend a quarter of the guide wavelength beyond the crossing point. The ML extends beyond the crossover and is terminated in an open circuit. Similarly, the slotline extends beyond the crossover and is terminated in a short circuit. Coupling between two lines occurs by means of the magnetic field. In the intersection of the two lines, a short circuit of the ML cancels the field of the ML (*E*-field that is perpendicular to the substrate plane), and an open circuit of the slotline reinforces the field of the slotline (*E*-field that is tangential to the slot). This transition works on a bandwidth of 30% or more. To improve bandwidth (up to one decade), microstrip and slotline stubs can be realized in the form of circular geometry of various diameters (see Figure 10 of Table 14.2) [22].

A transition from coplanar waveguide to ML is illustrated in Figure 8(a) of Table 14.2 [23]. Center conductors of the two transmission lines are continuous, with small width compensation. The ground plane of the CPW is coupled to the ground plane of the ML by the overlap of the two ground planes.

An overlay transition between an ML and CPW is shown in Figure 8(b) of Table 14.2 [23, 24]. The coplanar waveguide and ML lie on opposite sides of a single substrate and share the same ground plane. Coupling between both transmission lines increases with the overlap area, and at the same time characteristics of the transition become more frequency dependent.

Figure 11 of Table 14.2 shows a transition between slotlines SLL1 and SLL2 with two opened quarter-wavelength stubs. These stubs are connected in series.

A broad bandwidth transition (more than two octaves) between a coplanar waveguide and slotline is shown in Figure 12 of Table 14.2 [23]. This transition using a coplanar waveguide radial stub with a diameter of $\Lambda/4$ would give a wider bandwidth. The CPW and slotline are connected without banding of transmission lines. Therefore, the circuit is simple and more flexible.

Figure 14 of Table 14.2 illustrates transition between a coplanar waveguide and ML. Two series slotline stubs are used.

A transition circuit from a CPW to SLL is shown in Figure 15 of Table 14.2 [18, 23]. The CPW and slotline cross each other at a right angle. In this uniplanar approach, the CPW extends one quarter-wavelength beyond the slotline and terminates with an open end, while the slotline extends one quarter wavelength beyond the CPW and terminates with a short end. These extensions are used as tuning matching stubs. The slotline characteristic impedance can be chosen to be as high as possible to increase the bandwidth.

A transition between two coplanar waveguides CPW1 and CPW2 (see Figure 16 of Table 14.2) includes two quarter-wavelength open-circuited slotline stubs connected in parallel [25].

14.3. FABRICATION ASPECTS

Directions of modern microwave technology are smaller sized, lighter weight, and of increased complexity at a lower cost. As a result, over the past 30 years, many conventional waveguide and coaxial components have been replaced by MICs.

RF and MICs can be divided into three categories: hybrid MICs (HMICs), monolithic MICs (MMICs), and a combination of HMICs with MMICs (HMMICs).

14.3.1. HMICs

In HMICs, discrete solid-state active devices and passive components are mounted on a dielectric or ferrite substrate and connected to the passive circuits and transmission lines, which are deposited on the same substrate.

The high dielectric constant of the substrate can bring down the size of the module. Alumina (Al_2O_3, $\varepsilon = 9.6$–9.9) is the most popular substrate material, which provides good low-loss performance. However, in millimeter-wave devices, due to fabrication tolerances, the substrate dielectric constant should be low. Quartz with $\varepsilon = 3.78$ is more suitable for high-frequency application (> 20 GHz), because it provides relaxed dimensional tolerances and a higher Q-factor. AlN and BeO substrates provide excel-

lent thermal conductivity, but these materials are still a very expensive alternative. Soft Teflon material with a permittivity of 2 to 10 provides low cost but poor thermal transfer. Table A.1 of Appendix A describes characteristics of microwave substrates for HMICs [26, 27].

Passive circuits of HMICs use distributed elements, lumped elements, or a combination of both. The distributed microwave passive circuits are fabricated by using two main technological processes: thin film and thick film. Also, there are several different techniques used to fabricate planar circuits, which include PCB, LTCC, DBC, and others.

Thick-film technology [28–32] is useful in low-cost manufacture and has been developed for HMICs operating at frequencies up to about 20 GHz. The thick-film technology includes printing, baking, and trimming processes. Special pastes are placed on a screen with areas opened for circuit pattern. Some of the paste is squeezed through these open areas and paste is transferred onto the substrate. Conductive paste (silver, gold, palladium-gold, and so forth) is used for conductors, resistive paste is used for resistors, and dielectric paste is used for capacitors and coupled lines. Cleaning and drying take place after printing. Then a baking process returns the material to the solid state. After baking, laser trimming is used to adjust resistors. To complete the circuits, other passive and active components are typically attached by soldering. The most commonly used dielectric materials are Al_2O_3 (96%), AlN, and BeO (see Appendix A). Thick-film technology allows a combination of RF and digital functions on a common alumina substrate.

Thin-film technology [30, 32, 33] involves sputtering a metal (chromium, nickel, and so forth) that has good adhesive performance with substrate to form a thin (approximately 100°–200°A) adhesive layer. The next step is sputtering a layer of Au having a similar thickness. After this step is the optical printing. The circuit pattern is formed by using photolithographic techniques. A photoresist for optical printing is exposed to collimated ultraviolet light. After etching, the photoresist is removed. Then, a high-conductivity metal is electroplated on to provide the necessary thickness of the metal film of three to five skin depths. The skin depths vary for different metals and depend on the microwave frequency (see Appendix B). Finally, gold electroplating provides an environmental protective layer. A gold-plated surface can weaken a solder joint because of migration of the gold into the solder connection during solder reflow.

Pretinning the solderable gold surface prior to assembly can help reduce the gold migration. The key adhesion factor (metal to dielectric substrate) is surface roughness. The surface should be polished to roughly an order of magnitude better than the resistive film thickness. Typical substrate materials are Al_2O_3 (99.6%), AlN, BeO, and quartz (see Appendix A).

Thin-film technology provides excellent characteristics: minimum lines and space width (~0.0005 in.) and resistor tolerances (~0.1%). In comparison with thick-film technology, the thin-film process can achieve a higher accuracy of print circuit and about 20% less loss. However, the thin-film process is very expensive, and the dielectric surface must be extremely smooth for good adhesion.

Printed circuit technology is used to etch the required patterns on the copper laminated plastic substrates. These plastics of soft substrate, coming under the organic group (see Table A.2 of Appendix A), have low dielectric constants, are easy to machine (by milling, drilling, and punching), have low cost and low loss, and are the most commonly used materials for HMICs. The most widely used materials are woven Teflon fiberglass, microfiber Teflon glass, polyolefin, and so forth, varying in dielectric constant from 2.2 to 10.5. It is very important to select the correct dielectric substrate for both electrical and cost considerations.

Dielectric materials are available with copper cladding on one or both sides of a substrate. The copper cladding is specified in ounces. This refers to the weight of copper used per square foot of surface. Common weights are 0.5 oz, 1 oz, and 2 oz, and corresponding copper thickness as specified being 0.7 mil, 1.4 mil, and 2.8 mil. For the PTFE dielectric material, the coefficient of thermal expansion is close to that of copper, and therefore the printed circuit board has good dimensional stability and plated through-hole reliability.

Two basic types of copper are available for PCBs: electrodeposite (ED) and rolled annealed (RA) copper. RA copper has higher resistance to tensile stress and to repeated bending and more conductivity than ED copper. ED copper provides a rough surface, which is desirable for good adhesion to the dielectric substrate. For plated-through-hole design, additional ED copper is plated.

Thinner copper is preferred because it requires less etching, and therefore improves width and space tolerances. A tolerance of +/–0.5 mil is common for 0.5-oz cladding, and a tolerance of +/–1.0 mil is common for

1-oz cladding. At the same time, the thinnest metal has to meet other requirements: losses and power handling (see Chapter 2).

The poor corrosion properties of bare copper make it undesirable for practical application. Conventional tin-lead plating is quite satisfactory for lower frequencies in the range of 1 GHz. At higher frequencies, the skin-effect phenomenon affects the circuit performance. Solder plating is generally the most popular plating finish. Gold is a very good conductor and has excellent corrosion resistance. However, when the copper-gold combination is etched, accelerated etching takes place on copper because of electromagnetic potentials, resulting in poor edge definition. An additional nickel barrier between copper and gold ensures gold/copper diffusion.

During the etching process, a chemically resistant mask in the shape of the desired circuit is applied to the metal. This process forms different passive elements, transmission lines, and interconnections. Other components (resistors, capacitors, inductors, and active elements) are assembled using soldering techniques or conductive epoxy. Where components are soldered to the tracks, it is useful to apply a solder mask to prevent the solder from being drawn away from solder pad areas.

Advantages of the print circuit technology are low cost, low conductor loss, and simplicity in producing HMICs. Disadvantages are high dielectric loss for frequencies greater than 10 GHz, low thermal conductivity, large size, and radiation due to the low dielectric constant of the substrate.

The *DBC* process [34] is used for directly bonding the copper sheet to the ceramic or ferrite substrate, after which a pattern is formed thereon by masking and etching. The use of 10-mil-thick solid copper foil provides lateral as well as vertical heat flow, resulting in a very low thermal resistance. For high-power applications, the substrate selection is very important. Aluminum nitride (AlN) and beryllium oxide (BeO) have excellent thermal conductivities (see Table A.1 of Appendix A). AlN offers several unique performance features. This material is nontoxic (which reduces the health risk during all fabrication operations), the thermal conductivity is more stable and is over five times greater than the more commonly used alumina (Al_2O_3), and the coefficient of thermal expansion is more closely matched to CTEs of Si and GaAs used in solid-state devices. DBC is the process in which copper foil is eutectically attached to the substrate surface. The result is an extremely strong bond of the high-conductivity copper to the substrate. The DBC film has nearly twice the adhesive strength

of the thick-film material. Using DBC, the copper foil can easily be extended beyond the edge of the substrate to form copper tabs necessary for the drop-in devices [34]. On the other hand, the patterning accuracy of a DBC film is somewhat inferior to thin and thick films. Also, the cost of parts manufactured through DBC is relatively high. In general, the combination of DBC and thick-film technology offers a designer a wide range of choices for optimizing the characteristics of HMICs.

LTCC technology is a low-cost multilayer ceramic process for fabricating high-performance RF and microwave components. The main stages of this process are next [35, 36]. The ceramic layers are cut into the correct size sheets. Via holes and cavities for connections between layers are then punched or drilled into the different tale layers. The via holes are filled with metal paste such as silver or copper, and then thick-film processing is used to print metallization patterns. Conductive, dielectric, and resistive pastes are applied on each ceramic sheet. The numerous sheets are then inspected, assembled and laminated together and cofired at around +850°C. There is only a single firing operation, reducing production time and cost. The process flow for LTCC allows for the simultaneous processing of individual layers to reduce cost and increase yield. Many passive components are built as distributed elements. The remaining lumped-element components and IC are mounted on top of the LTCC module substrate. This configuration allows the manufacture of multifunctional modules which combine active and passive integration.

The resulting design is a high-density hermetic multilayer structure that can be readily surface mounted. LTCC uses ceramics substrates based on glass compositions similar to those used in thick-film dielectrics (96% alumina; see Appendix A). LTCC offers many advantages for achieving improved reliability, temperature performance, and higher packaging densities in RF/microwave and digital integrated circuits. The disadvantage of the LTCC technology is that tape shrinkage of between 12% and 16% occurs in the *X*- and *Y*-axes and slightly more in the *Z*-axis during the firing process.

14.3.2. MMICs

MMICs are fabricated using a high-volume semiconductor technique. In MMICs active and passive devices are grown and deposited on common

semi-insulating substrate. Such circuits are produced by the processes of epitaxial growth, ion implantation, masked impurity diffusion, oxide growth, and oxide etching.

MMICs offer benefits of small size, low weight, broader bandwidth than hybrid circuits, and high reliability [37–39]. Monolithic technology can be cost-effective only in case of large volume system requirements. Disadvantages of MMICs are their expense in small quantities (below several hundred), difficult adjustment, limited heat dissipation, inherent resistive losses, and low yield because processing steps and tolerances are very tight.

The base materials generally used in MMICs are high-resistivity Si and semi-insulating GaAs (see Table A.3 of Appendix A). GaAs MMIC technology is used in the design of extremely wideband, low-power, low-noise, high-speed devices. Silicon monolithic circuits, compared to GaAs circuits, can provide higher power dissipation and low loss and cost. Silicon technology offers low-cost components for small portable wireless communication systems. Silicon is the most stable and reliable semiconductor.

Active devices, passive elements, transmission lines, and interconnections should be realized on the same substrate. The biggest problem is substrate loss, especially for high frequencies. One integration option is quasi-monolithic circuits where heteroepitaxy techniques are used to grow semiconductor layers on the dielectric substrate (e.g., silicon-on-sapphire combination). In the silicon-on-sapphire structure, the high resistivity sapphire substrate replaces the semi-insulating silicon, thus eliminating the losses associated with the low-resistivity Si substrate [40].

Glass microwave integrated circuits (GMICs) [40, 41] with glass/silicon technology are a good choice for high-frequency application. Epitaxial Si is used for active devices, and low-loss glass dielectric is used to fabricate passive elements. The expansion characteristics of silicon and glass are very close. GMIC provides good reproducibility and is suitable for hybrid applications as well as integration of multichip MMIC design.

REFERENCES

1. Gilbert, K., "Microwaves as a Profession—We Need to Tell the Story!" *Microwave Product,* July 2000, p. 3.

2. Maloratsky, L. G., "Reviewing the Basics of Microstrip Lines," *Microwaves & RF*, March 2000, pp. 79–88.

3. Laverghetta, T., *Microwave Materials and Fabrication Techniques,* Third Edition, Norwood, MA: Artech House, 2000.

4. Bufford, B., "Metal-Injection Molding Cuts Packaging Costs," *Microwave & RF,* February 1999, pp. 118–123.

5. Bierman, H., "Designers Strive for Low Cost MMIC Packages," *Microwave Journal*, September 1992, pp.100-106.

6. Contolatis, A., and V. Socolov, "90° RF Vertical Interconnects," *Microwave Journal,* June 1993, pp. 102, 104.

7. Gu, Q., and Y. E. Yang, "Modeling and Analysis of Vias in Multilayered Integrated Circuits," *IEEE Trans. on Microwave Theory Tech,* Vol. 4, No. 2, February 1993, pp. 206–213.

8. Izadian, J. S., and S. M. Izadian, *Microwave Transition Design,* Norwood MA: Artech House, 1988.

9. Hercovici, N. I., N. K. Das, and J. Klugman, "A Microstrip Array Fed by a New Type of Multilayer Feeding Network," *Microwave Journal,* July 1995, pp. 124–134.

10. Ho, C.-H., L. Fan, and K. Chang, "Experimental Investigations of CPW-Slotline Transitions for Uniplanar Microwave Integrated Circuits," *IEEE MTT-S International Microwave Symp. Dig.,* Atlanta, Georgia, Vol. 2, 1993, pp. 877–880.

11. Maloratsky, L. G., and S. Y. London, "Quarter-Wavelength *N*-Way Power Dividers/Combiners: Historical Aspects and New Modifications," *Microwave Journal*, September 2003, pp. 194–202.

12. Wilkinson, E., "N-Way Hybrid Power Divider," *IRE Trans. Microwave Theory Tech.,* Vol. MTT-8, No. 1, January 1960, pp. 116–118.

13. Choung, Y. H., and W. C. Wong, "Microwave and Millimeter-Wave Slotline Transition Design," *Microwave Journal,* March 1994, pp. 77–89.

14. Simon, W., et al., "Design of Passive Components for K-Band Communication Modules in LTTC Environment," *International Symp. on Microelectronics,* IMAPS, TP2, Chicago, Illinois, 1999.

15. Gvozdev, V. I., and E. I. Nephyedov, *Three Dimensional Microwave Integrated Circuits,* Moscow, Russia: Nauka, 1985.

16. Maloratsky, L. G., "Reviewing the Basics of Suspended Striplines," *Microwave Journal,* October 2002, pp. 82–98.

17. Herrick, K. J., and L. P. B. Katehi, "Microtechnology in the Development of Three-Dimensional Circuits," *IEEE Trans. on Microwave Theory Tech.,* Vol. 46, No. 11, November 1998, pp. 1832–1843.

18. Chen, C., and Alexopoulos, N.G., "Optimization of Aperture Transitions for Multiport Microstrip Circuits," *IEEE Trans. on Microwave Theory Tech.,* Vol. 44, No. 12, December 1996.

19. Cohn, S. B., "Slot-Line on a Dielectric Substrate," *IEEE Trans. on Microwave Theory Tech.,* Vol. 17, 1969, pp. 768–778.

20. Radmanesh, M. M., and B. W. Arnold, "Generalized Microstrip-Slotline Transitions: Theory and Simulation vs. Experiment," *Microwave Journal,* June 1993, pp. 88–94.

21. Gupta, K. C., R. Garg, and I. J. Bahl, *Microstrip Lines and Slotlines,* 2nd ed., Norwood, MA: Artech House, 1996.

22. De Ronde, F. C., "A New Class of Microstrip Directional Couplers," *Digest of Tech. Papers, G-MTT Symp.,* 1970, pp. 184–189.

23. Hougart, M., and C. Aury, "Various Excitation of Coplanar Waveguides," *IEEE MTT-S Int. Microwave Symp. Digest,* 1979.

24. Burke, J. J., and R. W. Jackson, "Surface-to-Surface Transition Via Electromagnetic Coupling of Microstrip and Coplanar Waveguide," *IEEE Trans. on Microwave Theory Tech.,* Vol. 37, No. 3, March 1989, pp. 519–525.

25. Ho, C.-H., L. Fan, and K. Chang, "Broad-Band Uniplanar Hybrid-Ring and Branch-Line Couplers," *IEEE Trans. on Microwave Theory Tech.,* Vol. 41, No. 12, December 1993, pp. 2116–2125.

26. Daigle, B., "PCB Materials and Design Approaches for Commercial Microwave Applications," *Microwave Journal,* February 1996, pp. 94–98.

27. Bahl, I. J., and K. Ely, "Modern Microwave Substrate Materials," *Microwave Journal,* 1990 State of the Art Reference, pp. 131–145.

28. Bahl, I. J., and P. Bhartia, *Microwave Solid State Circuit Design,* New York: John Wiley & Sons, 1988.

29. Caulton, M., and H. Sobol, "Microwave Integrated-Circuit Technology—A Survey," *IEEE J. Solid State Circuits,* SC-5, December 1970, pp. 292–303.

30. Ramy, J.-P., et al., "Optimization of the Thick- and Thin-Film Technologies for Microwave Circuits on Alumina and Fused Silica Substrates," *IEEE Trans. on Microwave Theory Tech.,* Vol. MTT-26, No. 10, October 1978, pp. 814–820.

31. Harper, C. A. (ed.), *Handbook of Thick Film Hybrid Microelectronics,* New York: McGraw-Hill, 1974.

32. Maisseel, L. I., and R. Gland, *Handbook of Thin-Film Processing,* New York: McGraw-Hill, 1983.

33. Roddy, D., *Microwave Technology,* Englewood Cliffs, NJ: Prentice Hall, 1986.

34. Iwase, N., et al., "Thick Film and Direct Bond Copper Forming Technologies for Aluminum Nitride Substrate," *IEEE Trans. CHMT,* HMT-8, No. 2, 1985, pp. 253–258.

35. Eustice, A. L., et al., "Low Temperature Co-Fireable Ceramics: A New Approach for Electronic Packaging," *Proc. of 36th Electronic Component Conference,* Seattle, Washington, May 5–7, 1986, pp. 37–47.

36. Scratom, C. Q., and J. C. Lawson, "LTCC Technology: Where We Are and Where We're Going To," *Proc. of the IEEE MTT-S International Topical Symposium for Wireless Applications,* February 1999, pp. 193–200.

37. Hoffman, R. K., *Handbook of Microwave Integrated Circuits*, Boston: Artech House, 1987.

38. Goyal, R., et al., *Monolithic Microwave Integrated Circuits: Technology and Design,* Norwood, MA: Artech House, 1989.

39. Abbott, D. A., et al., "Monolithic Gallium Arsenide Circuits Show Great Promise," *Microwave Systems News,* August 1979, pp. 73–79.

40. Eron, M., J. Perko, and R. J. Gibson, "Fabrication Process Combines Low Cost and High Reliability," *Microwaves & RF,* October 1993, pp. 61–68.

41. Danehy, K., and M. Wolf, "mm-Wave Microelectronics Manufacturing," *Microwave Journal,* September 1998, pp. 138–146.

This Page Intentionally Left Blank

APPENDIX A

Substrates

This appendix describes properties of commercial dielectrics, ferrite, and semiconductor substrate materials using in RF and microwave integrated circuits.

Table A.1 illustrates properties of typical HMIC substrate materials.

Table A.2 shows properties of typical PCB substrate materials.

Table A.3 illustrates comparison of MMIC substrate materials.

TABLE A.1. Properties of Typical HMIC Substrate Materials

Material	Dielectric Constant @ 10 GHz	Dissipation Factor @ 10 GHz	Volume Resistivity $\Omega - cm$	Thermal Conductivity $W/m\text{-}K$	CTE $X10^{-6}/°C$	Density g/cm^3	Dielectric Strength KV/mm
Alumina Al_2O_3 96%	9.5	0.0004	$>10^{14}$	28	6.7	3.8	23.6
Alumina Al_2O_3 99.6%	9.8	0.0002	$>10^{14}$	36	6.9	3.97	10
Aluminum Nitride ALN 99.5%	8.8	0.001	$>10^{13}$	140–230	4.4	3.26	>5
Supphire	9.4; 11.6	0.0001	$>10^{16}$	46	5.3	3.97	40
Beryllia BeO	6.6	0.003	$>10^{14}$	260	9	2.9	9.6
Fuzed Quartz	3.78	0.0001	$>10^{14}$	1.0	0.55	2.2	100
Ferrite/garnet	13–16	0.0005	$>10^{12}$	3.0	8–9	5.3	400

TABLE A.2. Properties of Typical PCB Substrate Materials

Material	Dielectric Constant @ 10 GHz	Dissipation Factor @ 10 GHz	Volume Resistivity $\Omega - cm$	Thermal Conductivity $W/m\text{-}K$	CTE $X10^{-6}/°C$	Dielectric Strength KV/mm
FR-4	4.3	0.01	6×10^6		15 (x-y) 50 (z)	50
Duroid-5880 Rogers Cor.	2.2	0.0009	2×10^7	0.26	31 (x) 48 (y) 237 (z)	
TMM-10 Rogers Cor.	9.2	0.0017	2×10^7	0.73	16 (x-y) 20 (z)	
TLE- 95 Taconic	2.95	0.0028	10^7	0.23	9-12 (x-y) 70 (z)	>60
RF-35 Taconic	3.5	0.0018	10^9	0.2	19-24 (x-y) 64 (z)	41
Di Clad 522 Arlon	2.5	0.0025	10^7		10-17 (x-y) 250 (z)	45
Di Clad 810 Arlon	10.5	0.0015	1.6×10^5			60

TABLE A.3. Comparison of MMIC Substrates

Material	Dielectric Constant	Dissipation Factor	Volume Resistivity $\Omega - cm$	Thermal Conductivity $W/m\text{-}K$	Density g/cm^3	Surface Roughness μm	Max. Operation Temperature $°C$
Si	11.7	0.001–0.01	10^3–10^5	151	2.3	1.0	250
Ga As	12.9	0.006	10^7–10^9	54	5.3	1.0	350

APPENDIX B

Properties of Metals

The electrical and mechanical properties of commonly used metals in RF and microwave integrated circuits are given in Table B.1.

TABLE B.1. Properties of Metals

Metal	Volume Resistivity $\Omega - cm$	Thermal Conductivity $W/m\text{-}K$	Normalized Skin Depth $\delta\sqrt{f} \times 10^{3}\,\mu in$ $(GHz)^{1/2}$	Skin Depth δ @ 10 GHz $x10^{3}(\mu in)$	CTE ppm/°C	Density g/cm^{3}	Adherence to Substrate
Copper	1.72	392	82	25.9	18	8.94	poor
Silver	1.62	406	79.7	25.2	21	10.49	poor
Gold	2.44	295	97	30.7	15	19.3	poor
Aluminum	2.62	217	102.4	32.4	26	2.7	poor
Nickel	7.4	91.6	164	52	13.3	8.9	good
Tantalum	13.5	57.5	244	77.2	6.6	16.6	good
Platinum	10.6	70.7	204	64.5	8.9	21.45	
Molibdenum	5.7	145.4	149	47.1	4.6	10.2	fair
Vanadium	19.6	31.6	147.5	46.6	6.0	6.1	fair
TIN	11.4	73.2			23.5	7.3	

APPENDIX C

Two-Port Network Representations

This appendix illustrates normalized transfer and scattering matrices of typical two-port networks used in RF and microwave integrated circuits (Table C.1); relationships between classical normalized transfer matrices $[A]$- (or $[ABCD]$-), normalized impedance matrices $[Z]$, and normalized admittance matrices $[Y]$ (Table C.2); relationships between classical normalized transfer matrices $[A]$- (or $[ABCD]$-), wave normalized transfer matrices $[T]$, and normalized wave scattering matrices $[S]$ (Table C.3), and relationships between normalized and non-normalized matrices.

TABLE C.1. *A-* (or *ABCD-*), *T-*, and *S*–Matrices for Typical Two-Port Networks

Element Name	Circuit	$[A]$ or $[ABCD]$	$[T]$	$[S]$
Series impedance		$\begin{bmatrix} \sqrt{R} & \dfrac{Z}{\sqrt{R}} \\ 0 & \dfrac{1}{\sqrt{R}} \end{bmatrix}$	$\begin{bmatrix} \dfrac{Z+R+1}{2\sqrt{R}} & \dfrac{R-Z-1}{2\sqrt{R}} \\ \dfrac{Z+R-1}{2\sqrt{R}} & \dfrac{R-Z+1}{2\sqrt{R}} \end{bmatrix}$	$\begin{bmatrix} \dfrac{Z+R-1}{Z+R+1} & \dfrac{2\sqrt{R}}{Z+R+1} \\ \dfrac{2\sqrt{R}}{Z+R+1} & \dfrac{Z-R+1}{Z+R+1} \end{bmatrix}$
Shunt admittance		$\begin{bmatrix} \sqrt{R} & 0 \\ Y\sqrt{R} & \dfrac{1}{\sqrt{R}} \end{bmatrix}$	$\begin{bmatrix} \dfrac{R(1+Y)+1}{2\sqrt{R}} & \dfrac{R(1+Y)-1}{2\sqrt{R}} \\ \dfrac{R(1-Y)-1}{2\sqrt{R}} & \dfrac{R(1-Y)+1}{2\sqrt{R}} \end{bmatrix}$	$\begin{bmatrix} \dfrac{R(1-Y)-1}{R(1+Y)+1} & \dfrac{2\sqrt{R}}{R(1+Y)+1} \\ \dfrac{2\sqrt{R}}{R(1+Y)+1} & \dfrac{1-R(1+Y)}{R(1+Y)+1} \end{bmatrix}$
Section of uniform line without losses		$\begin{bmatrix} \cos\Theta & i\sin\Theta \\ i\sin\Theta & \cos\Theta \end{bmatrix}$	$\begin{bmatrix} e^{i\Theta} & 0 \\ 0 & e^{-i\Theta} \end{bmatrix}$	$\begin{bmatrix} 0 & e^{-i\Theta} \\ e^{-i\Theta} & 0 \end{bmatrix}$
Section of uniform line with losses		$\begin{bmatrix} \cosh\gamma l & \sinh\gamma l \\ \sinh\gamma l & \cosh\gamma l \end{bmatrix}$	$\begin{bmatrix} e^{\gamma l} & 0 \\ 0 & e^{-\gamma l} \end{bmatrix}$	$\begin{bmatrix} 0 & e^{-\gamma l} \\ e^{-\gamma l} & 0 \end{bmatrix}$

TABLE C.1. *A*- (or *ABCD*-), *T*-, and *S*–Matrices for Typical Two-Port Networks *(continued)*

Element Name	Circuit	[A] or [ABCD]	[T]	[S]
Connection of lines with different impedances	z_1 $\mid$ z_2	$\begin{bmatrix} \sqrt{R} & 0 \\ 0 & \dfrac{1}{\sqrt{R}} \end{bmatrix}$	$\begin{bmatrix} \dfrac{R+1}{2\sqrt{R}} & \dfrac{R-1}{2\sqrt{R}} \\ \dfrac{R-1}{2\sqrt{R}} & \dfrac{R+1}{2\sqrt{R}} \end{bmatrix}$	$\begin{bmatrix} \dfrac{R-1}{R+1} & \dfrac{2\sqrt{R}}{R+1} \\ \dfrac{2\sqrt{R}}{R+1} & \dfrac{R-1}{R+1} \end{bmatrix}$
Ideal transformer	$1{:}k$	$\begin{bmatrix} \dfrac{1}{k} & 0 \\ 0 & k \end{bmatrix}$	$\dfrac{1}{2k} \times \begin{bmatrix} 1+k^2 & 1-k^2 \\ 1-k^2 & 1+k^2 \end{bmatrix}$	$\dfrac{1}{1+k^2} \times \begin{bmatrix} 1-k^2 & 2k \\ 2k & k^2-1 \end{bmatrix}$

$$Z = \frac{z}{z_1}, \; R = \frac{z_2}{z_1}, \; Y = \frac{1}{Z} = \frac{z_1}{z}, \; \Theta = \frac{2\pi l}{\Lambda} = \beta l, \; \gamma = \alpha + i\beta,$$

where z_1 and z_2 are characteristic impedances of input and output lines; Z and z are normalized and non-normalized impedances; l is the length of the line; Λ is the guide wavelength; γ is the propagation constant; α is the attenuation constant; β is the phase shift constant.

TABLE C.2. Relationships Between *A*- (or *ABCD*-), *Z*-, and *Y*-Matrices

	[Z]	[Y]	[A] or [ABCD]
[Z]	$\begin{bmatrix} Z_{11} & Z_{12} \\ Z_{21} & Z_{22} \end{bmatrix}$	$\begin{bmatrix} \dfrac{Y_{22}}{|Y|} & \dfrac{-Y_{12}}{|Y|} \\[2ex] \dfrac{-Y_{21}}{|Y|} & \dfrac{Y_{11}}{|Y|} \end{bmatrix}$	$\begin{bmatrix} \dfrac{A_{11}}{A_{21}} & \dfrac{-|A|}{A_{21}} \\[2ex] \dfrac{1}{A_{21}} & \dfrac{-A_{22}}{A_{21}} \end{bmatrix}$
[Y]	$\begin{bmatrix} \dfrac{Z_{22}}{|Z|} & \dfrac{Z_{12}}{|Z|} \\[2ex] \dfrac{Z_{21}}{|Z|} & \dfrac{Z_{11}}{|Z|} \end{bmatrix}$	$\begin{bmatrix} Y_{11} & Y_{12} \\ Y_{21} & Y_{22} \end{bmatrix}$	$\begin{bmatrix} \dfrac{A_{22}}{A_{12}} & \dfrac{|A|}{A_{12}} \\[2ex] \dfrac{1}{A_{12}} & \dfrac{A_{11}}{A_{12}} \end{bmatrix}$
[A] or [ABCD]	$\begin{bmatrix} \dfrac{Z_{11}}{Z_{21}} & \dfrac{|Z|}{Z_{21}} \\[2ex] \dfrac{1}{Z_{21}} & \dfrac{Z_{22}}{Z_{21}} \end{bmatrix}$	$\begin{bmatrix} \dfrac{Y_{22}}{Y_{21}} & \dfrac{1}{Y_{21}} \\[2ex] \dfrac{|Y|}{Y_{21}} & \dfrac{Y_{11}}{Y_{21}} \end{bmatrix}$	$\begin{bmatrix} A_{11} & A_{12} \\ A_{21} & A_{22} \end{bmatrix}$

$$|Z| = \frac{1}{|Y|} = Z_{11}Z_{22} - Z_{12}Z_{21} = -\frac{A_{12}}{A_{21}} \; ; \; |Y| = Y_{11}Y_{22} - Y_{12}Y_{21} = -\frac{A_{21}}{A_{12}} \; ; \; |A| = A_{11}A_{22} - A_{12}A_{21}$$

TABLE C.3. Relationships Between *S*-, *T*-, and *A*- (or *ABCD*-) Matrices

	[A] or [ABCD]	[T]	[S]
[A]	$\begin{bmatrix} A_{11} & A_{12} \\ A_{21} & A_{22} \end{bmatrix}$	$\dfrac{1}{2}\begin{bmatrix} T_{11}+T_{21}+T_{12}+T_{22} & T_{11}+T_{21}-T_{12}-T_{22} \\ T_{11}-T_{21}+T_{12}-T_{22} & T_{11}-T_{21}-T_{12}+T_{22} \end{bmatrix}$	$\dfrac{1}{2S_{21}}\times\begin{bmatrix} S_{12}S_{21}-(1+S_{11})(S_{22}-1) & (1+S_{11})(1+S_{22})-S_{12}S_{21} \\ (1-S_{22})(1-S_{11})-S_{12}S_{21} & (1-S_{11})(1+S_{22})+S_{12}S_{21} \end{bmatrix}$
[T]	$\dfrac{1}{2}\begin{bmatrix} A_{11}+A_{12}+A_{21}+A_{22} & A_{11}-A_{12}+A_{21}-A_{22} \\ A_{11}+A_{12}-A_{21}-A_{22} & A_{11}-A_{12}-A_{21}+A_{22} \end{bmatrix}$	$\begin{bmatrix} T_{11} & T_{12} \\ T_{21} & T_{22} \end{bmatrix}$	$\begin{bmatrix} \dfrac{1}{S_{21}} & -\dfrac{S_{22}}{S_{21}} \\ \dfrac{S_{11}}{S_{21}} & -\dfrac{|S|}{S_{21}} \end{bmatrix}$
[S]	$\dfrac{1}{|A|-(A_{11}+A_{21})(A_{21}+A_{22})}\times$ $\begin{bmatrix} |A|-(A_{11}+A_{21})\times(A_{21}+A_{22}) & -2|A|A_{21} \\ -2A_{21} & |A|-(A_{22}-A_{21})\times(A_{11}+A_{21}) \end{bmatrix}$	$\begin{bmatrix} \dfrac{T_{21}}{T_{11}} & \dfrac{|T|}{T_{11}} \\ \dfrac{1}{T_{11}} & -\dfrac{T_{12}}{T_{11}} \end{bmatrix}$	$\begin{bmatrix} S_{11} & S_{12} \\ S_{21} & S_{22} \end{bmatrix}$

$$|T|=T_{11}T_{22}-T_{12}T_{21}=\frac{S_{12}}{S_{21}}\;;\quad |S|=S_{11}S_{22}-S_{12}S_{21}=-\frac{T_{22}}{T_{11}}$$

C.1. RELATIONSHIPS BETWEEN NORMALIZED AND NON-NORMALIZED MATRICES

$$\begin{bmatrix} A_{11} & A_{12} \\ A_{21} & A_{22} \end{bmatrix} = \begin{bmatrix} a_{11}\sqrt{\dfrac{z_2}{z_1}} & \dfrac{a_{12}}{\sqrt{z_1 z_2}} \\ a_{21}\sqrt{z_1 z_2} & a_{22}\sqrt{\dfrac{z_1}{z_2}} \end{bmatrix}; \quad \begin{bmatrix} a_{11} & a_{12} \\ a_{21} & a_{22} \end{bmatrix} = \begin{bmatrix} A_{11}\sqrt{\dfrac{z_1}{z_2}} & A_{12}\sqrt{z_1 z_2} \\ \dfrac{A_{21}}{\sqrt{z_1 z_2}} & A_{22}\sqrt{\dfrac{z_2}{z_1}} \end{bmatrix};$$

$$\begin{bmatrix} Z_{11} & Z_{12} \\ Z_{21} & Z_{22} \end{bmatrix} = \begin{bmatrix} \dfrac{z_{11}}{z_1} & \dfrac{z_{12}}{\sqrt{z_1 z_2}} \\ \dfrac{z_{21}}{\sqrt{z_1 z_2}} & \dfrac{z_{22}}{z_2} \end{bmatrix}; \quad \begin{bmatrix} z_{11} & z_{12} \\ z_{21} & z_{22} \end{bmatrix} = \begin{bmatrix} Z_{11} z_1 & Z_{12}\sqrt{z_1 z_2} \\ Z_{21}\sqrt{z_1 z_2} & Z_{22} z_2 \end{bmatrix};$$

$$\begin{bmatrix} Y_{11} & Y_{12} \\ Y_{21} & Y_{22} \end{bmatrix} = \begin{bmatrix} y_{11} z_1 & y_{12}\sqrt{z_1 z_2} \\ y_{21}\sqrt{z_1 z_2} & y_{22} z_2 \end{bmatrix}; \quad \begin{bmatrix} y_{11} & y_{12} \\ y_{21} & y_{22} \end{bmatrix} = \begin{bmatrix} \dfrac{Y_{11}}{z_1} & \dfrac{Y_{12}}{\sqrt{z_1 z_2}} \\ \dfrac{Y_{21}}{\sqrt{z_1 z_2}} & \dfrac{Y_{22}}{z_2} \end{bmatrix};$$

$$\begin{bmatrix} T_{11} & T_{12} \\ T_{21} & T_{22} \end{bmatrix} = \sqrt{\dfrac{z_2}{z_1}}\begin{bmatrix} t_{11} & t_{12} \\ t_{21} & t_{22} \end{bmatrix}; \quad \begin{bmatrix} t_{11} & t_{12} \\ t_{21} & t_{22} \end{bmatrix} = \sqrt{\dfrac{z_1}{z_2}}\begin{bmatrix} T_{11} & T_{12} \\ T_{21} & T_{22} \end{bmatrix};$$

$$\begin{bmatrix} S_{11} & S_{12} \\ S_{21} & S_{22} \end{bmatrix} = \begin{bmatrix} s_{11} & \sqrt{\dfrac{z_2}{z_1}}s_{12} \\ \sqrt{\dfrac{z_1}{z_2}}s_{21} & s_{22} \end{bmatrix}; \quad \begin{bmatrix} s_{11} & s_{12} \\ s_{21} & s_{22} \end{bmatrix} = \begin{bmatrix} S_{11} & \sqrt{\dfrac{z_1}{z_2}}S_{12} \\ \sqrt{\dfrac{z_2}{z_1}}S_{21} & S_{22} \end{bmatrix}$$

APPENDIX D

List of Symbols

Symbols	Meaning	Unit
a	Filter insertion loss	dB
$a_1, a_2, \ldots$	Element traveling waves	
$a_{11}, a_{12}, \ldots$	Elements of the non-normalized classical transfer matrix	
$A_{11}, A_{12}, \ldots$	Elements of the normalized classical transfer matrix	
A_{dis}	Normalized dissipated power	
b	Height of stripline	
$b_1, b_2, \ldots$	Reflected traveling waves	
B	Normalized susceptance	
c	Velocity of light	(3×10^8) meter/second
$C_{12}, C_{13}, \ldots$	Coupling, losses, or isolation	dB

Symbols	Meaning	Unit
C	Capacitance	Farad
f	Frequency	Hertz
f_0	Center frequency	Hertz
f_c	Cutoff frequency	Hertz
g_I	g-values of the lowpass prototype structure	
G	Integration index	
h	Substrate thickness of microstrip line	inch
H	Height	inch
I	Current	Ampere
k	Propagation constant	
k_m	Coefficient of magnetic coupling	
K	Voltage coupling factor	
l	Length	inch
L	Inductance	Henry
m	Admittance ratio	
n	Number of sections	
P	Power	Watt
q	Filling factor	
Q	Quality factor	
R	Resistance	Ohm
R_s	Surface resistance	Ohm/square
S	Gap or distance between coupled lines	inch

Symbols	Meaning	Unit
$s_{11}, s_{12}, \ldots$	Elements of the non-normalized scattering matrix	
$S_{11}, S_{12}, \ldots$	Elements of the normalized scattering matrix	
t	Thickness of planar conductor	inch
$t_{11}, t_{12}, \ldots$	Elements of the non-normalized transfer matrix	
$T_{11}, T_{12}, \ldots$	Elements of the normalized transfer matrix	
v	Velocity	m/s
V	Voltage	Volt
W	Width of conductors	Inch
W_B	Relative bandwidth	
$Y_{11}, Y_{12}, \ldots$	Elements of the normalized admittance matrix	
$y_{11}, y_{12}, \ldots$	Elements of the non-normalized admittance matrix	
$y_1, y_2, \ldots$	Non-normalized admittances	
$Y_1, Y_2, \ldots$	Normalized admittances	
z_{11}, z_{12}	Elements of the non-normalized impedance matrix	
Z_{11}, Z_{12}	Elements of the normalized impedance matrix	
Z_0	Characteristic impedance	Ohm
Z_{0e}	Even-mode characteristic impedance	Ohm
Z_{0o}	Odd-mode characteristic impedance	Ohm
α	Attenuation constant	
α_c	Attenuation due to conductor loss	

Symbols	Meaning	Unit
α_d	Attenuation due to dielectric loss	
α_r	Attenuation due to radiation loss	
β	Phase constant	
Γ	Reflection coefficient	
g	Propagation constant	
d	Skin depth	
e	Permittivity	
ε_0	Permittivity of free space	8.854183×10^{-12} F/m
$\varepsilon_{\mathit{eff}}$	Effective permittivity	
j	Phase shift	
l	Free space wavelength	meter
Λ	Guide wavelength	meter
Θ	Electrical length	degree
m	Permeability	H/cm
ρ_s	Resistivity	Ohm-m
s	Conductivity	S/m
ω_c	Cutoff frequency	rad/s

Index